Atmospheric Wave-Mean Flow Interactions

by

Declan Quinn

B.Sc., The National University of Ireland, 1996

M.Sc., The National University of Ireland, 1997

A THESIS SUBMITTED IN PARTIAL FULFILLMENT OF
THE REQUIREMENTS FOR THE DEGREE OF

MASTER OF SCIENCE

in

THE FACULTY OF GRADUATE STUDIES

(Department of Mathematics)

We accept this thesis as conforming
to the required standard

THE UNIVERSITY OF BRITISH COLUMBIA

August 2000

In presenting this thesis in partial fulfilment of the requirements for an advanced degree at the University of British Columbia, I agree that the Library shall make it freely available for reference and study. I further agree that permission for extensive copying of this thesis for scholarly purposes may be granted by the head of my department or by his or her representatives. It is understood that copying or publication of this thesis for financial gain shall not be allowed without my written permission.

Department of MATHEMATICS.

The University of British Columbia
Vancouver, Canada

Date 3/8/2005.

Abstract

The interactions between the zonally-averaged flow and the various eddy circulations in the atmosphere are studied using NCEP/NCAR Reanalysis data. The contributions to zonal- and potential temperature-tendency and zonal kinetic energy production due to both the Ferrel and Hadley circulations are determined. Inferences are then made regarding the processes which affect the strong cores of the jet stream and the forms of zonally-averaged models of the atmosphere that are appropriate for studies of this type.

It will be shown that there is considerable wave-mean flow interaction in the atmosphere, with the circulation induced by eddy motions being primarily responsible for the maintainance and seasonal variations of the zonally-averaged jet core. This study also provides a repository of derived atmospheric quantities for the years 1989-1993.

CONTENTS

List of Figures

1. Introduction

Of perennial interest in the meteorological community are the processes maintaining and affecting the westerly upper-air jet streams along with the effect of these wind-speed maxima on synoptic-scale atmospheric waves. First investigated in depth during the Second World War, the subsequent rise of civil aviation has provided the impetus for many studies of mid-latitude upper-air phenomena.

The aims of this project are:

- to study the processes which affect the strong cores of the jet-stream
- to extend the results of [Pfe81] to the Southern Hemisphere and to the Arctic region; also, to improve the quality of these results in the equatorial regions
- to determine the relative importance of transient eddy and stationary eddy upward fluxes of heat and momentum and thus investigate the conjecture of [SPS70] that the vertical transient eddy flux of momentum by the synoptic-scale eddies is much greater than the vertical stationary eddy flux
- to extend the eddy-transport statistics computed by [PO92] to seasonal- and monthly-mean conditions
- to provide a baseline for possible futher investigations of the effect of the

ENSO phenomenon on the global circulation of the atmosphere

- to provide a mathematical framework for investigating the transport of ozone from its region of manufacture at the Equator to the region of destruction near the poles

It is primarily the availability of high-quality data that makes these aims feasible and, although much of the data are still somewhat questionable, with some data being more artifacts of the reanalysis model than actual measured quantities, the results should give insight into the processes maintaining the thermal-wind balance in the atmosphere.

2. Notation

Definition 2.1. *The zonal-averaging operator is*

$$[A] = \frac{1}{2\pi} \int_0^{2\pi} A \, d\lambda.$$

The departure from this average is

$$A^* = A - [A] \, .$$

Definition 2.2. *The time-averaging operator is*

$$\overline{A} = \frac{1}{t_2 - t_1} \int_{t_1}^{t_2} A \, dt.$$

The departure from this average is

$$A' = A - \overline{A}.$$

Using these definitions[1], one may write

$$A = \left[\overline{A}\right] + \overline{A^*} + [A]' + A'^*$$

These may be interpreted as decomposing a variable into:

1. a steady, zonally-symmetric component

2. a steady, zonally-asymmetric (i.e. stationary eddy) component

3. a time-varying, zonally-symmetric component (e.g. an index cycle fluctuation in the case $A = u$)

4. a time-varying, zonally-asymmetic component (e.g. a quantity associated with a storm or other transient, local event)

Other useful identities, which will be used implicitly throughout the present investigation, may be derived:

$$[AB] = [A][B] + [A^*B^*] \tag{2.1}$$

$$\left[\overline{AB}\right] = \left[\overline{A}\right]\left[\overline{B}\right] + \left[\overline{A^*B^*}\right] + \left[\overline{A'B'}\right] \tag{2.2}$$

[1] This notational scheme is a reversal of that of [Pfe81], but is in keeping with the more accepted conventions of [PO92] and [OR71].

$$\left[\overline{A'B'}\right] = \overline{[A]'[B]'} + \left[\overline{A'^*B'^*}\right] \tag{2.3}$$

Throughout the body of this work, reference is made to the decomposition of fluxes into various stationary and transient, zonally symmetric and asymmetric components; the decompositions used are

- **meridional transport**:

$$\left[\overline{Av}\right] = \left[\overline{A}\right]\left[\overline{v}\right] + \left[\overline{A^*v^*}\right] + \overline{[A]'[v]'} + \left[\overline{A'^*v'^*}\right] \tag{2.4}$$

- **downward transport**:

$$\left[\overline{A\omega}\right] = \left[\overline{A}\right]\left[\overline{\omega}\right] + \left[\overline{A^*\omega^*}\right] + \overline{[A]'[\omega]'} + \left[\overline{A'^*\omega'^*}\right] \tag{2.5}$$

where $\left[\overline{A}\right]\left[\overline{v}\right]$ and $\left[\overline{A}\right]\left[\overline{\omega}\right]$ represent the transport of A by the steady circulation in the (ϕ, p)-plane.

3. Model

The model used for the calculations is briefly described below; a detailed derivation of the model equations is given in Appendix B.

The basic equations are the zonally-averaged momentum equation (refer to Appendix B.3.3)

$$\frac{\partial [u]}{\partial t} = [v]\left(f - \frac{\partial ([u]\cos\phi)}{R\cos\phi\partial\phi}\right) - [\omega]\frac{\partial [u]}{\partial p} - \frac{\partial ([u^*v^*]\cos^2\phi)}{R\cos^2\phi\partial\phi} - \frac{\partial [u^*\omega^*]}{\partial p} + [F\lambda], \tag{3.1}$$

the zonally-averaged thermodynamic equation (refer to Appendix B.3.4)

$$\frac{\partial [\theta]}{\partial t} = -\frac{[v]}{R}\frac{\partial [\theta]}{\partial \phi} - [\omega]\frac{\partial [\theta]}{\partial p} - \frac{\partial ([\theta^*v^*]\cos\phi)}{R\cos\phi\partial\phi} - \frac{\partial [\theta^*\omega^*]}{\partial p} + \left(\frac{p_{00}}{p}\right)\kappa\frac{[Q]}{c_p}, \tag{3.2}$$

and the zonally-averaged thermal wind equation (refer to Appendix B.3.5)

$$\tilde{f}\frac{\partial [u]}{\partial p} = \frac{R_d p^{\kappa-1}}{p_{00}\kappa}\frac{1}{R}\frac{\partial [\theta]}{\partial \phi}, \tag{3.3}$$

where $\tilde{f} = \left(f + \frac{2[u]\tan\phi}{R}\right)$. Here, t represents time, R is the earth's radius, R_d is the gas constant, ϕ represents latitude, p represents pressure, p_{00} is a reference pressure level (1000 hPa), u is eastward velocity, v is northward velocity, ω $(= \frac{dp}{dt})$ is the

vertical velocity in pressure coordinates, θ is potential temperature, f $(= 2\Omega \sin\phi)$ is the Coriolis parameter, $F\lambda$ is the zonal forcing, Q is the diabatic heating, c_p is the constant pressure heat capacity of air and $\kappa = \frac{R_d}{c_p}$. Also, it is useful to define the static stability parameter $S_p = -\frac{p\kappa}{p_{00}\kappa}\frac{\partial\theta}{\partial p}$.

One may define a streamfunction ψ associated with the mean meridional circulation $([v], [\omega])$ and derive the following diagnostic equation for the streamfunction (see Appendix C)

$$\begin{aligned} & D[S_p]\frac{\partial^2\psi}{\partial\eta^2} + 2\frac{Dp^\kappa}{p_{00}\kappa}\frac{\partial[\theta]}{\partial\eta}\frac{\partial^2\psi}{\partial\eta\partial p} + \frac{Dp\kappa}{p_{00}\kappa}\frac{\partial[\theta]}{\partial\eta}\left(\frac{\kappa-1}{p}\frac{\partial\psi}{\partial\eta}\right) + \frac{Dp\kappa}{p_{00}\kappa}\frac{\partial^2[\theta]}{\partial\eta^2}\frac{\partial\psi}{\partial p} + \frac{\partial\left(C\frac{\partial\psi}{\partial p}\right)}{\cos\phi\partial p} \\ = & \frac{\partial H}{\partial\eta} + \frac{\partial\chi}{\partial p}, \end{aligned} \tag{3.4}$$

where

$$\begin{aligned} C &= \frac{\tilde{f}}{\cos\phi}\left(f - \frac{\partial([u]\cos\phi)}{R\partial\eta}\right) \\ D &= \frac{R_d}{p}\frac{1}{R^2} \\ [S_p] &= -\frac{p\kappa}{p_{00}\kappa}\frac{\partial[\theta]}{\partial p} \\ H &= \frac{R_d p^{\kappa-1}}{p_{00}\kappa R}\left(\left(\frac{p_{00}}{p}\right)\kappa\frac{[Q]}{c_p} - \frac{\partial([\theta^*v^*]\cos\phi)}{R\partial\eta} - \frac{\partial[\theta^*\omega^*]}{\partial p}\right) \qquad (3.5) \\ \chi &= \frac{\tilde{f}}{\cos\phi}\left(\frac{\partial([u^*v^*]\cos^2\phi)}{R\cos\phi\partial\eta} + \frac{\partial[u^*\omega^*]}{\partial p} - [F_\lambda]\right) \qquad (3.6) \end{aligned}$$

$$[v] = \frac{1}{\cos\phi}\frac{\partial\psi}{\partial p} \tag{3.7}$$

$$[\omega] = -\frac{1}{R}\frac{\partial\psi}{\partial\eta} \tag{3.8}$$

$$\eta = \sin\phi.$$

A description of each variable, and its associated units, is given in Appendix A.

The above model equations differ from those of [Pfe81] by their presentation in terms of potential temperature rather than absolute temperature[2]. The equations originally presented in [Kuo56] differ substantially from the more modern presentations of this model, with Kuo's decomposition across time-scales leading to a bewildering array of model equations. It is felt that the current approach is more appropriate to the type of model calculations undertaken herein, with no assumptions being made implicitly.

While the Transformed Eulerian-Mean formulation of such a zonally-averaged model of the atmosphere (as introduced by [AM76] and further discussed by [AHL87]) is possible, it shall be seen that such a cogitated set of equations is

[2] Also, it appears that there is an error, or at least an implicit assumption, in the published formulae of [Pfe81], with the contribution by $-\frac{\partial[\theta^*\omega^*]}{\partial p}$ having been transformed incorrectly in the formulation of H. The effect of this term is, according to the derivations of [PO92] and [Kuo56], expected to be secondary under the quasi-geostrophic assumption.

not necessary for the type of investigation presented herein. The principal motivation for use of a TEM formulation of a zonally-averaged model is to combine the direct effect of eddy motions with that of the eddy-induced circulation. It shall be seen, however, that the eddies still play an important rôle in affecting the zonally-averaged jet core.

4. Data

The data used in this model are all products of the NCEP/NCAR Reanalysis project. A comprehensive overview of the project is provided by [KKK+96]; a précis relevant only to the data actually used will be provided here.

The bulk of the data used is taken from gridded NCEP/NCAR reanalyses; a description of the treatment of the diabatic heating data is given below. The daily data is provided on a $2.5° \times 2.5°$ grid and 12 pressure levels are chosen.

The selected levels are 1000 hPa, 925 hPa, 850 hPa, 700 hPa, 600 hPa, 500 hPa, 400 hPa, 300 hPa, 250 hPa, 200 hPa, 150 hPa, 100 hPa and latitudes $87.5°S - 87.5°N$ are chosen for the five-year periods 1959-1963 and 1989-1993. Monthly-mean values of each of the variables and fluxes are calculated using the flux-decompositions given in equations (2.4) and (2.5). The results presented here are for 1989-1993. Calculations for 1959-1963 for the eddy-induced circulation were also carried out to check the implementation of the model through comparison with the results of [Pfe81].

The original NCEP/NCAR Reanalysis Project daily-averaged data were downloaded from the NOAA web-site[3] in the form of *GRIB* files for geopotential height

[3]The daily data are stored at *http://sgi62.wwb.noaa.gov:8080/reanlm//test.daily.prs/*, with an overview of the NCEP/NCAR Reanalysis Project to be found at *http://wesley.wwb.noaa.gov/reanalysis.html.*

(HGT), temperature T (TMP), u wind (UGRD), v wind (VGRD) and pressure vertical velocity ω (VVEL) for each of the years. *GrADS*[4] control files were then created for the five years of each variable and the corresponding index files were created using the *gribmap* utility. The data was then written to binary files using *GrADS* and imported into *Matlab*, where all further calculations were performed.

4.1. Preprocessing of diabatic heating data

The monthly-mean model-derived diabatic heating fields[5] for 1979-1993[6] were downloaded from the NOAA archive in the form of *GRIB* files and then processed to ultimately produce the data required for model calculations. The data are provided on 27 model σ-levels on a Gaussian grid with a longitudinal resolution of 1.875° and a latitudinal resolution of 94 Gaussian levels (an approximate resolution of 1.9°). The vertical levels for $\sigma = \frac{p}{p_s}$ and their approximate pressure-level equivalents are:

[4] See *http://www.iges.org/grads* for a description of the software.

[5] The supplied data appears to have been weighted as $\frac{Q}{c_p}$ by NCEP, although this is undocumented.

[6] The data for January 1982 were inexplicably absent.

σ-level	nearest p-level (hPa)	σ-level	nearest p-level (hPa)
0.9950	1000	0.3717	400
0.9820		0.3122	300
0.9640		0.2582	250
0.9420		0.2102	200
0.9155	925	0.1682	150
0.8835		0.1323	
0.8454	850	0.1023	100
0.8009		0.0778	70
0.7499		0.0578	50
0.6934	700	0.0413	
0.6323		0.0278	30
0.5678		0.0174	20
0.5012	500	0.0093	10
0.4352			

The extraction and processing procedure is as follows:

- The data for the period 1989-93 are indexed to *GrADS*-compatible format by using the *gribmap* utility.

- The fields, provided by NCAR, relevant to determining diabatic heating[7] are combined by

$$Q = CNVHR + LRGHR + LWHR$$

[7]It should be noted that these fields are all model-derived fields rather than calculated directly from observational data. However, other repositories of diabatic heating data use a finite difference form of the thermodynamic equation to determine $Q\ \left(= c_p T \frac{d \ln \theta}{dt}\right)$, providing data of dubious quality, which are fundamentally unsuitable for budget calculations.

$$+SHAHR + SWHR + VDFHR, \tag{4.1}$$

where

$$\begin{aligned} CNVHR &= \text{Deep convective heating rate} \\ LRGHR &= \text{Large-scale condensation heating rate} \\ LWHR &= \text{Long-wave radiative heating rate} \\ SHAHR &= \text{Shallow convective heating rate} \\ SWHR &= \text{Short-wave radiative heating rate} \\ VDFHR &= \text{Vertical diffusion heating rate} \end{aligned}$$

- The Q field (on the σ-level Gaussian grid) is calculated from the *GRIB* data using the above expression and the resulting values are then interpolated and extrapolated on to the same pressure levels as the atmospheric data in the previous section using $1 - D$ cubic splines at each grid-point.

- The NCEP/NCAR data-set also provides monthly-mean surface pressure; this is used to discard all those values of Q which are on virtual pressure levels (i.e. pressure levels which are below the Earth's surface)[8].

[8] This procedure, of course, introduces an unquantifiable bias into the boundary-layer diabatic heating data.

- Annual, seasonal and monthly mean values of Q are now calculated and zonally averaged.

- By experiment, it was determined that it is now reasonable to extrapolate downwards for one pressure level from the Q values retained in the last step. This is accomplished by cubic spline extrapolation at each grid-point.

- To convert the Gaussian-grid data to a latitudinal resolution of 2.5° compatible with the data of the previous section a bi-cubic spline interpolation technique in the $\phi - p$ plane is used. To calculate usable values at the polar 1000 hPa latitudes, symmetry extending for 2 grid-points is assumed about the poles and the interpolation is performed on this extended grid.

- The resulting Q field on p-levels with a latitudinal resolution of 2.5° is the sole source for all calculations involving diabatic heating.

4.2. Calculated quantities

The following are the quantities calculated from the above data for use in the numerical solution of the model equation and the budget calculations:

$[\overline{u}]$	steady, zonally-averaged zonal wind
$[\overline{\theta}]$	steady, zonally-averaged potential temperature
$[\overline{Q}]$	steady, zonally-averaged diabatic heating
$[\overline{\theta^*}\ \overline{v^*}]$	meridional heat transport by stationary eddies
$[\overline{\theta'}]\,[\overline{v'}]$	meridional heat transport by zonally-symmetric transient eddies
$[\overline{\theta^{*'} v^{*'}}]$	meridional heat transport by zonally-asymmetric transient eddies
$[\overline{\theta^*}\ \overline{\omega^*}]$	downward heat transport by stationary eddies
$[\overline{\theta'}]\,[\overline{\omega'}]$	downward heat transport by zonally-symmetric transient eddies
$[\overline{\theta^{*'}\omega^{*'}}]$	downward heat transport by zonally-asymmetric transient eddies
$[\overline{u^*}\ \overline{v^*}]$	northward zonal momentum transport by stationary eddies
$[\overline{u'}]\,[\overline{v'}]$	northward zonal momentum transport by zonally-symmetric transient eddies
$[\overline{u^{*'} v^{*'}}]$	northward zonal momentum transport by zonally-asymmetric transient eddies
$[\overline{u^*}\ \overline{\omega^*}]$	downward zonal momentum transport by stationary eddies
$[\overline{u'}]\,[\overline{\omega'}]$	downward zonal momentum transport by zonally-symmetric transient eddies
$[\overline{u^{*'}\omega^{*'}}]$	downward zonal momentum transport by zonally-asymmetric transient eddies

4.3. Comparison with data of previous studies

The use of reanalysis model data represents a significant departure from previous studies to investigate wave-mean flow interactions in the atmosphere. The data used by [Pfe81] are principally taken from two sources:

- the tabulated data of [OR71] (stemming from a large data compilation project coordinated by the Massachusetts Institute of Technology)
- the energy-balance investigations of [NVDF69] (which is a compilation of results from many different studies)

These sources suffer from a significant number of disadvantages:

- poor upper-air coverage - the number of radiosonde measurements providing information in the upper troposphere and lower stratosphere is extremely small
- poor spatial coverage - over oceanic areas, even to this day, there are vast data voids which may only partially be filled by satellite data
- large inaccuracy in some fields - a particular instance of this is the vertical velocity field of [OR71], whose authors suggest that one should only consider the qualitative nature of the statistics (i.e. whether fluxes are upwards or downwards)
- gross simplifications in some measurements - these are particularly evident in [NVDF69] where, as an example, boundary layer heating is taken as being between 1000 hPa and 700 hPa

5. Numerical solution of meridional streamfunction equation

The streamfunction is discretised on a 71×12 grid (covering latitudes $87.5°S - 87.5°N$[9] and levels $1000\ hPa - 100\ hPa$) with latitudinal coordinate $\eta\ (= \sin\phi)$ and vertical coordinate p. Thus, the gridpoint intervals are unequal in both directions:

- The latitudinal coordinate is discretised as

$$\eta_i = \sin\left(i \times 2.5° - 90°\right) = \sin\left((i - 36) \times 2.5°\right).$$

- The vertical coordinate is discretised as p_j, with

j	1	2	3	4	5	6	7	8	9	10	11	12
p_j (in hPa)	1000	925	850	700	600	500	400	300	250	200	150	100

The various spatial derivatives of the streamfunction are discretised as follows[10]:

[9] To avoid complexities from dealing with the removable singularities of terms involving $\eta|_{\phi=\pm 90°}$, the poles are not included in this discretisation scheme.

[10] Where possible, central difference approximations are used; at the boundaries of the domain forward- and backward-differences are used, as appropriate.

- $\left.\frac{\partial\psi}{\partial\eta}\right|_{(\eta_i,p_j)} \simeq \begin{cases} \frac{\psi(\eta_2,p_j)-\psi(\eta_1,p_j)}{\eta_2-\eta_1}, \text{ for } i=1 \\ \frac{\psi(\eta_{i+1},p_j)-\psi(\eta_{i-1},p_j)}{\eta_{i+1}-\eta_{i-1}}, \text{ for } i=2,\ldots,70 \\ \frac{\psi(\eta_{71},p_j)-\psi(\eta_{70},p_j)}{\eta_{71}-\eta_{70}}, \text{ for } i=71 \end{cases}$

- $\left.\frac{\partial\psi}{\partial p}\right|_{(\eta_i,p_j)} \simeq \begin{cases} \frac{\psi(\eta_i,p_2)-\psi(\eta_i,p_1)}{p_2-p_1}, \text{ for } j=1 \\ \frac{\psi(\eta_i,p_{j+1})-\psi(\eta_i,p_{j-1})}{p_{i+1}-p_{i-1}}, \text{ for } j=2,\ldots,11 \\ \frac{\psi(\eta_i,p_{12})-\psi(\eta_i,p_{11})}{p_{12}-p_{11}}, \text{ for } j=12 \end{cases}$

- $\left.\frac{\partial^2\psi}{\partial\eta^2}\right|_{(\eta_i,p_j)} \simeq \begin{cases} \frac{\frac{\psi(\eta_3,p_j)-\psi(\eta_1,p_j)}{\eta_3-\eta_1}-\frac{\psi(\eta_2,p_j)-\psi(\eta_1,p_j)}{\eta_2-\eta_1}}{\eta_2-\eta_1}, \text{ for } i=1 \\ \frac{\frac{\psi(\eta_{i+1},p_j)-\psi(\eta_i,p_j)}{\eta_{i+1}-\eta_i}-\frac{\psi(\eta_i,p_j)-\psi(\eta_{i-1},p_j)}{\eta_i-\eta_{i-1}}}{\frac{\eta_{i+1}-\eta_{i-1}}{2}}, \text{ for } i=2,\ldots,70 \\ \frac{\frac{\psi(\eta_{71},p_j)-\psi(\eta_{70},p_j)}{\eta_{71}-\eta_{70}}-\frac{\psi(\eta_{71},p_j)-\psi(\eta_{69},p_j)}{\eta_{71}-\eta_{69}}}{\eta_{71}-\eta_{70}}, \text{ for } i=71 \end{cases}$

- $\left.\frac{\partial^2\psi}{\partial p^2}\right|_{(\eta_i,p_j)} \simeq \begin{cases} \frac{\frac{\psi(\eta_i,p_3)-\psi(\eta_i,p_1)}{p_3-p_1}-\frac{\psi(\eta_i,p_2)-\psi(\eta_i,p_1)}{p_2-p_1}}{p_2-p_1}, \text{ for } j=1 \\ \frac{\frac{\psi(\eta_i,p_{j+1})-\psi(\eta_i,p_j)}{p_{i+1}-p_i}-\frac{\psi(\eta_i,p_j)-\psi(\eta_i,p_{j-1})}{p_i-p_{i-1}}}{\frac{p_{i+1}-p_{i-1}}{2}}, \text{ for } j=2,\ldots,11 \\ \frac{\frac{\psi(\eta_i,p_{12})-\psi(\eta_i,p_{11})}{p_{12}-p_{11}}-\frac{\psi(\eta_i,p_{11})-\psi(\eta_i,p_{10})}{p_{11}-p_{10}}}{p_{12}-p_{11}}, \text{ for } j=12 \end{cases}$

- $\left.\frac{\partial^2\psi}{\partial\eta\partial p}\right|_{(\eta_i,p_j)} = \left.\frac{\partial\left(\frac{\partial\psi}{\partial p}\right)}{\partial\eta}\right|_{(\eta_i,p_j)}$ is evaluated using the formulae for $\left.\frac{\partial\psi}{\partial p}\right|_{(\eta_i,p_j)}$ and $\left.\frac{\partial\psi}{\partial\eta}\right|_{(\eta_i,p_j)}$.

The streamfunction problem was solved by direct inversion of the 852×852 matrix, assuming zero boundary conditions on both the lateral, upper and lower

boundaries. Other solution methods were considered, but given that the typical solution time for the direct inversion is $\sim 30\ s$ in comparison with the data preprocessing which takes hours or days, a fast solution scheme was not deemed necessary. Additionally, the difficulty of obtaining a good initial estimate of the solution renders many iterative schemes unworkable. A range of schemes from [BBC+94] was attempted, but convergence difficulties, accompanied by implementational complications, rendered these unsuitable for the required once-off solutions of the discretised streamfunction equation.

The streamfunction equation is solved:

- for each month and season of the year and for the annual average,
- to separately determine the eddy-induced and diabatic heating-induced circulations and the circulation due to their combined effects,

giving a total of 57 matrix inversions[11].

Throughout this study, the forcing by surface wind stress is ignored (i.e. $F\lambda \equiv 0$). While estimates of the surface wind stress do exist[12], these are particularly

[11] A relaxation scheme was chosen by [Pfe81], possibly reflecting the available computational resources at the time of that study; however, no details of the numerical solution scheme are given.

[12] The most comprehensive appears to be those of the ECMWF, although these are only available for a short range of dates.

unreliable over land areas, indicating that such archives of data are, at best, appropriate only for regional, oceanic studies.

The derived quantities and the results shown in the body of this work will be those for annual- and seasonal-mean conditions; for readability, the corresponding plots for monthly-mean conditions will be deferred to Appendix D.

6. Distributions of zonal wind, potential temperature and diabatic heating and eddy fluxes of heat and momentum

6.1. Zonal wind, potential temperature and diabatic heating

Shown in Figures 6.1 and 6.2 are the annual and seasonal means of zonal-mean wind $[\overline{u}]$ and potential temperature $[\overline{\theta}]$, respectively. Evident in these plots are the jet-stream maxima in the mid-latitude upper troposphere and the corresponding strong meridional temperature gradient implied by the thermal wind relationship

$$\left(f + \frac{2\tan\phi}{R}u\right)\frac{\partial u}{\partial p} = \frac{R_d p^{\kappa-1}}{p_{00}\kappa}\frac{1}{R}\frac{\partial\theta}{\partial\phi}.$$

Also evident are the predominant easterlies in the trade-wind belt, extending all the way to the upper troposphere. Given the high terrain of Antarctica, as well as the sparse data available, the apparent easterlies south of $70°S$ are rather suspect[13]. The zonal wind speed maxima, found at 200 mb in all seasons and in the annual average, are aligned with the regions of the largest values of the meridional temperature gradient, in accordance with the requirements of thermal

[13]The data compiled by [PO92] shows a strong weakening of westerly win as one approaches the Antarctic; the authors do note, however, that such statistics may stem either from a selective loss of weather balloons or the sparse synoptic network in south of $60°S$.

wind balance, with the maximum values of $[\overline{u}]$ being found during the winter season in each hemisphere. As one might expect from the greater temperature variability in the Northern Hemisphere (which is due to less oceanic coverage and hence the reduced thermal inertia reflected by the lower-tropospheric values of $[\overline{\theta}]$), the annual cycle is most pronounced in the boreal mid-latitudes. The largest values of $[\overline{u}]$, however, are found in the Southern Hemisphere, reflecting the largely zonal nature of the global circulation there.

Shown in Figure 6.3 are the annual and seasonal means of zonal-mean diabatic heating. The dominant feature is the quasi-barotropic region of diabatic heating extending for a range of approximately 20° near the equator. The migration of the region of strong heating is seen to very clearly follow the annual cycle of the angle of insolation. It can also be seen that there is some diabatic heating in the boundary layer extending from the equatorial region to the midlatitudes. It is not apparent whether the large values of diabatic cooling in the Antarctic lower troposphere are an effect of the large surface albedo there (due to the ice-albedo feedback mechanism outlined by [PO92]) or simply the high-terrain or poor data coverage of that region. Examination of the separate contributions to diabatic heating (from equation (4.1)) shows that the release of latent heat dominates near the Equator and it is radiative cooling that dominates near the poles and at

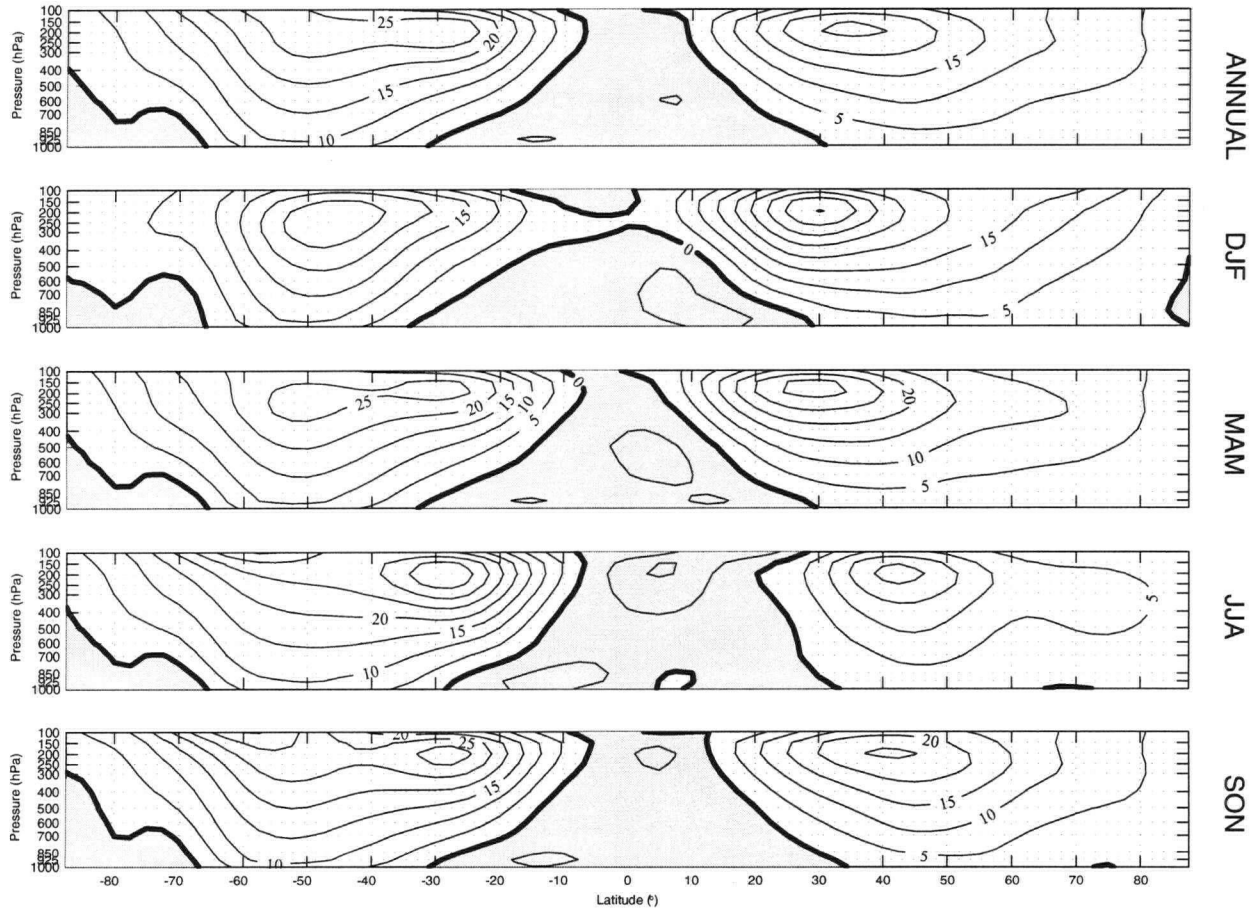

Figure 6.1: Annual and seasonal-mean distributions of $[\overline{u}]$. Units are $m\ s^{-1}$ and the contour interval is 5 $m\ s^{-1}$.

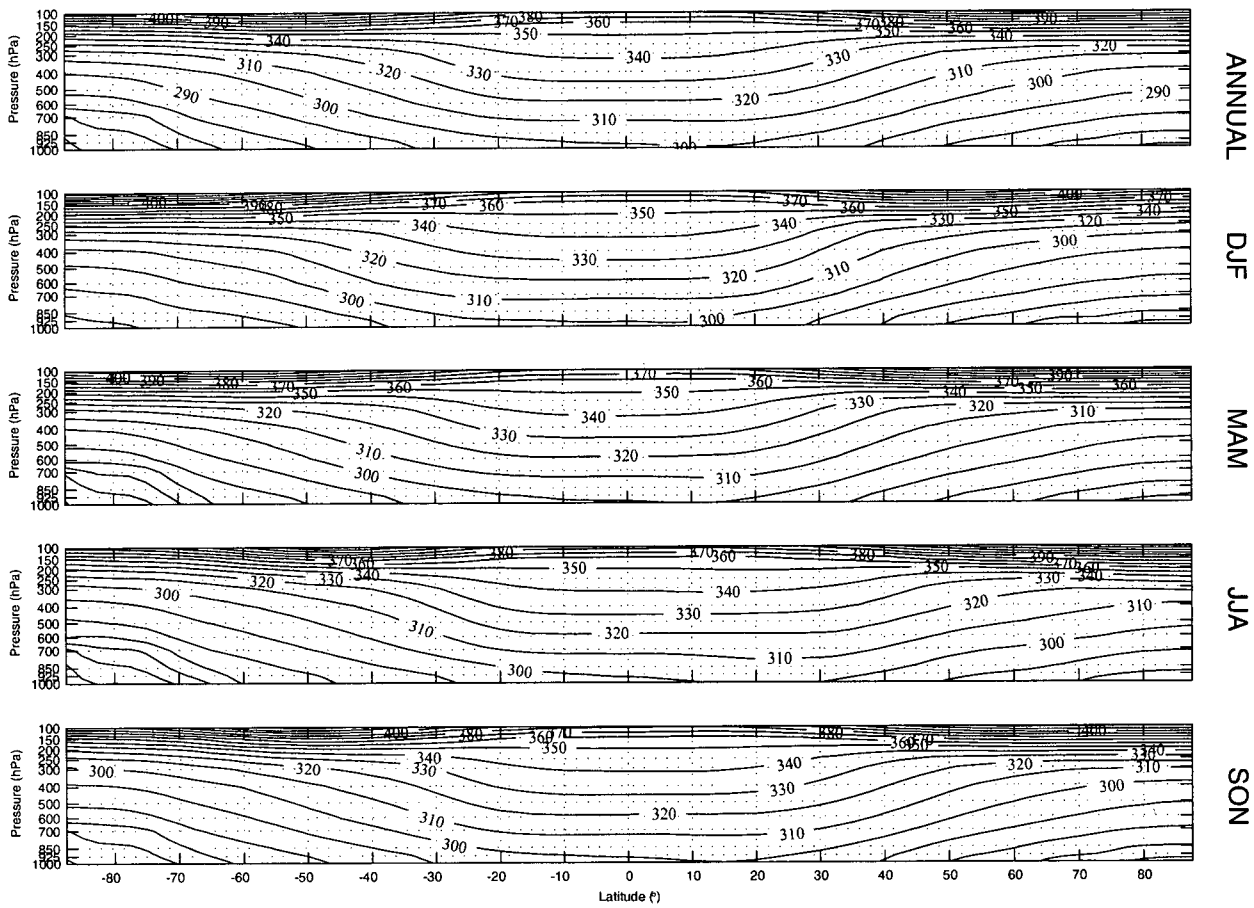

Figure 6.2: Annual and seasonal-mean distributions of $[\overline{\theta}]$. Units are K and the contour interval is 10 K.

high altitudes.

6.2. Eddy fluxes of heat and momentum

Shown in Figures 6.4, 6.5 and 6.6 are the annual and seasonal means of stationary-eddy, transient zonally-symmetric eddy and transient zonally-asymmetric eddy components of northward momentum transport. The northward momentum flux is concentrated at 200 hPa at all times throughout the year, with the transient zonally-symmetric eddies making an insignificant contribution. The stationary-eddy component, $[\overline{u}^{*}\,\overline{v}^{*}]$, is significant only in the Northern Hemisphere mid-latitudes and equatorial upper troposphere, with net northward transport in the midlatitudes peaking in the boreal winter and a seasonally-reversing equatorward transport at the Equator. Examining the transient zonally-asymmetric component, $\left[\overline{u^{*'}v^{*'}}\right]$, one sees that this is the dominant contribution, with a clear annual cycle in the Northern Hemisphere, peaking in wintertime, being reinforced by the aforementioned standing eddy component. The net southward transport in the Southern Hemisphere has typically larger magnitudes than its boreal counterpart, with the annual cycle being less evident. In contrast with the results of [PO92], which shows a region of strong northward momentum transport in the Antarctic troposphere by the transient eddies, Figure 6.6 shows little transport (this is

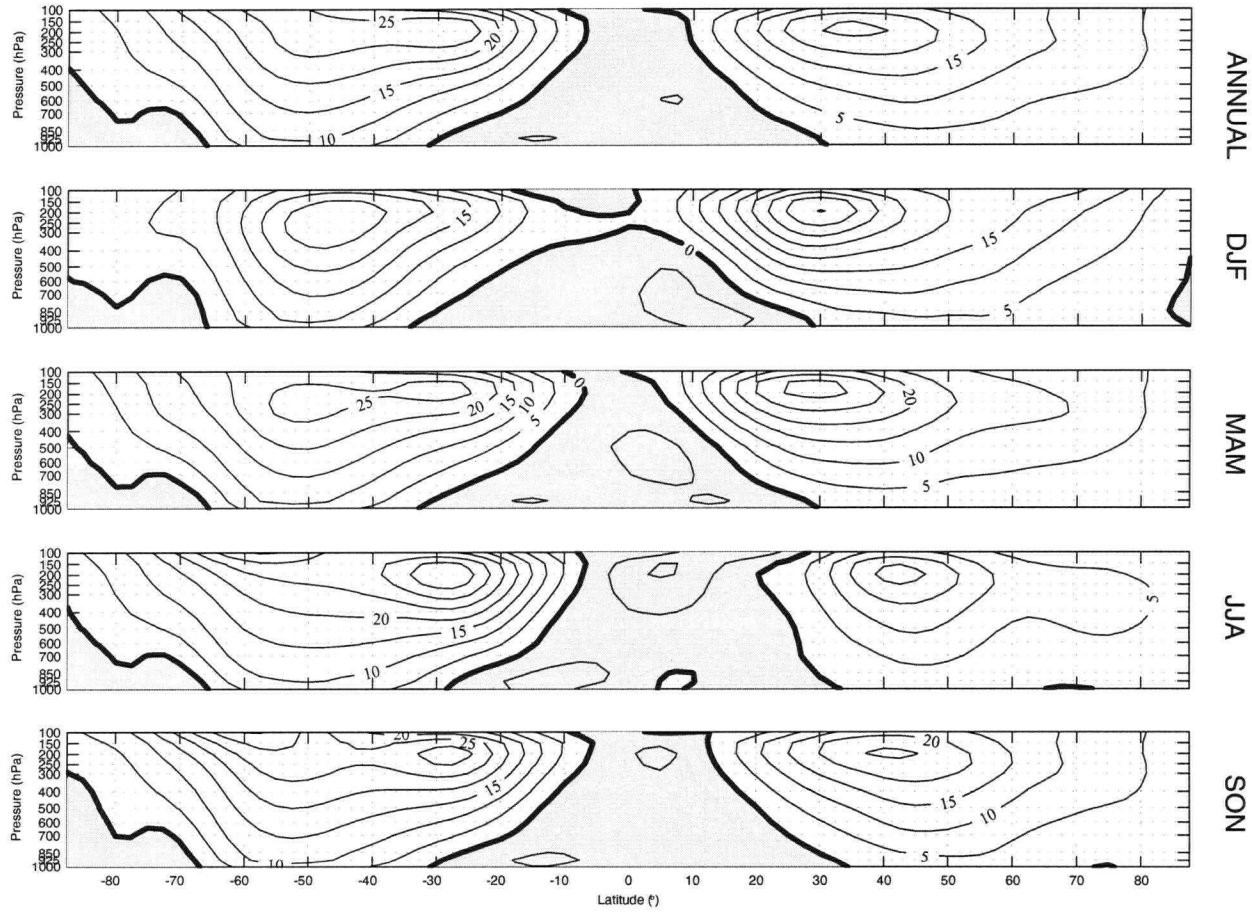

Figure 6.3: Annual and seasonal-mean distributions of $\frac{[\overline{Q}]}{c_p}$. Units are $K\ s^{-1}$ and the contour interval is $1 \times 10^{-5}\ K\ s^{-1}$.

in agreement with [Pfe81]); the sparse synoptic network for the data-sources of [PO92] may again be responsible for this discrepancy.

Shown in Figures 6.7, 6.8 and 6.9 are the annual and seasonal means of stationary-eddy, transient zonally-symmetric eddy and transient zonally-asymmetric eddy components of downward momentum transport. The predominant values appear to be the lower-tropospheric stationary eddy contribution, $[\overline{u}^* \, \overline{\omega}^*]$, south of $65°S$. Closer consideration of the topography of this region, along with consideration of the data quality-control mechanism used, reveals that these results stem from an analysis that, at best, is heavily skewed and, at worst, could result from some poor physical parameterisation in the NCEP/NCAR reanalysis model. For this reason a contouring scheme is chosen whereby both the very large (and hence suspect) values are plotted, along with values in the range expected from previous studies. Ignoring these possibly misleading results, Figure 6.7 suggests that the stationary eddy component makes a significant contribution to the net downward momentum flux in the equatorial upper troposphere around 250 hPa, with no particular seasonality in evidence. Comparison with the results of [Pfe81] reveals a similar centre of upward flux in the mid troposphere at $40°N$ during winter and spring and the same pattern of Equatorial upper-tropospheric maxima throughout the year. No other significant similarities are apparent. The tran-

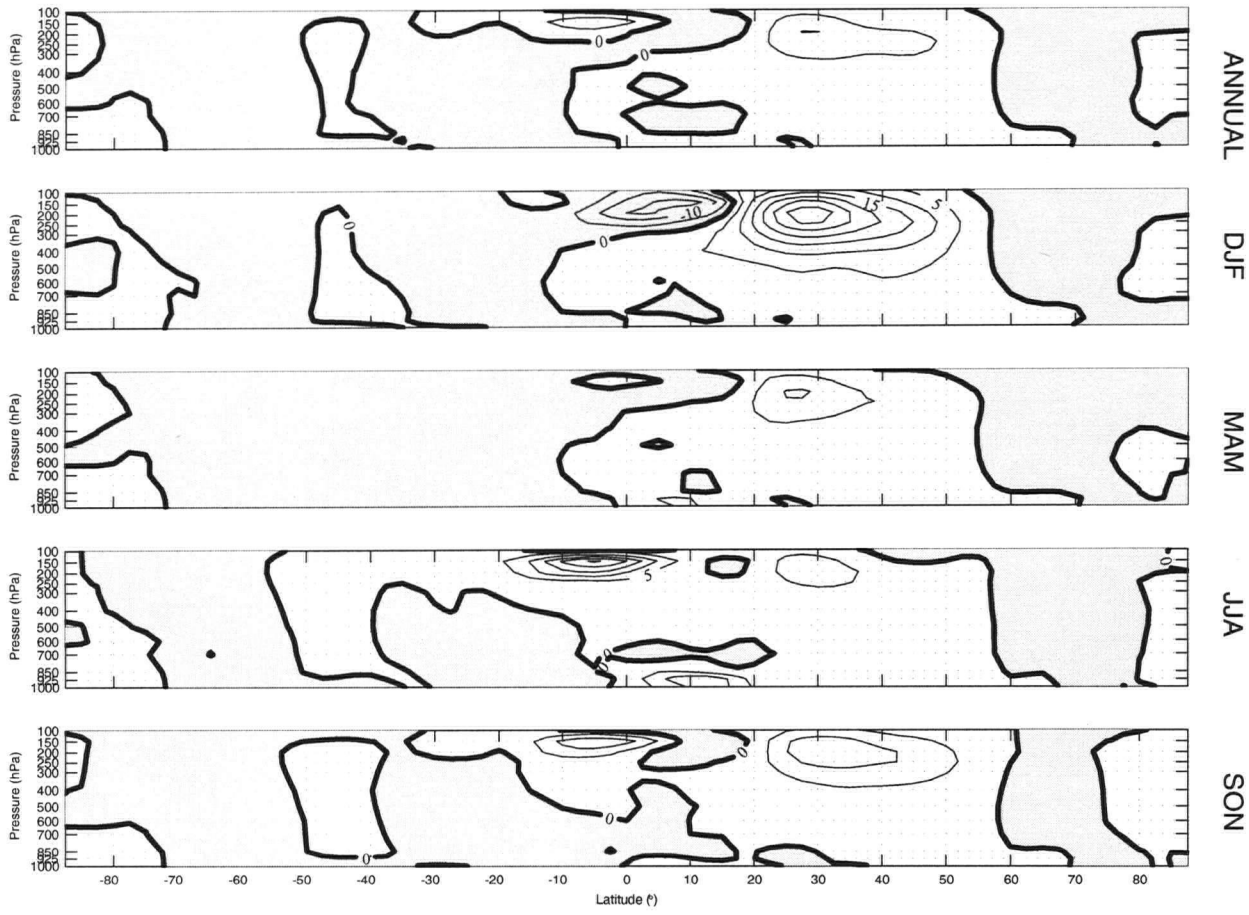

Figure 6.4: Annual and seasonal-mean distributions of $[\overline{u}^* \ \overline{v}^*] \cos^2 \phi$ (stationary eddies). Units are $m^2 \ s^{-2}$ and the contour interval is $5 \ m^2 \ s^{-2}$.

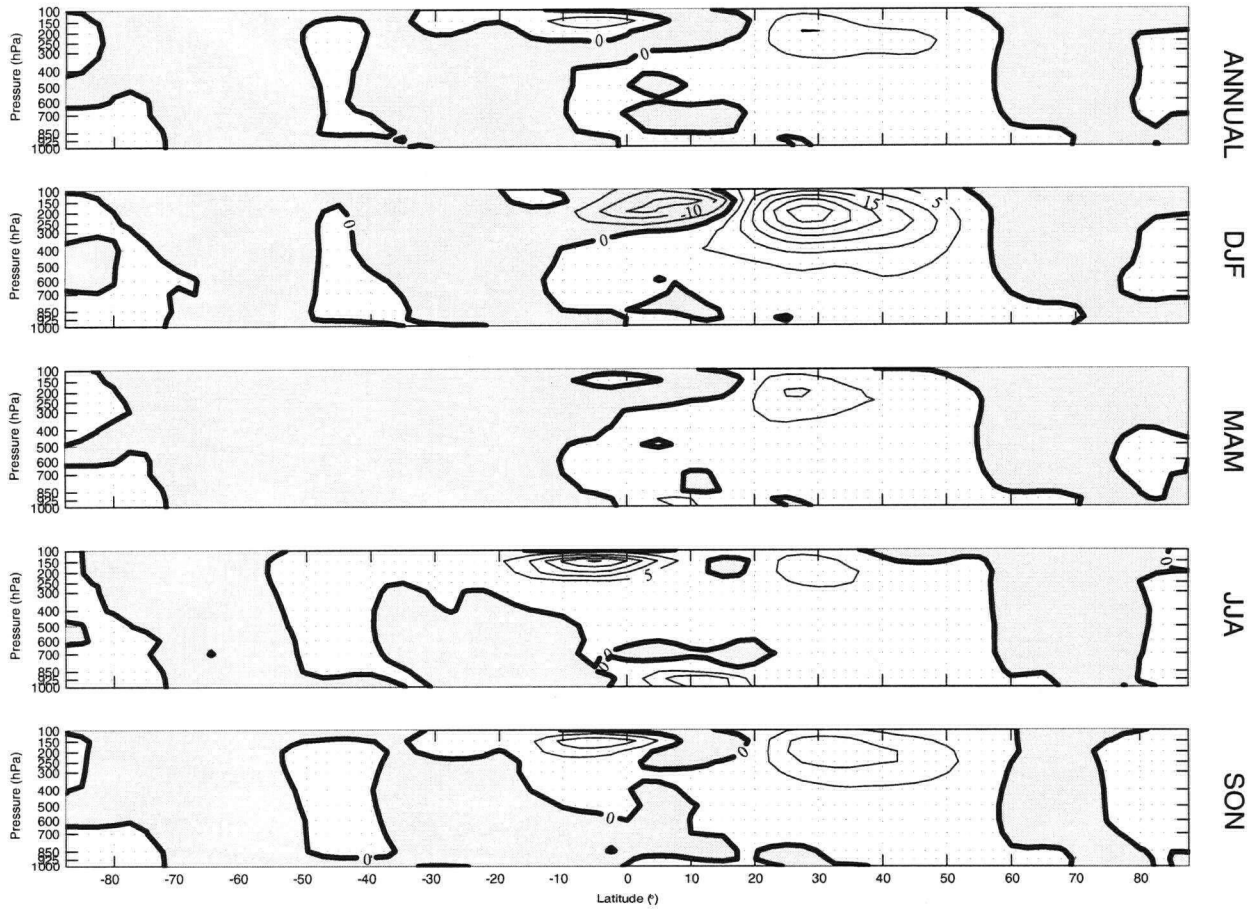

Figure 6.5: Annual and seasonal-mean distributions of $\overline{[u'][v']}\ \cos^2\phi$ (transient, zonally-symmetric eddies). Units are $m^2\ s^{-2}$ and the contour interval is $0.5\ m^2\ s^{-2}$.

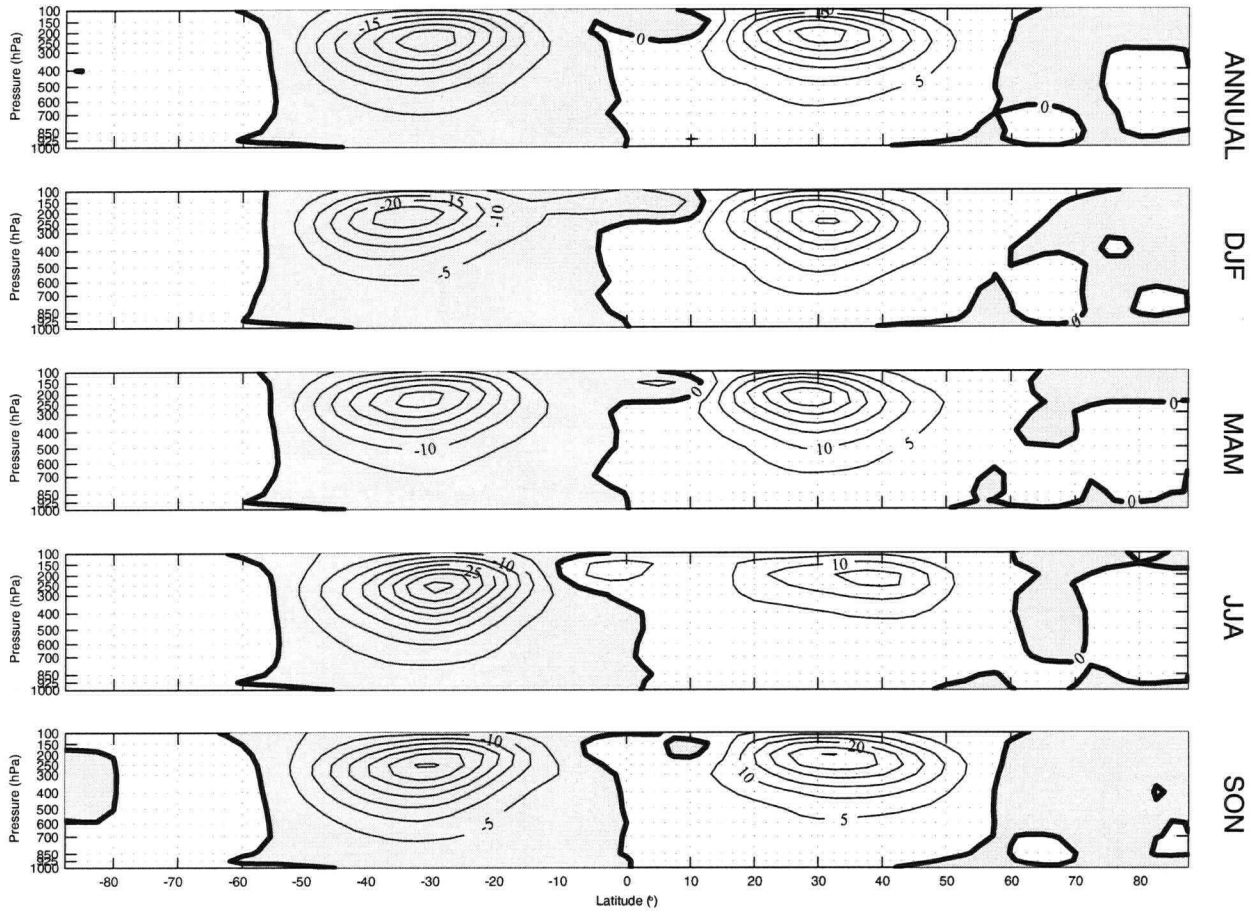

Figure 6.6: Annual and seasonal-mean distributions of $\left[\overline{u^{*\prime}v^{*\prime}}\right] \cos^2\phi$ (transient, zonally-asymmetric eddies). Units are $m^2\ s^{-2}$ and the contour interval is 5 $m^2\ s^{-2}$.

sient, zonally-asymmetric eddy component depicted in Figure 6.9 has strong net upward flux of zonal momentum in both hemispheres, with peak values reached at about 350 hPa between $20° - 40°$ in each of the corresponding winters. Examination of the magnitude of the contributions confirms the conjecture of [SPS70] that the vertical flux of momentum by synoptic-scale eddies dwarfs that of the standing eddies. A previously unnoted feature of the downward flux of momentum is the region of relatively significant values of $\left[\overline{u^{*\prime}\omega^{*\prime}}\right]$ at 600 hPa between $60°S - 80°S$, with a strong annual cycle peaking in the austral winter. The origin of this region of strong downward zonal momentum flux is unclear. The transient, zonally-symmetric fluxes of downward momentum transport, shown in Figure 6.8, are negligible through the year.

Shown in Figures 6.10, 6.11 and 6.12 are the annual and seasonal means of stationary-eddy, transient zonally-symmetric eddy and transient zonally-asymmetric eddy components of northward heat transport, respectively. Throughout the year, the standing and synoptic eddy-fluxes of heat are directed equatorward between $20°S - 20°N$ and poleward elsewhere. The stationary-eddy component of heat transport (Figure 6.10), $\left[\overline{\theta}^{*}\,\overline{v}^{*}\right]\cos\phi$, is negligible almost everywhere, except in the Northern Hemisphere mid-latitude upper troposphere at 200 hPa between October and March. A maximum at 850 hPa also appears about this time at the

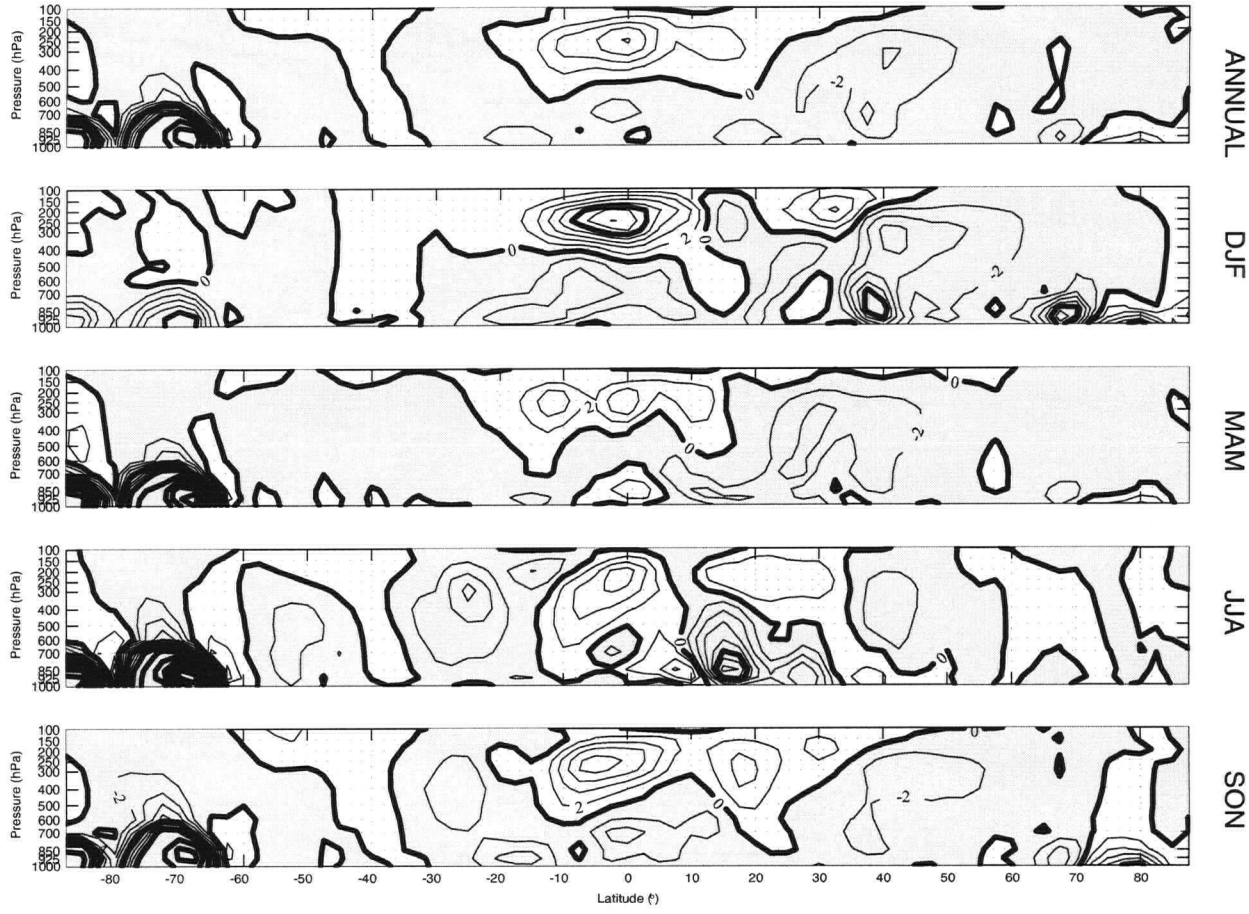

Figure 6.7: Annual and seasonal-mean distributions of $[\overline{u}^* \ \overline{\omega}^*]$ (stationary eddies). Units are $10^{-2}\ m\ Pa\ s^{-2}$ and the contour intervals are $2 \times 10^{-2}\ m\ Pa\ s^{-2}$ (light contours) and $10 \times 10^{-2}\ m\ Pa\ s^{-2}$ (dark contours).

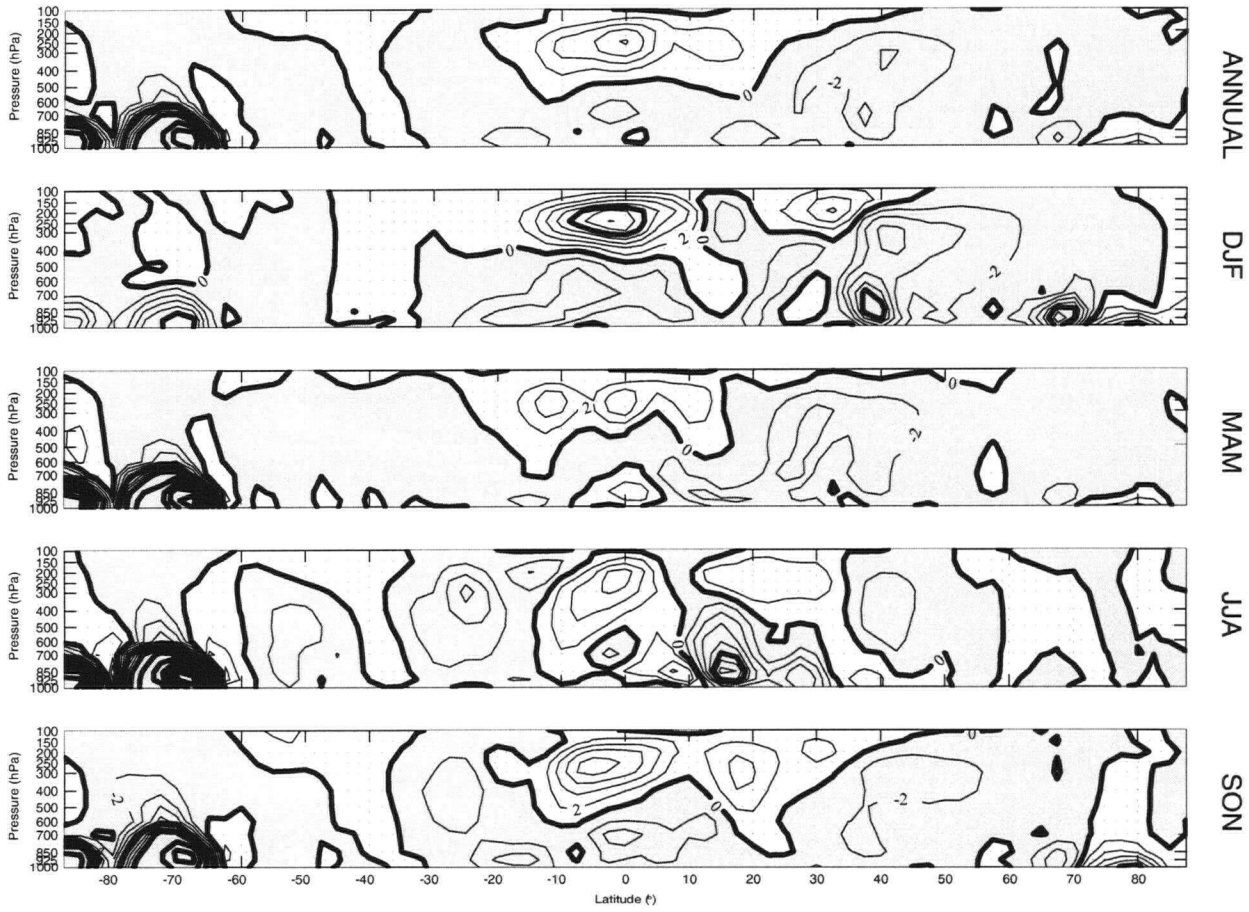

Figure 6.8: Annual and seasonal-mean distributions of $\overline{[u']\,[\omega']}$ (transient, zonally-symmetric eddies). Units are $10^{-2}\ m\ Pa\ s^{-2}$ and the contour intervals are $0.5 \times 10^{-2}\ m\ Pa\ s^{-2}$ (light contours) and $5 \times 10^{-2}\ m\ Pa\ s^{-2}$ (dark contours).

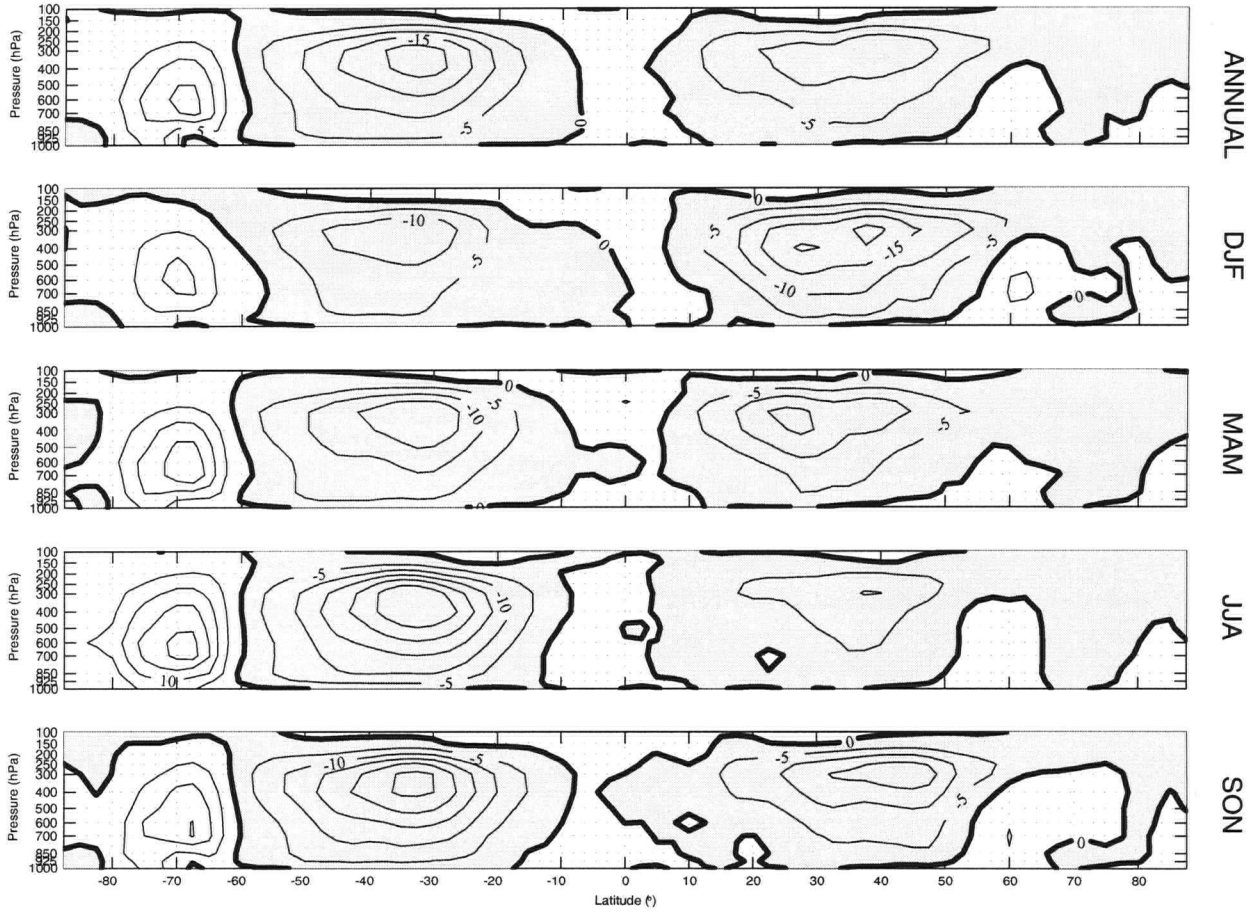

Figure 6.9: Annual and seasonal-mean distributions of $\left[\overline{u^{*\prime}\omega^{*\prime}}\right]$ (transient, zonally-asymmetric eddies). Units are $10^{-2}\ m\ Pa\ s^{-2}$ and the contour intervals are $5 \times 10^{-2}\ m\ Pa\ s^{-2}$.

same latitude. The Southern Hemisphere upper troposphere appears to have an intruding region of southward heat transport between August and November, possibly an indicator of the more active lower stratosphere during the austral Spring (as remarked upon by [TW98]).The maxima in the lower troposphere here are, however, quite suspect for reasons previously discussed. The transient, zonally-asymmetric meridional heat transport (Figure 6.12), $\left[\overline{\theta^{*\prime} v^{*\prime}}\right] \cos\phi$, exhibits the same directions of transport characteristic of the standing eddy component, but with greater symmetry about the equator. Strong mid-latitude regions of poleward transport appear at both 200 hPa and 850 hPa throughout the year, with a seasonal cycle of magnitude strongly in evidence; reinforcement by the stationary eddy component is also in evidence, along with the springtime intrusion of poleward heat transport in the Southern Hemisphere. The transient, zonally-symmetric component (Figure 6.11), $\overline{[\theta']\,[v']} \cos\phi$, again makes minimal contribution.

Shown in Figures 6.13, 6.14 and 6.15 are the annual and seasonal means of stationary-eddy, transient zonally-symmetric eddy and transient zonally-asymmetric eddy components of downward heat transport, respectively. Shown in Figure 6.13 is the stationary-eddy component, $\left[\overline{\theta}^{*}\, \overline{\omega}^{*}\right]$, which is upward throughout most of the atmosphere, with regions of weak downward heat transport to be found in

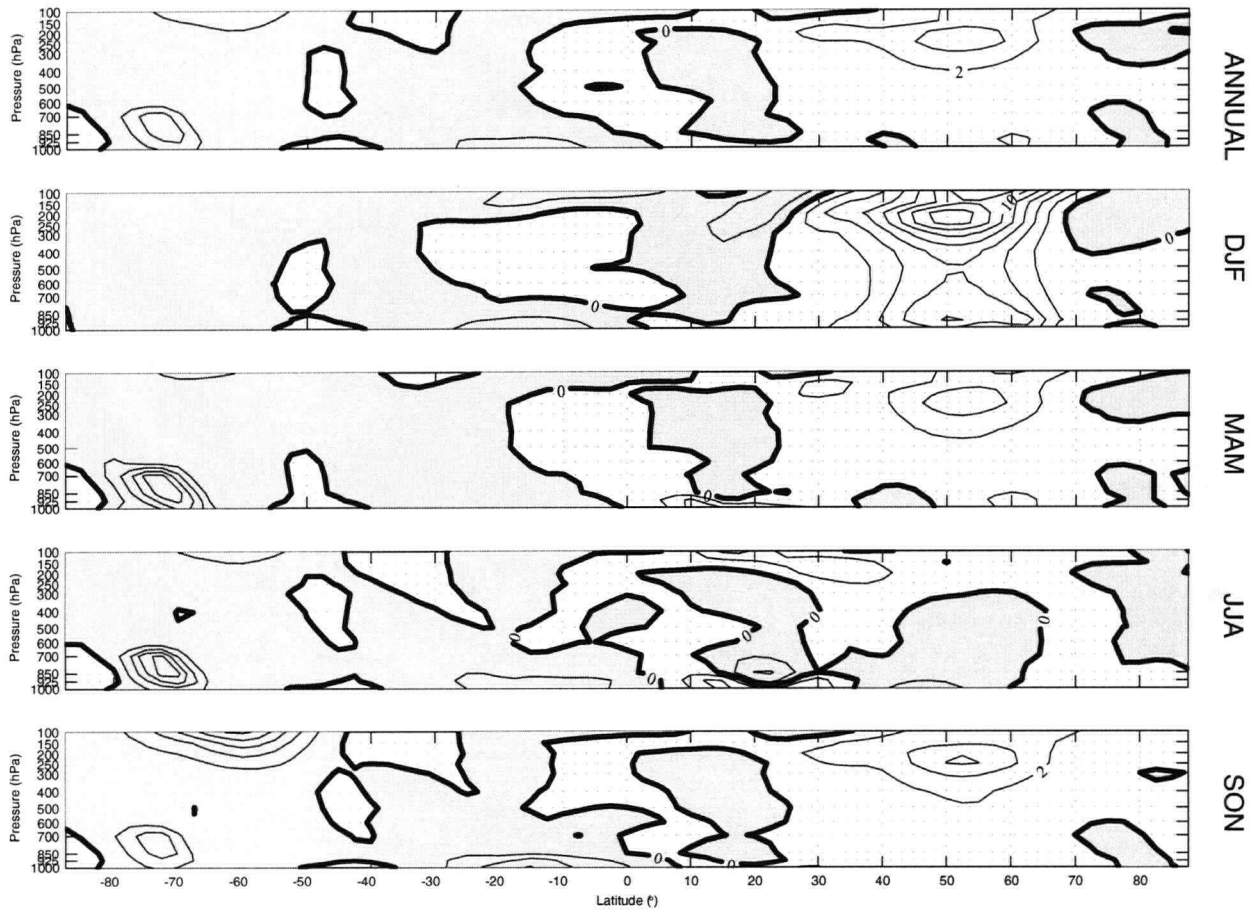

Figure 6.10: Annual and seasonal-mean distributions of $\left[\overline{\theta}^{*}\ \overline{v}^{*}\right] \cos\phi$ (stationary eddies). Units are $K\ s^{-1}$ and the contour interval is $2\ K\ s^{-1}$.

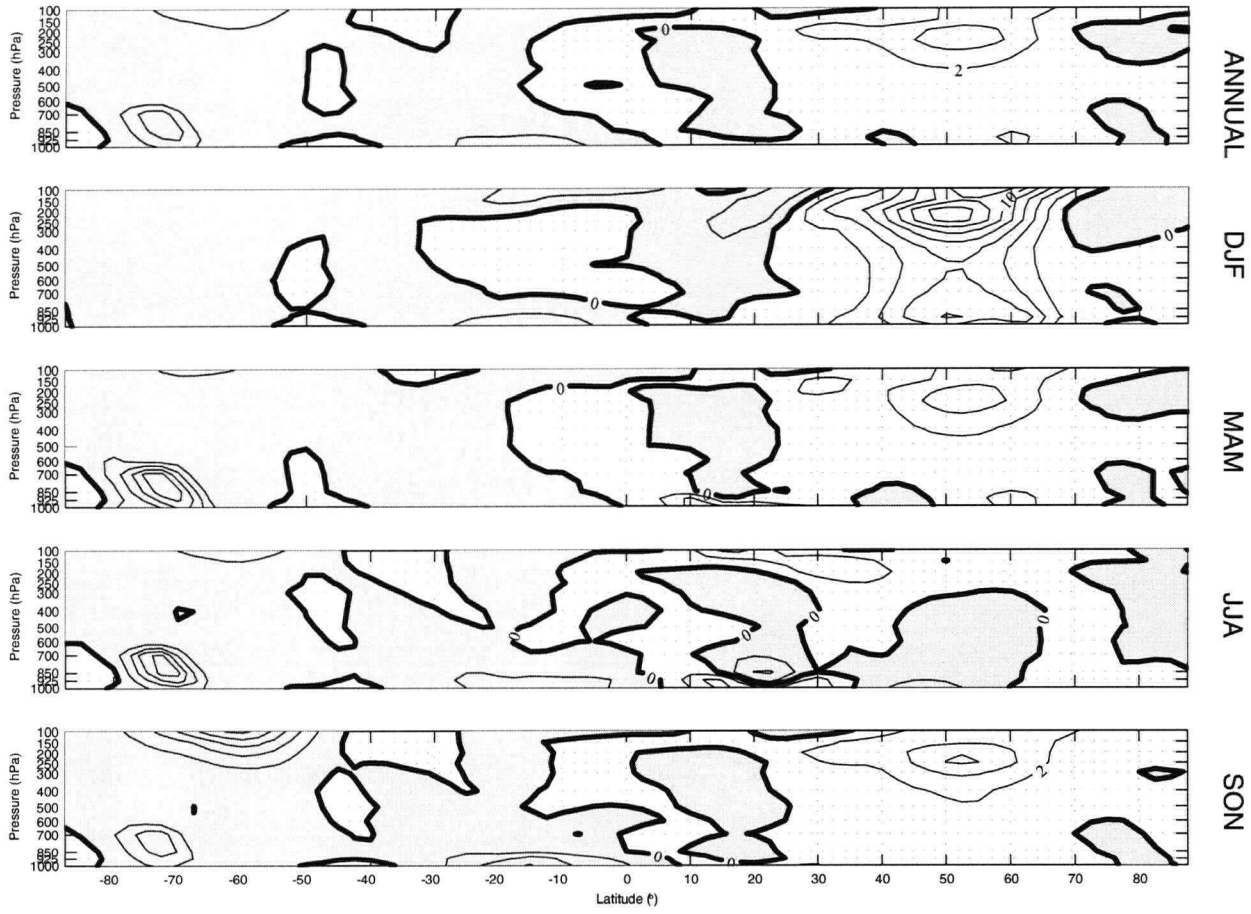

Figure 6.11: Annual and seasonal-mean distributions of $\overline{[\theta'][v']}\cos\phi$ (transient, zonally-symmetric eddies). Units are $K\ s^{-1}$ and the contour interval is $0.1\ K\ s^{-1}$.

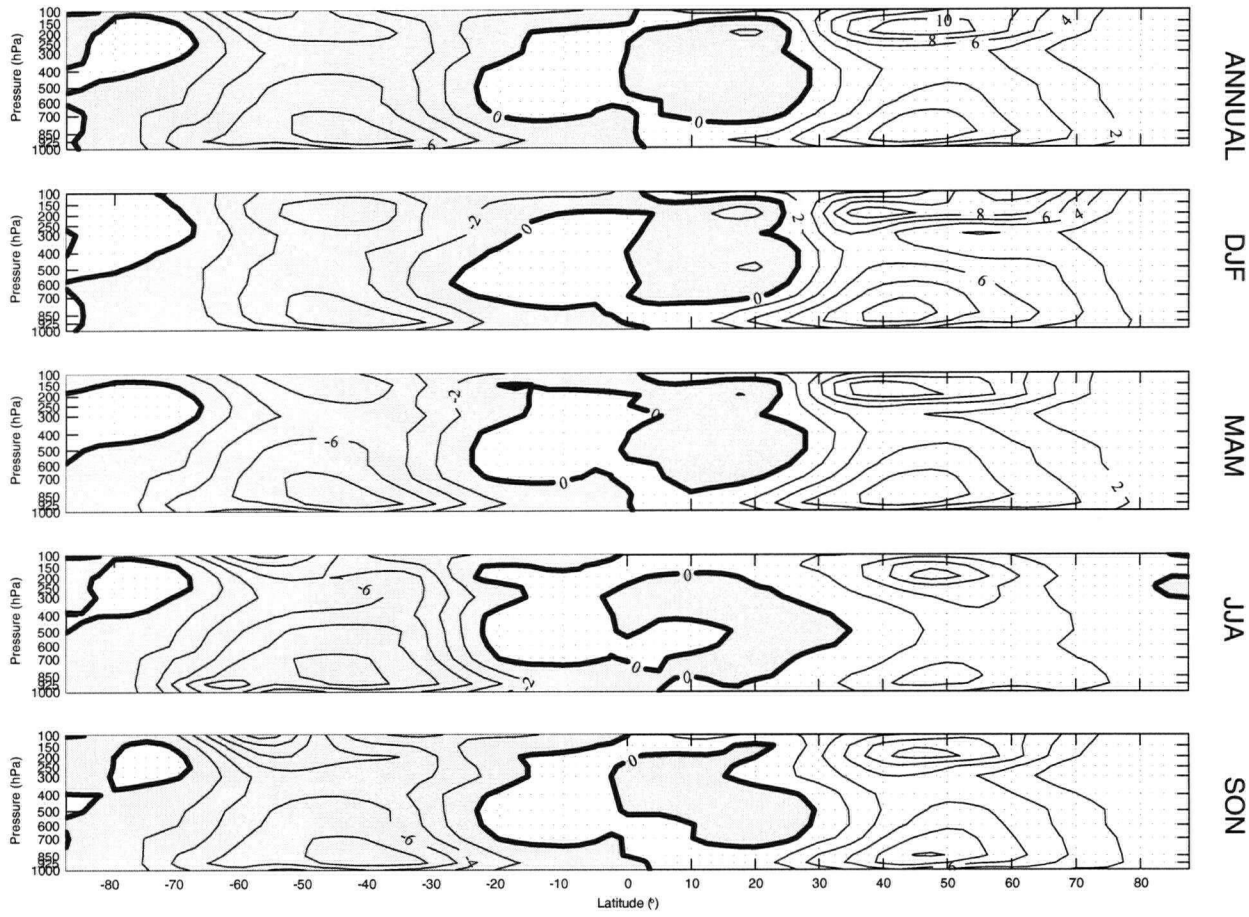

Figure 6.12: Annual and seasonal-mean distributions of $\left[\overline{\theta^{*\prime} v^{*\prime}}\right] \cos\phi$ (transient, zonally-asymmetric eddies). Units are $K\ s^{-1}$ and the contour interval is $2\ K\ s^{-1}$.

the lower stratosphere and in the Southern Hemisphere between $60°S - 40°S$. Large values of upward heat transport are to be found near the Equatorial surface, with the latitude of the maxima possibly following the seasonal migration of the Inter-Tropical Convergence Zone; this is readily apparent only from consideration of monthly-mean plots. South of $60°S$, the large values of upward heat transport cannot be explained by consideration of orography alone; no anecdotal evidence appears to exist which would provide a possible explanation. The transient, zonally-asymmetric component (Figure 6.15), $\left[\overline{\theta^{*\prime}\omega^{*\prime}}\right]$, again appears to exhibit the greatest symmetry about the Equator, along with more significant values than the stationary-eddy contribution and the most clearly defined annual cycle. Most apparent are the regions of broad upward heat flux between $30° - 80°$ and $1000\ hPa - 250\ hPa$ in both hemispheres, dominating the total heat flux. A region of weak downward heat transport appears in the equatorial mid-troposphere, along with weak downward heat transport in the lower stratosphere. A small region of significant upward heat transport appears at the surface at about $70°S$ between March and September; as this region extends up to $700\ hPa$, this phenomenon may be associated with the surface albedo being altered by seasonal changes in the extent of the ice-cover near Antarctica. Consideration of the transient, zonally-symmetric component (Figure 6.14), $\overline{[\theta']\,[\omega']}$, reveals a negligible

contribution by this quantity.

6.3. Calculation of heat- and momentum-flux forcings

The total northward and upward momentum fluxes are shown in Figures 6.16 and 6.17 respectively. In both cases, it is the transient, zonally-asymmetric contribution, with occasional reinforcement by the stationary eddies, which dominates. The predominant poleward and upward transport of zonal momentum is a reflection of the requirement of northward angular momentum transport, chiefly accomplished by synoptic-scale motions, as outlined by [PO92].

The total northward and upward heat fluxes are shown in Figures 6.18 and 6.19 respectively. Again, it is the transient, zonally-asymmetric component which is most evident, with contributions by the stationary-eddy component in the high-latitude lower troposphere. The strong poleward and upward heat flux in the mid-latitude troposphere, principally by synoptic-scale systems, supports the results of [Cha47] for the global energy balance.

These values, together with diabatic heating data, are used to calculate the fluxes of heat and momentum, H and χ respectively, associated with the Hadley

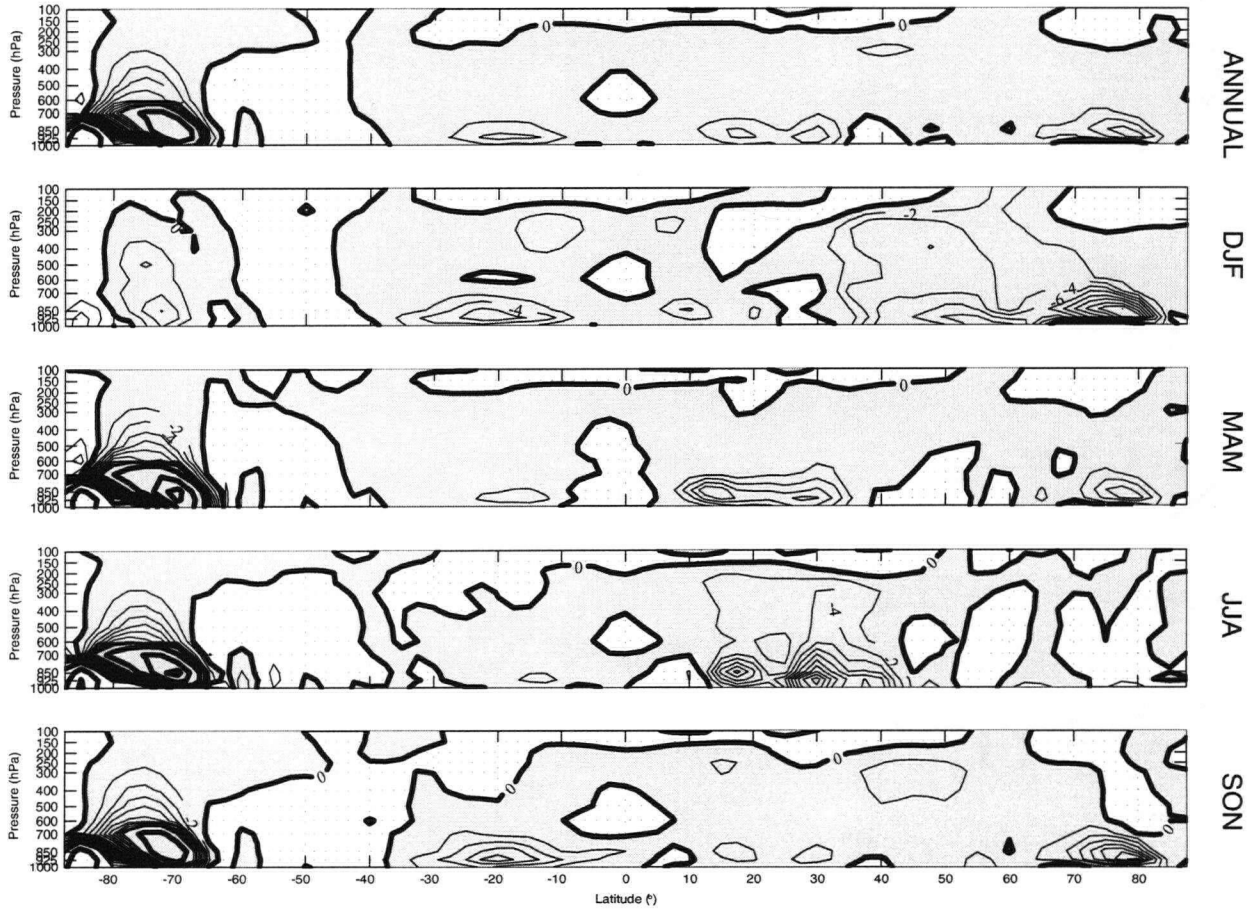

Figure 6.13: Annual and seasonal-mean distributions of $\left[\overline{\theta}^{*}\,\overline{\omega}^{*}\right]$ (stationary eddies). Units are $10^{-2}\ Pa\ K\ s^{-1}$ and the contour intervals are $2 \times 10^{-2}\ Pa\ K\ s^{-1}$ (light contours) and $30 \times 10^{-2}\ Pa\ K\ s^{-1}$ (dark contours).

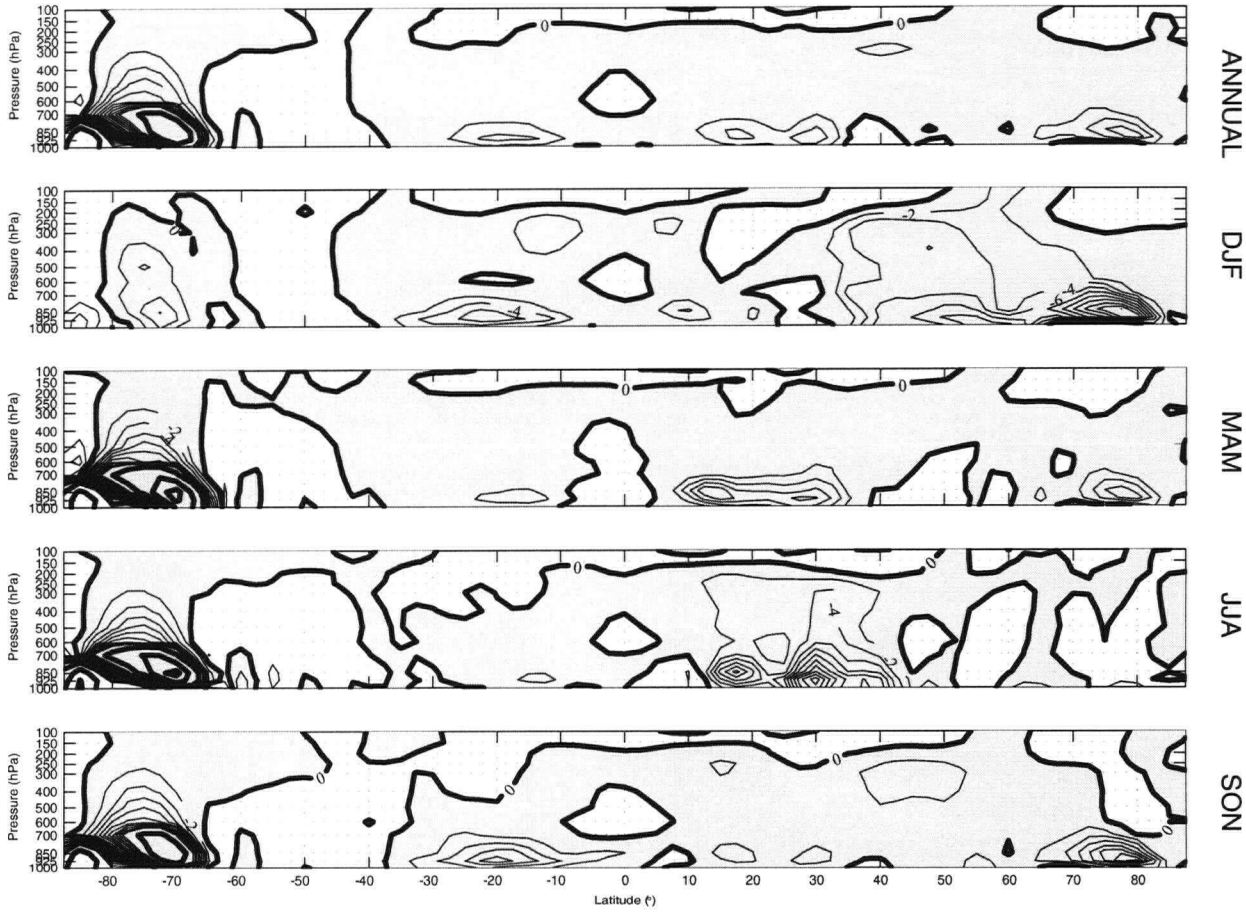

Figure 6.14: Annual and seasonal-mean distributions of $\overline{[\theta'][\omega']}$ (transient, zonally-symmetric eddies). Units are $10^{-2}\ Pa\ K\ s^{-1}$ and the contour intervals are $1 \times 10^{-2}\ Pa\ K\ s^{-1}$ (light contours) and $10 \times 10^{-2}\ Pa\ K\ s^{-1}$ (dark contours).

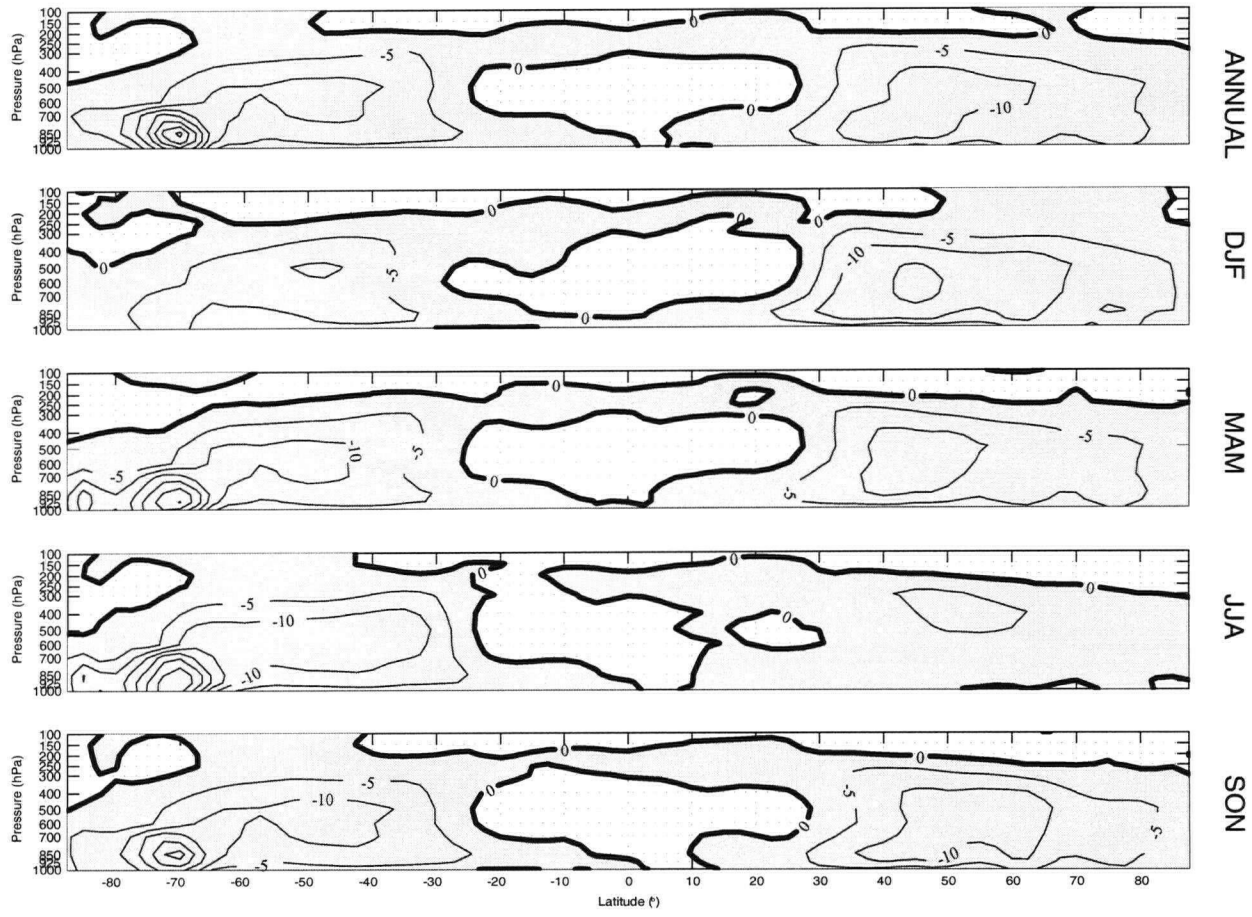

Figure 6.15: Annual and seasonal-mean distributions of $\left[\overline{\theta^{*\prime}\omega^{*\prime}}\right]$ (transient, zonally-asymmetric eddies). Units are $10^{-2}\ Pa\ K\ s^{-1}$ and the contour intervals are $5 \times 10^{-2}\ Pa\ K\ s^{-1}$.

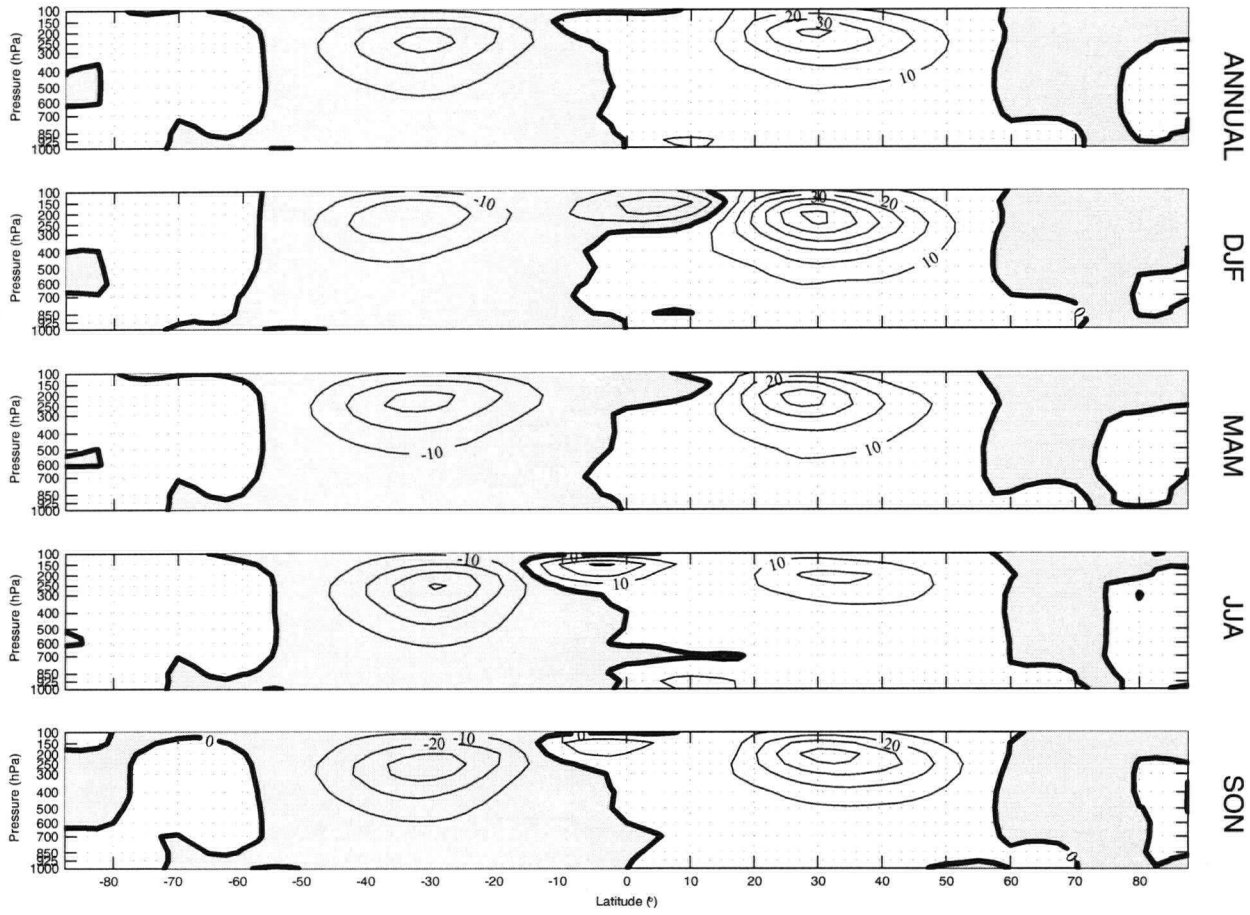

Figure 6.16: Annual and seasonal-mean distributions of northward momentum flux. Units are $m^2\ s^{-2}$ and the contour interval is $10\ m^2\ s^{-2}$.

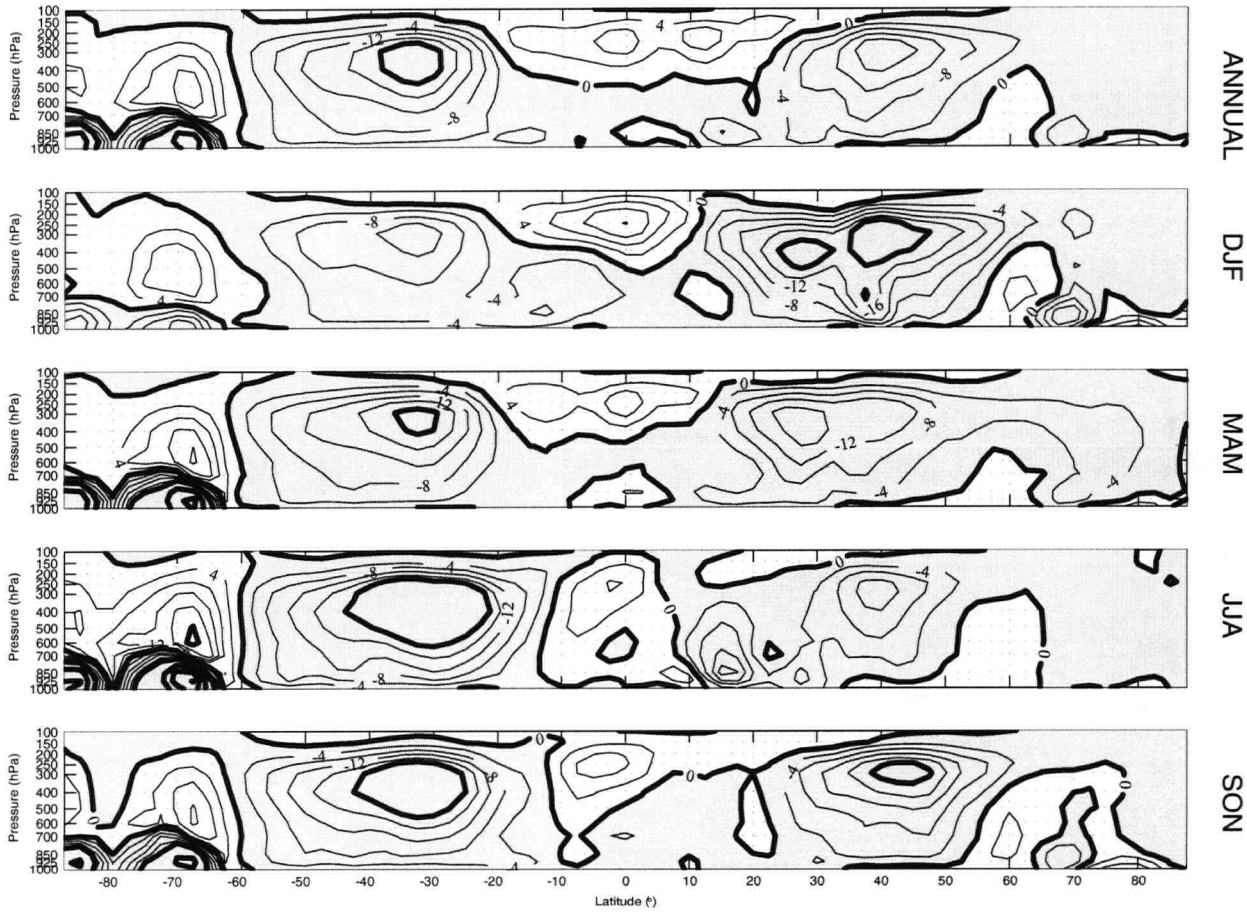

Figure 6.17: Annual and seasonal-mean distributions of upward momentum flux. Units are $10^{-2}\, m\ Pa\ s^{-2}$ and the contour intervals are $4 \times 10^{-2}\, m\ Pa\ s^{-2}$ (light contours) and $20 \times 10^{-2}\, m\ Pa\ s^{-2}$ (dark contours).

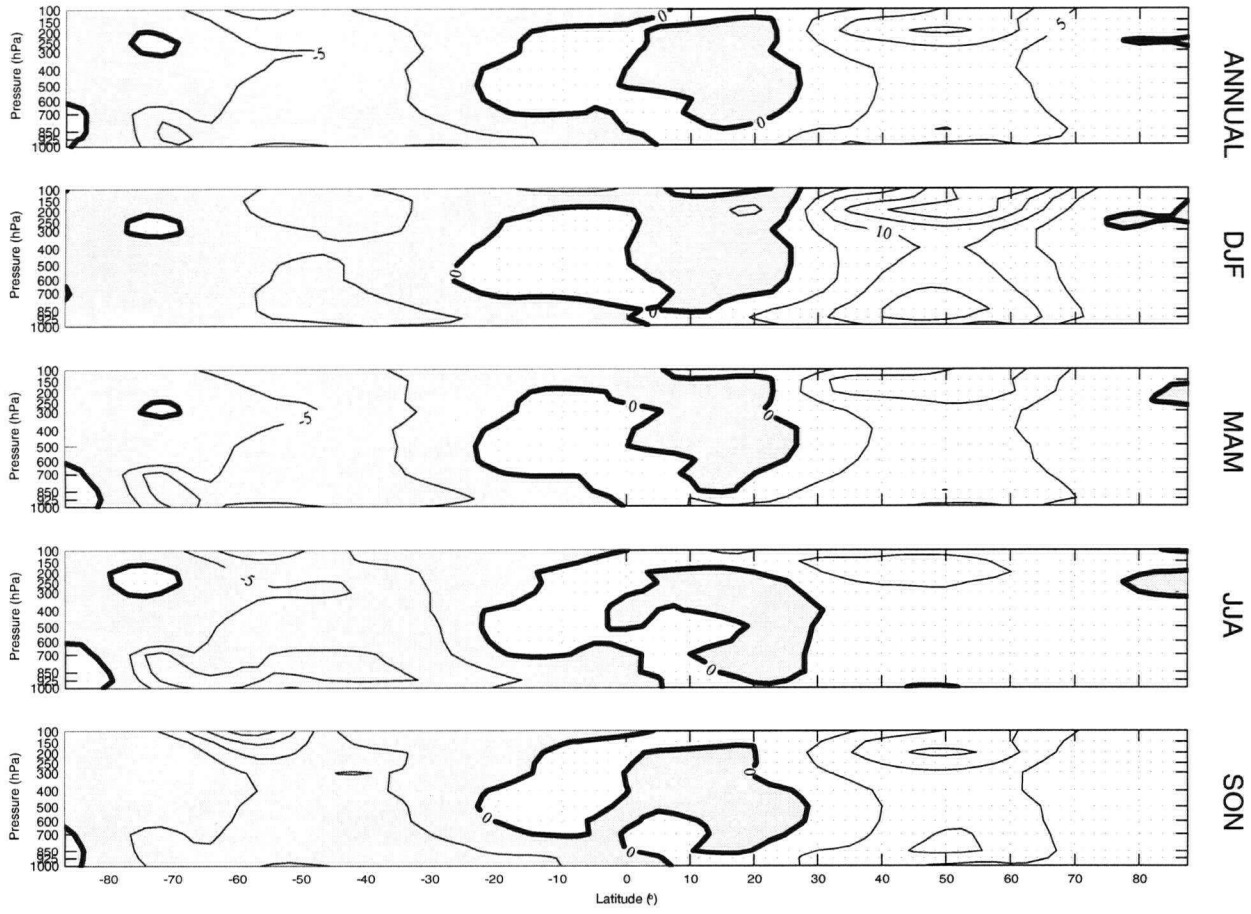

Figure 6.18: Annual and seasonal-mean distributions of northward heat flux. Units are $K\ s^{-1}$ and the contour interval is $5\ K\ s^{-1}$.

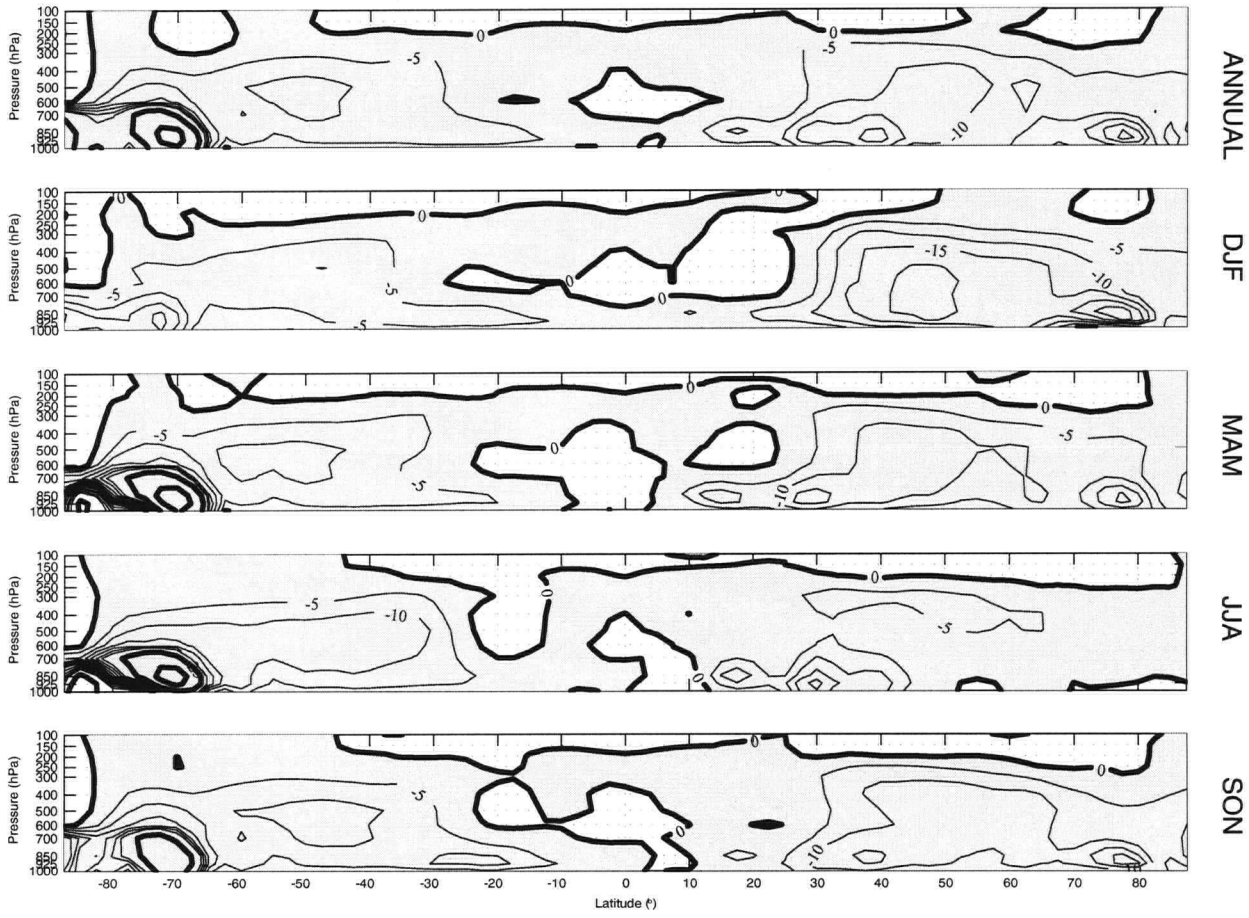

Figure 6.19: Annual and seasonal-mean distributions of upward heat flux. Units are 10^{-2} Pa K s^{-1} and the contour intervals are 5×10^{-2} Pa K s^{-1} (light contours) and 50×10^{-2} Pa K s^{-1} (dark contours).

and Ferrel cells, along with their combined effect:

$$
\begin{aligned}
H_{\text{Hadley}} &= \frac{R_d p^{\kappa-1}}{p_{00}\kappa R}\left(\frac{p_{00}}{p}\right)\kappa\frac{[Q]}{c_p} \\
H_{\text{Ferrel}} &= -\frac{R_d p^{\kappa-1}}{p_{00}\kappa R}\left(\frac{\partial\left([\theta^* v^*]\cos\phi\right)}{R\partial\eta}+\frac{\partial\left[\theta^*\omega^*\right]}{\partial p}\right) \\
H &= \frac{R_d p^{\kappa-1}}{p_{00}\kappa R}\left(\left(\frac{p_{00}}{p}\right)\kappa\frac{[Q]}{c_p}-\frac{\partial\left([\theta^* v^*]\cos\phi\right)}{R\partial\eta}-\frac{\partial\left[\theta^*\omega^*\right]}{\partial p}\right) \\
\chi_{\text{Hadley}} &\equiv 0 \\
\chi_{\text{Ferrel}} &= \frac{\tilde{f}}{\cos\phi}\left(\frac{\partial\left([u^* v^*]\cos^2\phi\right)}{R\cos\phi\partial\eta}+\frac{\partial\left[u^*\omega^*\right]}{\partial p}\right) \\
\chi &= \frac{\tilde{f}}{\cos\phi}\left(\frac{\partial\left([u^* v^*]\cos^2\phi\right)}{R\cos\phi\partial\eta}+\frac{\partial\left[u^*\omega^*\right]}{\partial p}\right),
\end{aligned}
$$

remembering that $[F_\lambda] \equiv 0$.

From these quantities, the heat and momentum flux forcing functions are calculated:

$$
\begin{aligned}
\text{total eddy flux forcing} &= \frac{\partial H_{\text{Ferrel}}}{\partial\eta}+\frac{\partial\chi_{\text{Ferrel}}}{\partial p} \\
\text{total diabatic heating forcing} &= \frac{\partial H_{\text{Hadley}}}{\partial\eta} \\
\text{total streamfunction forcing} &= \frac{\partial H}{\partial\eta}+\frac{\partial\chi}{\partial p}=\frac{\partial\left(H_{\text{Ferrel}}+H_{\text{Hadley}}\right)}{\partial\eta}+\frac{\partial\chi_{\text{Ferrel}}}{\partial p}
\end{aligned}
$$

and the streamfunction equation is solved numerically for each of the three choices of forcing, with momentum and thermodynamic budgets being calculated for each

resulting distribution of ψ.

7. Streamfunction ψ

The streamfunctions depicting the diabatic heating- and eddy- induced mean meridional circulations in the annual mean and for all the seasons, ψ_{Hadley} and ψ_{Ferrel}, are shown in Figures 7.1 and 7.2 respectively. The streamfunction corresponding to the combined effects, ψ, is shown in Figure 7.3. In each case, positive values represent represent clockwise motion and negative values an anticlockwise circulation (consistent with equations (3.7) and (3.8)).

The effect of diabatic heating is seen to principally drive a direct circulation around the equator; this is the Hadley circulation[14]. Both the latitude and magnitude of the circulation is seen to strongly follow the angle of insolation, with the regions of subtropical subsidence also being seen to vary with the seasons. The effective disappearance of the Hadley cell in the summer hemisphere is strongly evident (as with the mass streamfunction computed by [PO92]). Notable from Figure 7.3, in spite of the apparent strong diabatic heating in the lower troposphere south of $70°S$, is the absence of any thermally-forced circulation there. An indication that is not simply a consequence of the imposed null boundary condition is the appearance of large values of ψ_{Hadley} near the Equatorial surface.

[14] A historical overview of the origins of the names for the various circulations may be found in [Lor67].

The eddy fluxes of heat and momentum drive, in each hemisphere, a relatively strong direct circulation near the Equator, a strong indirect circulation in the midlatitudes and a weak direct circulation in the polar latitudes. The tropical cells exhibit the same pattern of seasonal variability as those generated by diabatic heating. However, the extratropical cells do not appear to shift in position during the course of the year, although the circulations' peak valus show strong seasonal variation in intensity, with small seasonal shift in latitude. It should be noted that the peak values of the streamfunction in the Hadley circulation (Figure 7.1) will substantially dominate those of the Ferrel circulation (Figure 7.2), except in the mid-latitudes. The assumption of [Pfe81] that the circulation shows strong Equatorial symmetry across the seasons is thus seen to be fallacious.

From consideration of the individual circulations depicted in Figures 7.1 and 7.2, one expects a broad reinforcement of the direct circulation near the equator, with opposing values outside the tropics. The picture of the net circulation provided by the combined effect of eddy-fluxes and diabatic heating, depicted in Figure 7.3, is one of strong direct circulation near the Equator with a substantially weaker indirect circulation in the mid-latitudes, varying both in latitude and intensity with the seasons. The polar direct circulations are barely in evidence, being only readily apparent in the Southern Hemisphere during the austral

autumn and winter.

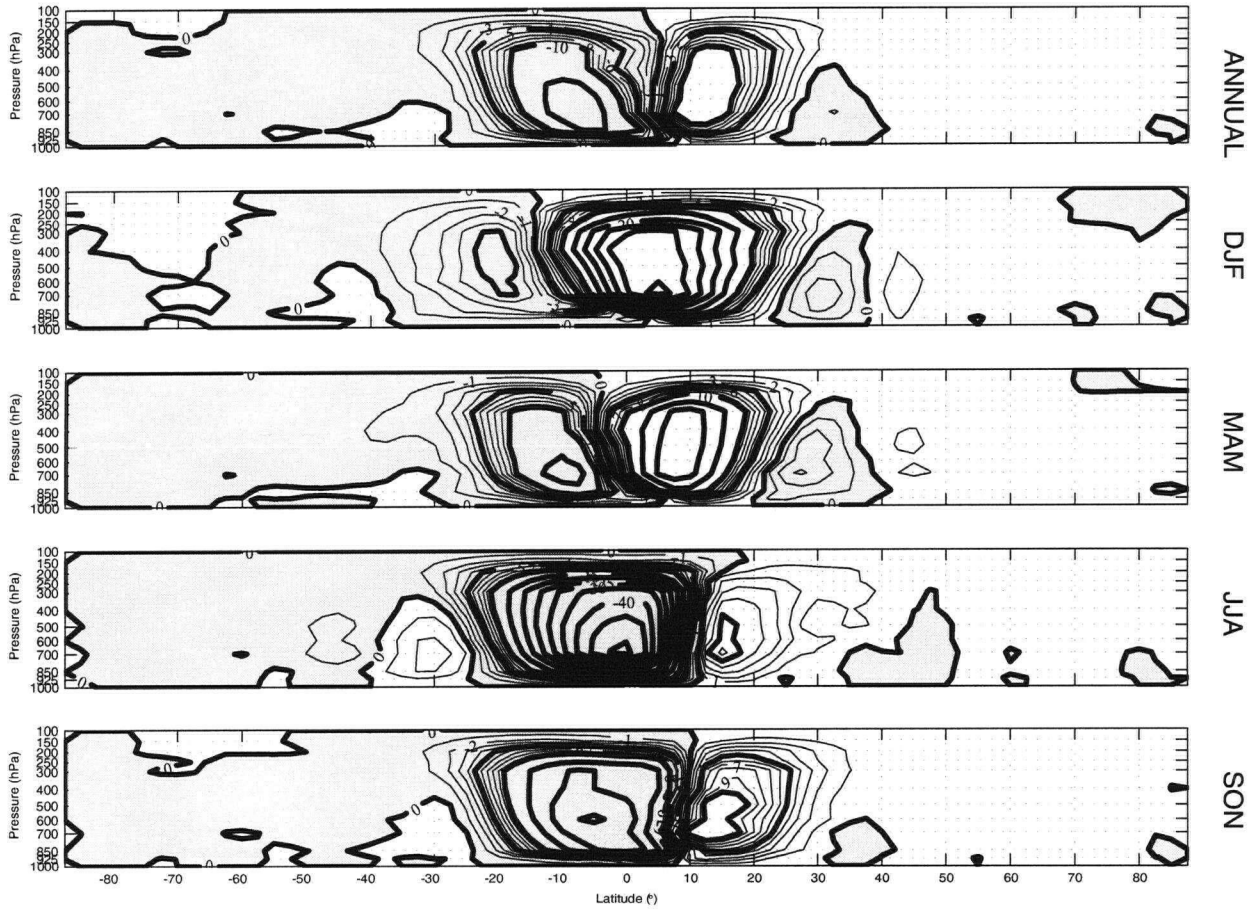

Figure 7.1: Annual and seasonal-mean distributions of ψ due to diabatic heating (Hadley circulation, ψ_{Hadley}). Units are $10^3\ m\ Pa\ s^{-1}$ and the contour intervals are $1 \times 10^3\ m\ Pa\ s^{-1}$ (light contours) and $5 \times 10^3\ m\ Pa\ s^{-1}$ (dark contours).

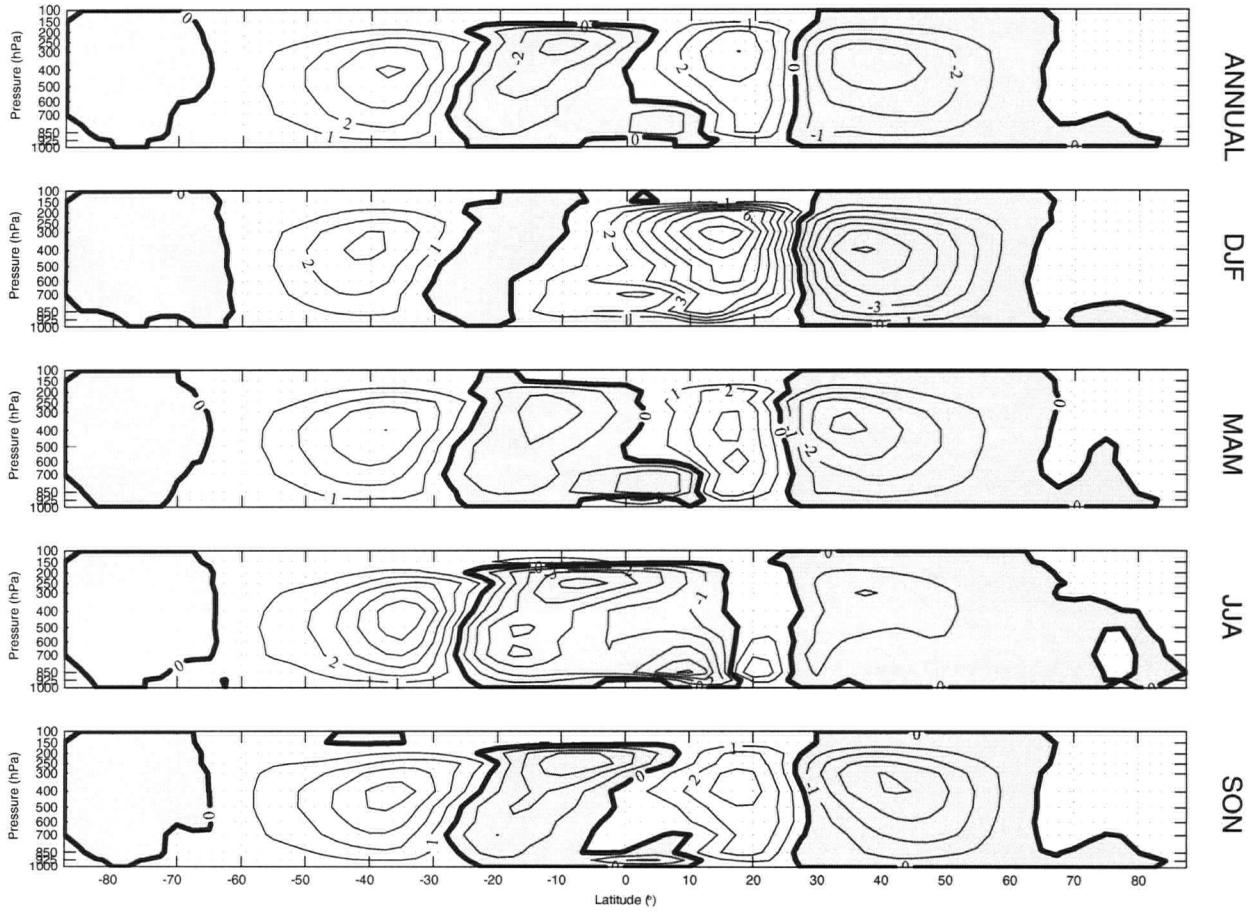

Figure 7.2: Annual and seasonal-mean distributions of the eddy-induced component of ψ (Ferrel circulation, ψ_{Ferrel}). Units are $10^3\ m\ Pa\ s^{-1}$ and the contour interval is $1 \times 10^3\ m\ Pa\ s^{-1}$.

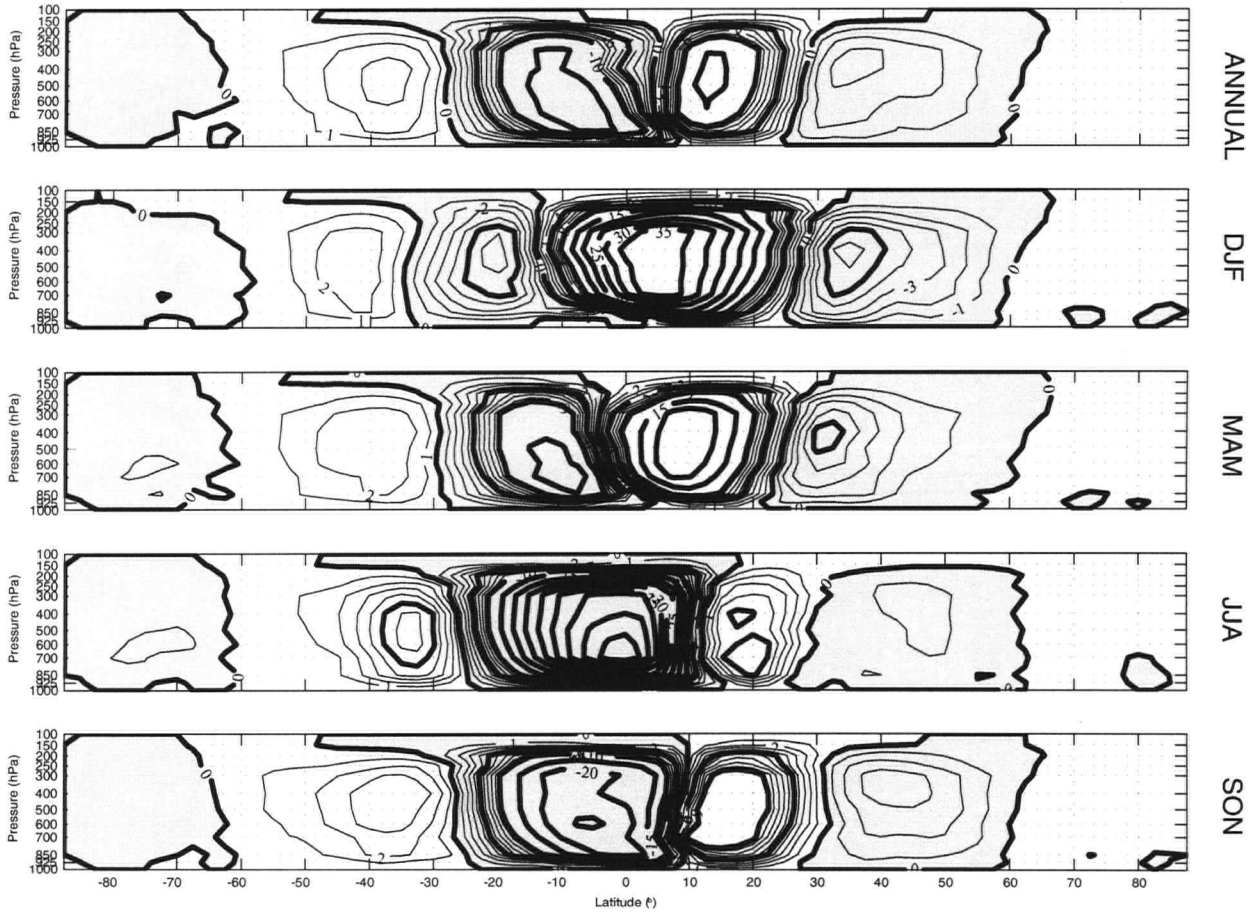

Figure 7.3: Annual and seasonal-mean distributions of ψ. Units are $10^3\ m\ Pa\ s^{-1}$ and the contour intervals are $1 \times 10^3\ m\ Pa\ s^{-1}$ (light contours) and $5 \times 10^3\ m\ Pa\ s^{-1}$ (dark contours).

8. Momentum and heat budgets

The values of ψ determined by numerical solution of the streamfunction equation (3.4) for the cases of eddy-driven, diabatic heating-driven and total circulation are used to evaluate (through equations (3.7) and (3.8)) the terms involving $[v]$ and $[\omega]$ in equations (3.5) and (3.6).

8.1. Budgets of eddy-driven circulation

For the eddy-driven circulation, the momentum tendency is given by

$$\frac{\partial [u]}{\partial t} = \underbrace{[v]\left(f - \frac{\partial ([u]\cos\phi)}{R\cos\phi\partial\phi}\right) - [\omega]\frac{\partial [u]}{\partial p}}_{(v,\omega)\text{ terms}} \underbrace{- \frac{\partial ([u^*v^*]\cos^2\phi)}{R\cos^2\phi\partial\phi} - \frac{\partial [u^*\omega^*]}{\partial p}}_{\text{Eddy terms}}$$

and the potential temperature tendency is given by

$$\frac{\partial [\theta]}{\partial t} = \underbrace{-\frac{[v]}{R}\frac{\partial [\theta]}{\partial \phi} - [\omega]\frac{\partial [\theta]}{\partial p}}_{(v,\omega)\text{ terms}} \underbrace{- \frac{\partial ([\theta^*v^*]\cos\phi)}{R\cos\phi\partial\phi} - \frac{\partial [\theta^*\omega^*]}{\partial p}}_{\text{Eddy terms}}$$

where the streamfunction equation (3.4) is solved with forcing of $\frac{\partial H_{\text{Ferrel}}}{\partial \eta} + \frac{\partial \chi_{\text{Ferrel}}}{\partial p}$ and the values of $[v]$ and $[\omega]$ are determined from ψ_{Ferrel}. Zonal-momentum budgets for annual- and seasonal-mean conditions are shown in Figures 8.1-8.5, with

potential temperature budgets for annual- and seasonal-mean conditions shown in Figures 8.7-8.11.

Throughout the year, the contribution to the momentum tendency by the circulation in the Ferrel cell is concentrated in the upper part of the atmosphere ($200\ hPa - 250\ hPa$), with the maximum migrating between $35° - 45°$ and strengthening with the annual cycle to reach a peak in wintertime. The contribution to $\frac{\partial [u]}{\partial t}$ by the eddy motions is very similar to this, although opposite in sign and with magnitudes $\sim 25\%$ greater. Momentum tendencies due to the (v, ω) terms are always opposite in the upper and lower troposphere, with the secondary centres appearing near the surface. The boundary-layer peaks in momentum tendency found by [Pfe81] are not so much in evidence in the current investigation, possibly due to the model-based nature of the NCEP/NCAR data set and the consequent interpolation from σ-levels, along with a large sensitivity to the choice of contouring levels. There is, apparently, strong wave-mean flow interaction, with values of $\sim 2 \times 10^{-5}\ m\ s^{-1}\ day^{-1}$ surprisingly evident in the wintertime upper troposphere, providing deceleration of the mean zonal flow far equatorward of the jet-stream maxima. Comparison of the polarity of the momentum tendency in regions equatorward and poleward of the jet-stream maxima (from Figure 6.1) shows that the momentum tendencies produced by eddy motions strongly mimic

the migration of the jet stream.

Consideration of the production of zonal kinetic energy, $[u]\frac{\partial[u]}{\partial t}$, by the eddy motions and the associated eddy-induced mean meridional circulation shows a net production in the mid-latitudes and a decrease near the equator and the higher latitudes; an annual cycle is strongly evident, with adjacent peaks in the wintertime upper tropical atmosphere. The regions of strong production, shown in Figure 8.6, are at exactly the same latitudes and altitudes as the jet-stream maxima of Figure 6.1, in sharp contrast with the results of [Pfe81].

The contribution to the zonally-averaged potential temperature tendency by the eddy-induced meridional circulation is opposite in sign to that induced directly by the eddies and is typically smaller in magnitude. The eddy-induced tendency is for heating throughout the atmosphere poleward of 45° (although this region extends to 30° at the altitude of the jet-stream maxima), with the largest values appearing during the winter in each hemisphere. There is also a strong eddy-induced upper-tropospheric cooling at 25° during the boreal winter. In contrast, the eddies typically have a cooling influence throughout the tropical and subtropical atmosphere. Examining the vertical variations of $\frac{\partial[\theta]}{\partial t}$, one may see that the general effect of the eddies in the southern polar regions is to destabilise the atmosphere. The general structure of the potential temperature tendency in

the higher latitudes is heating throughout the troposphere, with the secondary circulation apparently moving the eddy-induced heating maximum slightly poleward. Comparison of the plots of potential temperature tendency with Figure 6.2 shows that the distribution of $\frac{\partial[\theta]}{\partial t}$ can account for some changes in the meridional temperature gradient across the seasons.

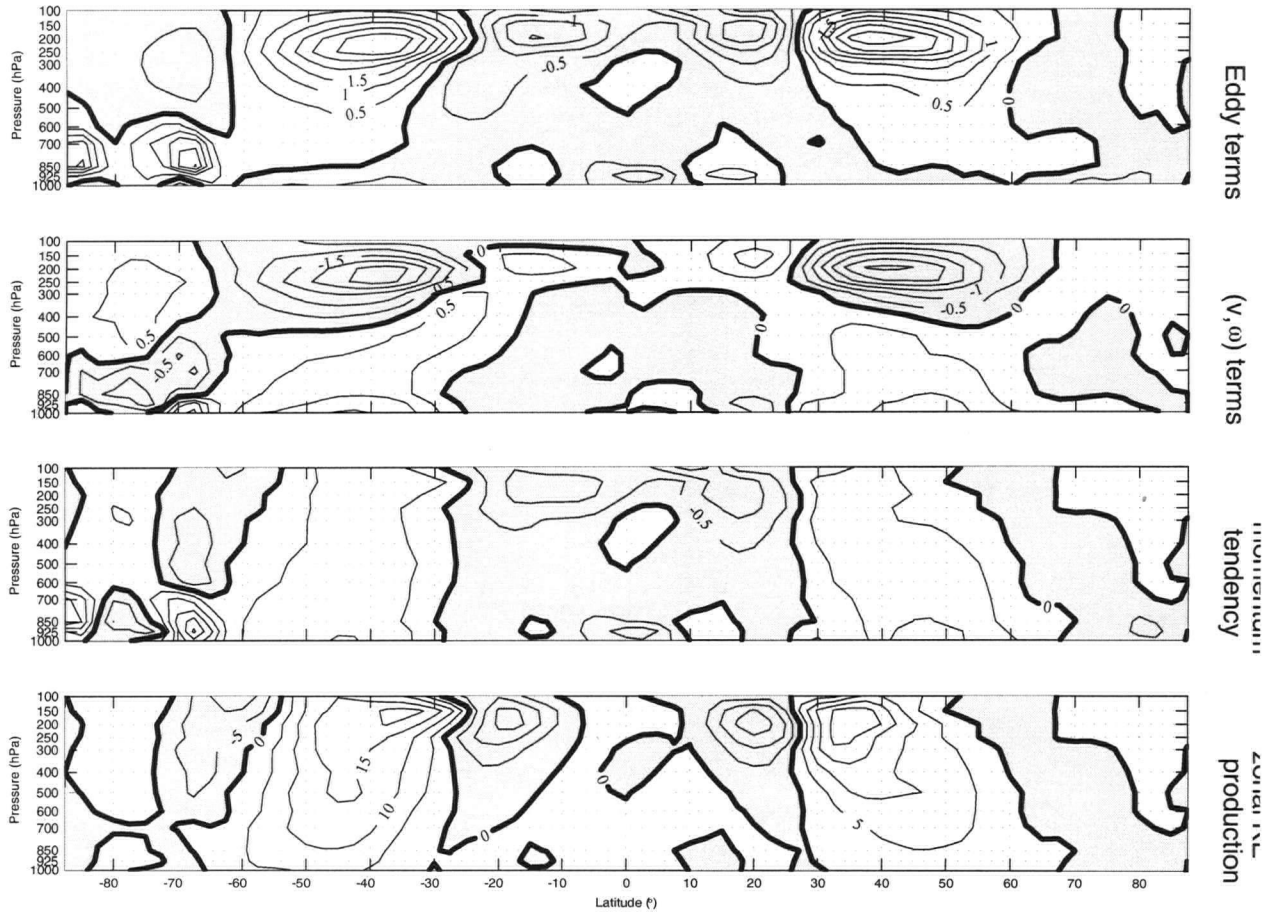

Figure 8.1: Annual average momentum budget (top three panels) and zonal kinetic energy production due to eddy-flux forcing. For the top three panels, the units are $10^{-5}\ m\ s^{-2}$ and the contour interval is $0.5 \times 10^{-5}\ m\ s^{-2}$. For the bottom panel, the units are $10^{-5}\ m^2\ s^{-3}$ and the contour interval is $5 \times 10^{-5}\ m^2\ s^{-3}$.

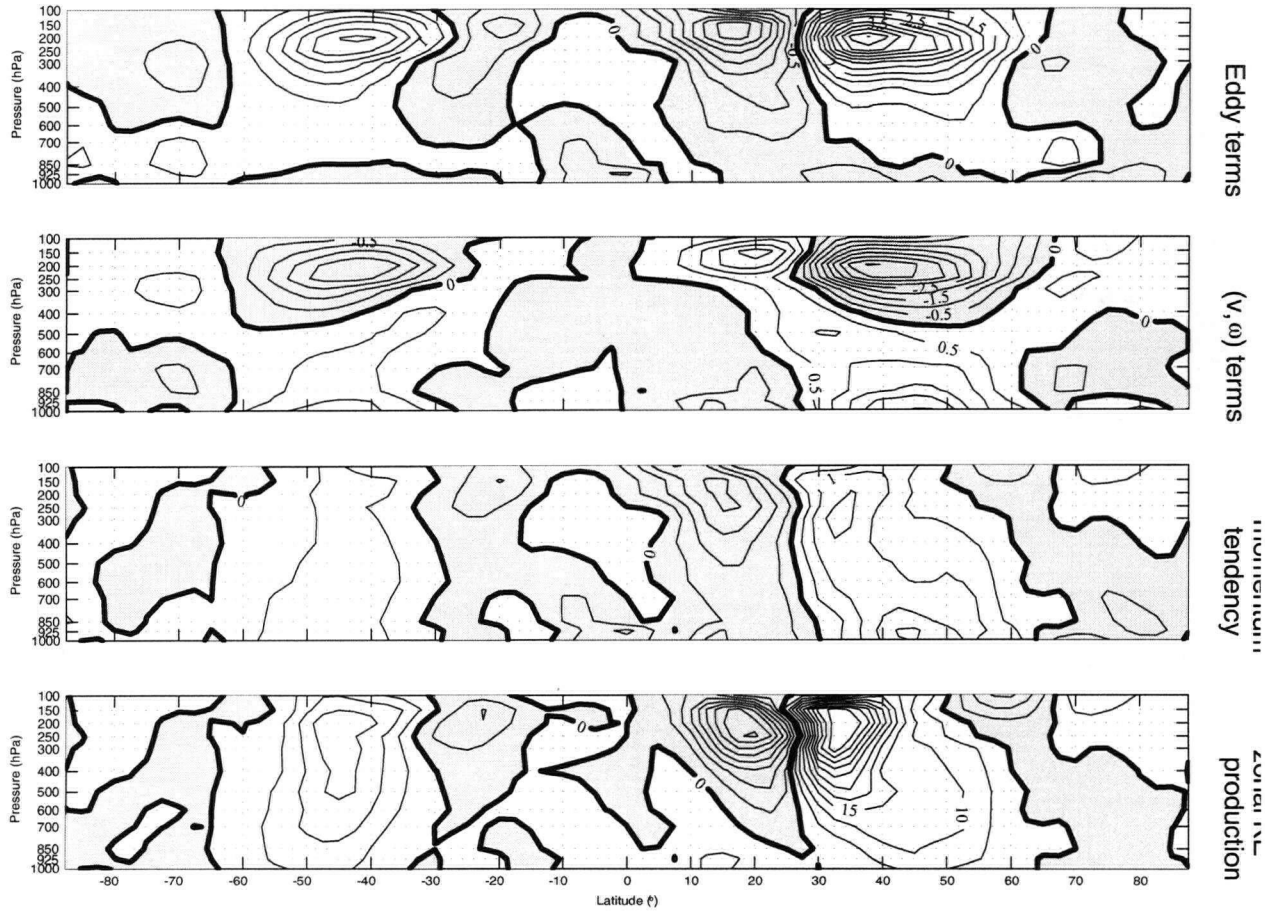

Figure 8.2: Average winter (DJF) momentum budget (top three panels) and zonal kinetic energy production due to eddy-flux forcing. For the top three panels, the units are $10^{-5}\ m\ s^{-2}$ and the contour interval is $0.5 \times 10^{-5}\ m\ s^{-2}$. For the bottom panel, the units are $10^{-5}\ m^2\ s^{-3}$ and the contour interval is $5 \times 10^{-5}\ m^2\ s^{-3}$.

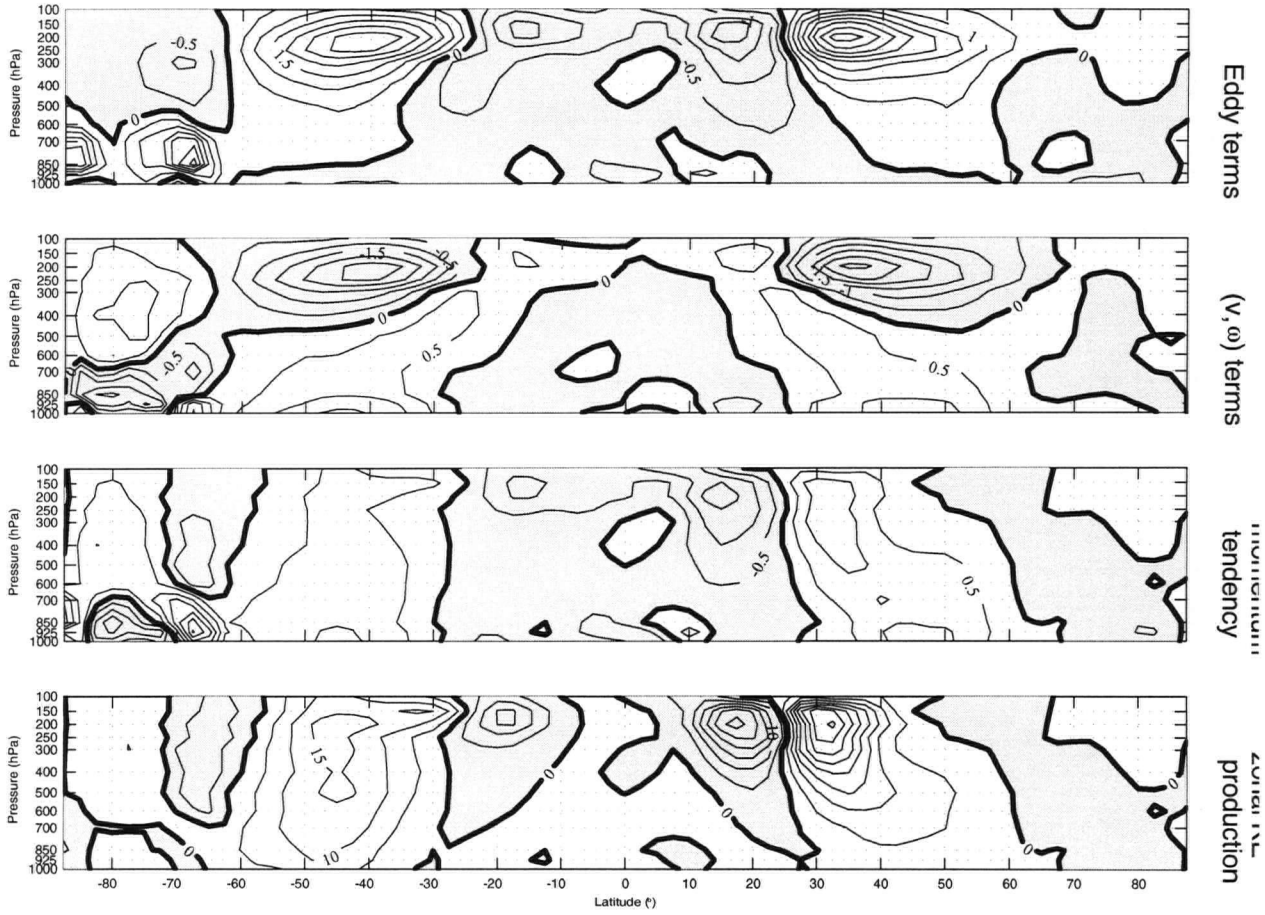

Figure 8.3: Average spring (MAM) momentum budget (top three panels) and zonal kinetic energy production due to eddy-flux forcing. For the top three panels, the units are 10^{-5} m s^{-2} and the contour interval is 0.5×10^{-5} m s^{-2}. For the bottom panel, the units are 10^{-5} m^2 s^{-3} and the contour interval is 5×10^{-5} m^2 s^{-3}.

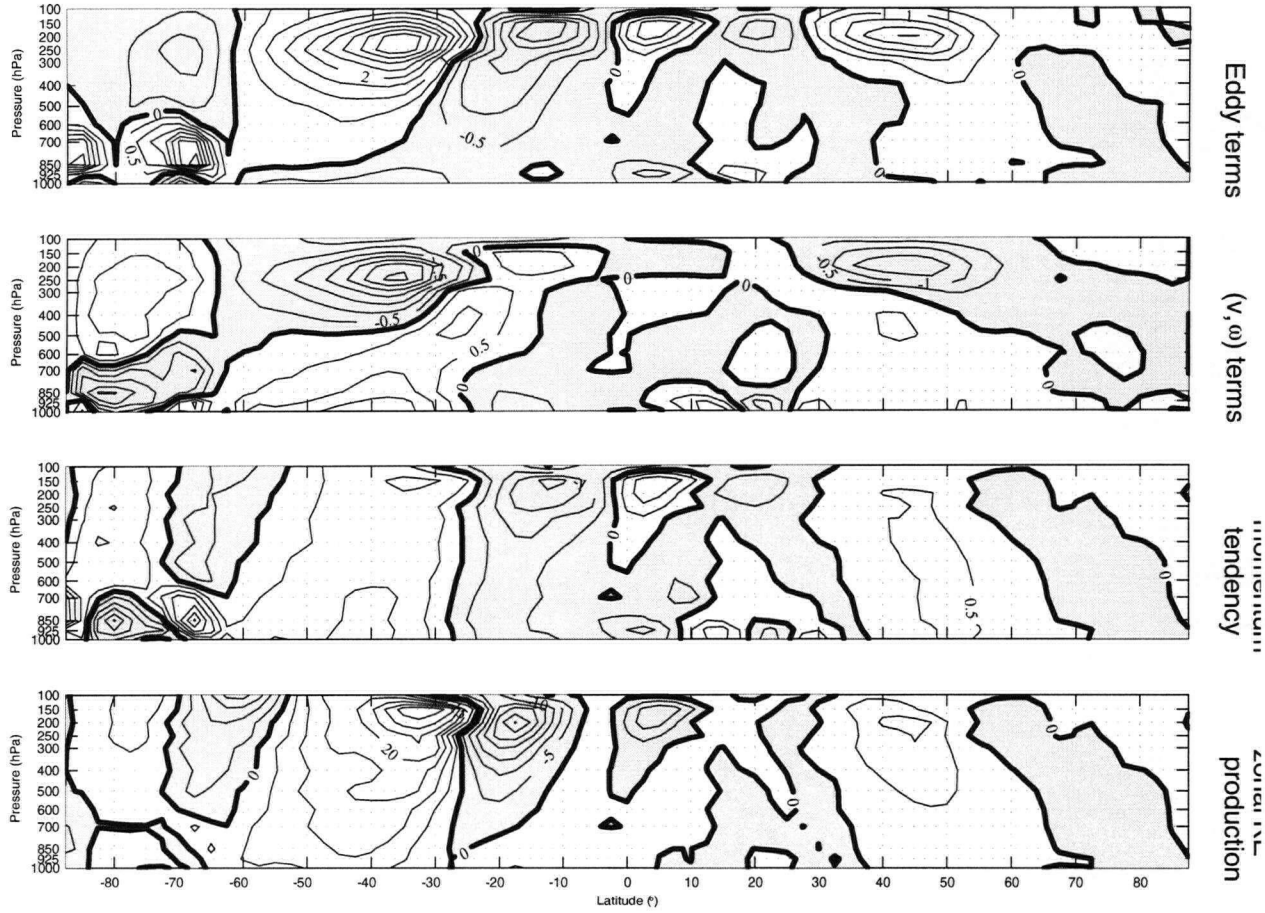

Figure 8.4: Average summer (JJA) momentum budget (top three panels) and zonal kinetic energy production due to eddy-flux forcing. For the top three panels, the units are 10^{-5} m s^{-2} and the contour interval is 0.5×10^{-5} m s^{-2}. For the bottom panel, the units are 10^{-5} m^2 s^{-3} and the contour interval is 5×10^{-5} m^2 s^{-3}.

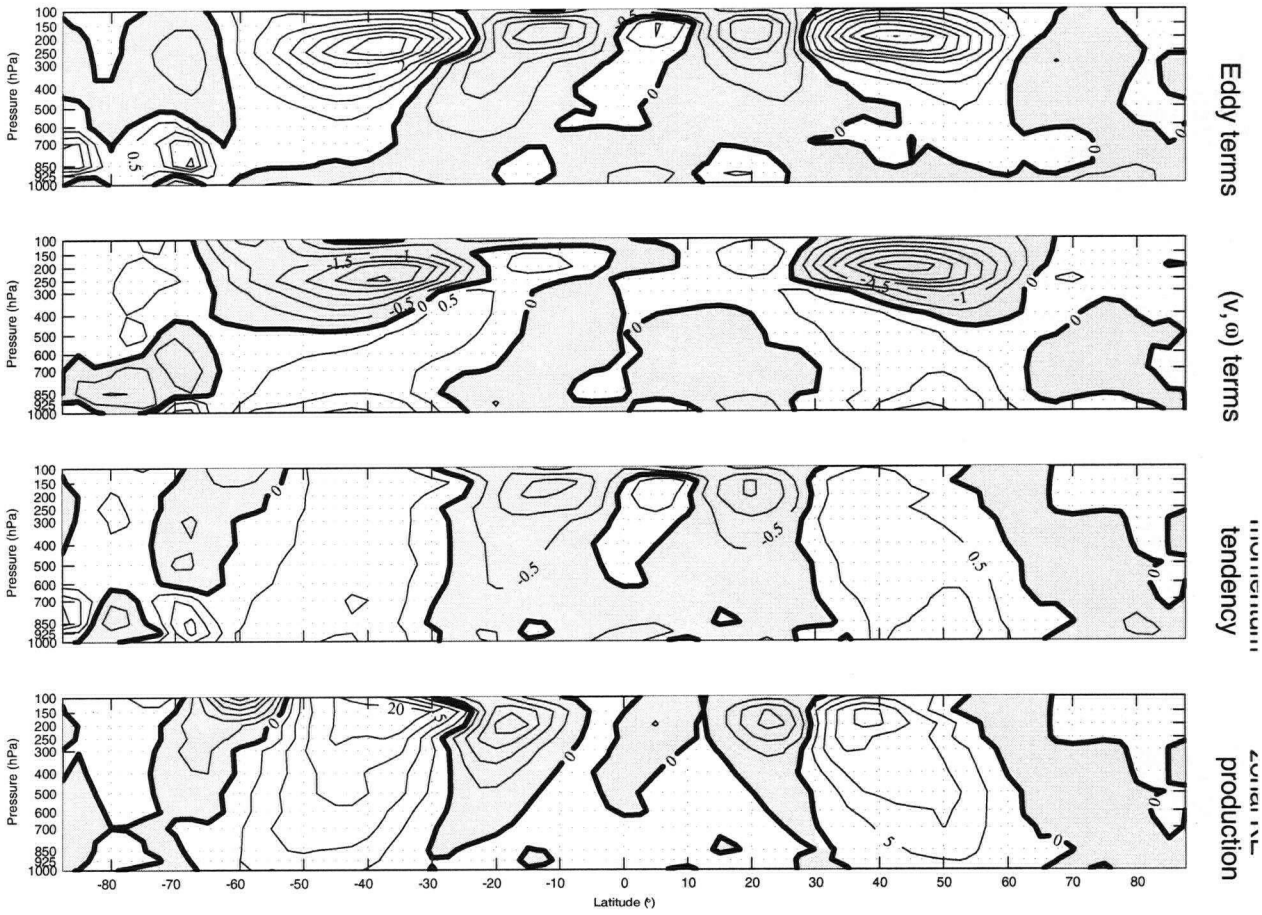

Figure 8.5: Average autumn (SON) momentum budget (top three panels) and zonal kinetic energy production due to eddy-flux forcing. For the top three panels, the units are $10^{-5}\ m\ s^{-2}$ and the contour interval is $0.5 \times 10^{-5}\ m\ s^{-2}$. For the bottom panel, the units are $10^{-5}\ m^2\ s^{-3}$ and the contour interval is $5 \times 10^{-5}\ m^2\ s^{-3}$.

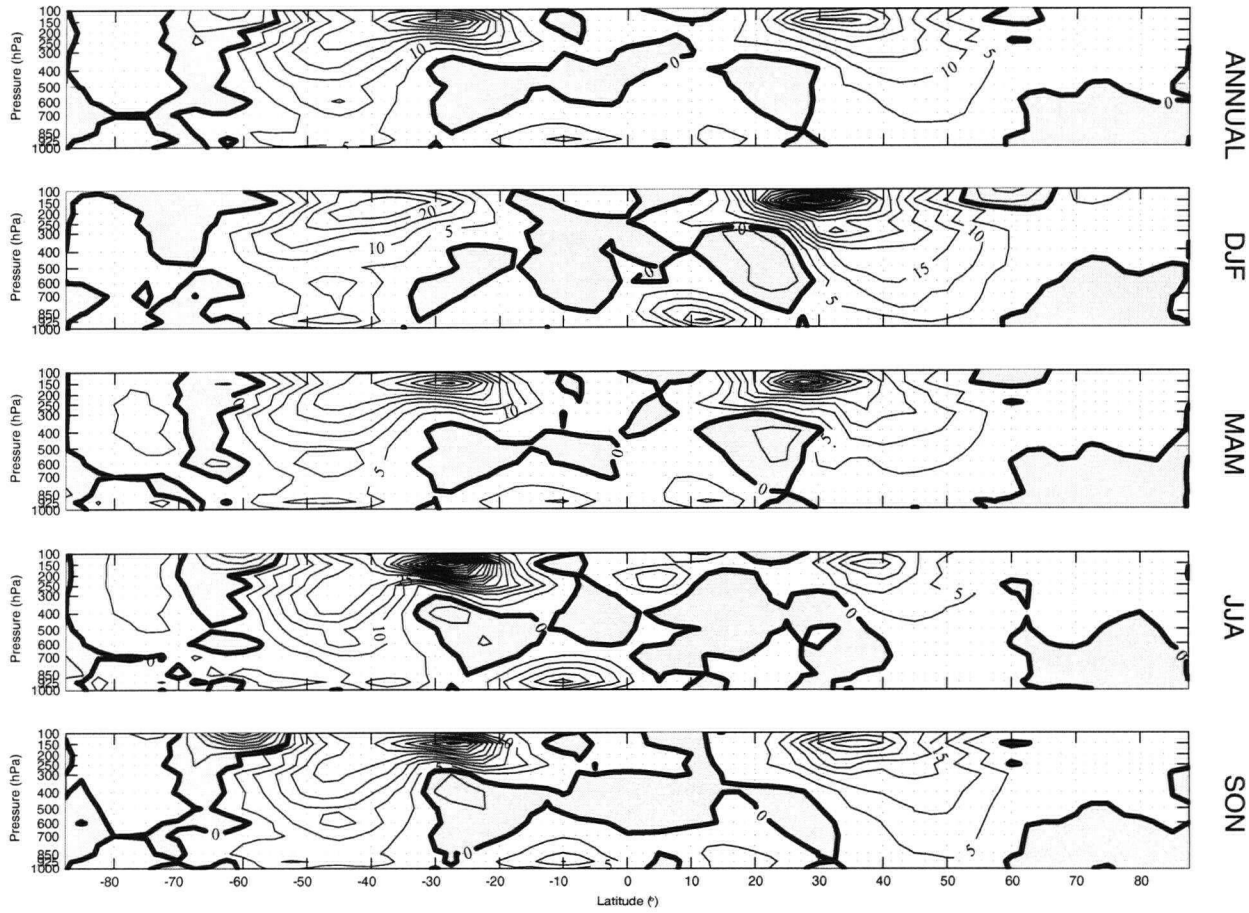

Figure 8.6: Annual- and seasonal-average zonal kinetic energy production due to eddy-flux forcing. The units are 10^{-5} m^2 s^{-3} and the contour interval is 5×10^{-5} m^2 s^{-3}.

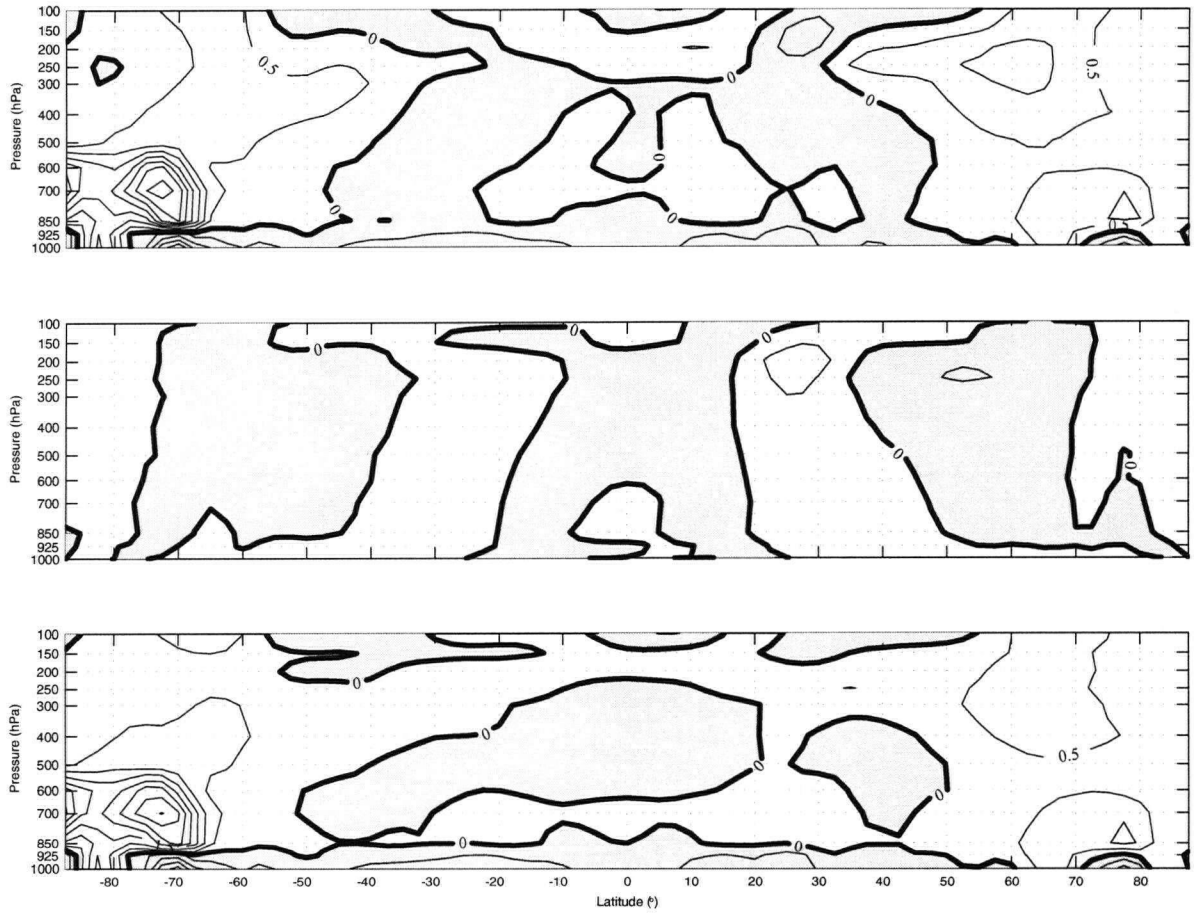

Figure 8.7: Annual average heat budget due to eddy-flux forcing. The units are $10^{-5}\ K\ s^{-1}$ and the contour interval is $0.5 \times 10^{-5}\ K\ s^{-1}$.

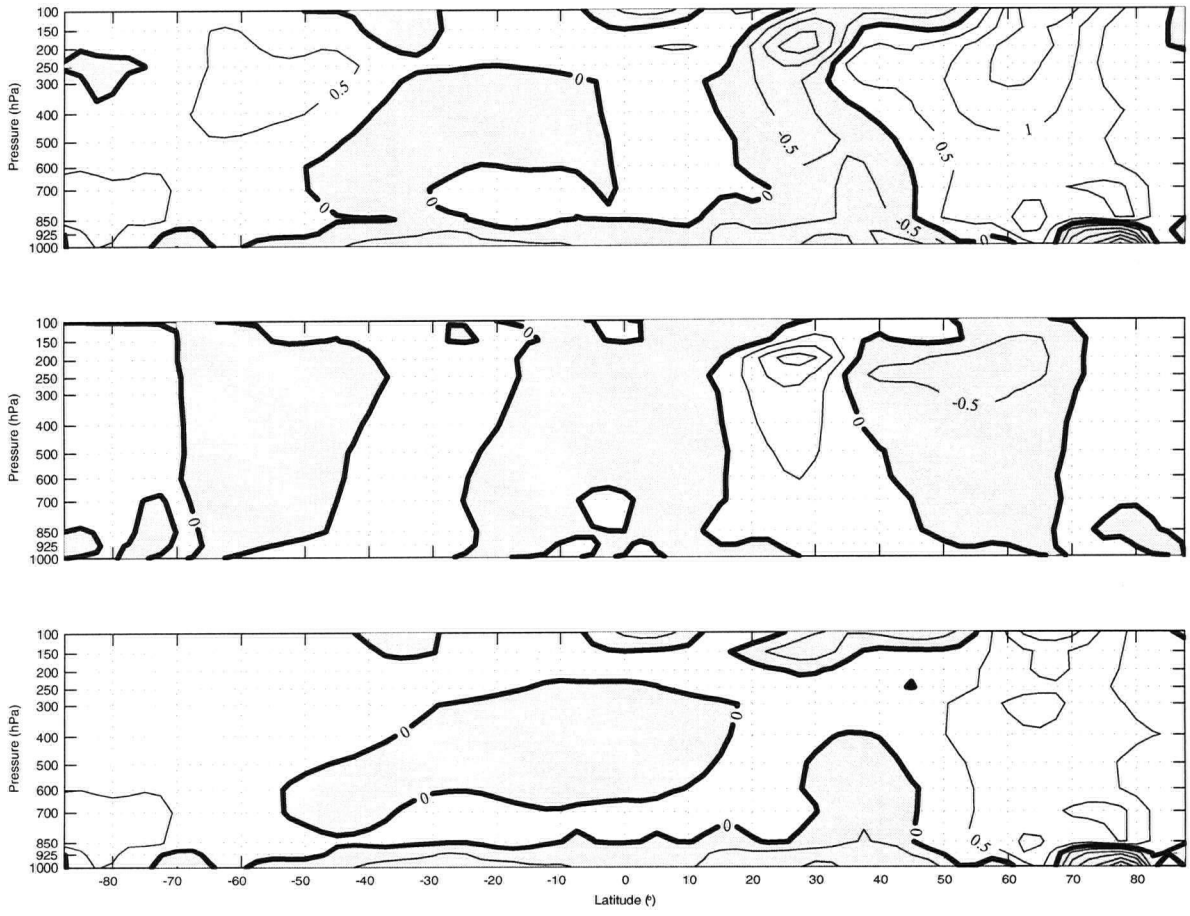

Figure 8.8: Average winter (DJF) heat budget due to eddy-flux forcing. The units are $10^{-5}\ K\ s^{-1}$ and the contour interval is $0.5 \times 10^{-5}\ K\ s^{-1}$.

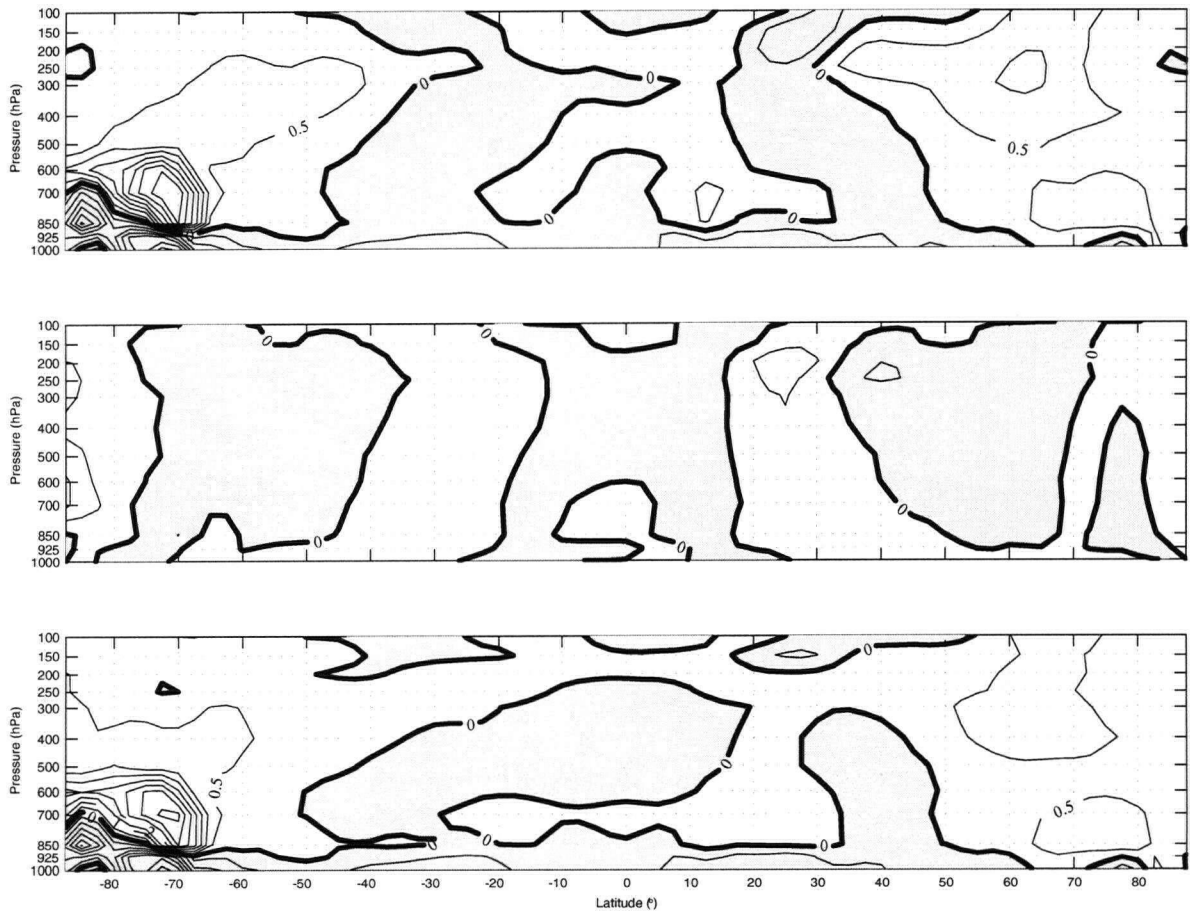

Figure 8.9: Average spring (MAM) heat budget due to eddy-flux forcing. The units are $10^{-5}\ K\ s^{-1}$ and the contour interval is $0.5 \times 10^{-5}\ K\ s^{-1}$.

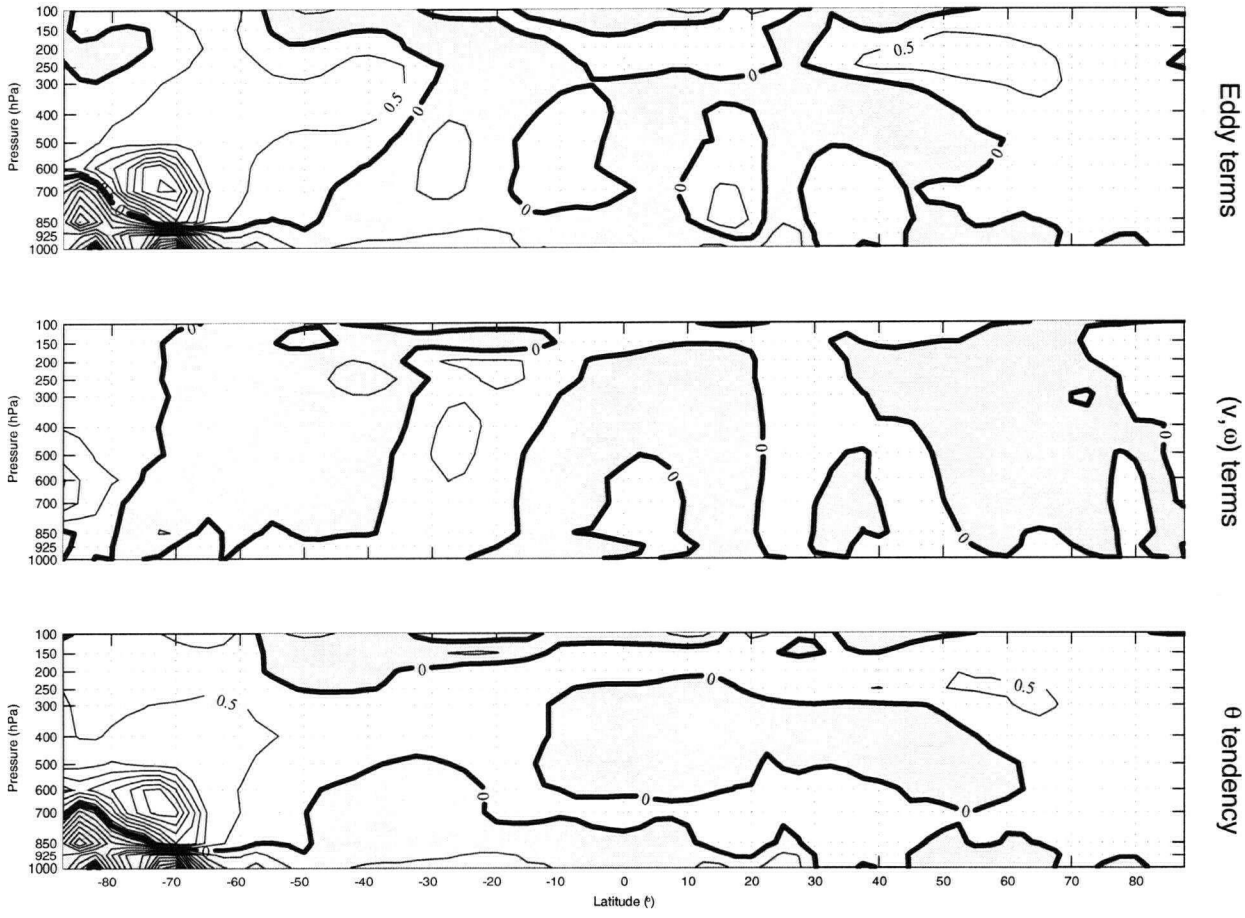

Figure 8.10: Average summer (JJA) heat budget due to eddy-flux forcing. The units are $10^{-5}\ K\ s^{-1}$ and the contour interval is $0.5 \times 10^{-5}\ K\ s^{-1}$.

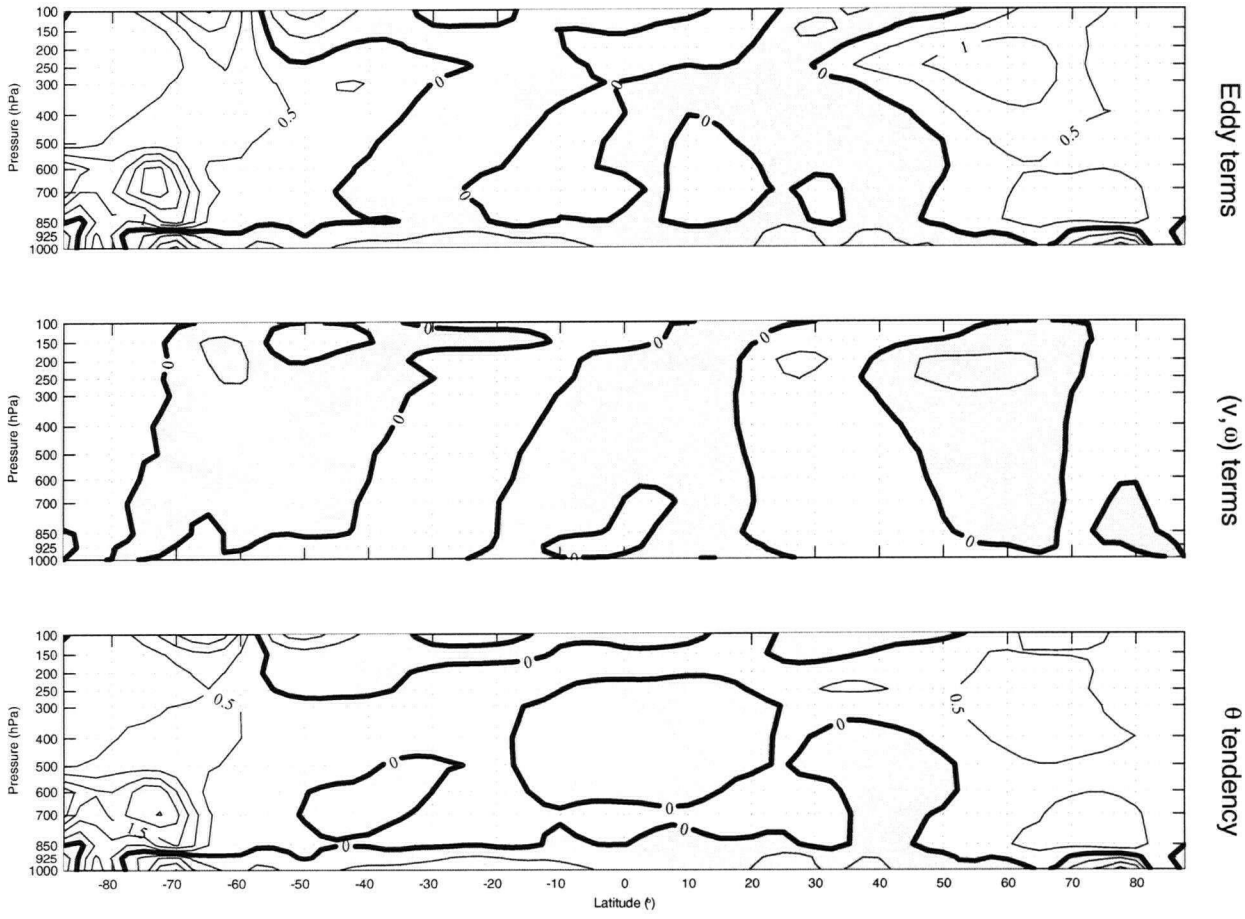

Figure 8.11: Average autumn (SON) heat budget due to eddy-flux forcing. The units are $10^{-5}\ K\ s^{-1}$ and the contour interval is $0.5 \times 10^{-5}\ K\ s^{-1}$.

8.2. Budgets of diabatic heating-driven circulation

For the circulation driven by diabatic heating, the momentum tendency is given by

$$\frac{\partial [u]}{\partial t} = \underbrace{[v]\left(f - \frac{\partial ([u]\cos\phi)}{R\cos\phi\partial\phi}\right) - [\omega]\frac{\partial [u]}{\partial p}}_{(v,\omega)\text{ terms}}$$

and the potential temperature tendency is given by

$$\frac{\partial [\theta]}{\partial t} = \underbrace{-\frac{[v]}{R}\frac{\partial [\theta]}{\partial \phi} - [\omega]\frac{\partial [\theta]}{\partial p}}_{(v,\omega)\text{ terms}} + \underbrace{\left(\frac{p_{00}}{p}\right)\kappa\frac{[Q]}{c_p}}_{\text{Diabatic Heating}}$$

where the streamfunction equation (3.4) is solved with forcing of $\frac{\partial H_{\text{Hadley}}}{\partial \eta}$ and the values of $[v]$ and $[\omega]$ are determined from ψ_{Hadley}. Zonal-momentum budgets for annual- and seasonal-mean conditions are shown in Figures 8.12-8.16, with potential temperature budgets for annual- and seasonal-mean conditions shown in Figures 8.17-8.21.

The momentum tendency induced by the Hadley circulation (precisely the (v, ω) terms outlined above) show significant values only between $30°S - 30°N$; significant accelerations on the order of $2 - 4\ m\ s^{-1}\ day^{-1}$ are evident in the wintertime between $100\ hPa - 250\ hPa$, with decelerations of comparable magnitude in the boundary layer, slightly equatorward of these peaks. There is substan-

tial zonal kinetic energy production in regions poleward of the equatorial upper tropospheric maxima in zonal wind tendency, with clear maxima evident both throughout the year and in the annual average. The location of the maxima in momentum tendency are, as with the eddy-induced tendency, far equatorward of the mid-latitude jet stream maxima, thus indicating that diabatic heating cannot alone account for the variations in the zonally averaged jet core.

Examination of the diabatic heating, $\left(\frac{p_{00}}{p}\right)\kappa\frac{[Q]}{c_p}$, reveals a structure of strong heating in the equatorial troposphere between $15°S - 15°N$, weaker heating in the equatorial lower stratosphere between $30°S - 30°N$ and relatively strong heating in the planetary boundary layer, up to about 850 hPa and between $60°S - 60°N$; the remainder of the troposphere shows strong cooling, with maxima obtained in the polar upper troposphere. Considerating, in addition, the effect of the induced Hadley circulation, the structure of the potential temperature tendency, $\frac{\partial[\theta]}{\partial t}$, will give a relatively weak net heating in the equatorial mid-troposphere and relatively strong near-surface heating between $60°S - 60°N$, with significant cooling throughout the remainder of the atmosphere and particularly strong cooling in the Arctic and Antarctic (with typical peak values of $\sim 1.5\ K\ day^{-1}$).

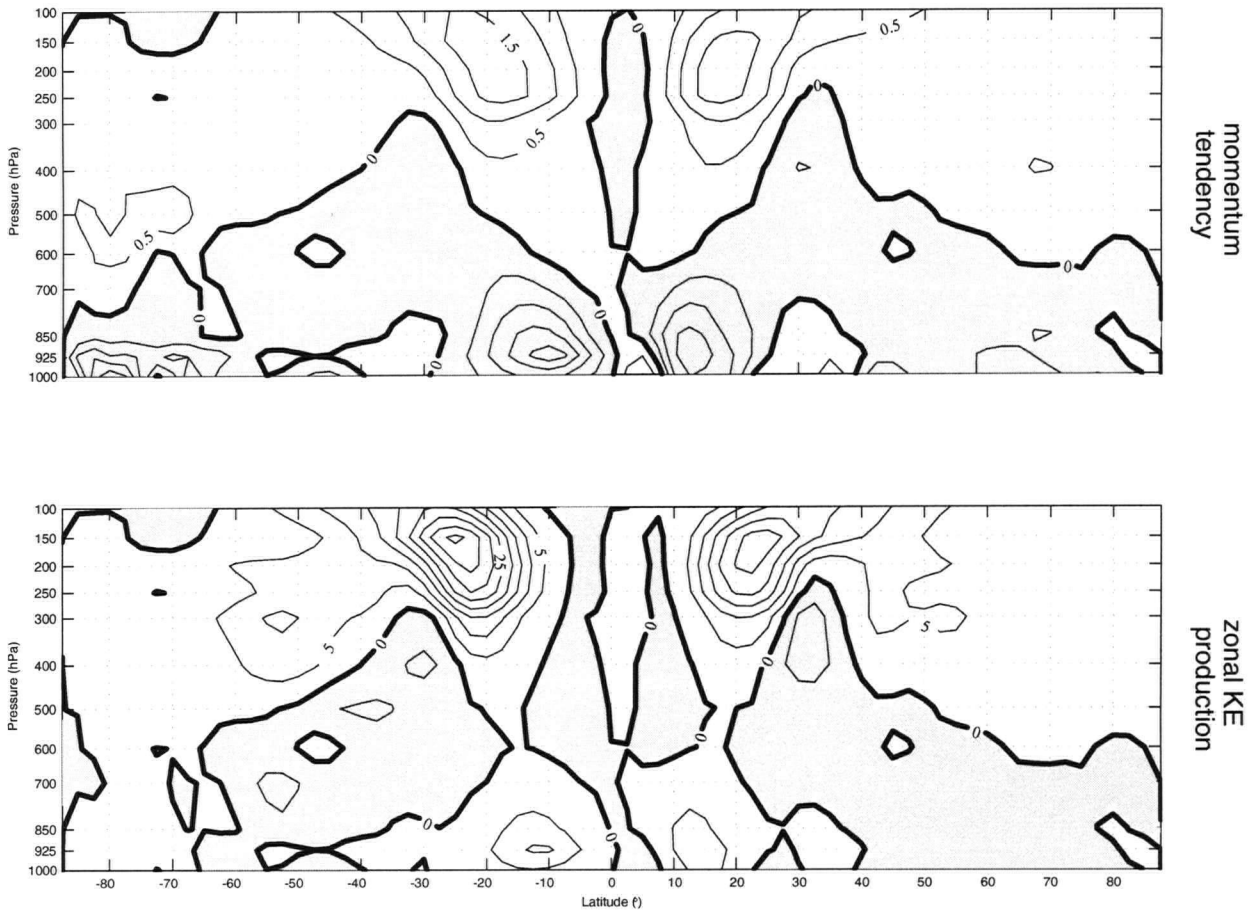

Figure 8.12: Annual average momentum tendency (top panel) and zonal kinetic energy production due to diabatic heating . For the top panel, the units are $10^{-5}\ m\ s^{-2}$ and the contour interval is $0.5 \times 10^{-5}\ m\ s^{-2}$. For the bottom panel, the units are $10^{-5}\ m^2\ s^{-3}$ and the contour interval is $5 \times 10^{-5}\ m^2\ s^{-3}$.

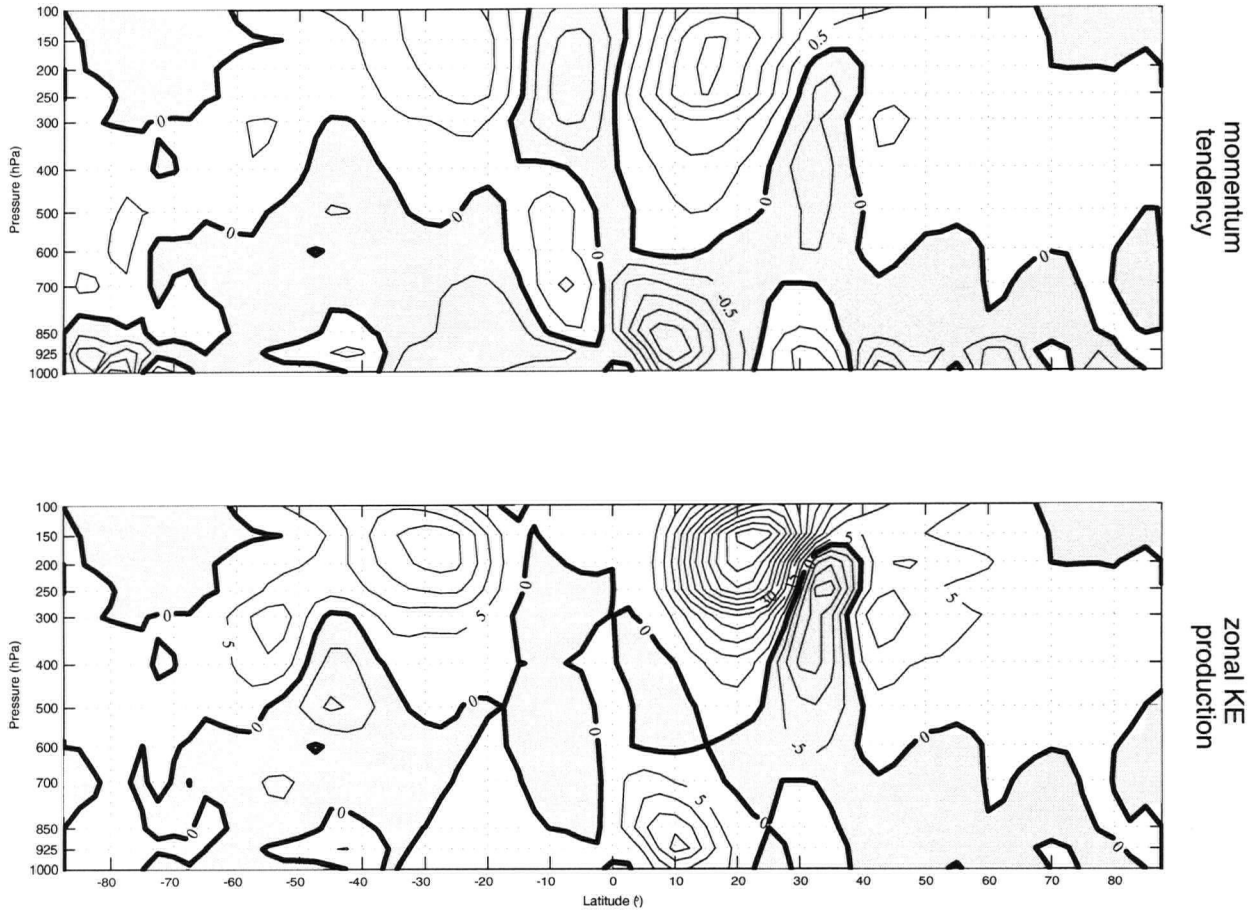

Figure 8.13: Average winter (DJF) momentum tendency (top panel) and zonal kinetic energy production due to diabatic heating. For the top panel, the units are $10^{-5}\ m\ s^{-2}$ and the contour interval is $0.5 \times 10^{-5}\ m\ s^{-2}$. For the bottom panel, the units are $10^{-5}\ m^2\ s^{-3}$ and the contour interval is $5 \times 10^{-5}\ m^2\ s^{-3}$.

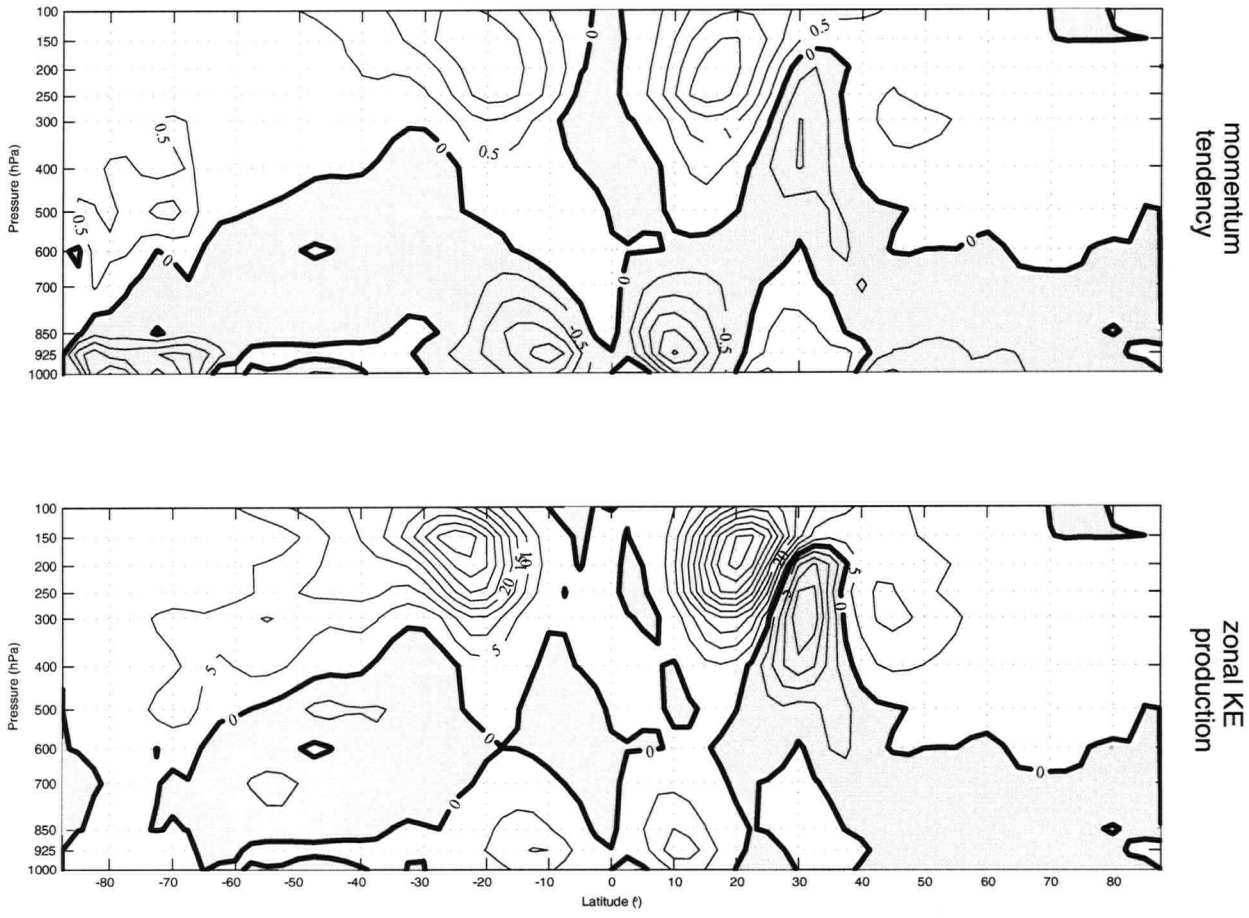

Figure 8.14: Average spring (MAM) momentum tendency (top panel) and zonal kinetic energy production due to diabatic heating. For the top panel, the units are $10^{-5}\ m\ s^{-2}$ and the contour interval is $0.5 \times 10^{-5}\ m\ s^{-2}$. For the bottom panel, the units are $10^{-5}\ m^2\ s^{-3}$ and the contour interval is $5 \times 10^{-5}\ m^2\ s^{-3}$.

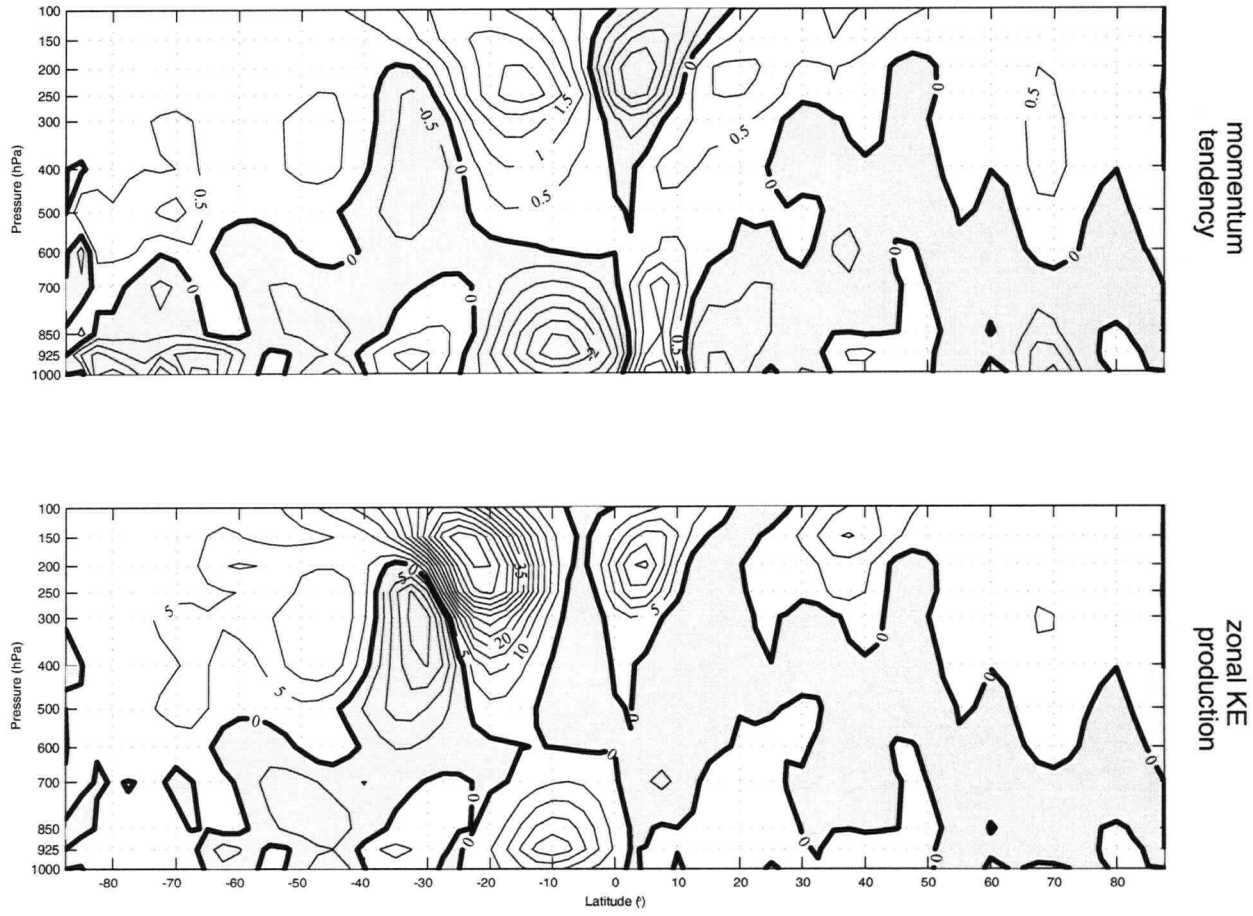

Figure 8.15: Average summer (JJA) momentum tendency (top panel) and zonal kinetic energy production due to diabatic heating. For the top panel, the units are $10^{-5}\ m\ s^{-2}$ and the contour interval is $0.5 \times 10^{-5}\ m\ s^{-2}$. For the bottom panel, the units are $10^{-5}\ m^2\ s^{-3}$ and the contour interval is $5 \times 10^{-5}\ m^2\ s^{-3}$.

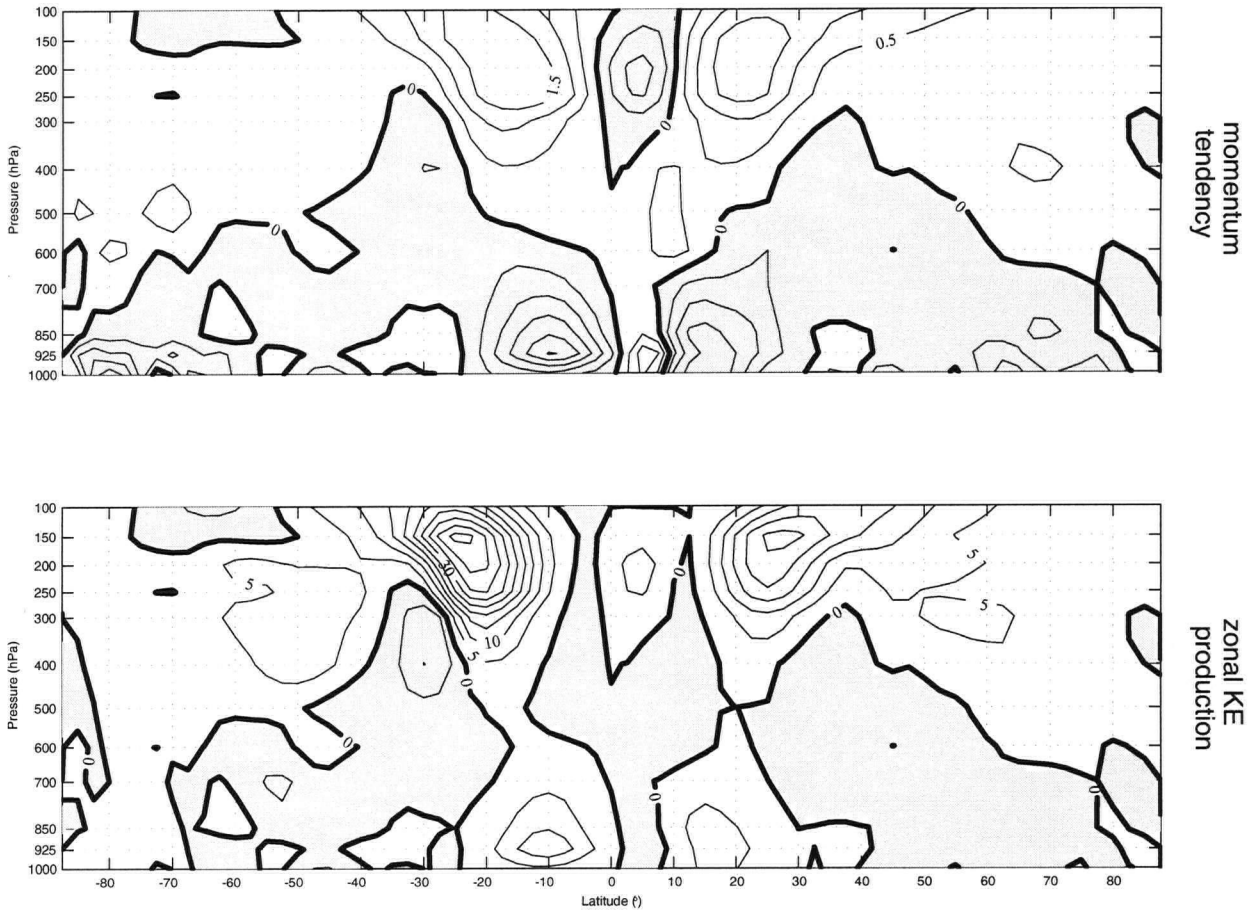

Figure 8.16: Average autumn (SON) momentum tendency (top panel) and zonal kinetic energy production due to diabatic heating. For the top panel, the units are $10^{-5}\ m\ s^{-2}$ and the contour interval is $0.5 \times 10^{-5}\ m\ s^{-2}$. For the bottom panel, the units are $10^{-5}\ m^2\ s^{-3}$ and the contour interval is $5 \times 10^{-5}\ m^2\ s^{-3}$.

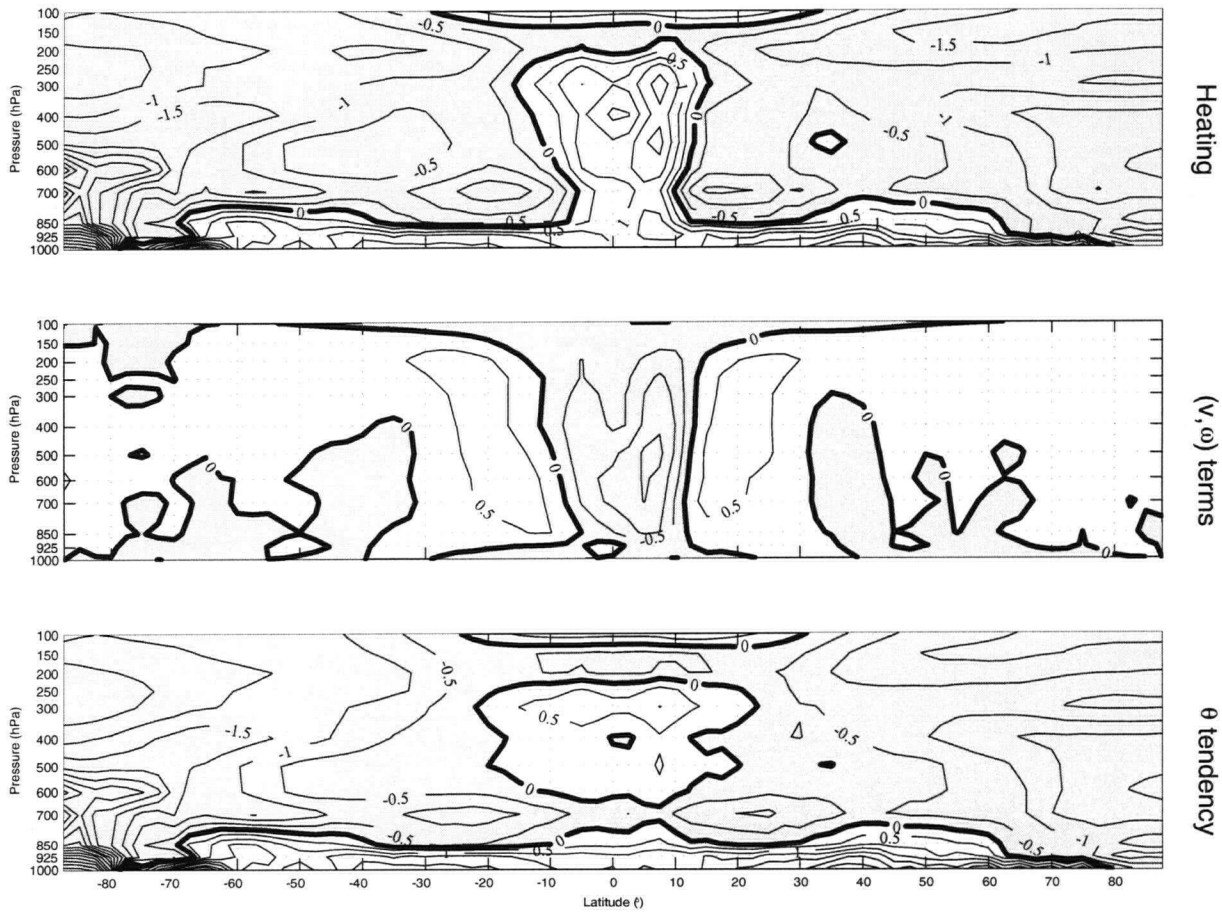

Figure 8.17: Annual average heat budget due to diabatic heating. The units are $10^{-5}\ K\ s^{-1}$ and the contour interval is $0.5 \times 10^{-5}\ K\ s^{-1}$.

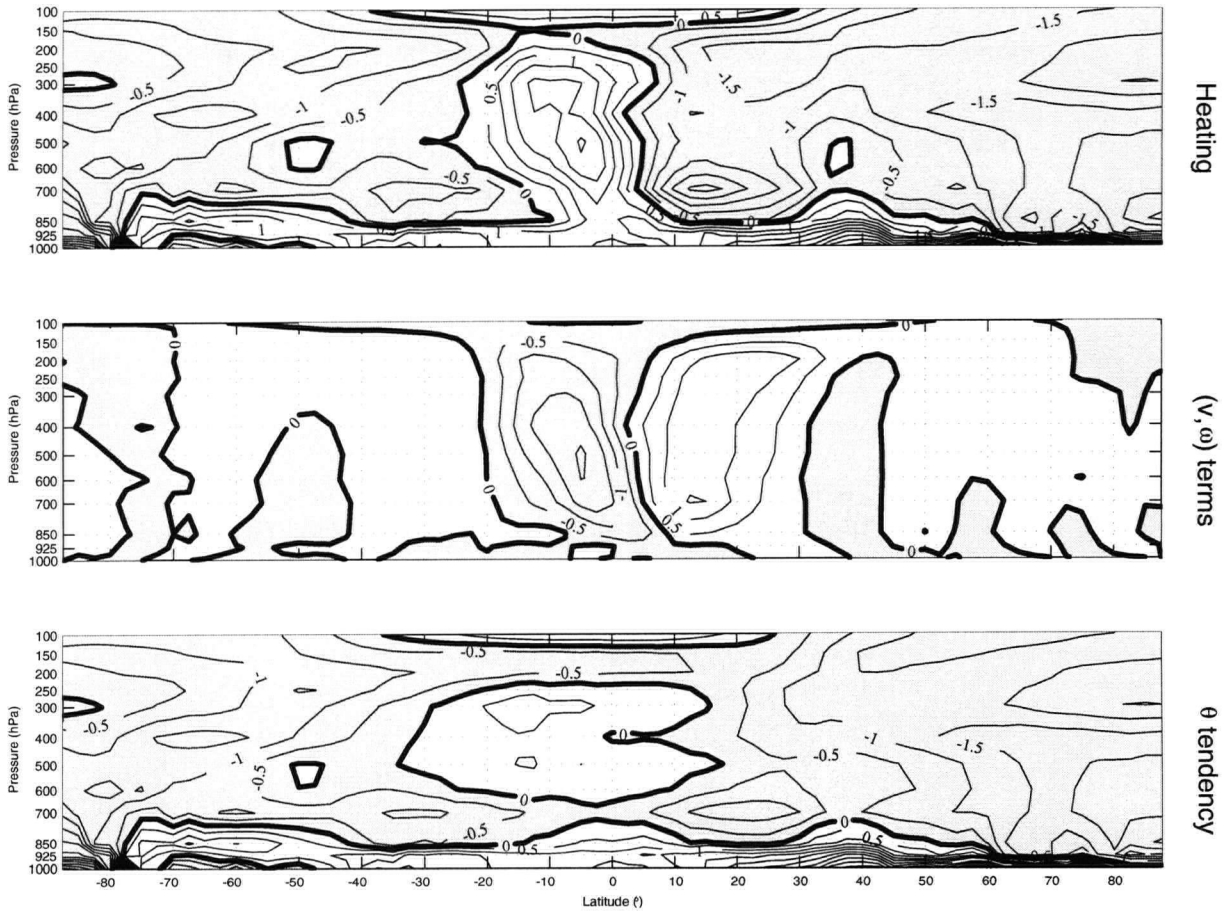

Figure 8.18: Average winter (DJF) heat budget due to diabatic heating. The units are $10^{-5}\ K\ s^{-1}$ and the contour interval is $0.5 \times 10^{-5}\ K\ s^{-1}$.

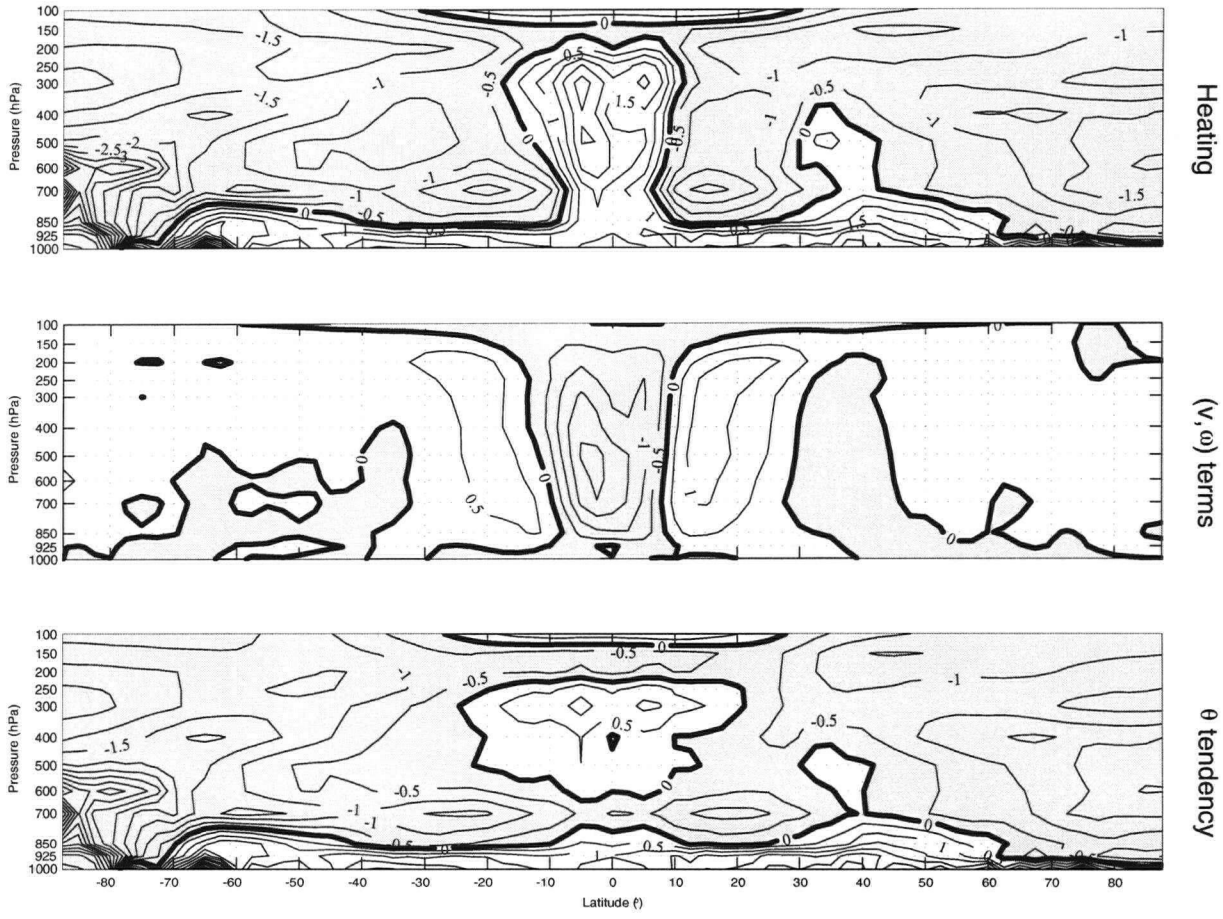

Figure 8.19: Average spring (MAM) heat budget due to diabatic heating. The units are $10^{-5}\ K\ s^{-1}$ and the contour interval is $0.5 \times 10^{-5}\ K\ s^{-1}$.

Figure 8.20: Average summer (JJA) heat budget due to diabatic heating. The units are $10^{-5}\ K\ s^{-1}$ and the contour interval is $0.5 \times 10^{-5}\ K\ s^{-1}$.

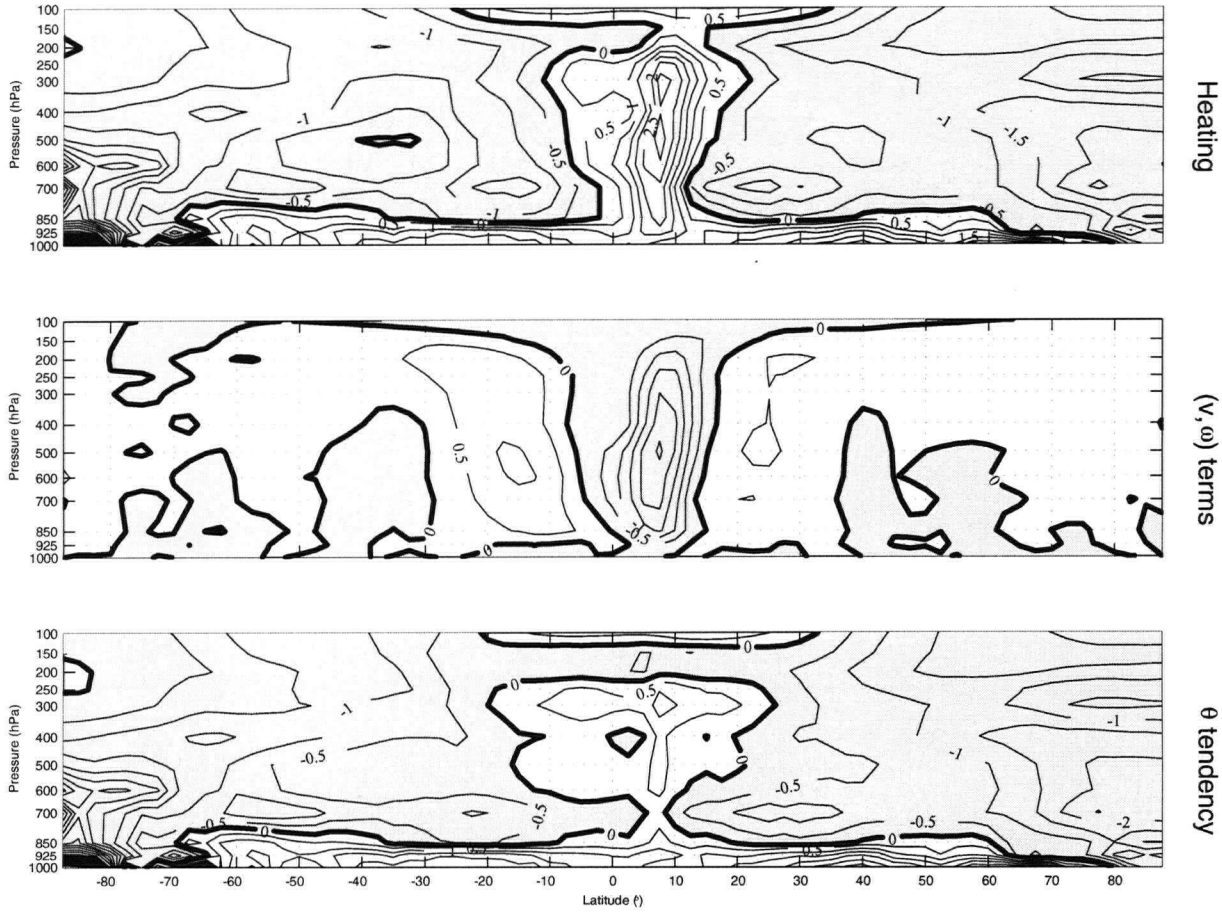

Figure 8.21: Average autumn (SON) heat budget due to diabatic heating. The units are $10^{-5}\ K\ s^{-1}$ and the contour interval is $0.5 \times 10^{-5}\ K\ s^{-1}$.

8.3. Budgets of total circulation

For the total circulation, the momentum tendency is given by

$$\frac{\partial [u]}{\partial t} = \underbrace{[v]\left(f - \frac{\partial ([u]\cos\phi)}{R\cos\phi\partial\phi}\right) - [\omega]\frac{\partial [u]}{\partial p}}_{(v,\omega)\text{ terms}} \underbrace{- \frac{\partial ([u^*v^*]\cos^2\phi)}{R\cos^2\phi\partial\phi} - \frac{\partial [u^*\omega^*]}{\partial p}}_{\text{Eddy terms}}$$

and the potential temperature tendency is given by

$$\frac{\partial [\theta]}{\partial t} = \underbrace{-\frac{[v]}{R}\frac{\partial [\theta]}{\partial\phi} - [\omega]\frac{\partial [\theta]}{\partial p}}_{(v,\omega)\text{ terms}} \underbrace{- \frac{\partial ([\theta^*v^*]\cos\phi)}{R\cos\phi\partial\phi} - \frac{\partial [\theta^*\omega^*]}{\partial p}}_{\text{Eddy terms}} \underbrace{+ \left(\frac{p_{00}}{p}\right)\kappa\frac{[Q]}{c_p}}_{\text{Diabatic heating}}$$

where the streamfunction equation (3.4) is solved with forcing of $\frac{\partial\left(H_{\text{Ferrel}}+H_{\text{Hadley}}\right)}{\partial\eta} + \frac{\partial\chi_{\text{Ferrel}}}{\partial p}$ and the values of $[v]$ and $[\omega]$ are determined from ψ. Zonal-momentum budgets for annual- and seasonal-mean conditions are shown in Figures 8.22-8.26, with potential temperature budgets for annual- and seasonal-mean conditions shown in Figures 8.27-8.31.

Unlike the study of [Pfe81], where data from vastly different sources were drawn together in an attempt to synthesise the combined effect of eddy- and diabatic heating-induced motions, the current investigation relies solely on data from one source; however, even if one ignores the inevitable distorting effect of

the various interpolation schemes, one is still left with the drawback that there is an unquantifiable influence of the reanalysis model's various parameterisation and assimilation schemes inherent in the results. Assuming that, at the very least, the qualitative nature of the results are correct, and making the further assumption that comparison with the most trustworthy of the synoptic fields will reveal questionable results, some conclusions on the effect of the combined influences may be drawn.

Focusing attention on the momemtum tendency, $\frac{\partial[u]}{\partial t}$, the principal regions of net positive acceleration are in the mid-latitudes, with peaks in the boundary layer near 40° and in the sub-tropics, with maxima obtained in the upper troposphere around 30°. Comparison of these tendencies with those resulting from the Hadley and Ferrel circulations alone suggest that the peak positive tendencies at 150 hPa are primarily due to the eddy-induced circulation and the near-surface peaks result from the diabatic heating-induced circulation. Strong cancellation both in the momentum tendency and the zonal kinetic energy production is evident between the eddy-induced and diabatic heating-induced circulations. Deceleration appears to mostly occur in the equatorial lower troposphere and more weakly near the Arctic surface, with weak upper tropospheric decelerations consistent with the requirements of thermal wind balance (equation (3.3)) associated with

the calculated potential temperature tendencies discussed presently.

Examining the potential temperature tendency of the combined motions, one sees that the general pattern throughout the year is of a weak heating in the equatorial mid-troposphere and heating of a somewhat greater magnitude in the boundary layer, occasionally extending as far as 80°; the general tendency is for a cooling elsewhere throughout the year. The diabatic heating provides the principal contribution to $\frac{\partial[\theta]}{\partial t}$, with a broader region of heating in the equatorial mid-troposphere than would be provided by the Hadley circulation alone and the Ferrel circulation providing tendencies of slightly lower magnitude in the mid-latitude troposphere. In summary, one sees that the combined effects of the eddy- and diabatic heating-induced circulations is to increase the equator-to-pole temperature gradient in the mid to upper troposphere throughout the year and to reduce it in the lower troposphere between the Arctic and Antarctic circles; this is compatible with the observed pattern of positive momentum tendencies in the upper atmosphere. There is also tendency to destabilise the lower troposphere between 1000 $hPa - 700\ hPa$ and the upper troposphere between $30°S - 30°N$.

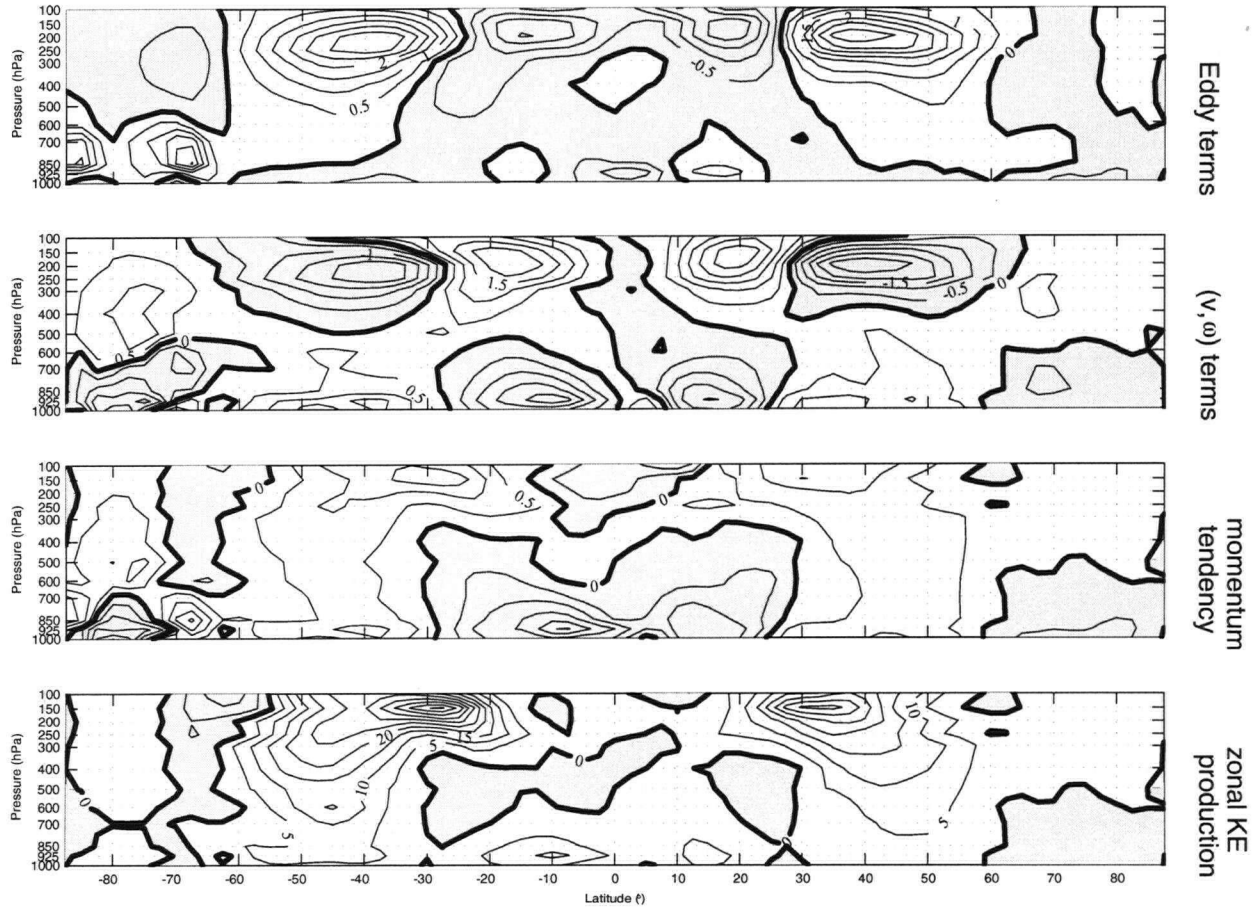

Figure 8.22: Annual momentum budget (top three panels) and zonal kinetic energy production due to the combined effects of the eddies and diabatic heating. For the top three panels, the units are $10^{-5}\ m\ s^{-2}$ and the contour interval is $0.5 \times 10^{-5}\ m\ s^{-2}$. For the bottom panel, the units are $10^{-5}\ m^2\ s^{-3}$ and the contour interval is $5 \times 10^{-5}\ m^2\ s^{-3}$.

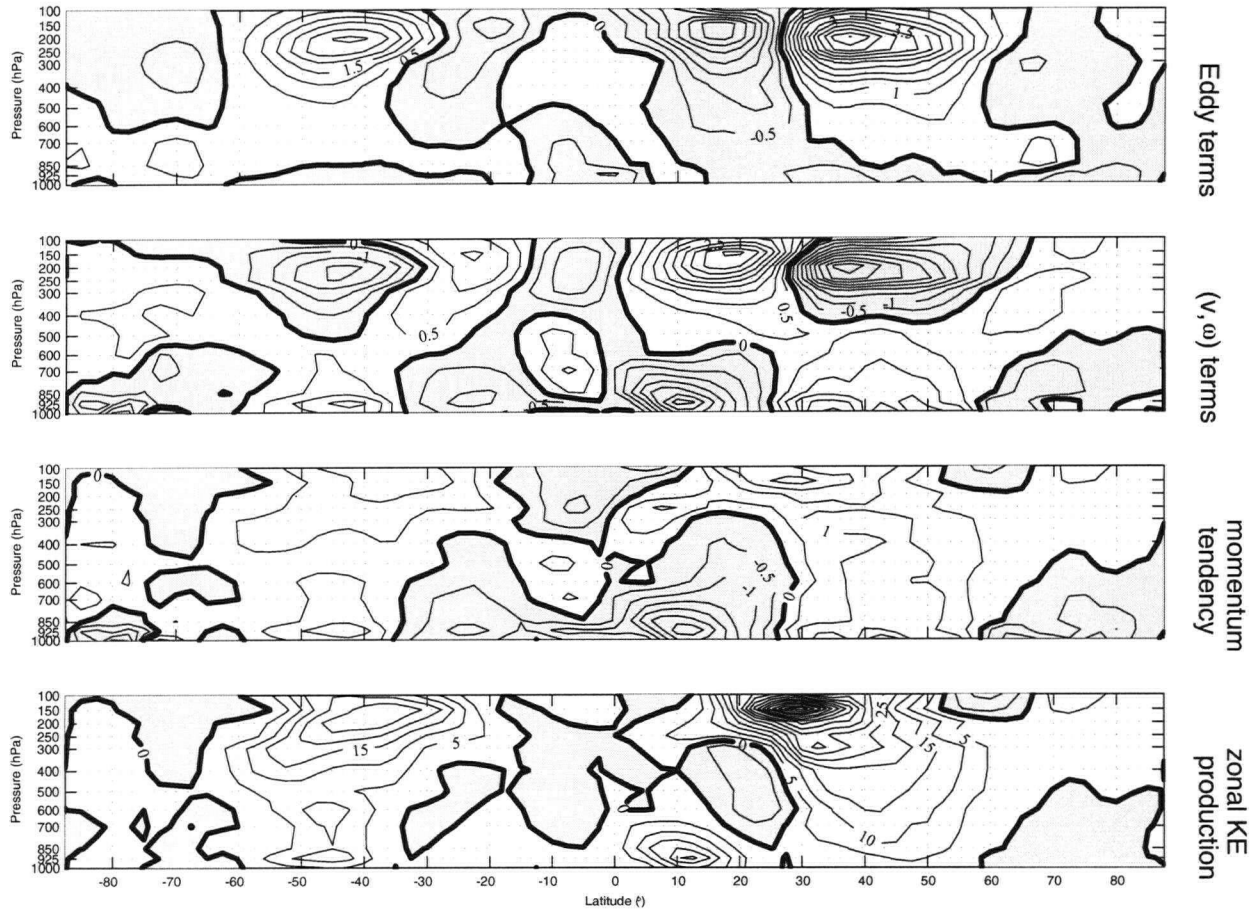

Figure 8.23: Average winter (DJF) momentum budget (top three panels) and zonal kinetic energy production due to the combined effects of the eddies and diabatic heating. For the top three panels, the units are $10^{-5}\ m\ s^{-2}$ and the contour interval is $0.5 \times 10^{-5}\ m\ s^{-2}$. For the bottom panel, the units are $10^{-5}\ m^2\ s^{-3}$ and the contour interval is $5 \times 10^{-5}\ m^2\ s^{-3}$.

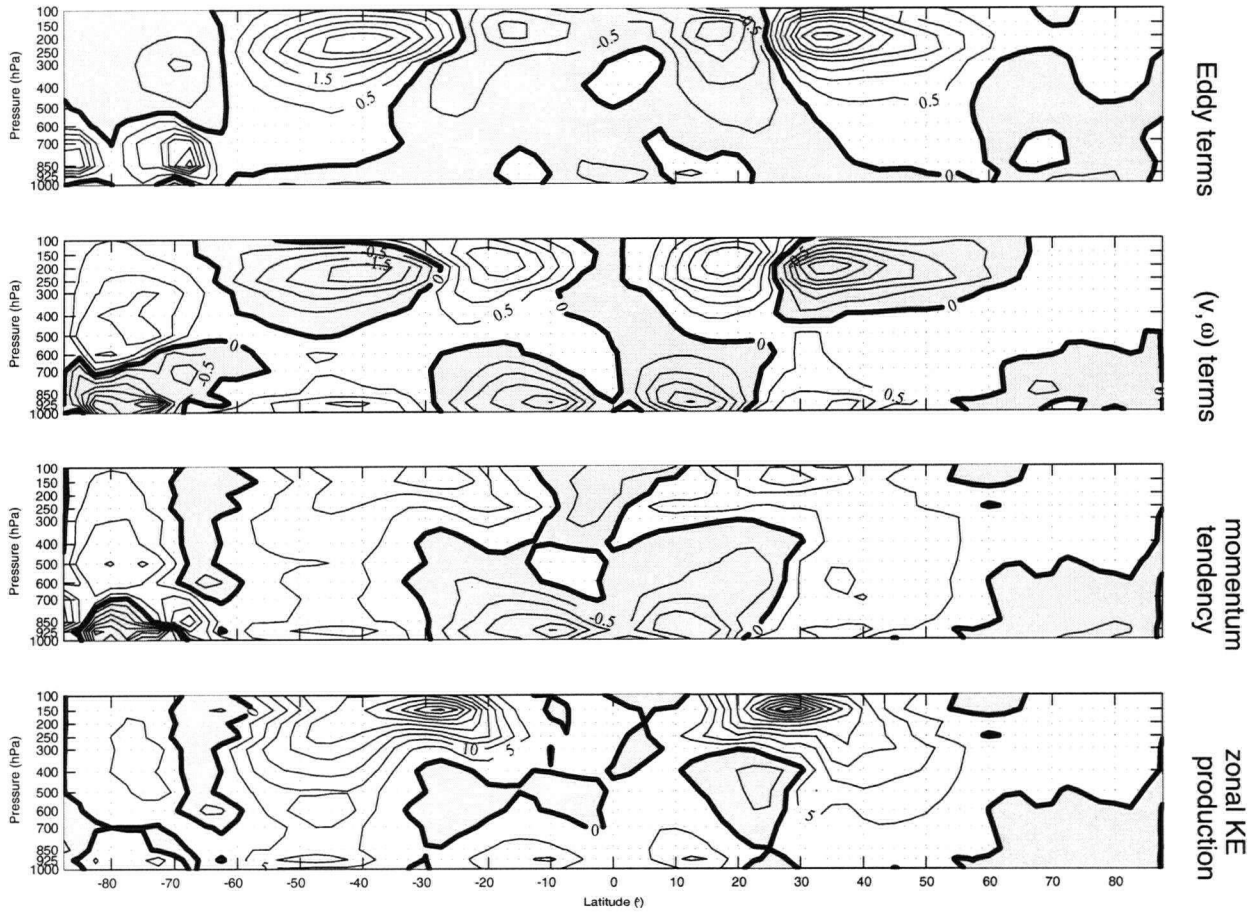

Figure 8.24: Average spring (MAM) momentum budget (top three panels) and zonal kinetic energy production due to the combined effects of the eddies and diabatic heating. For the top three panels, the units are $10^{-5}\ m\ s^{-2}$ and the contour interval is $0.5 \times 10^{-5}\ m\ s^{-2}$. For the bottom panel, the units are $10^{-5}\ m^2\ s^{-3}$ and the contour interval is $5 \times 10^{-5}\ m^2\ s^{-3}$.

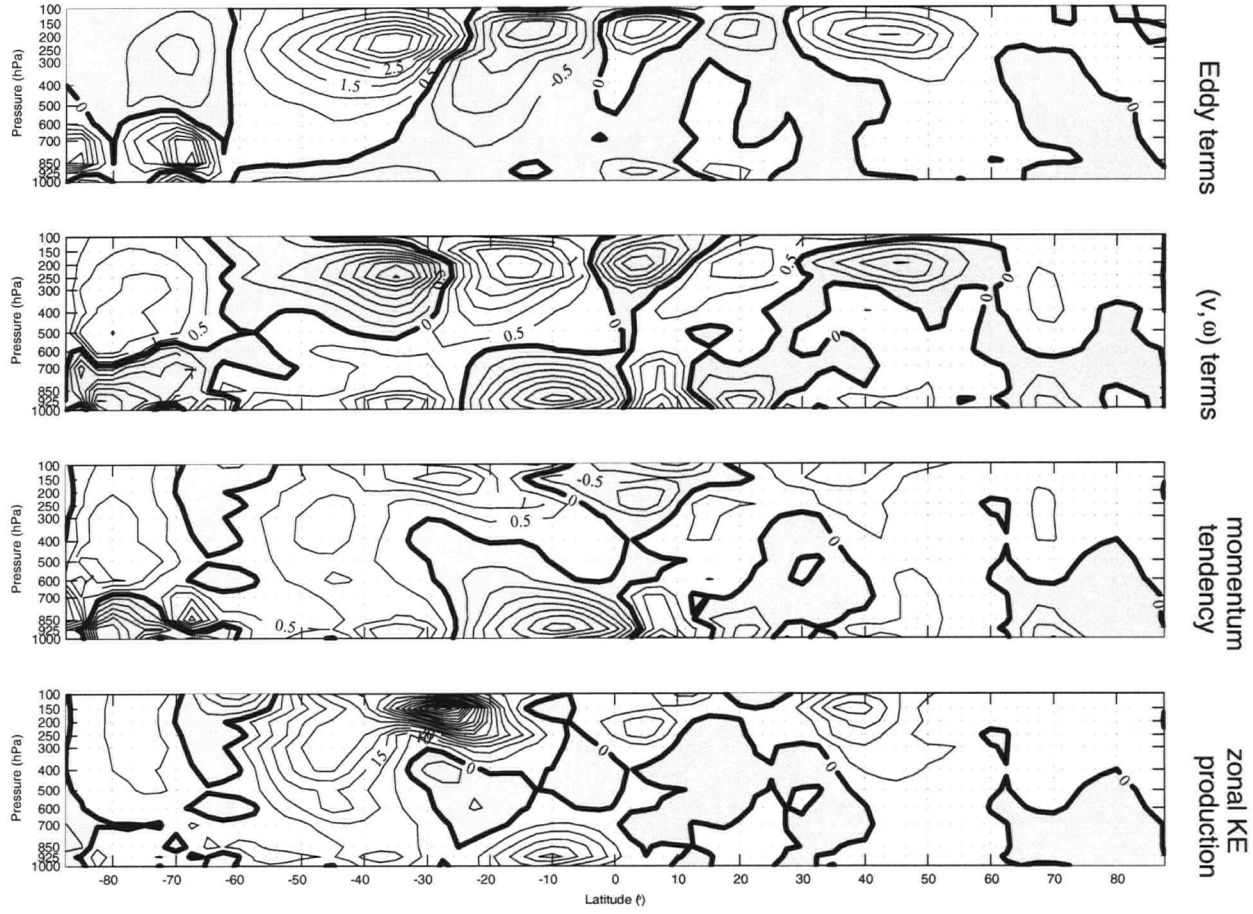

Figure 8.25: Average summer (JJA) momentum budget (top three panels) and zonal kinetic energy production due to the combined effects of the eddies and diabatic heating. For the top three panels, the units are $10^{-5}\ m\ s^{-2}$ and the contour interval is $0.5 \times 10^{-5}\ m\ s^{-2}$. For the bottom panel, the units are $10^{-5}\ m^2\ s^{-3}$ and the contour interval is $5 \times 10^{-5}\ m^2\ s^{-3}$.

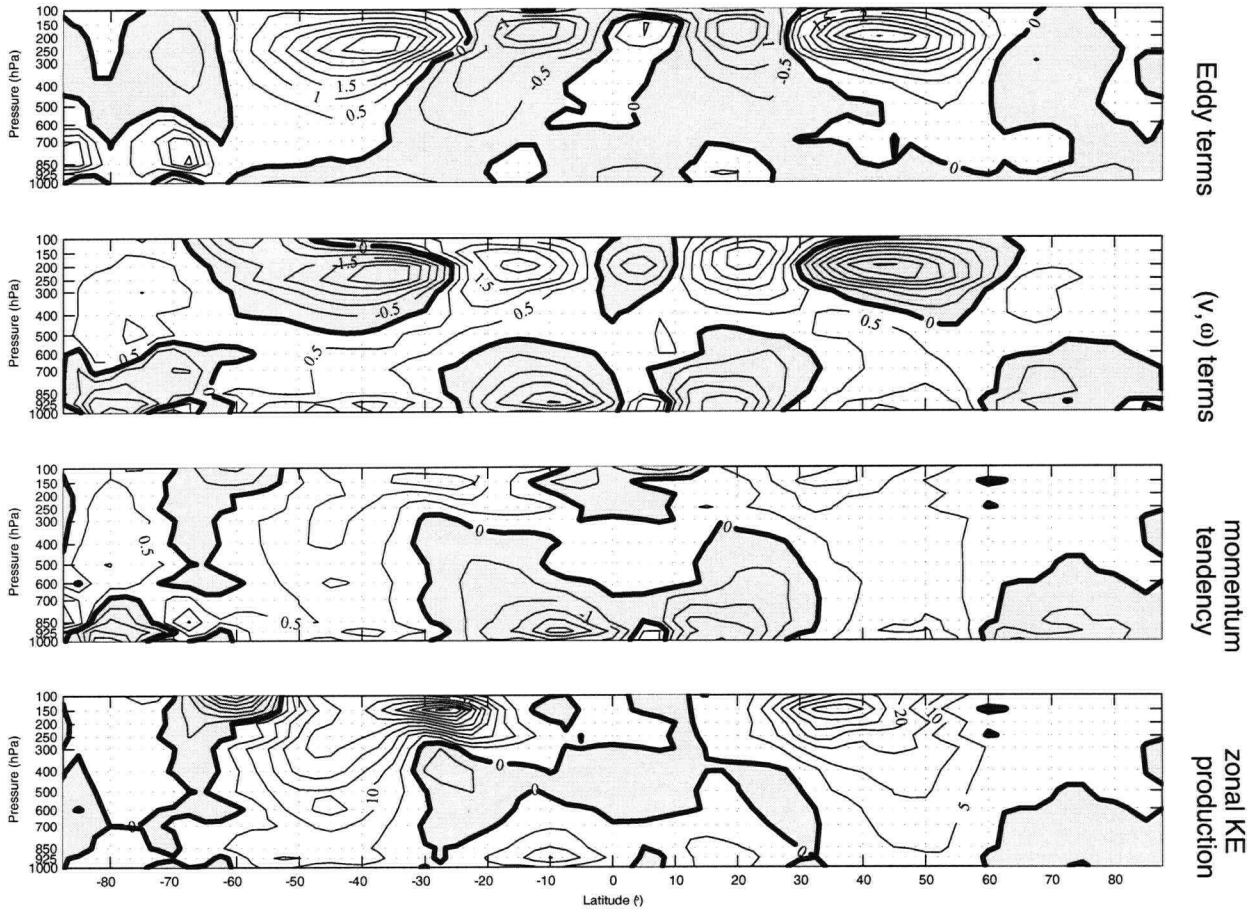

Figure 8.26: Average autumn (SON) momentum budget (top three panels) and zonal kinetic energy production due to the combined effects of the eddies and diabatic heating. For the top three panels, the units are $10^{-5}\ m\ s^{-2}$ and the contour interval is $0.5 \times 10^{-5}\ m\ s^{-2}$. For the bottom panel, the units are $10^{-5}\ m^2\ s^{-3}$ and the contour interval is $5 \times 10^{-5}\ m^2\ s^{-3}$.

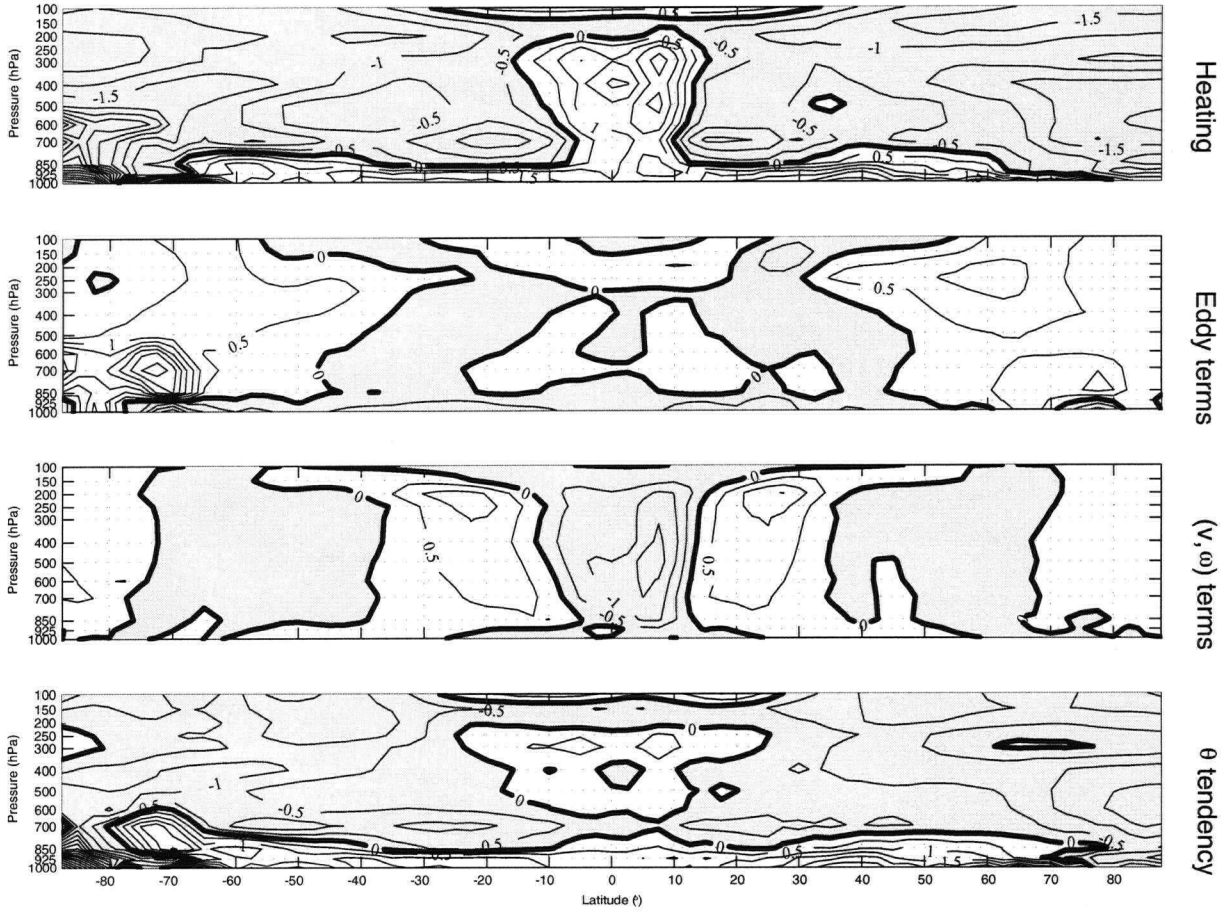

Figure 8.27: Annual average heat budget for the combined action of diabatic heating and eddy fluxes of heat and momentum. The units are $10^{-5}\ K\ s^{-1}$ and the contour interval is $0.5 \times 10^{-5}\ K\ s^{-1}$.

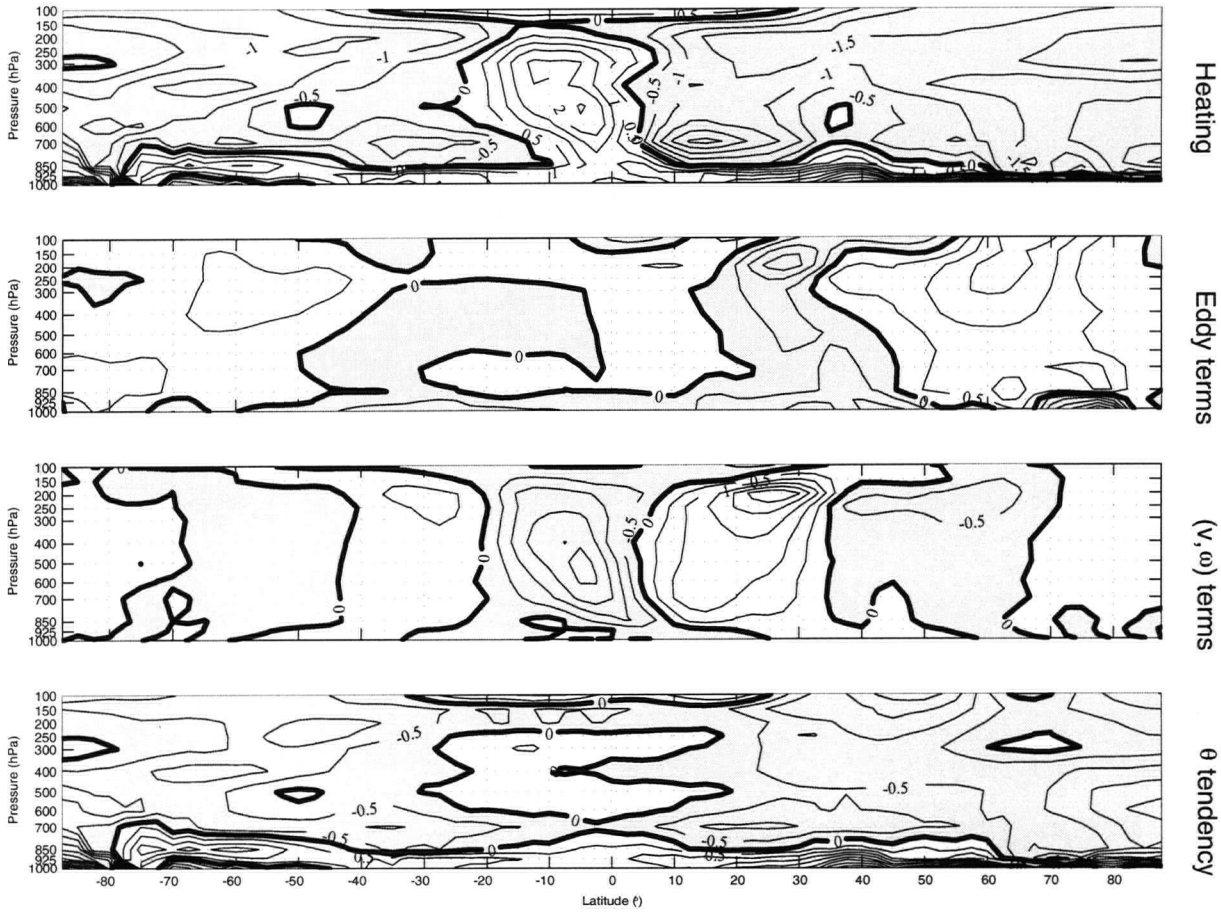

Figure 8.28: Average winter (DJF) heat budget for the combined action of diabatic heating and eddy fluxes of heat and momentum. The units are $10^{-5}\ K\ s^{-1}$ and the contour interval is $0.5 \times 10^{-5}\ K\ s^{-1}$.

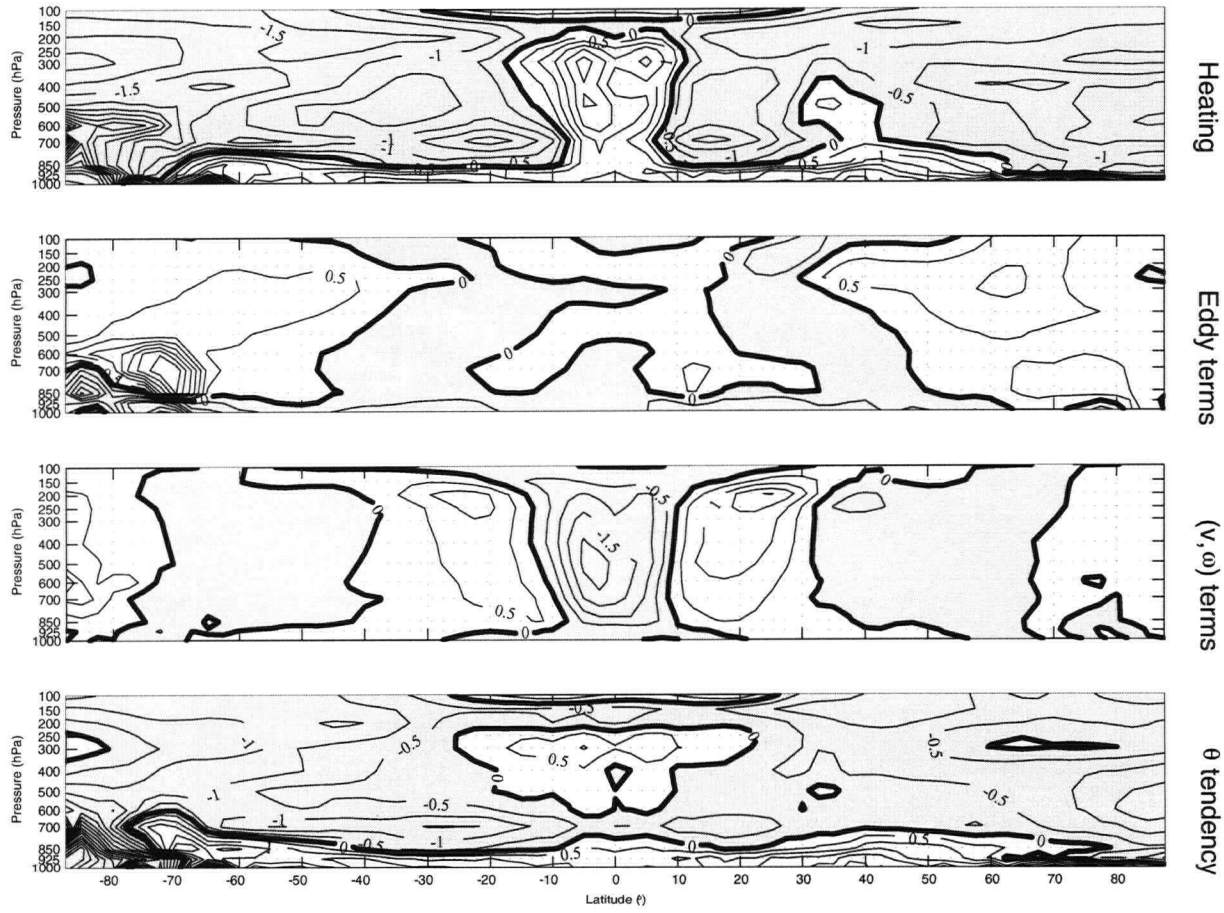

Figure 8.29: Average spring (MAM) heat budget for the combined action of diabatic heating and eddy fluxes of heat and momentum. The units are $10^{-5}\ K\ s^{-1}$ and the contour interval is $0.5 \times 10^{-5}\ K\ s^{-1}$.

Figure 8.30: Average summer (JJA) heat budget for the combined action of diabatic heating and eddy fluxes of heat and momentum. The units are $10^{-5}\ K\ s^{-1}$ and the contour interval is $0.5 \times 10^{-5}\ K\ s^{-1}$.

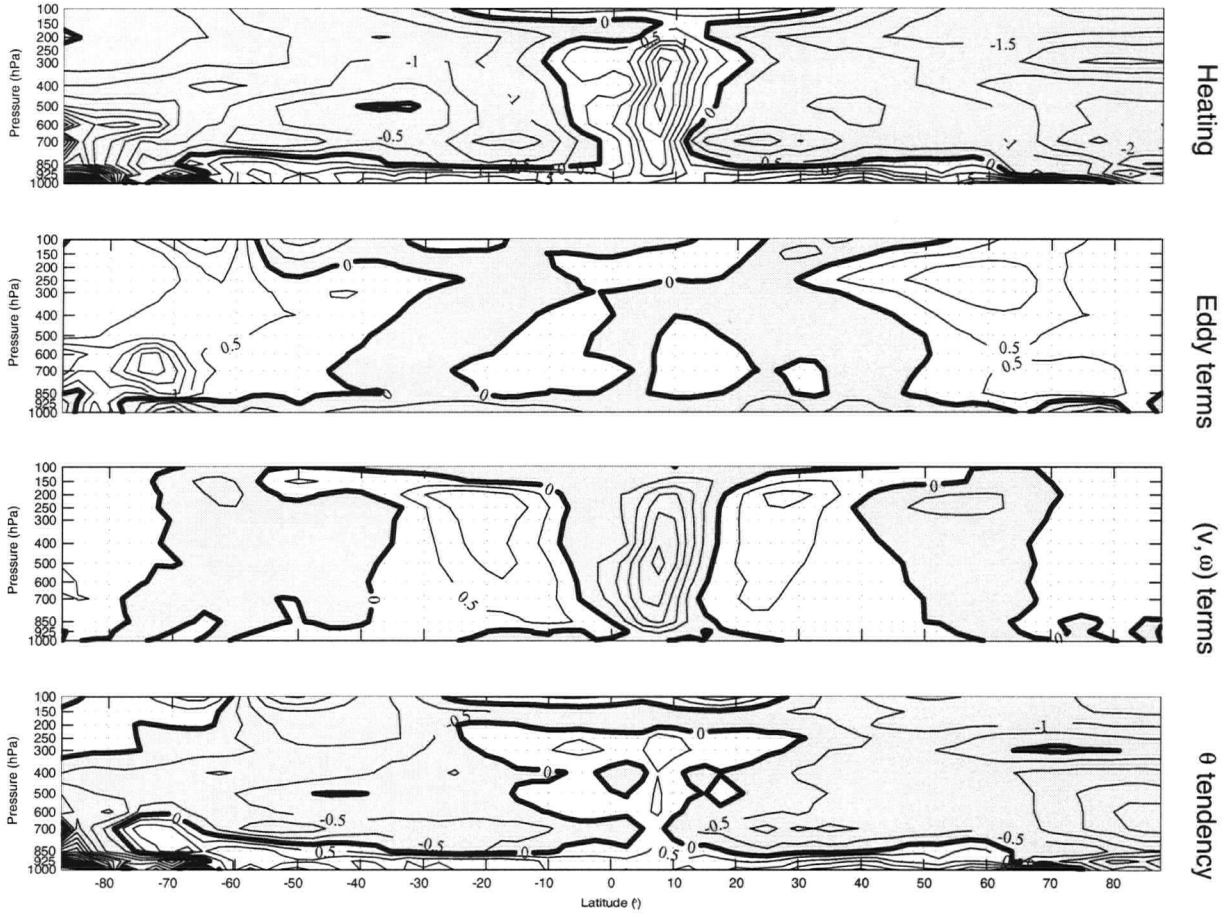

Figure 8.31: Average autumn (SON) heat budget for the combined action of diabatic heating and eddy fluxes of heat and momentum. The units are $10^{-5}\ K\ s^{-1}$ and the contour interval is $0.5 \times 10^{-5}\ K\ s^{-1}$.

9. Conclusions

The results of this thesis suggest indicate that there is considerable wave-mean flow interaction in the Earth's atmosphere, with the circulation induced by eddy motions being primarily responsible for the maintenance and seasonal variations of the zonally-averaged jet core.

In the mid-latitudes, the peak values of momentum tendency due to the Ferrel circulation will lead to westerly winds $\sim 45\ ms^{-1}$ in the upper troposphere and $\sim 60\ ms^{-1}$ near the surface over the course of a month. The Hadley circulation, in contrast, leads to centres of significantly stronger momentum tendencies in the equatorial and subtropical upper- and lower-troposphere. These, however, are strongly counterbalanced by momentum tendencies resulting from the eddy-induced circulation, leaving peak easterly residual tendencies of $\sim 3\ ms^{-1}$ in the tropical boundary layer (which one would expect to be substantially decreased by the previously-neglected surface wind stress $F\lambda$) and $\sim 1\ ms^{-1}$ in the tropical upper troposphere.

The streamfunction results determined by the model presented herein may be used in investigations of material transport in the atmosphere (as outlined by [AHL87]) and so may give an indication of the processes by which the zonally-

symmetric transport of ozone in its region of production in the Equatorial upper troposphere to its regions of destruction in the polar lower-stratosphere takes place. Additionally, the results presented in this study provide a baseline for further investigations of the effect of the ENSO phenomenon on the global circulation of the atmosphere (as 1989-1993 were non-El Niño years).

The validity of these conclusions rests, of course, on the veracity of the data supplied through the NCEP/NCAR Reanalysis project and the unimportance of those terms neglected in the derivation of the model equations.

References

[AHL87] David G. Andrews, James R. Holton, and Conway B. Leovy. *Middle Atmosphere Dynamics*, volume 40 of *International Geophysics Series.* Academic Press, 1987.

[AM76] D. G. Andrews and M. E. McIntyre. Planetary waves in horizontal and vertical shear: The generalized eliassen-palm relation and the mean zonal acceleration. *Journal of the Atmospheric Sciences*, 33(11):2031–2048, November 1976.

[BBC+94] R. Barrett, M. Berry, T. F. Chan, J. Demmel, J. Donato, J. Dongarra, V. Eijkhout, R. Pozo, C. Romine, and H. Van der Vorst. *Templates for the Solution of Linear Systems: Building Blocks for Iterative Methods, 2nd Edition.* SIAM, Philadelphia, PA, 1994.

[Cha47] J. G. Charney. The dynamics of long waves in a baroclinic westerly current. *Journal of Meteorology*, 4(5):135–162, October 1947.

[KKK+96] E. Kalnay, M Kanamitsu, R. Kistler, W. Collins, D. Deaven, L. Gandin, M. Iredell, S. Saha, G. White, J. Woollen, Y. Zhu, A. Leetmaa, R. Reynolds, M. Chelliah, W. Ebisuzaki, W. Higgins,

J. Janowiak, K. C. Mo, C. Ropelewski, J. Wang, Roy Jenne, and Dennis Joseph. The ncep/ncar 40-year reanalysis project. *Bulletin of the American Meteorological Society*, 77(3):437–471, March 1996.

[Kuo56] H.-L. Kuo. Forced and free meridional circulations in the atmosphere. *Journal of Meteorology*, 13:561–568, December 1956.

[Lor67] Edward N. Lorenz. *The Nature and Theory of the General Circulation of the Atmosphere.* World Meteorolgical Organization, 1967.

[NVDF69] R. E. Newell, D. G. Vincent, T. G. Dopplick, and D. Ferruzza. The energy balance of the global atmosphere. In G. A. Corby, editor, *The Global Circulation of the Atmosphere*, pages 42–90. Royal Meteorological Society, August 1969.

[OR71] Abraham H. Oort and Eugene M. Rasmusson. Atmospheric circulation statistics. Technical report, National Oceanographic and Atmospheric Administration, 1971.

[Pfe81] Richard L. Pfeffer. Wave-mean flow interactions in the atmosphere. *Journal of the Atmospheric Sciences*, 38:1340–1359, July 1981.

[PO92] José P. Peixoto and Abraham H. Oort. *Physics of Climate.* American Institute of Physics, 1992.

[SPS70] V. P. Starr, J. P. Peixoto, and J. E. Sims. A method for the study of the zonal kinetic energy balance in the atmosphere. *Pure and Applied Geophysics*, 80:346–357, 1970.

[TW98] David W. J. Thompson and John M. Wallace. Structure of the arctic and antarctic oscillations. *Journal of Climate (submitted)*, October 1998.

A. Table of symbols

Symbol	*Units*	*Description*
c_p	$\frac{J}{kg\ K}$	atmospheric specific heat at constant pressure ($= 1004\ J\ kg^{-1}\ K^{-1}$)
f	$\frac{1}{s}$	Coriolis parameter ($= 2\Omega \sin\phi$)
g	$\frac{m}{s^2}$	acceleration due to gravity ($= 9.81\ m\ s^{-2}$ at sea level)
p	Pa	pressure
p_{00}	Pa	reference pressure ($1000\ hPa$)
t	s	time
u	$\frac{m}{s}$	zonal velocity
v	$\frac{m}{s}$	meridional velocity
z	m	geometric height above the Earth's surface

Symbol	*Units*	*Description*
$F\lambda$	$\frac{m}{s^2}$	zonal forcing
$F\phi$	$\frac{m}{s^2}$	meridional forcing
H	$\frac{m^2}{kg\ s}$	heat flux forcing
Q	$\frac{K}{s}$	diabatic heating
R	m	radius of the Earth
R_d	$\frac{J}{kg\ K}$	gas constant for dry air ($= 287\ J\ kg^{-1}\ K^{-1}$)
S_p	$\frac{K}{Pa}$	static stability ($= -\frac{p\kappa}{p_{00}\kappa}\frac{\partial\theta}{\partial p}$)
T	K	temperature

Symbol	*Units*	*Description*
η	(none)	($= \sin\phi$)
θ	K	potential temperature
κ	(none)	$\frac{R_d}{c_p}$
λ	rad	longitude
ρ	$\frac{kg}{m^3}$	density
ϕ	rad	latitude
χ	$\frac{m}{s^3}$	momentum flux forcing
ψ	$\frac{m\ Pa}{s}$	streamfunction
ω	$\frac{Pa}{s}$	pressure vertical velocity
Ω	$\frac{rad}{s}$	rotation rate of the Earth ($= 7.292 \times 10^{-5}\ rad\ s^{-1}$)

B. Derivation of model equations

B.1. Governing equations

In the (λ, ϕ, p, t) system, the appropriately scaled equations of horizontal motion are

$$\frac{du}{dt} = \frac{\tan\phi}{R}uv + fv - \frac{g\partial z}{R\cos\phi\partial\lambda} + F_\lambda, \tag{B.1}$$

$$\frac{dv}{dt} = -\frac{\tan\phi}{R}u^2 - fu - \frac{g\partial z}{R\partial\phi} + F_\phi, \tag{B.2}$$

where

$$\frac{d}{dt} = \frac{\partial}{\partial t} + u\frac{\partial}{R\cos\phi\partial\lambda} + v\frac{\partial}{R\partial\phi} + \omega\frac{\partial}{\partial p}, \tag{B.3}$$

$$\omega = \frac{dp}{dt}. \tag{B.4}$$

The equation of continuity is

$$\frac{\partial u}{R\cos\phi\partial\lambda} + \frac{\partial\left(v\cos\phi\right)}{R\cos\phi\partial\phi} + \frac{\partial\omega}{\partial p} = 0. \tag{B.5}$$

The hydrostatic equation is

$$\frac{\partial p}{\partial z} \simeq -\rho g. \tag{B.6}$$

The ideal-gas law and the expression for potential temperature are

$$p = \rho R_d T, \tag{B.7}$$

$$\theta = T\left(\frac{p_{00}}{p}\right)^{\kappa}, \tag{B.8}$$

where p_{00} is a reference level ($\simeq 1000\ hPa$) and $\kappa = \frac{R_d}{c_p} \simeq 0.286$.

The first law of thermodynamics is

$$c_p \frac{T}{\theta}\frac{d\theta}{dt} = Q, \tag{B.9}$$

where $c_p \simeq 1004\ J\ kg^{-1}\ K^{-1}$ and Q is the net heating rate per unit mass.

B.2. Derivation of thermal wind equation

The thermal wind equation for u may be found by scale analysis of equation (B.2):

$$0 \simeq -\frac{\tan\phi}{R}u^2 - fu - \frac{g\partial z}{R\partial\phi}.$$

Differentiating w.r.t. p gives

$$\begin{aligned}\left(f+\frac{2\tan\phi}{R}u\right)\frac{\partial u}{\partial p} &= -\frac{\partial}{\partial p}\left(\frac{g\partial z}{R\partial\phi}\right)\\ &= -\frac{g}{R}\frac{\partial^2 z}{\partial p\partial\phi}.\end{aligned}$$

Changing the order of differentiation and using the hydrostatic equation (B.6) together with the idea gas law (B.7) gives

$$\begin{aligned}\left(f+\frac{2\tan\phi}{R}u\right)\frac{\partial u}{\partial p} &= \frac{1}{R}\frac{\partial\left(\frac{1}{\rho}\right)}{\partial\phi}\\ &= \frac{1}{R}\left(-\rho^{-2}\right)\frac{\partial\rho}{\partial\phi}\\ &= -\frac{1}{R\rho^2}\frac{\partial\left(\frac{p}{R_dT}\right)}{\partial\phi}\\ &= -\frac{p}{RR_d\rho^2}\frac{\partial\left(\frac{1}{T}\right)}{\partial\phi}\\ &= -\frac{p}{RR_d\rho^2}\left(-T^{-2}\right)\frac{\partial T}{\partial\phi}\\ &= \frac{p}{RR_d\rho^2T^2}\frac{\partial T}{\partial\phi},\end{aligned}$$

which gives

$$\left(f+\frac{2\tan\phi}{R}u\right)\frac{\partial u}{\partial p}=\frac{R_d}{pR}\frac{\partial T}{\partial\phi}. \tag{B.10}$$

Using the definition of potential temperature (B.8) gives

$$\begin{aligned}\left(f+\frac{2\tan\phi}{R}u\right)\frac{\partial u}{\partial p} &= \frac{R_d}{p}\frac{1}{R}\frac{\partial\left(\theta\frac{p^\kappa}{p_{00}^\kappa}\right)}{\partial\phi}\\ &= \frac{R_d}{p}\frac{p^\kappa}{p_{00}^\kappa}\frac{1}{R}\frac{\partial\theta}{\partial\phi}\\ &= \frac{R_d p^{\kappa-1}}{p_{00}^\kappa}\frac{1}{R}\frac{\partial\theta}{\partial\phi}\end{aligned}$$

which finally results in the alternative thermal wind equation

$$\left(f+\frac{2\tan\phi}{R}u\right)\frac{\partial u}{\partial p}=\frac{R_d p^{\kappa-1}}{p_{00}^\kappa}\frac{1}{R}\frac{\partial\theta}{\partial\phi}. \tag{B.11}$$

B.3. Derivation of zonally-averaged equations of motion

B.3.1. Derivation of zonally-averaged mass-continuity equation

The mass continuity equation (B.5) may be zonally-averaged to give

$$\frac{\partial\left([v]\cos\phi\right)}{R\cos\phi\partial\phi}+\frac{\partial[\omega]}{\partial p}=0. \tag{B.12}$$

Multiplying the original mass continuity equation (B.5) by some quantity A

and zonally-averaging gives

$$\begin{aligned}
\left[A\frac{\partial u}{R\cos\phi\partial\lambda}+A\frac{\partial\left(v\cos\phi\right)}{R\cos\phi\partial\phi}+A\frac{\partial\omega}{\partial p}\right] &= 0 \\
[A]\left[\frac{\partial u}{R\cos\phi\partial\lambda}+\frac{\partial\left(v\cos\phi\right)}{R\cos\phi\partial\phi}+\frac{\partial\omega}{\partial p}\right]+\left[A^*\frac{\partial u^*}{R\cos\phi\partial\lambda}\right]+\left[A^*\frac{\partial\left(v^*\cos\phi\right)}{R\cos\phi\partial\phi}\right]+\left[A^*\frac{\partial\omega^*}{\partial p}\right] &= 0,
\end{aligned}$$

which, upon using equation (B.5), becomes

$$\left[A^*\frac{\partial u^*}{R\cos\phi\partial\lambda}\right]+\left[A^*\frac{\partial\left(v^*\cos\phi\right)}{R\cos\phi\partial\phi}\right]+\left[A^*\frac{\partial\omega^*}{\partial p}\right]=0. \tag{B.13}$$

With the choice $A=u$ this gives the relationship

$$\left[u^*\frac{\partial u^*}{R\cos\phi\partial\lambda}\right]+\left[u^*\frac{\partial\left(v^*\cos\phi\right)}{R\cos\phi\partial\phi}\right]+\left[u^*\frac{\partial\omega^*}{\partial p}\right]=0,$$

which yields the useful identity

$$\left[u^*\frac{\partial\left(v^*\cos\phi\right)}{R\cos\phi\partial\phi}\right]+\left[u^*\frac{\partial\omega^*}{\partial p}\right]=0. \tag{B.14}$$

B.3.2. Derivation of the zonally-averaged ideal gas law and potential temperature equations

The ideal gas law equation (B.7) may be decomposed into

$$p = R_d \left[\rho\right] \left[T\right] + R_d \left[\rho^* T^*\right].$$

Alternatively, one may write

$$R_d T = \frac{p}{\rho}$$

which may be zonally-averaged to

$$R_d \left[T\right] = p \left[\frac{1}{\rho}\right]. \tag{B.15}$$

The expression for potential temperature (B.8) may be zonally-averaged to give

$$\left[\theta\right] = \left[T\right] \left(\frac{p_{00}}{p}\right)^{\kappa} \tag{B.16}$$

and

$$\theta^* = T^* \left(\frac{p_{00}}{p}\right)^{\kappa}.$$

B.3.3. Derivation of the zonally-averaged zonal momentum equation

Starting from equation (B.1) one may express the evolution of zonal velocity in the Eulerian form

$$\frac{\partial u}{\partial t} = -u\frac{\partial u}{R\cos\phi\partial\lambda} - v\frac{\partial u}{R\partial\phi} - \omega\frac{\partial u}{\partial p} + \frac{\tan\phi}{R}uv + fv - \frac{g\partial z}{R\cos\phi\partial\lambda} + F_\lambda.$$

Taking the zonal average of this equation, one arrives at

$$\begin{aligned}\frac{\partial [u]}{\partial t} &= -\left[u\frac{\partial u}{R\cos\phi\partial\lambda}\right] - \left[v\frac{\partial u}{R\partial\phi}\right] - \left[\omega\frac{\partial u}{\partial p}\right] + \frac{\tan\phi}{R}[uv] + f[v] - \left[\frac{g\partial z}{R\cos\phi\partial\lambda}\right] + [F_\lambda] \\ &= -\left[v\frac{\partial u}{R\partial\phi}\right] - \left[\omega\frac{\partial u}{\partial p}\right] + \frac{\tan\phi}{R}[uv] + f[v] + [F_\lambda].\end{aligned}$$

Using identity (2.1) one may write

$$\frac{\partial [u]}{\partial t} = -\frac{[v]}{R}\frac{\partial [u]}{\partial\phi} - \frac{1}{R}\left[v^*\frac{\partial u^*}{\partial\phi}\right] - \left[\omega\frac{\partial u}{\partial p}\right] + \frac{\tan\phi}{R}[u][v] + \frac{\tan\phi}{R}[u^*v^*] + f[v] + [F_\lambda],$$

which may be rewritten as

$$\begin{aligned}\frac{\partial [u]}{\partial t} &= [v]\left(f + \frac{\tan\phi}{R}[u] - \frac{1}{R}\frac{\partial [u]}{\partial\phi}\right) - \frac{1}{R}\left[v^*\frac{\partial u^*}{\partial\phi}\right] - \left[\omega\frac{\partial u}{\partial p}\right] + \frac{\tan\phi}{R}[u^*v^*] + [F_\lambda] \\ &= [v]\left(f - \frac{\cos\phi\frac{\partial [u]}{\partial\phi} - \sin\phi[u]}{R\cos\phi}\right) - \frac{1}{R}\left[v^*\frac{\partial u^*}{\partial\phi}\right] - \left[\omega\frac{\partial u}{\partial p}\right] + \frac{\tan\phi}{R}[u^*v^*] + [F_\lambda]\end{aligned}$$

$$= [v]\left(f - \frac{\partial\left([u]\cos\phi\right)}{R\cos\phi\partial\phi}\right) - \frac{1}{R}\left[v^*\frac{\partial u^*}{\partial\phi}\right] - \left[\omega\frac{\partial u}{\partial p}\right] + \frac{\tan\phi}{R}\left[u^*v^*\right] + \left[F_\lambda\right].$$

Now,

$$\begin{aligned}
-\left[\omega\frac{\partial u}{\partial p}\right] &= -[\omega]\frac{\partial[u]}{\partial p} - \left[\omega^*\frac{\partial u^*}{\partial p}\right] \\
&= -[\omega]\frac{\partial[u]}{\partial p} - \frac{\partial[u^*\omega^*]}{\partial p} + \left[u^*\frac{\partial\omega^*}{\partial p}\right] \\
&= -[\omega]\frac{\partial[u]}{\partial p} - \frac{\partial[u^*\omega^*]}{\partial p} - \left[\frac{u^*\partial\left(v^*\cos\phi\right)}{R\cos\phi\partial\phi}\right],
\end{aligned}$$

from equation (B.14). Substituting this into the expression for the evolution of zonal velocity yields

$$\begin{aligned}
\frac{\partial[u]}{\partial t} &= [v]\left(f - \frac{\partial\left([u]\cos\phi\right)}{R\cos\phi\partial\phi}\right) - \frac{1}{R}\left[v^*\frac{\partial u^*}{\partial\phi}\right] - [\omega]\frac{\partial[u]}{\partial p} - \frac{\partial[u^*\omega^*]}{\partial p} - \left[\frac{u^*\partial\left(v^*\cos\phi\right)}{R\cos\phi\partial\phi}\right] \\
&\quad + \frac{\tan\phi}{R}\left[u^*v^*\right] + \left[F_\lambda\right] \\
&= [v]\left(f - \frac{\partial\left([u]\cos\phi\right)}{R\cos\phi\partial\phi}\right) - \frac{1}{R\cos\phi}\left[v^*\cos\phi\frac{\partial u^*}{\partial\phi}\right] - [\omega]\frac{\partial[u]}{\partial p} - \frac{\partial[u^*\omega^*]}{\partial p} \\
&\quad - \left[\frac{u^*\partial\left(v^*\cos\phi\right)}{R\cos\phi\partial\phi}\right] + \frac{\sin\phi}{R\cos\phi}\left[u^*v^*\right] + \left[F_\lambda\right] \\
&= [v]\left(f - \frac{\partial\left([u]\cos\phi\right)}{R\cos\phi\partial\phi}\right) - \frac{1}{R\cos\phi}\left[v^*\cos\phi\frac{\partial u^*}{\partial\phi} + \frac{u^*\partial\left(v^*\cos\phi\right)}{\partial\phi} - \sin\phi u^*v^*\right] \\
&\quad - [\omega]\frac{\partial[u]}{\partial p} - \frac{\partial[u^*\omega^*]}{\partial p} + \left[F_\lambda\right] \\
&= [v]\left(f - \frac{\partial\left([u]\cos\phi\right)}{R\cos\phi\partial\phi}\right) - \frac{1}{R\cos\phi}\left[\frac{\partial\left(u^*v^*\cos\phi\right)}{\partial\phi} - \sin\phi u^*v^*\right]
\end{aligned}$$

$$
\begin{aligned}
& -[\omega]\frac{\partial[u]}{\partial p}-\frac{\partial[u^*\omega^*]}{\partial p}+[F_\lambda] \\
= \; & [v]\left(f-\frac{\partial([u]\cos\phi)}{R\cos\phi\partial\phi}\right)-\frac{1}{R\cos^2\phi}\left[\cos\phi\frac{\partial(u^*v^*\cos\phi)}{\partial\phi}-\sin\phi\cos\phi u^*v^*\right] \\
& -[\omega]\frac{\partial[u]}{\partial p}-\frac{\partial[u^*\omega^*]}{\partial p}+[F_\lambda] \\
= \; & [v]\left(f-\frac{\partial([u]\cos\phi)}{R\cos\phi\partial\phi}\right)-\frac{\partial([u^*v^*]\cos^2\phi)}{R\cos^2\phi\partial\phi}-[\omega]\frac{\partial[u]}{\partial p}-\frac{\partial[u^*\omega^*]}{\partial p}+[F_\lambda].
\end{aligned}
$$

B.3.4. Derivation of the zonally-averaged thermodynamic equation

Using the expression

$$
c_p\frac{T}{\theta}\frac{d\theta}{dt}=Q
$$

for the first law of thermodynamics (B.9), one may write

$$
\frac{d\theta}{dt}=\left(\frac{p_{00}}{p}\right)^{\kappa}\frac{Q}{c_p}
$$

which, in the Eulerian framework, may be rewritten as

$$
\frac{\partial\theta}{\partial t}=-u\frac{\partial\theta}{R\cos\phi\partial\lambda}-v\frac{\partial\theta}{R\partial\phi}-\omega\frac{\partial\theta}{\partial p}+\left(\frac{p_{00}}{p}\right)^{\kappa}\frac{Q}{c_p}.
$$

Taking the zonal average of this equation gives

$$\begin{aligned}
\frac{\partial [\theta]}{\partial t} &= -\left[u\frac{\partial \theta}{R\cos\phi\partial\lambda}\right] - \frac{1}{R}\left[v\frac{\partial\theta}{\partial\phi}\right] - \left[\omega\frac{\partial\theta}{\partial p}\right] + \left(\frac{p_{00}}{p}\right)^{\kappa}\frac{[Q]}{c_p} \\
&= -[u]\frac{\partial[\theta]}{R\cos\phi\partial\lambda} - \left[u^*\frac{\partial\theta^*}{R\cos\phi\partial\lambda}\right] - \frac{1}{R}\left[v\frac{\partial\theta}{\partial\phi}\right] - \left[\omega\frac{\partial\theta}{\partial p}\right] + \left(\frac{p_{00}}{p}\right)^{\kappa}\frac{[Q]}{c_p} \\
&= -\left[u^*\frac{\partial\theta^*}{R\cos\phi\partial\lambda}\right] - \frac{1}{R}\left[v\frac{\partial\theta}{\partial\phi}\right] - \left[\omega\frac{\partial\theta}{\partial p}\right] + \left(\frac{p_{00}}{p}\right)^{\kappa}\frac{[Q]}{c_p}.
\end{aligned}$$

Now,

$$\begin{aligned}
-\left[u^*\frac{\partial\theta^*}{R\cos\phi\partial\lambda}\right] - \left[\omega\frac{\partial\theta}{\partial p}\right] &= -\left[u^*\frac{\partial\theta^*}{R\cos\phi\partial\lambda}\right] - [\omega]\frac{\partial[\theta]}{\partial p} - \left[\omega^*\frac{\partial\theta^*}{\partial p}\right] \\
&= -\left[u^*\frac{\partial\theta^*}{R\cos\phi\partial\lambda}\right] - [\omega]\frac{\partial[\theta]}{\partial p} - \frac{\partial[\omega^*\theta^*]}{\partial p} + \left[\theta^*\frac{\partial\omega^*}{\partial p}\right] \\
&= -\left[u^*\frac{\partial\theta^*}{R\cos\phi\partial\lambda}\right] - [\omega]\frac{\partial[\theta]}{\partial p} - \frac{\partial[\omega^*\theta^*]}{\partial p} \\
&\quad -\left[\theta^*\frac{\partial u^*}{R\cos\phi\partial\lambda}\right] - \left[\theta^*\frac{\partial(v^*\cos\phi)}{R\cos\phi\partial\phi}\right] \\
&= -\frac{\partial[u^*\theta^*]}{R\cos\phi\partial\lambda} - [\omega]\frac{\partial[\theta]}{\partial p} - \frac{\partial[\omega^*\theta^*]}{\partial p} - \left[\theta^*\frac{\partial(v^*\cos\phi)}{R\cos\phi\partial\phi}\right] \\
&= -[\omega]\frac{\partial[\theta]}{\partial p} - \left[\theta^*\frac{\partial(v^*\cos\phi)}{R\cos\phi\partial\phi}\right] - \frac{\partial[\omega^*\theta^*]}{\partial p},
\end{aligned}$$

using equation (B.13).

Returning to the zonally-averaged thermodynamic equation and substituting

for $-\left[u^* \frac{\partial \theta^*}{R \cos\phi \partial \lambda}\right] - \left[\omega \frac{\partial \theta}{\partial p}\right]$:

$$\begin{aligned}
\frac{\partial [\theta]}{\partial t} &= -\frac{1}{R}\left[v\frac{\partial \theta}{\partial \phi}\right] - [\omega]\frac{\partial [\theta]}{\partial p} - \left[\theta^* \frac{\partial (v^* \cos\phi)}{R\cos\phi \partial\phi}\right] - \frac{\partial [\omega^*\theta^*]}{\partial p} + \left(\frac{p_{00}}{p}\right)^{\kappa}\frac{[Q]}{c_p} \\
&= -\frac{[v]}{R}\frac{\partial [\theta]}{\partial \phi} - \frac{1}{R}\left[v^*\frac{\partial \theta^*}{\partial \phi}\right] - [\omega]\frac{\partial [\theta]}{\partial p} - \left[\theta^* \frac{\partial (v^* \cos\phi)}{R\cos\phi \partial\phi}\right] - \frac{\partial [\omega^*\theta^*]}{\partial p} + \left(\frac{p_{00}}{p}\right)^{\kappa}\frac{[Q]}{c_p} \\
&= -\frac{[v]}{R}\frac{\partial [\theta]}{\partial \phi} - [\omega]\frac{\partial [\theta]}{\partial p} - \frac{1}{R\cos\phi}\left[v^*\cos\phi\frac{\partial \theta^*}{\partial \phi}\right] - \left[\theta^* \frac{\partial (v^* \cos\phi)}{R\cos\phi \partial\phi}\right] \\
&\quad -\frac{\partial [\omega^*\theta^*]}{\partial p} + \left(\frac{p_{00}}{p}\right)^{\kappa}\frac{[Q]}{c_p}.
\end{aligned}$$

Finally, one arrives at

$$\frac{\partial [\theta]}{\partial t} = -\frac{[v]}{R}\frac{\partial [\theta]}{\partial \phi} - [\omega]\frac{\partial [\theta]}{\partial p} - \frac{\partial ([v^*\theta^*]\cos\phi)}{R\cos\phi\partial\phi} - \frac{\partial [\omega^*\theta^*]}{\partial p} + \left(\frac{p_{00}}{p}\right)^{\kappa}\frac{[Q]}{c_p}.$$

B.3.5. Derivation of the zonally-averaged thermal wind equation

Taking the zonal average of the thermal wind equation (B.10) gives

$$\begin{aligned}
f\frac{\partial [u]}{\partial p} + \frac{2\tan\phi}{R}\left[u\frac{\partial u}{\partial p}\right] &= \frac{R_d}{pR}\frac{\partial T}{\partial \phi} \\
f\frac{\partial [u]}{\partial p} + \frac{2\tan\phi}{R}[u]\frac{\partial [u]}{\partial p} + \frac{2\tan\phi}{R}\left[u^*\frac{\partial u^*}{\partial p}\right] &= \frac{R_d}{pR}\frac{\partial T}{\partial \phi} \\
\left(f + \frac{2[u]\tan\phi}{R}\right)\frac{\partial [u]}{\partial p} + \frac{\tan\phi}{R}\left[\frac{\partial (u^*)^2}{\partial p}\right] &= \frac{R_d}{pR}\frac{\partial T}{\partial \phi}.
\end{aligned}$$

If the variance of u is neglected, one arrives at

$$\left(f + \frac{2\,[u]\tan\phi}{R}\right)\frac{\partial\,[u]}{\partial p} = \frac{R_d}{pR}\frac{\partial T}{\partial \phi}.$$

In terms of potential temperature, this relationship is

$$\left(f + \frac{2\,[u]\tan\phi}{R}\right)\frac{\partial\,[u]}{\partial p} = \frac{R_d p^{\kappa-1}}{p_{00}^{\kappa}}\frac{1}{R}\frac{\partial\,[\theta]}{\partial \phi}. \tag{B.17}$$

B.4. Governing equations for zonally-averaged motion

To summarise the equations derived above:

- The zonally-averaged zonal momentum equation is

$$\frac{\partial\,[u]}{\partial t} = [v]\left(f - \frac{\partial\left([u]\cos\phi\right)}{R\cos\phi\partial\phi}\right) - [\omega]\frac{\partial\,[u]}{\partial p} - \frac{\partial\,[u^*\omega^*]}{\partial p} - \frac{\partial\left([u^*v^*]\cos^2\phi\right)}{R\cos^2\phi\partial\phi} + [F\lambda]\,. \tag{B.18}$$

- The zonally-averaged thermodynamic equation is

$$\frac{\partial\,[\theta]}{\partial t} = -\frac{[v]}{R}\frac{\partial\,[\theta]}{\partial\phi} - [\omega]\frac{\partial\,[\theta]}{\partial p} - \frac{\partial\left([\theta^*v^*]\cos\phi\right)}{R\cos\phi\partial\phi} - \frac{\partial\,[\theta^*\omega^*]}{\partial p} + \left(\frac{p_{00}}{p}\right)^{\kappa}\frac{[Q]}{c_p}. \tag{B.19}$$

- The zonally-averaged mass continuity equation is

$$\frac{\partial\left([v]\cos\phi\right)}{R\cos\phi\partial\phi}+\frac{\partial[\omega]}{\partial p}=0. \tag{B.20}$$

- The thermal-wind equation is

$$\tilde{f}\frac{\partial[u]}{\partial p}=\frac{R_d}{pR}\frac{\partial T}{\partial\phi}, \tag{B.21}$$

or

$$\tilde{f}\frac{\partial[u]}{\partial p}=\frac{R_d p^{\kappa-1}}{p_{00}\kappa}\frac{1}{R}\frac{\partial[\theta]}{\partial\phi},$$

where $\tilde{f}=\left(f+\frac{2[u]\tan\phi}{R}\right)$.

C. Derivation of diagnostic streamfunction equation for mean meridional circulation

First, it is convenient to make the following change of coordinates

$$\eta = \sin\phi, \tag{C.1}$$

so

$$\frac{\partial}{\partial\eta} = \frac{\partial}{\cos\phi\partial\phi}.$$

The zonally-averaged mass continuity equation (B.20) may now be written as

$$\frac{\partial\left(\frac{[v]\cos\phi}{R}\right)}{\partial\eta} + \frac{\partial[\omega]}{\partial p} = 0.$$

This allows the definition of a streamfunction ψ:

$$[v] = \frac{1}{\cos\phi}\frac{\partial\psi}{\partial p},\ [\omega] = -\frac{1}{R}\frac{\partial\psi}{\partial\eta}. \tag{C.2}$$

Rewriting equations (B.18) and (B.19) in terms of derivates w.r.t. η and p

gives

$$\frac{\partial [u]}{\partial t} = [v]\left(f - \frac{\partial ([u]\cos\phi)}{R\partial\eta}\right) - [\omega]\frac{\partial [u]}{\partial p} - \frac{\partial [u^*\omega^*]}{\partial p} - \frac{\partial ([u^*v^*]\cos^2\phi)}{R\cos\phi\partial\eta} + [F_\lambda] \quad \text{(C.3)}$$

and

$$\frac{\partial [\theta]}{\partial t} = -\frac{[v]\cos\phi}{R}\frac{\partial [\theta]}{\partial \eta} - [\omega]\frac{\partial [\theta]}{\partial p} - \frac{\partial ([\theta^*v^*]\cos\phi)}{R\partial\eta} - \frac{\partial [\theta^*\omega^*]}{\partial p} + \left(\frac{p_{00}}{p}\right)^{\kappa}\frac{[Q]}{c_p}. \quad \text{(C.4)}$$

Changing meridional coordinate and differentiating equation (B.21) w.r.t. t allows one to write

$$\frac{\partial\left(\left(f + \frac{2\tan\phi}{R}[u]\right)\frac{\partial [u]}{\partial p}\right)}{\partial t} = \frac{R_d p^{\kappa-1}}{p_{00}^{\kappa}}\frac{1}{R}\frac{\cos\phi\partial^2[\theta]}{\partial t\partial\eta}.$$

Combining the derivative w.r.t p, making a change in the order of differentiation and expanding the derivative w.r.t. t gives

$$\frac{\partial\left(\tilde{f}\frac{\partial [u]}{\partial t}\right)}{\partial p} = \frac{R_d p^{\kappa-1}}{p_{00}^{\kappa}}\frac{1}{R}\frac{\cos\phi\partial\left(\frac{\partial [\theta]}{\partial t}\right)}{\partial\eta}$$

into which expressions (C.3) and (C.4) may be substituted:

$$\frac{\partial\left(\tilde{f}\left([v]\left(f-\frac{\partial([u]\cos\phi)}{R\partial\eta}\right)-[\omega]\frac{\partial[u]}{\partial p}-\frac{\partial[u^*\omega^*]}{\partial p}-\frac{\partial\left([u^*v^*]\cos^2\phi\right)}{R\cos\phi\partial\eta}+[F_\lambda]\right)\right)}{\partial p}$$

$$=\frac{R_d p^{\kappa-1}}{p_{00}^{\kappa}}\frac{1}{R}\frac{\cos\phi\partial\left(-\frac{[v]\cos\phi}{R}\frac{\partial[\theta]}{\partial\eta}-[\omega]\frac{\partial[\theta]}{\partial p}-\frac{\partial([\theta^*v^*]\cos\phi)}{R\partial\eta}-\frac{\partial[\theta^*\omega^*]}{\partial p}+\left(\frac{p_{00}}{p}\right)^{\kappa}\frac{[Q]}{c_p}\right)}{\partial\eta}.$$

Using the streamfunction definition (C.2) gives

$$\frac{\partial\left(\tilde{f}\left(\frac{1}{\cos\phi}\frac{\partial\psi}{\partial p}\left(f-\frac{\partial([u]\cos\phi)}{R\partial\eta}\right)+\frac{1}{R}\frac{\partial\psi}{\partial\eta}\frac{\partial[u]}{\partial p}-\frac{\partial[u^*\omega^*]}{\partial p}-\frac{\partial\left([u^*v^*]\cos^2\phi\right)}{R\cos\phi\partial\eta}+[F_\lambda]\right)\right)}{\cos\phi\partial p}$$

$$=\frac{R_d p^{\kappa-1}}{p_{00}^{\kappa}}\frac{1}{R}\frac{\partial\left(-\frac{\partial\psi}{R\partial p}\frac{\partial[\theta]}{\partial\eta}+\frac{1}{R}\frac{\partial\psi}{\partial\eta}\frac{\partial[\theta]}{\partial p}-\frac{\partial([\theta^*v^*]\cos\phi)}{R\partial\eta}-\frac{\partial[\theta^*\omega^*]}{\partial p}+\left(\frac{p_{00}}{p}\right)^{\kappa}\frac{[Q]}{c_p}\right)}{\partial\eta}$$

Moving terms involving ψ to the left-hand side and the remaining terms to the right-hand side gives

$$\frac{\partial\left(\tilde{f}\left(\frac{1}{\cos\phi}\frac{\partial\psi}{\partial p}\left(f-\frac{\partial([u]\cos\phi)}{R\partial\eta}\right)+\frac{1}{R}\frac{\partial\psi}{\partial\eta}\frac{\partial[u]}{\partial p}\right)\right)}{\cos\phi\partial p}-\frac{R_d p^{\kappa-1}}{p_{00}\kappa}\frac{1}{R}\frac{\partial\left(-\frac{\partial\psi}{R\partial p}\frac{\partial[\theta]}{\partial\eta}+\frac{1}{R}\frac{\partial\psi}{\partial\eta}\frac{\partial[\theta]}{\partial p}\right)}{\partial\eta}$$

$$=\frac{R_d p^{\kappa-1}}{Rp_{00}\kappa}\frac{\partial\left(-\frac{\partial([\theta^*v^*]\cos\phi)}{R\partial\eta}-\frac{\partial[\theta^*\omega^*]}{\partial p}+\left(\frac{p_{00}}{p}\right)\kappa\frac{[Q]}{c_p}\right)}{\partial\eta}$$

$$-\frac{\partial\left(\frac{\tilde{f}}{\cos\phi}\left(-\frac{\partial[u^*\omega^*]}{\partial p}-\frac{\partial\left([u^*v^*]\cos^2\phi\right)}{R\cos\phi\partial\eta}+[F_\lambda]\right)\right)}{\partial p}$$

which may be simplified to

$$\begin{aligned}
&\frac{\partial\left(\tilde{f}\left(\frac{1}{\cos\phi}\frac{\partial\psi}{\partial p}\left(f-\frac{\partial([u]\cos\phi)}{R\partial\eta}\right)+\frac{1}{R}\frac{\partial\psi}{\partial\eta}\frac{\partial[u]}{\partial p}\right)\right)}{\cos\phi\partial p}+\frac{R_d p^{\kappa-1}}{p_{00}\kappa}\frac{1}{R}\frac{\partial\left(\frac{\partial\psi}{R\partial p}\frac{\partial[\theta]}{\partial\eta}-\frac{1}{R}\frac{\partial\psi}{\partial\eta}\frac{\partial[\theta]}{\partial p}\right)}{\partial\eta}\\
=\;&\frac{R_d p^{\kappa-1}}{Rp_{00}\kappa}\frac{\partial\left(-\frac{\partial([\theta^*v^*]\cos\phi)}{R\partial\eta}-\frac{\partial[\theta^*\omega^*]}{\partial p}+\left(\frac{p_{00}}{p}\right)\kappa\frac{[Q]}{c_p}\right)}{\partial\eta}\\
&+\frac{\partial\left(\frac{\tilde{f}}{\cos\phi}\left(\frac{\partial[u^*\omega^*]}{\partial p}+\frac{\partial\left([u^*v^*]\cos^2\phi\right)}{R\cos\phi\partial\eta}-[F\lambda]\right)\right)}{\partial p}.
\end{aligned}$$

Defining

$$\begin{aligned}
H &= \frac{R_d p^{\kappa-1}}{p_{00}^{\kappa}R}\left(-\frac{\partial\left([\theta^*v^*]\cos\phi\right)}{R\partial\eta}-\frac{\partial[\theta^*\omega^*]}{\partial p}+\left(\frac{p_{00}}{p}\right)^{\kappa}\frac{[Q]}{c_p}\right)\\
\chi &= \frac{\tilde{f}}{\cos\phi}\left(\frac{\partial\left([u^*v^*]\cos^2\phi\right)}{R\cos\phi\partial\eta}+\frac{\partial[u^*\omega^*]}{\partial p}-[F_\lambda]\right)
\end{aligned}$$

allows one to write

$$\frac{\partial\left(\frac{\tilde{f}}{\cos\phi}\left(f-\frac{\partial([u]\cos\phi)}{R\partial\eta}\right)\frac{\partial\psi}{\partial p}\right)}{\cos\phi\partial p}+\frac{\partial\left(\tilde{f}\frac{\partial[u]}{\partial p}\frac{\partial\psi}{\partial\eta}\right)}{R\cos\phi\partial p}+\frac{R_d p^{\kappa-1}}{p_{00}^{\kappa}}\frac{1}{R^2}\frac{\partial\left(\frac{\partial[\theta]}{\partial\eta}\frac{\partial\psi}{\partial p}-\frac{\partial[\theta]}{\partial p}\frac{\partial\psi}{\partial\eta}\right)}{\partial\eta}=\frac{\partial H}{\partial\eta}+\frac{\partial\chi}{\partial p}.$$

This may be rewritten, taking $C=\frac{\tilde{f}}{\cos\phi}\left(f-\frac{\partial([u]\cos\phi)}{R\partial\eta}\right)$, $[S_p]=-\frac{p^{\kappa}}{p_{00}^{\kappa}}\frac{\partial[\theta]}{\partial p}$ and

$D = \frac{R_d}{p}\frac{1}{R^2}$ as

$$\begin{aligned}
\frac{\partial\left(C\frac{\partial\psi}{\partial p}\right)}{\cos\phi\partial p} + \frac{\partial\left(\tilde{f}\frac{\partial[u]}{\partial p}\frac{\partial\psi}{\partial\eta}\right)}{R\cos\phi\partial p} + \frac{R_d p^{\kappa-1}}{p_{00}^{\kappa}}\frac{\partial\left(\frac{\partial[\theta]}{\partial\eta}\frac{\partial\psi}{\partial p} - \frac{\partial[\theta]}{\partial p}\frac{\partial\psi}{\partial\eta}\right)}{\partial\eta} &= \frac{\partial H}{\partial\eta} + \frac{\partial\chi}{\partial p} \\
\frac{\partial\left(C\frac{\partial\psi}{\partial p}\right)}{\partial p} + \frac{\partial\left(\tilde{f}\frac{\partial[u]}{\partial p}\frac{\partial\psi}{\partial\eta}\right)}{R\cos\phi\partial p} + \frac{Dp^{\kappa}}{p_{00}^{\kappa}}\frac{\partial\left(\frac{\partial[\theta]}{\partial\eta}\frac{\partial\psi}{\partial p}\right)}{\partial\eta} - D\frac{\partial\left(\frac{p^{\kappa}}{p_{00}^{\kappa}}\frac{\partial[\theta]}{\partial p}\frac{\partial\psi}{\partial\eta}\right)}{\partial\eta} &= \frac{\partial H}{\partial\eta} + \frac{\partial\chi}{\partial p} \\
\frac{\partial\left(C\frac{\partial\psi}{\partial p}\right)}{\cos\phi\partial p} + \frac{\partial\left(\tilde{f}\frac{\partial[u]}{\partial p}\frac{\partial\psi}{\partial\eta}\right)}{R\cos\phi\partial p} + \frac{Dp^{\kappa}}{p_{00}^{\kappa}}\frac{\partial\left(\frac{\partial[\theta]}{\partial\eta}\frac{\partial\psi}{\partial p}\right)}{\partial\eta} + D\frac{\partial\left([S_p]\frac{\partial\psi}{\partial\eta}\right)}{\partial\eta} &= \frac{\partial H}{\partial\eta} + \frac{\partial\chi}{\partial p}.
\end{aligned}$$

Taking the left-hand side of this equation, expanding the derivative w.r.t. p in the second term and using the zonally-averaged thermal wind relationship (B.17) gives

$$\begin{aligned}
&\frac{\partial\left(C\frac{\partial\psi}{\partial p}\right)}{\cos\phi\partial p} + \frac{\partial\left(p^{\kappa-1}\frac{\partial[\theta]}{\partial\eta}\right)}{\partial p}\frac{R_d}{p_{00}\kappa}\frac{1}{R^2}\frac{\partial\psi}{\partial\eta} + \frac{\tilde{f}}{R\cos\phi}\frac{\partial[u]}{\partial p}\frac{\partial^2\psi}{\partial p\partial\eta} \\
&+\frac{Dp\kappa}{p_{00}\kappa}\frac{\partial\left(\frac{\partial[\theta]}{\partial\eta}\frac{\partial\psi}{\partial p}\right)}{\partial\eta} + D\frac{\partial\left([S_p]\frac{\partial\psi}{\partial\eta}\right)}{\partial\eta} \\
= &\frac{\partial\left(C\frac{\partial\psi}{\partial p}\right)}{\cos\phi\partial p} + \left(\frac{R_d}{R^2}\frac{p^{\kappa-1}}{p_{00}\kappa}\frac{\partial^2[\theta]}{\partial\eta\partial p} + \frac{\partial\left(\frac{R_d}{R^2}\frac{p^{\kappa-1}}{p_{00}\kappa}\right)}{\partial p}\frac{\partial[\theta]}{\partial\eta}\right)\frac{\partial\psi}{\partial\eta} + \frac{\tilde{f}}{R\cos\phi}\frac{\partial[u]}{\partial p}\frac{\partial^2\psi}{\partial p\partial\eta} \\
&+\frac{Dp\kappa}{p_{00}\kappa}\frac{\partial\left(\frac{\partial[\theta]}{\partial\eta}\frac{\partial\psi}{\partial p}\right)}{\partial\eta} + D\frac{\partial\left([S_p]\frac{\partial\psi}{\partial\eta}\right)}{\partial\eta} \\
= &\frac{\partial\left(C\frac{\partial\psi}{\partial p}\right)}{\cos\phi\partial p} + \left(-D\frac{\partial[S_p]}{\partial\eta} + \frac{\partial\left(\frac{R_d}{R^2}\frac{p^{\kappa-1}}{p_{00}\kappa}\right)}{\partial p}\frac{\partial[\theta]}{\partial\eta}\right)\frac{\partial\psi}{\partial\eta} + \frac{\tilde{f}}{R\cos\phi}\frac{\partial[u]}{\partial p}\frac{\partial^2\psi}{\partial p\partial\eta}
\end{aligned}$$

$$
\begin{aligned}
&+\frac{Dp\kappa}{p_{00}\kappa}\frac{\partial\left(\frac{\partial[\theta]}{\partial\eta}\frac{\partial\psi}{\partial p}\right)}{\partial\eta}+D\frac{\partial\left([S_p]\frac{\partial\psi}{\partial\eta}\right)}{\partial\eta}\\
=\;&\frac{\partial\left(C\frac{\partial\psi}{\partial p}\right)}{\cos\phi\partial p}+\left(-D\frac{\partial[S_p]}{\partial\eta}+(\kappa-1)D\frac{p^{\kappa-1}}{p_{00}\kappa}\frac{\partial[\theta]}{\partial\eta}\right)\frac{\partial\psi}{\partial\eta}+\frac{\tilde{f}}{R\cos\phi}\frac{\partial[u]}{\partial p}\frac{\partial^2\psi}{\partial p\partial\eta}\\
&+\frac{Dp\kappa}{p_{00}\kappa}\frac{\partial\left(\frac{\partial[\theta]}{\partial\eta}\frac{\partial\psi}{\partial p}\right)}{\partial\eta}+D[S_p]\frac{\partial^2\psi}{\partial\eta^2}+D\frac{\partial[S_p]}{\partial\eta}\frac{\partial\psi}{\partial\eta}\\
=\;&\frac{\partial\left(C\frac{\partial\psi}{\partial p}\right)}{\cos\phi\partial p}+(\kappa-1)D\frac{p^{\kappa-1}}{p_{00}\kappa}\frac{\partial[\theta]}{\partial\eta}\frac{\partial\psi}{\partial\eta}+\frac{\tilde{f}}{R\cos\phi}\frac{\partial[u]}{\partial p}\frac{\partial^2\psi}{\partial p\partial\eta}+\frac{Dp\kappa}{p_{00}\kappa}\frac{\partial\left(\frac{\partial[\theta]}{\partial\eta}\frac{\partial\psi}{\partial p}\right)}{\partial\eta}+D[S_p]\frac{\partial^2\psi}{\partial\eta^2}\\
=\;&\frac{\partial\left(C\frac{\partial\psi}{\partial p}\right)}{\cos\phi\partial p}+(\kappa-1)\frac{D}{p}\frac{p\kappa}{p_{00}\kappa}\frac{\partial[\theta]}{\partial\eta}\frac{\partial\psi}{\partial\eta}+D\frac{p\kappa}{p_{00}\kappa}\frac{\partial[\theta]}{\partial\eta}\frac{\partial^2\psi}{\partial p\partial\eta}+\frac{Dp\kappa}{p_{00}\kappa}\frac{\partial\left(\frac{\partial[\theta]}{\partial\eta}\frac{\partial\psi}{\partial p}\right)}{\partial\eta}+D[S_p]\frac{\partial^2\psi}{\partial\eta^2}\\
=\;&\frac{\partial\left(C\frac{\partial\psi}{\partial p}\right)}{\cos\phi\partial p}+D\frac{p\kappa}{p_{00}\kappa}\frac{\partial[\theta]}{\partial\eta}\left(\frac{\kappa-1}{p}\frac{\partial\psi}{\partial\eta}+\frac{\partial^2\psi}{\partial p\partial\eta}\right)+\frac{Dp\kappa}{p_{00}\kappa}\frac{\partial\left(\frac{\partial[\theta]}{\partial\eta}\frac{\partial\psi}{\partial p}\right)}{\partial\eta}+D[S_p]\frac{\partial^2\psi}{\partial\eta^2}\\
=\;&\frac{\partial\left(C\frac{\partial\psi}{\partial p}\right)}{\cos\phi\partial p}+D\frac{p\kappa}{p_{00}\kappa}\frac{\partial[\theta]}{\partial\eta}\left(\frac{\kappa-1}{p}\frac{\partial\psi}{\partial\eta}+\frac{\partial^2\psi}{\partial p\partial\eta}\right)+\frac{Dp\kappa}{p_{00}\kappa}\frac{\partial[\theta]}{\partial\eta}\frac{\partial^2\psi}{\partial\eta\partial p}\\
&+\frac{Dp\kappa}{p_{00}\kappa}\frac{\partial^2[\theta]}{\partial\eta^2}\frac{\partial\psi}{\partial p}+D[S_p]\frac{\partial^2\psi}{\partial\eta^2}\\
=\;&\frac{\partial\left(C\frac{\partial\psi}{\partial p}\right)}{\cos\phi\partial p}+D\frac{p\kappa}{p_{00}\kappa}\frac{\partial[\theta]}{\partial\eta}\left(\frac{\kappa-1}{p}\frac{\partial\psi}{\partial\eta}\right)+2\frac{Dp\kappa}{p_{00}\kappa}\frac{\partial[\theta]}{\partial\eta}\frac{\partial^2\psi}{\partial\eta\partial p}+\frac{Dp\kappa}{p_{00}\kappa}\frac{\partial^2[\theta]}{\partial\eta^2}\frac{\partial\psi}{\partial p}+D[S_p]\frac{\partial^2\psi}{\partial\eta^2}.
\end{aligned}
$$

This finally gives

$$
D[S_p]\frac{\partial^2\psi}{\partial\eta^2}+2\frac{Dp^{\kappa}}{p_{00}\kappa}\frac{\partial[\theta]}{\partial\eta}\frac{\partial^2\psi}{\partial\eta\partial p}+\frac{Dp\kappa}{p_{00}\kappa}\frac{\partial[\theta]}{\partial\eta}\left(\frac{\kappa-1}{p}\frac{\partial\psi}{\partial\eta}\right)+\frac{Dp\kappa}{p_{00}\kappa}\frac{\partial^2[\theta]}{\partial\eta^2}\frac{\partial\psi}{\partial p}+\frac{\partial\left(C\frac{\partial\psi}{\partial p}\right)}{\cos\phi\partial p}=\frac{\partial H}{\partial\eta}+\frac{\partial\chi}{\partial p}.
$$

D. Monthly plots

D.1. Distributions of zonal wind, potential temperature and diabatic heating

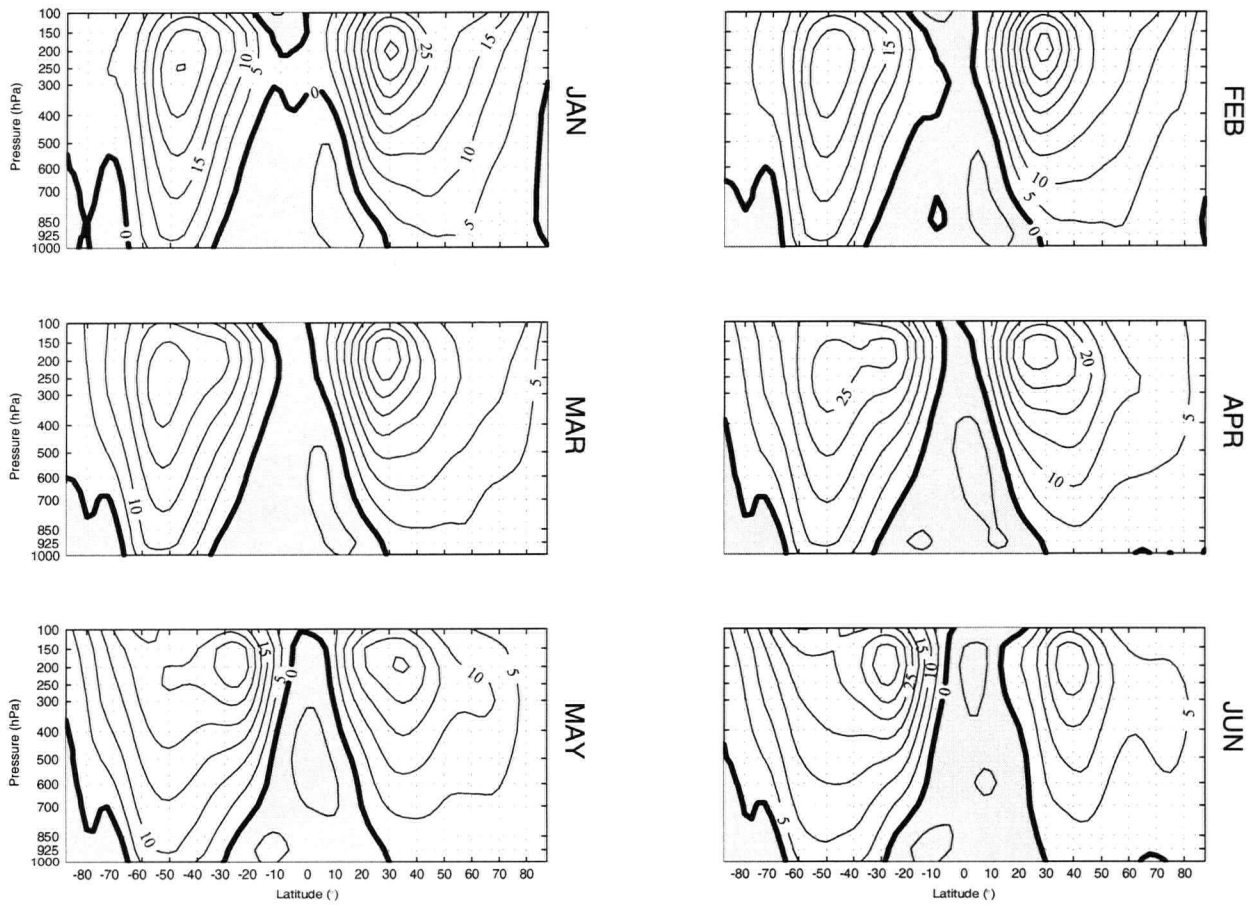

Figure D.1: January-June distributions of $[u]$. Units are $m\ s^{-1}$ and the contour interval is 5 $m\ s^{-1}$.

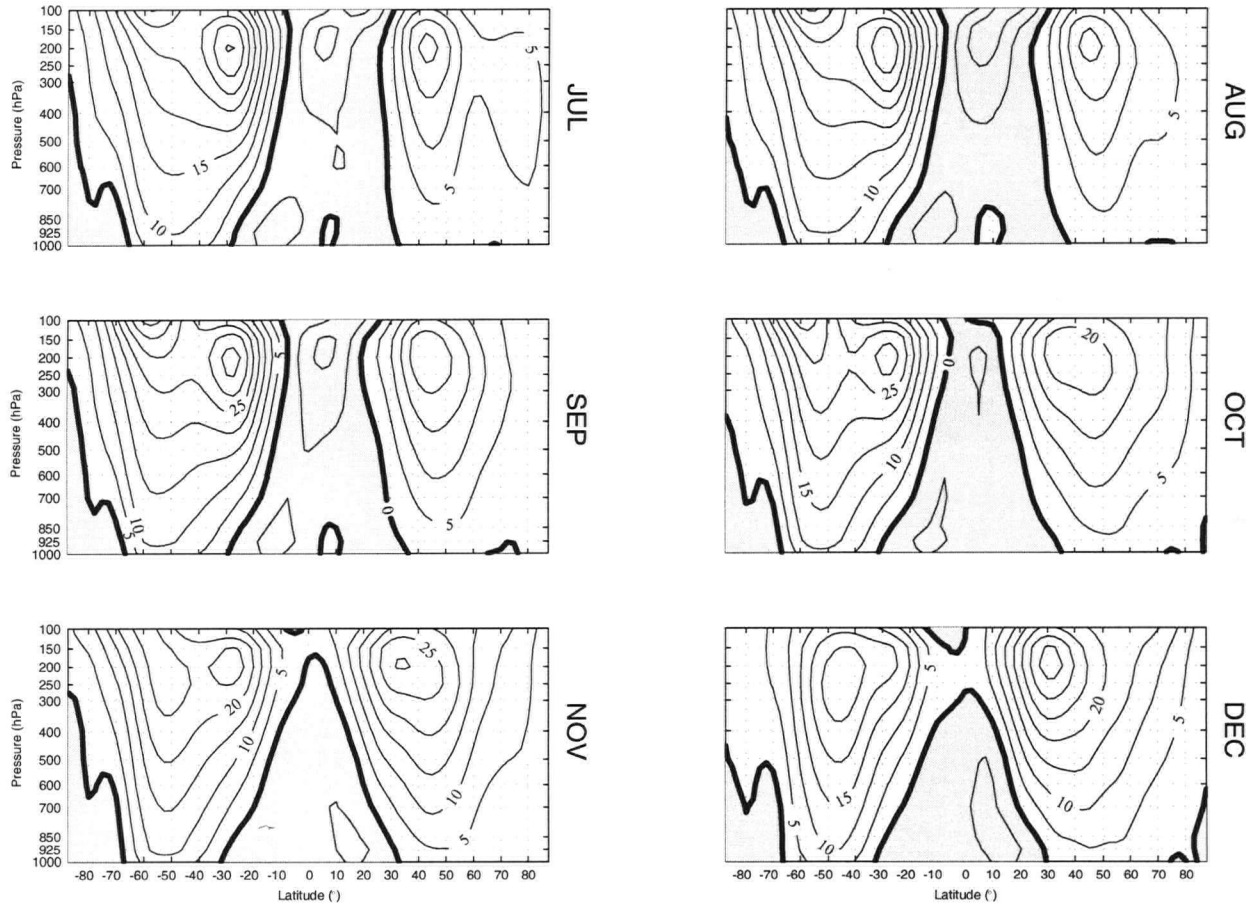

Figure D.2: July-December distributions of $[u]$. Units are $m\ s^{-1}$ and the contour interval is $5\ m\ s^{-1}$.

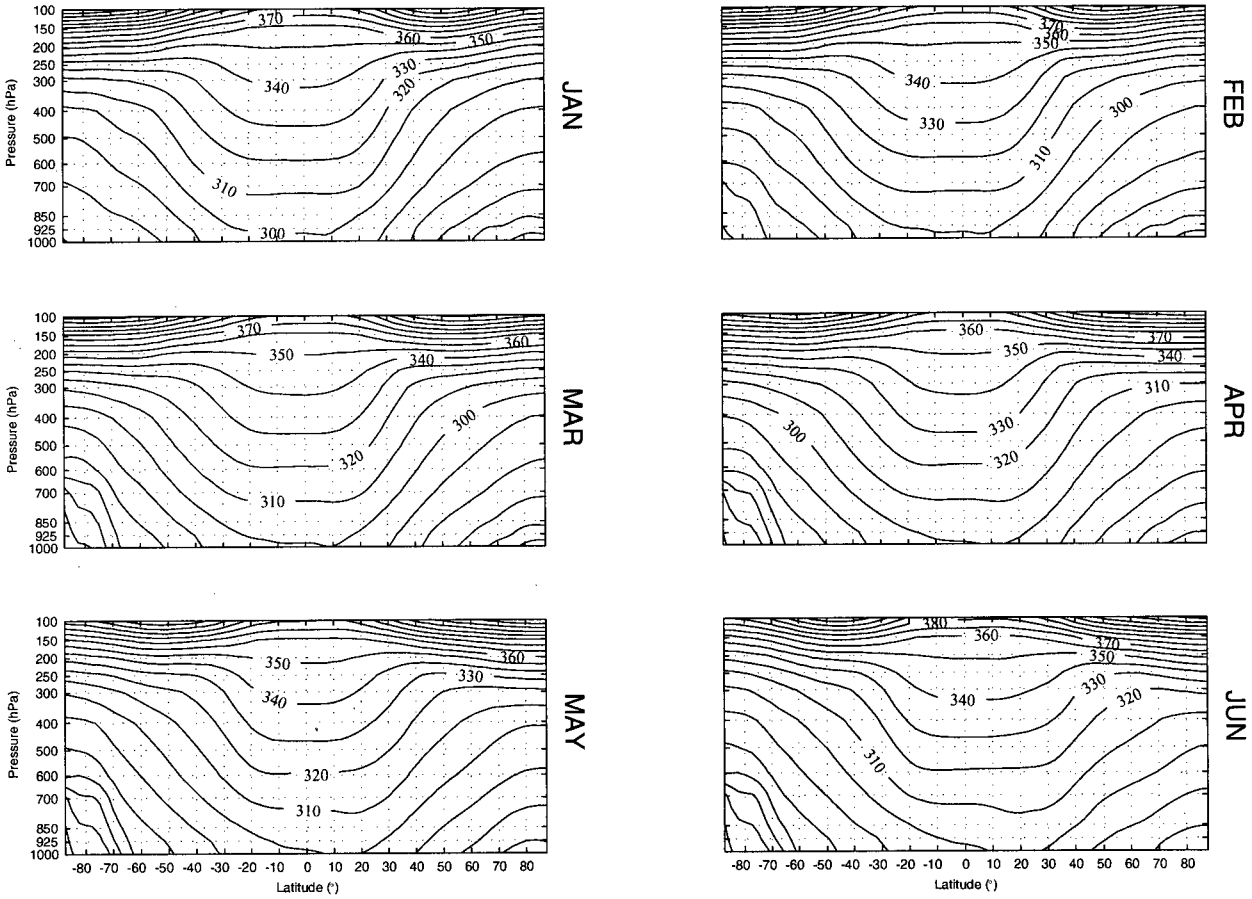

Figure D.3: January-June distributions of $[\theta]$. Units are K and the contour interval is 10 K.

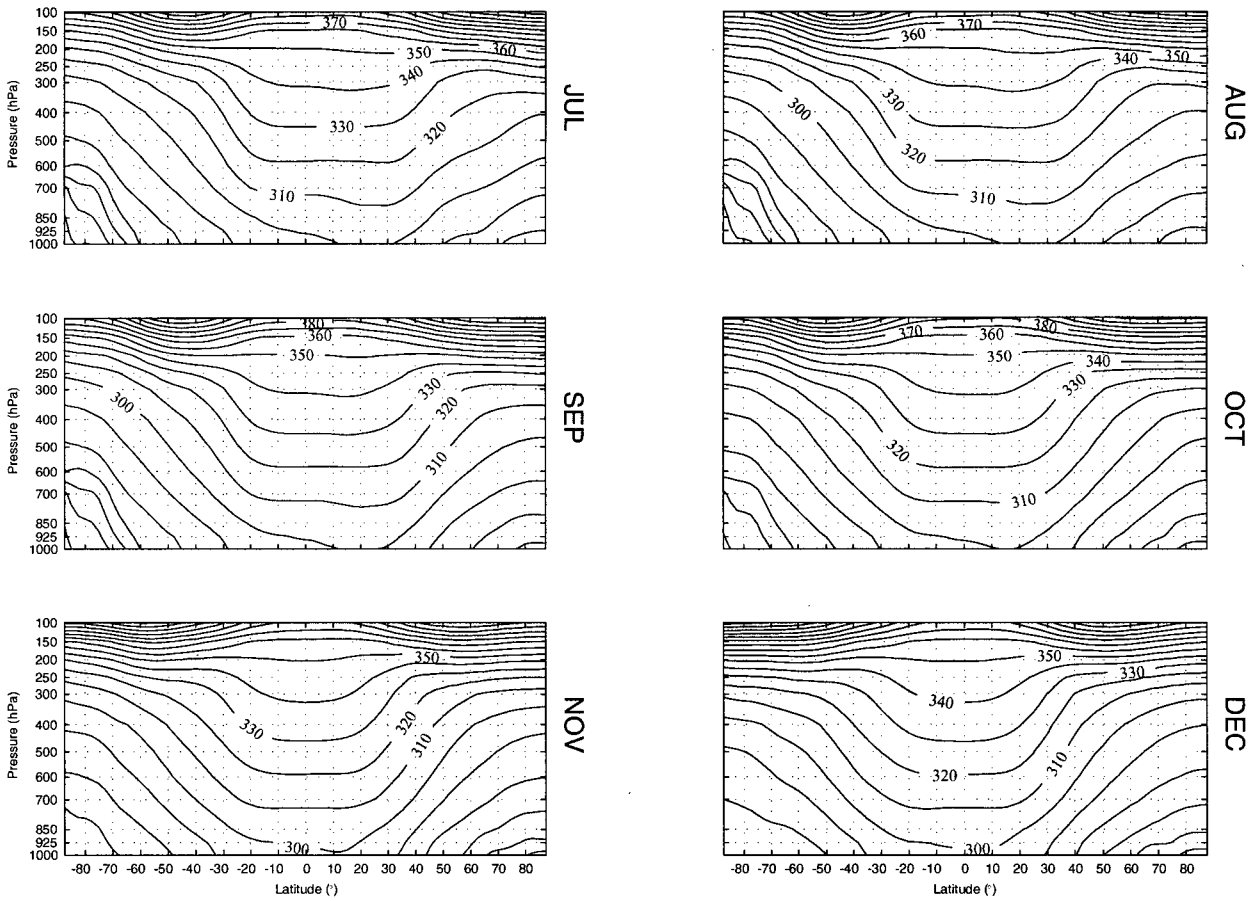

Figure D.4: July-December distributions of $[\theta]$. Units are K and the contour interval is 10 K.

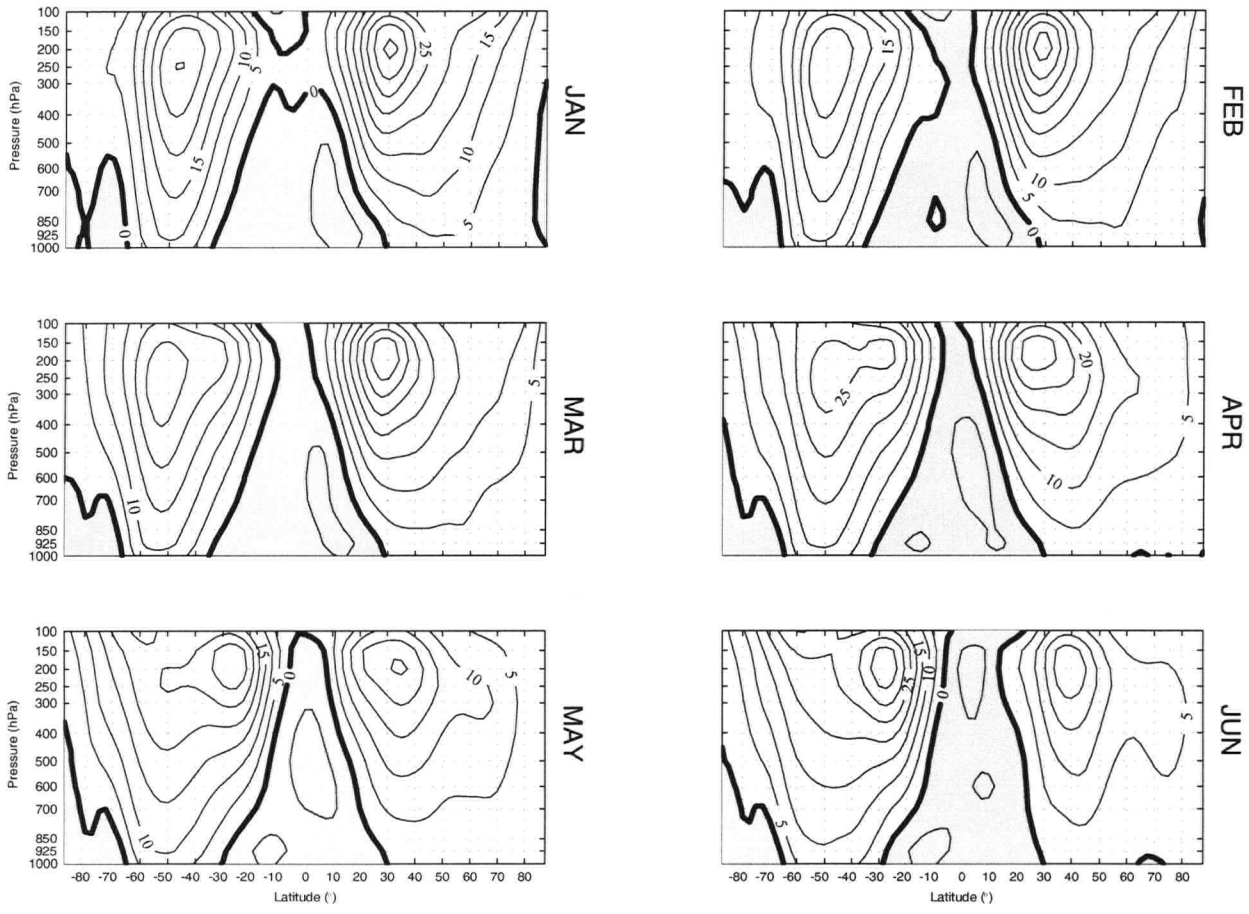

Figure D.5: January-June distributions of $[Q]$. Units are $K\ s^{-1}$ and the contour interval is $1 \times 10^{-5}\ K\ s^{-1}$.

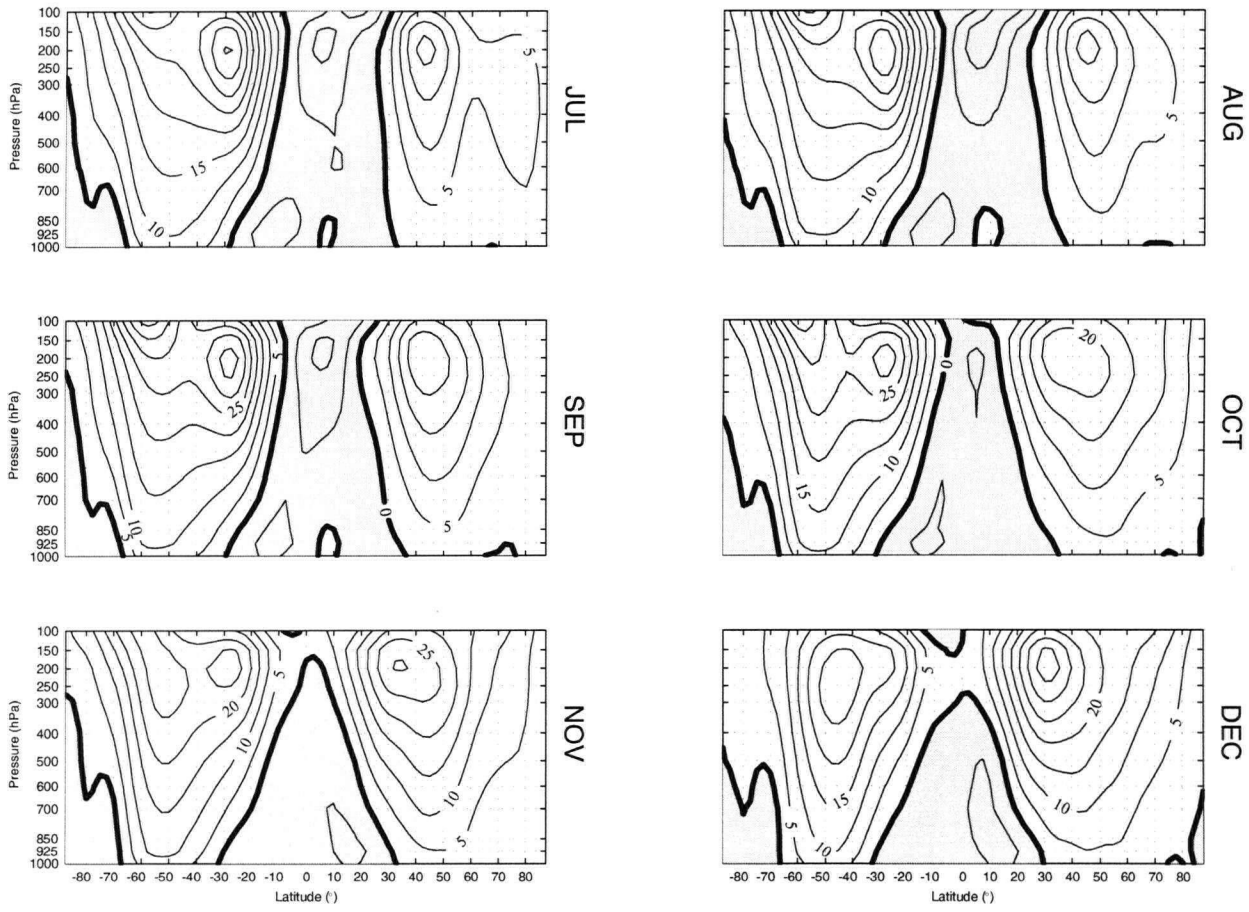

Figure D.6: July-December distributions of $[Q]$. Units are $K\ s^{-1}$ and the contour interval is $1 \times 10^{-5}\ K\ s^{-1}$.

D.2. Eddy fluxes of heat and momentum

D.2.1. Stationary eddies

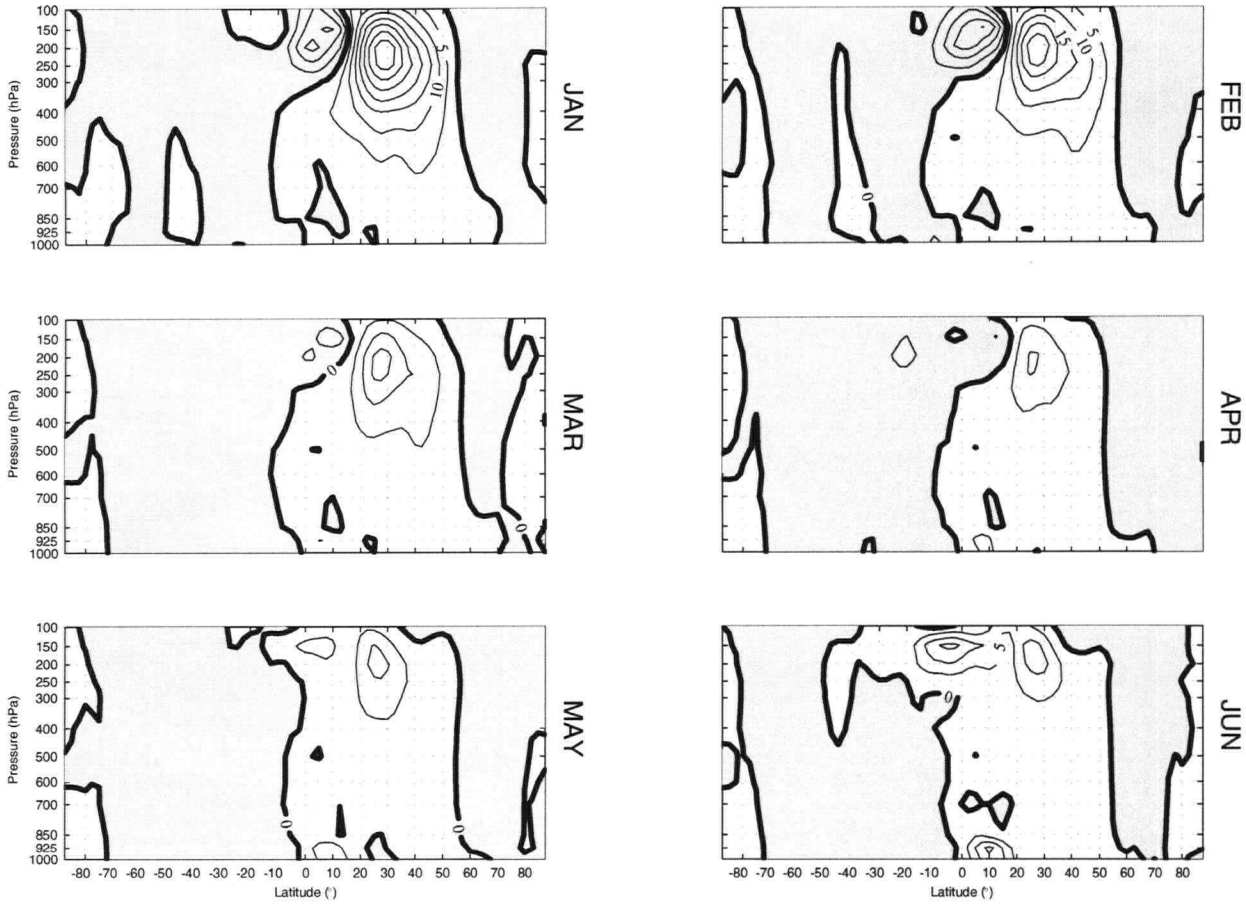

Figure D.7: January-June distributions of $[u^*v^*]\ \cos^2\phi$ for stationary eddies. Units are $m^2\ s^{-2}$ and the contour interval is $5\ m^2\ s^{-2}$.

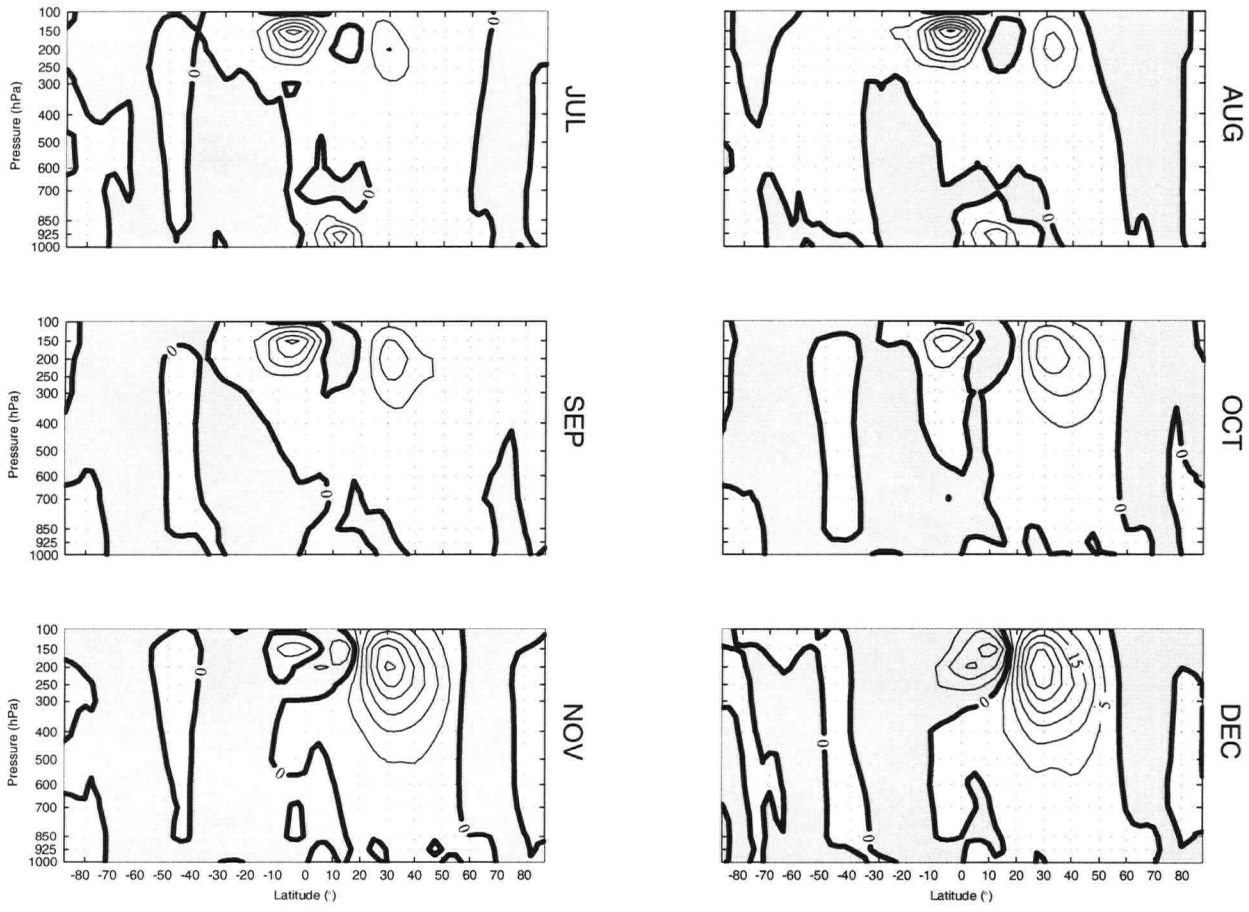

Figure D.8: July-December distributions of $[u^*v^*]\ \cos^2\phi$ for stationary eddies. Units are $m^2\ s^{-2}$ and the contour interval is $5\ m^2\ s^{-2}$.

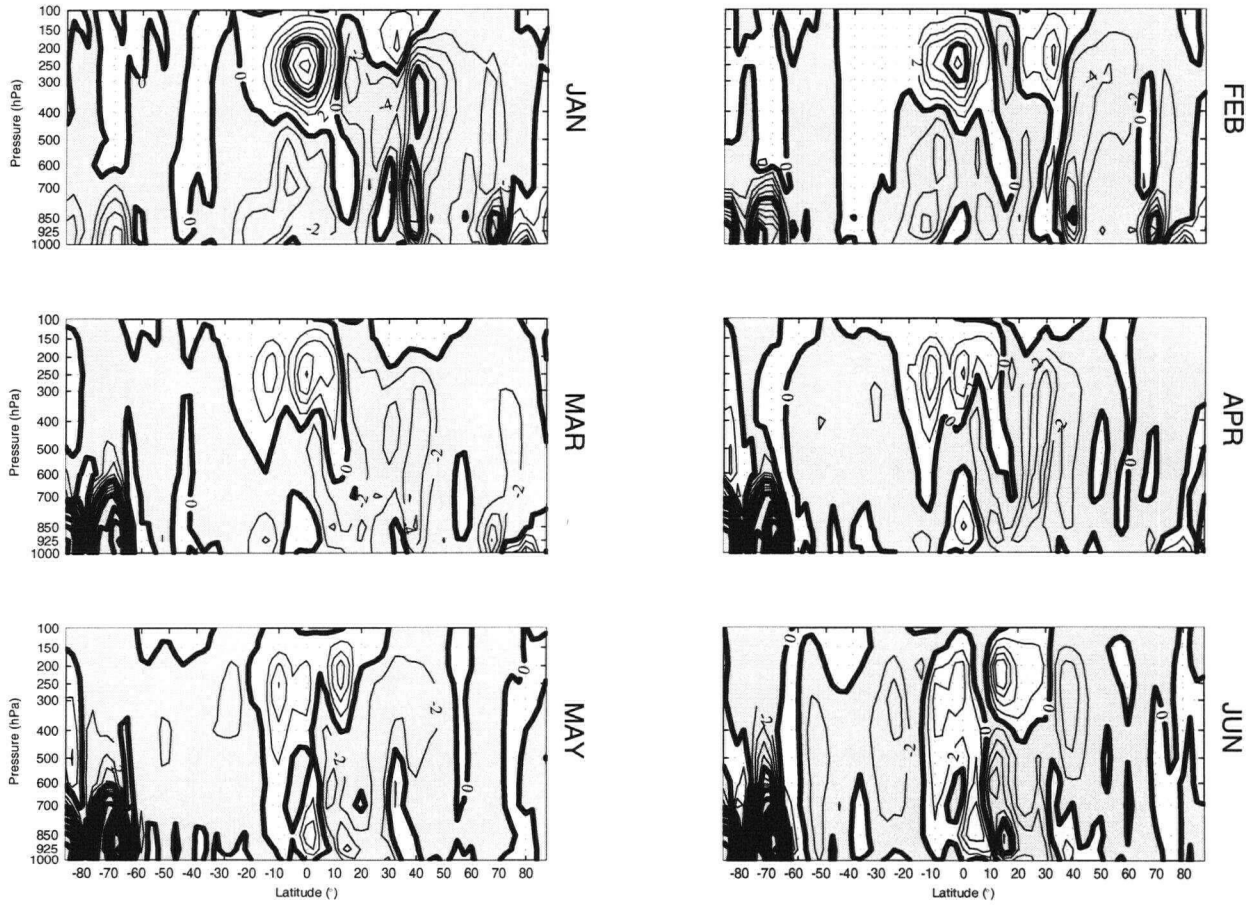

Figure D.9: January-June distributions of $[u^*\omega^*]$ for stationary eddies. Units are $10^{-2}\ m\ Pa\ s^{-2}$ and the contour intervals are $2 \times 10^{-2}\ m\ Pa\ s^{-2}$ (light contours) and $10 \times 10^{-2}\ m\ Pa\ s^{-2}$ (dark contours).

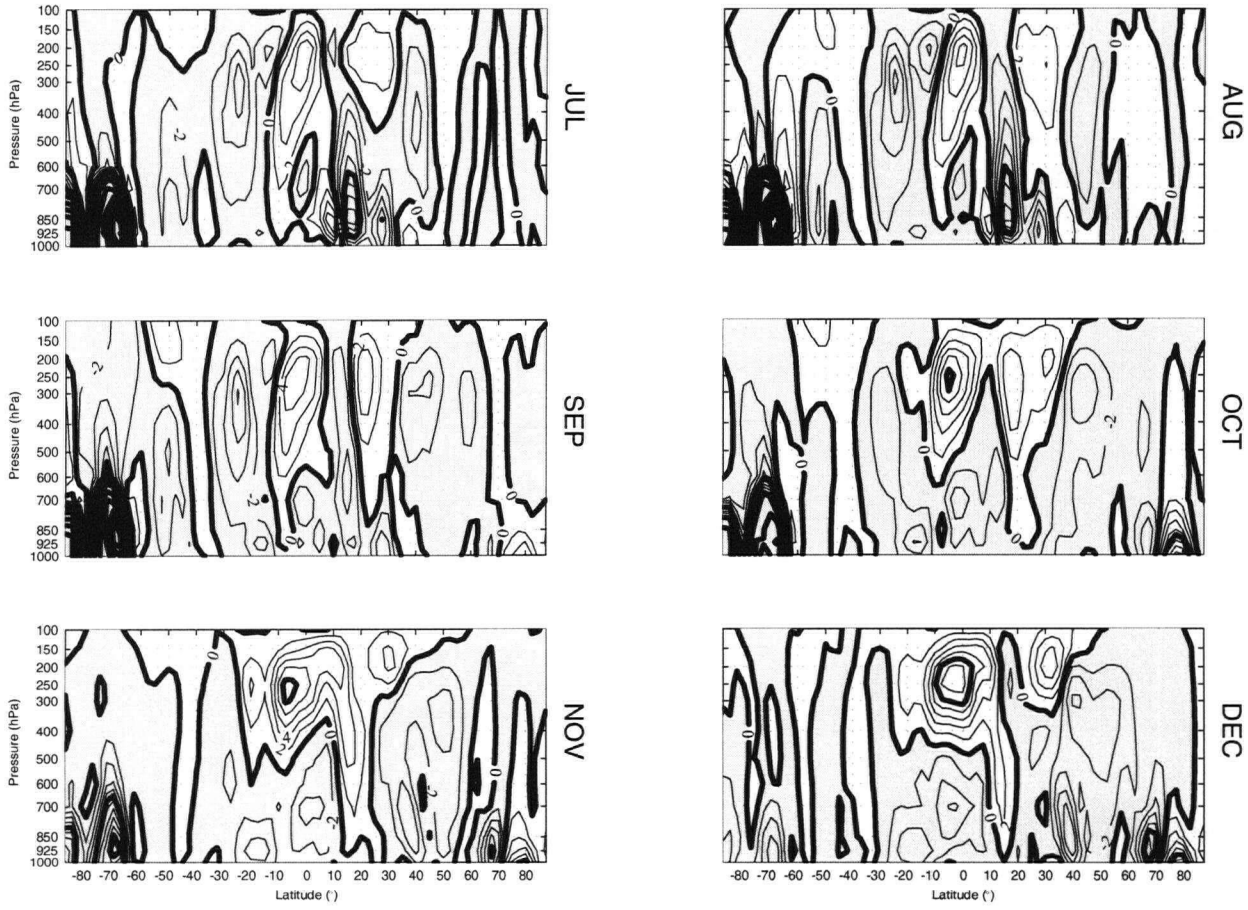

Figure D.10: July-December distributions of $[u^*\omega^*]$ for stationary eddies. Units are $10^{-2}\ m\ Pa\ s^{-2}$ and the contour intervals are $2 \times 10^{-2}\ m\ Pa\ s^{-2}$ (light contours) and $10 \times 10^{-2}\ m\ Pa\ s^{-2}$ (dark contours).

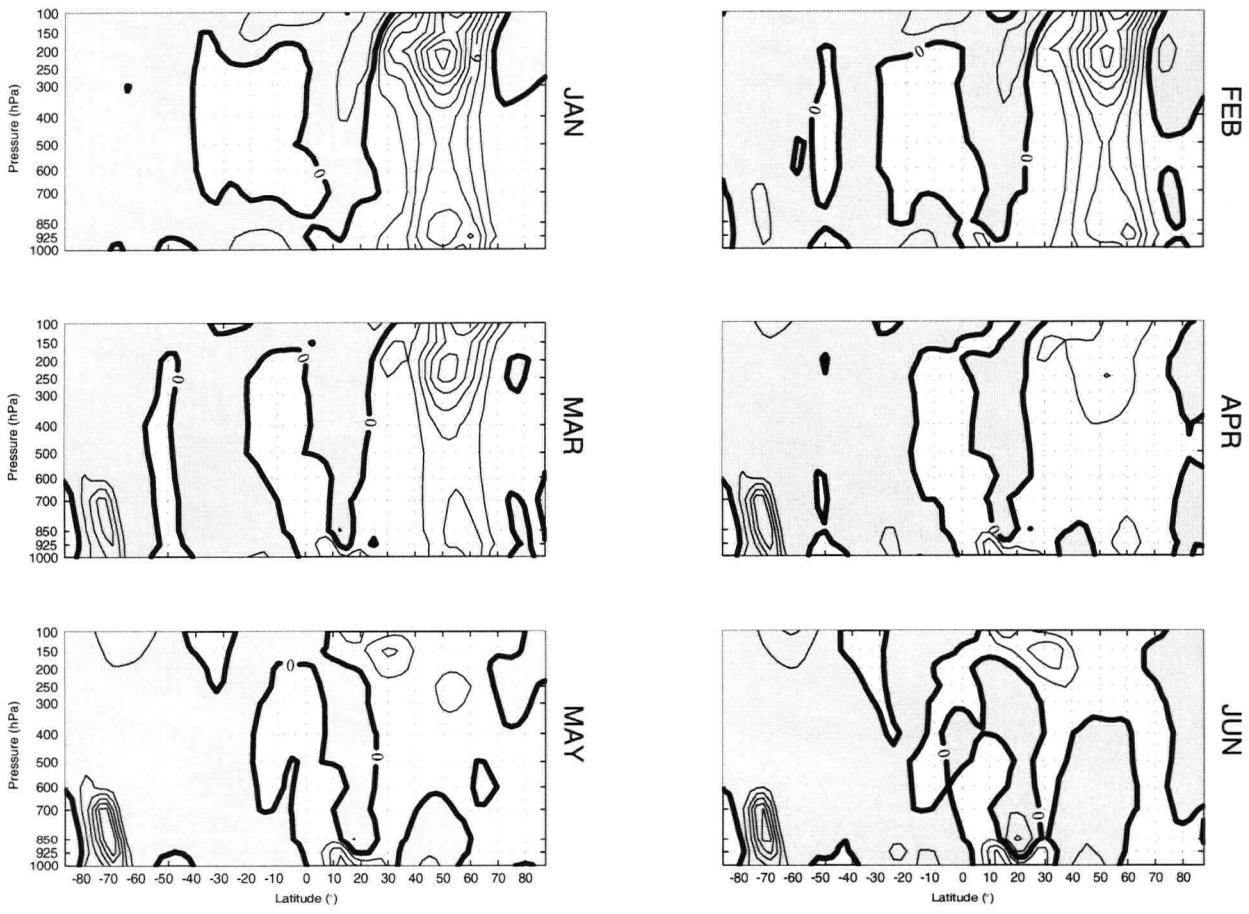

Figure D.11: January-June distributions of $[v^*\theta^*]\cos\phi$ for stationary eddies. Units are $K\ s^{-1}$ and the contour interval is $2\ K\ s^{-1}$.

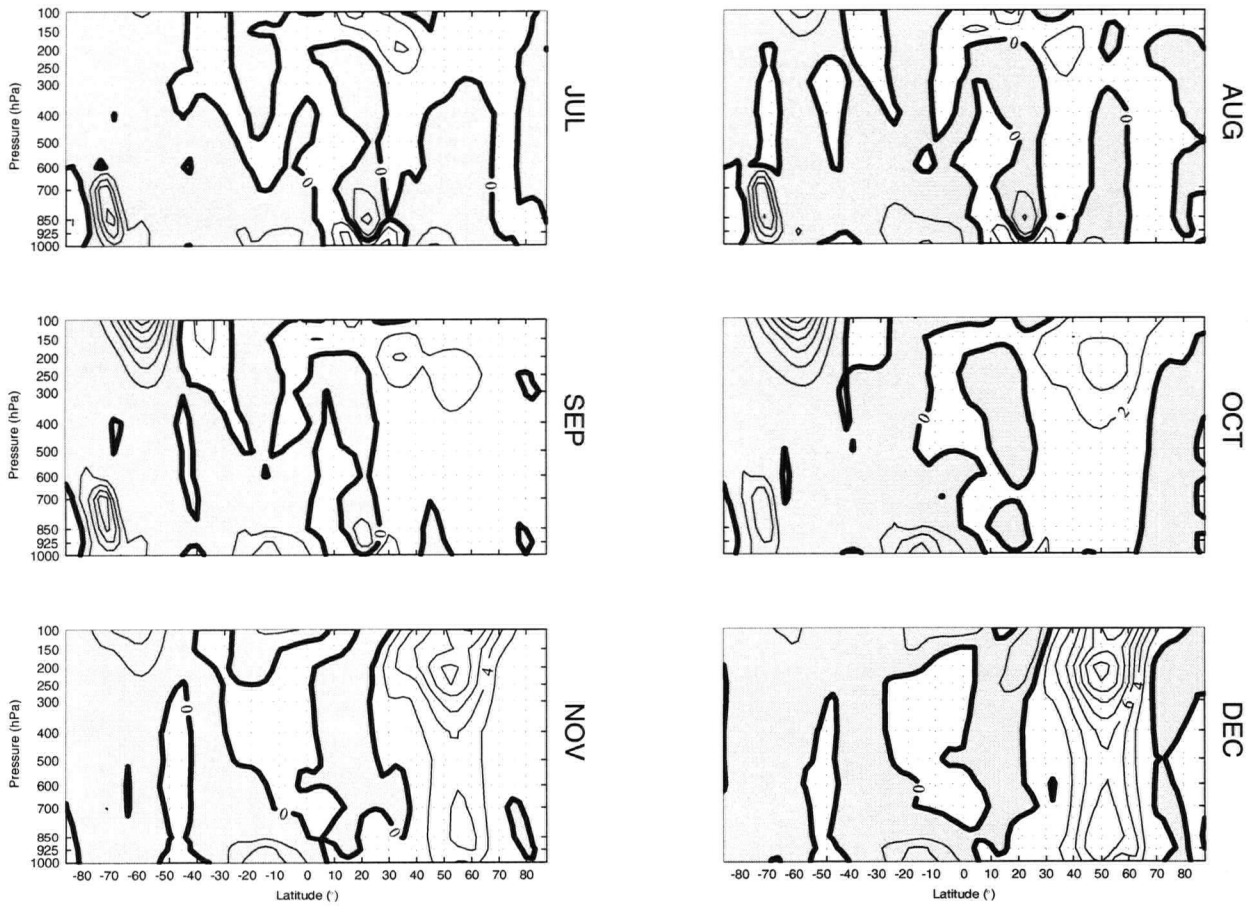

Figure D.12: July-December distributions of $[v^*\theta^*]\cos\phi$ for stationary eddies. Units are $K\ s^{-1}$ and the contour interval is $2\ K\ s^{-1}$.

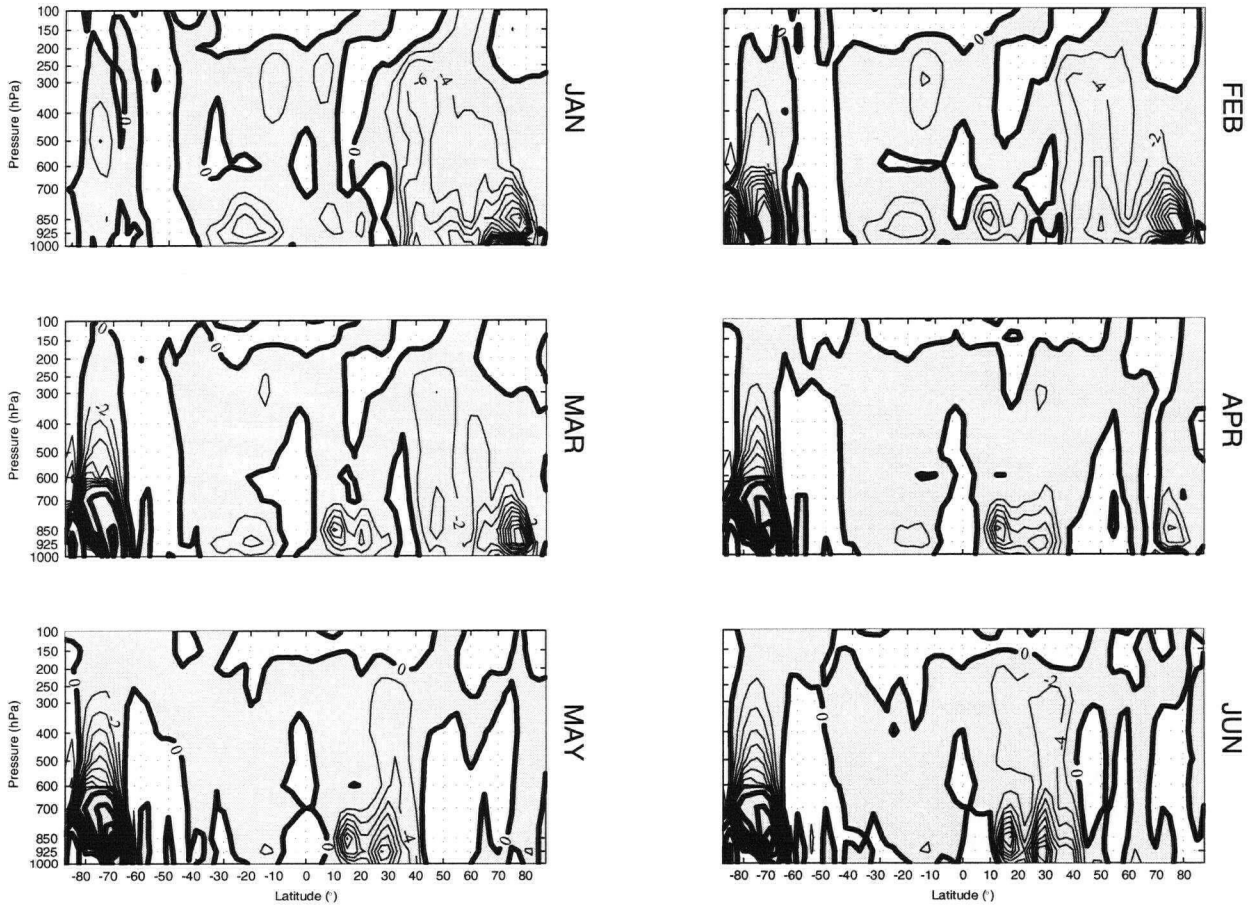

Figure D.13: January-June distributions of $[\omega^*\theta^*]$ for stationary eddies. Units are $10^{-2}\ Pa\ K\ s^{-1}$ and the contour intervals are $2 \times 10^{-2}\ Pa\ K\ s^{-1}$ (light contours) and $30 \times 10^{-2}\ Pa\ K\ s^{-1}$ (dark contours).

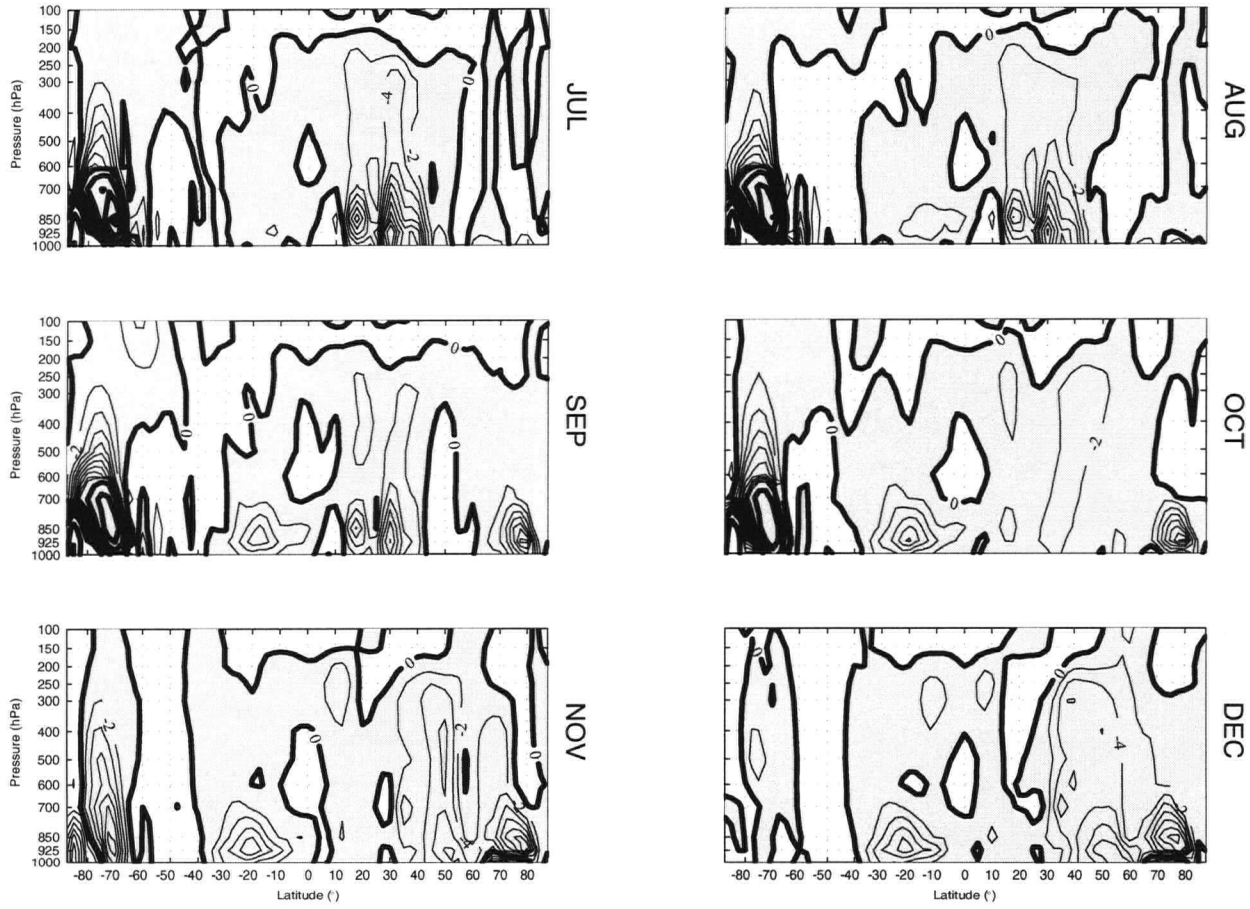

Figure D.14: July-December distributions of $[\omega^*\theta^*]$ for stationary eddies. Units are $10^{-2}\ Pa\ K\ s^{-1}$ and the contour intervals are $2 \times 10^{-2}\ Pa\ K\ s^{-1}$ (light contours) and $30 \times 10^{-2}\ Pa\ K\ s^{-1}$ (dark contours).

D.2.2. Transient, zonally-symmetric eddies

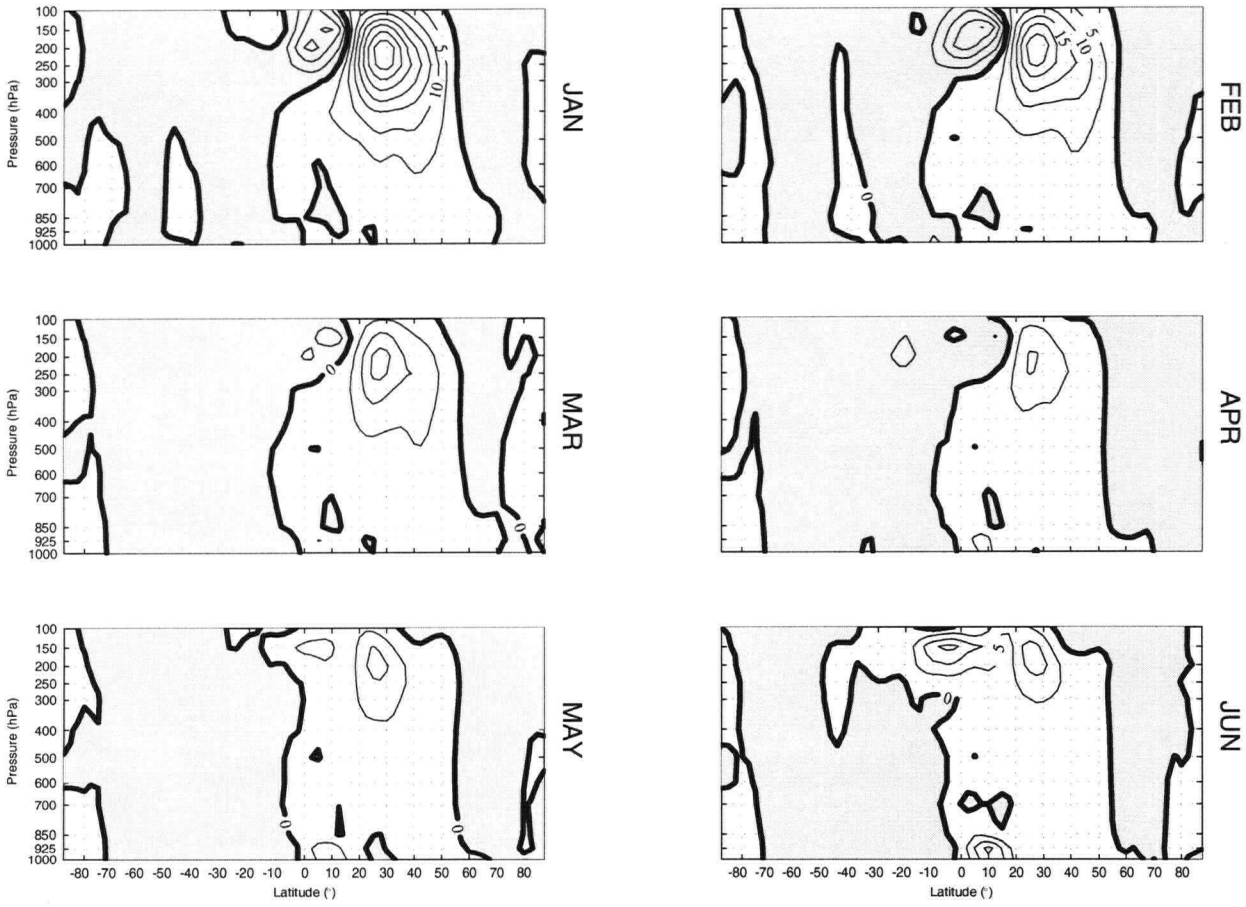

Figure D.15: January-June distributions of $[u^*v^*]\ \cos^2\phi$ for transient, zonally-symmetric eddies. Units are $m^2\ s^{-2}$ and the contour interval is $0.5\ m^2\ s^{-2}$.

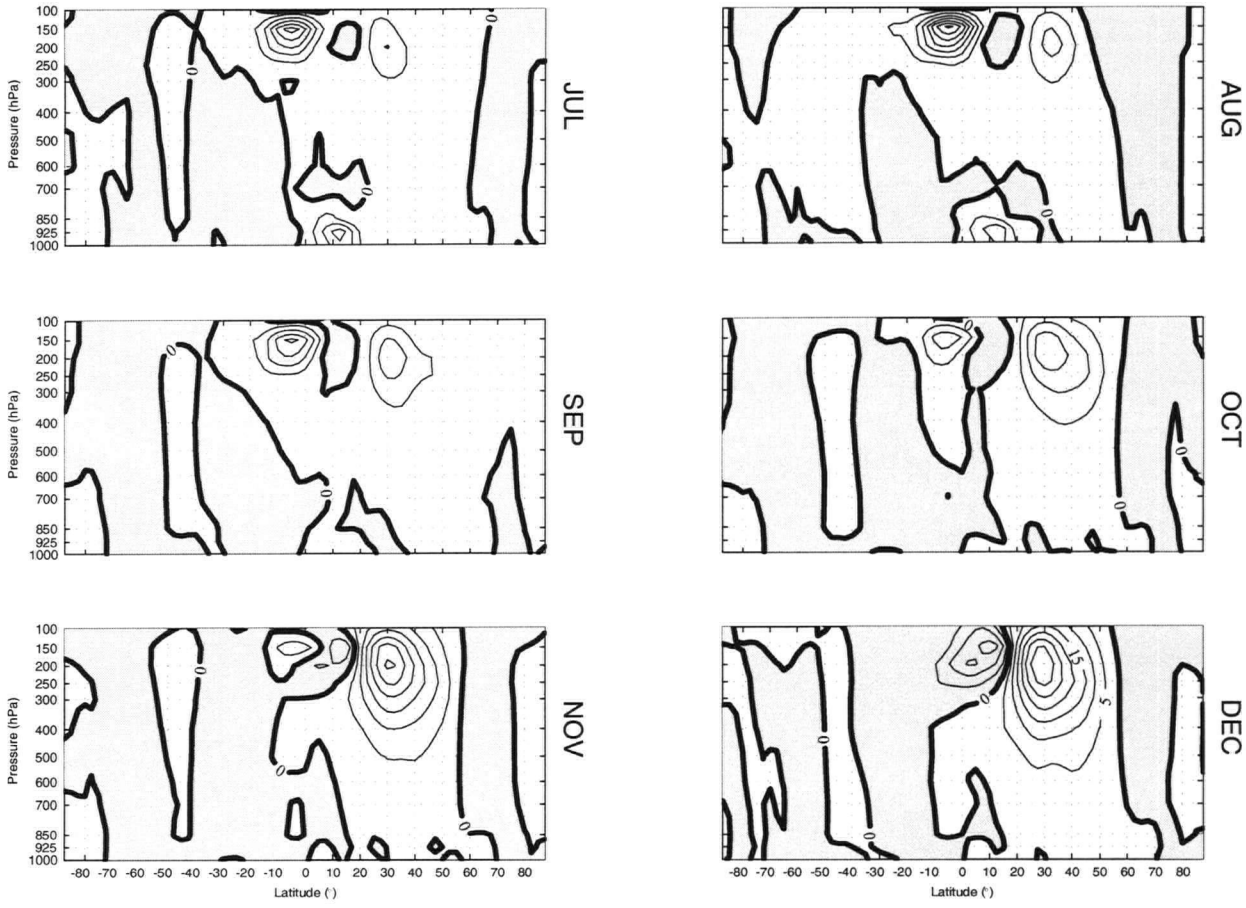

Figure D.16: July-December distributions of $[u^*v^*]\ \cos^2\phi$ for transient, zonally-symmetric eddies. Units are $m^2\ s^{-2}$ and the contour interval is $0.5\ m^2\ s^{-2}$.

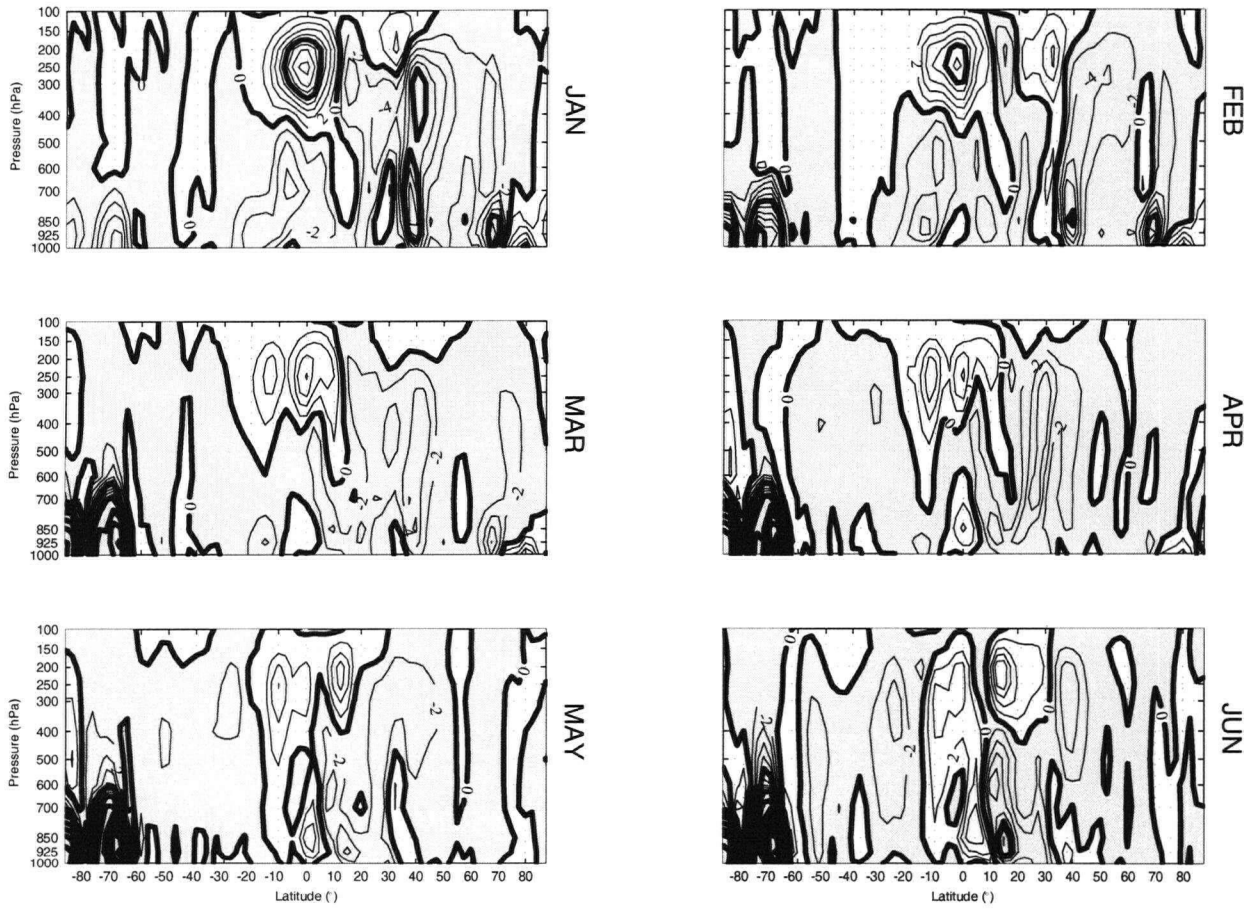

Figure D.17: January-June distributions of $[u^*\omega^*]$ for transient, zonally-symmetric eddies. Units are $10^{-2}\ m\ Pa\ s^{-2}$ and the contour intervals are $0.5\times10^{-2}\ m\ Pa\ s^{-2}$ (light contours) and $5\times10^{-2}\ m\ Pa\ s^{-2}$ (dark contours).

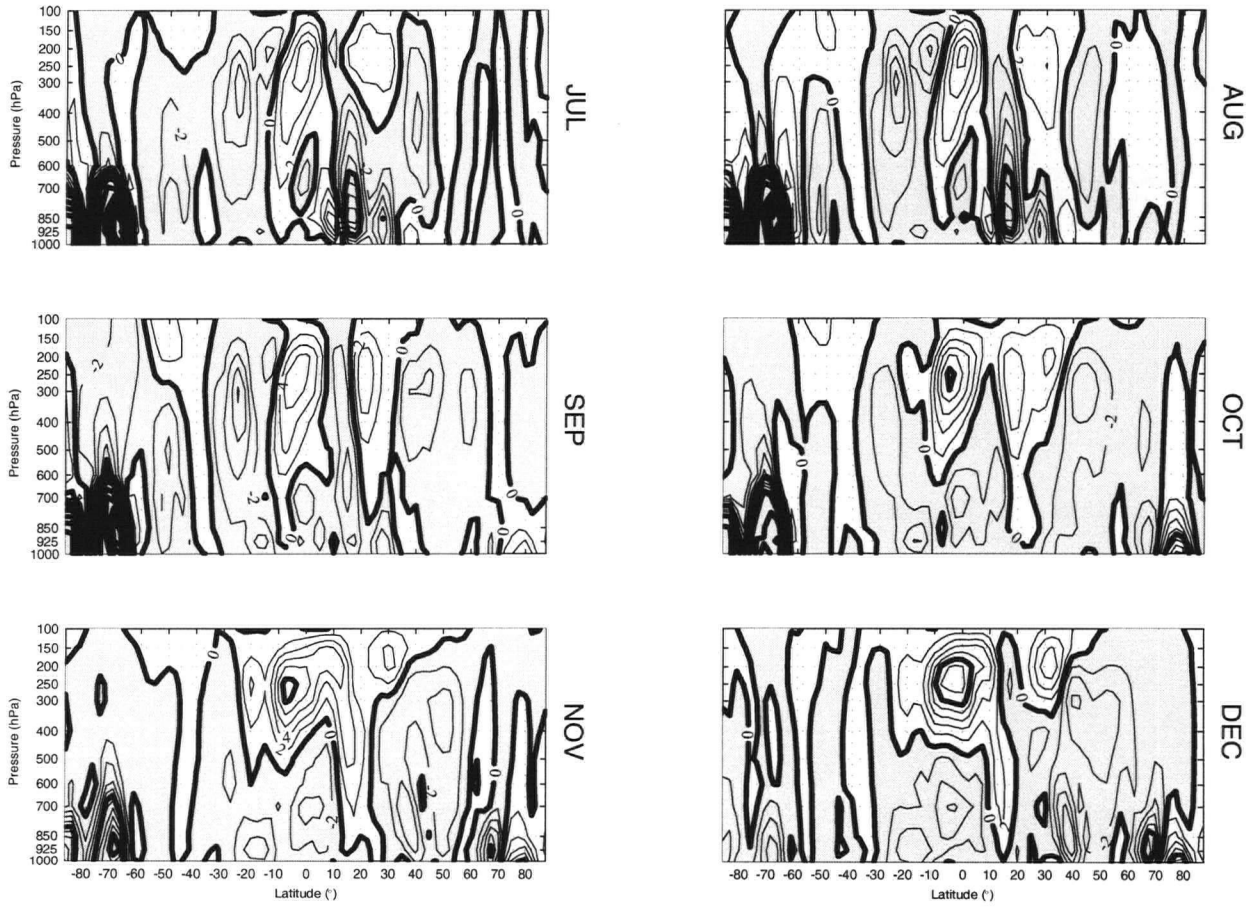

Figure D.18: July-December distributions of $[u^*\omega^*]$ for transient, zonally-symmetric eddies. Units are $10^{-2}\ m\ Pa\ s^{-2}$ and the contour intervals are $0.5 \times 10^{-2}\ m\ Pa\ s^{-2}$ (light contours) and $5 \times 10^{-2}\ m\ Pa\ s^{-2}$ (dark contours).

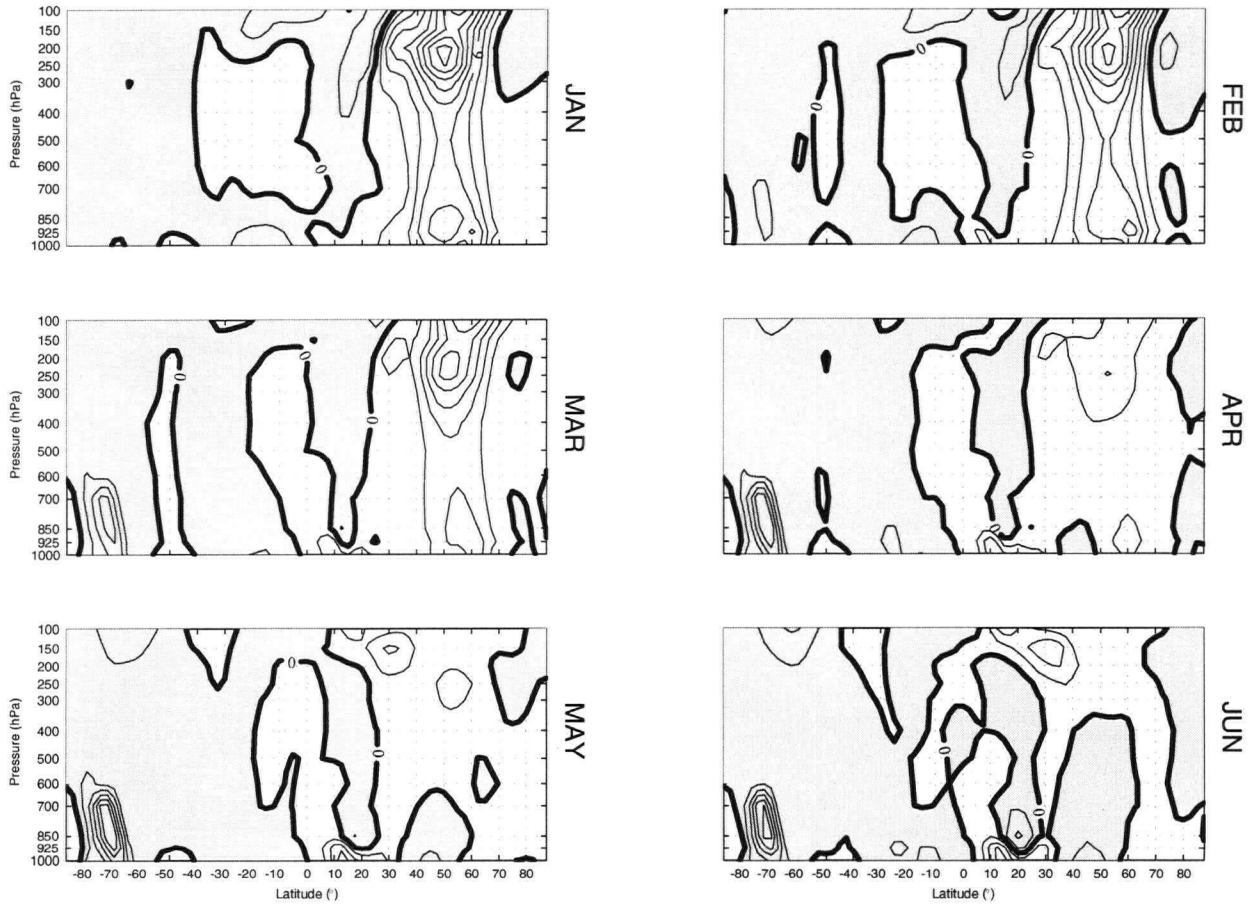

Figure D.19: January-June distributions of $[v^*\theta^*]\cos\phi$ for transient, zonally-symmetric eddies. Units are $K\ s^{-1}$ and the contour interval is $0.1\ K\ s^{-1}$.

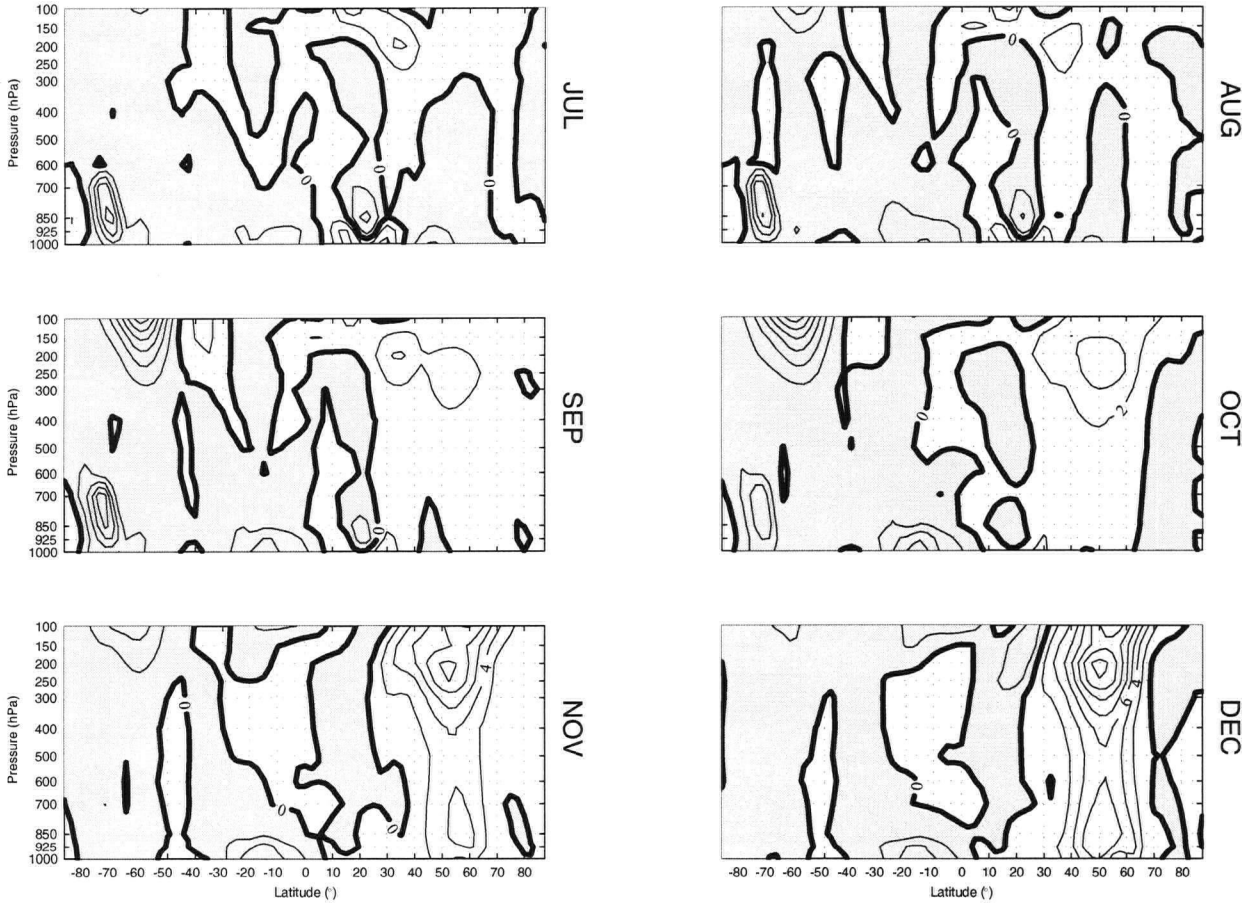

Figure D.20: July-December distributions of $[v^*\theta^*]\cos\phi$ for transient, zonally-symmetric eddies. Units are $K\ s^{-1}$ and the contour interval is $0.1\ K\ s^{-1}$.

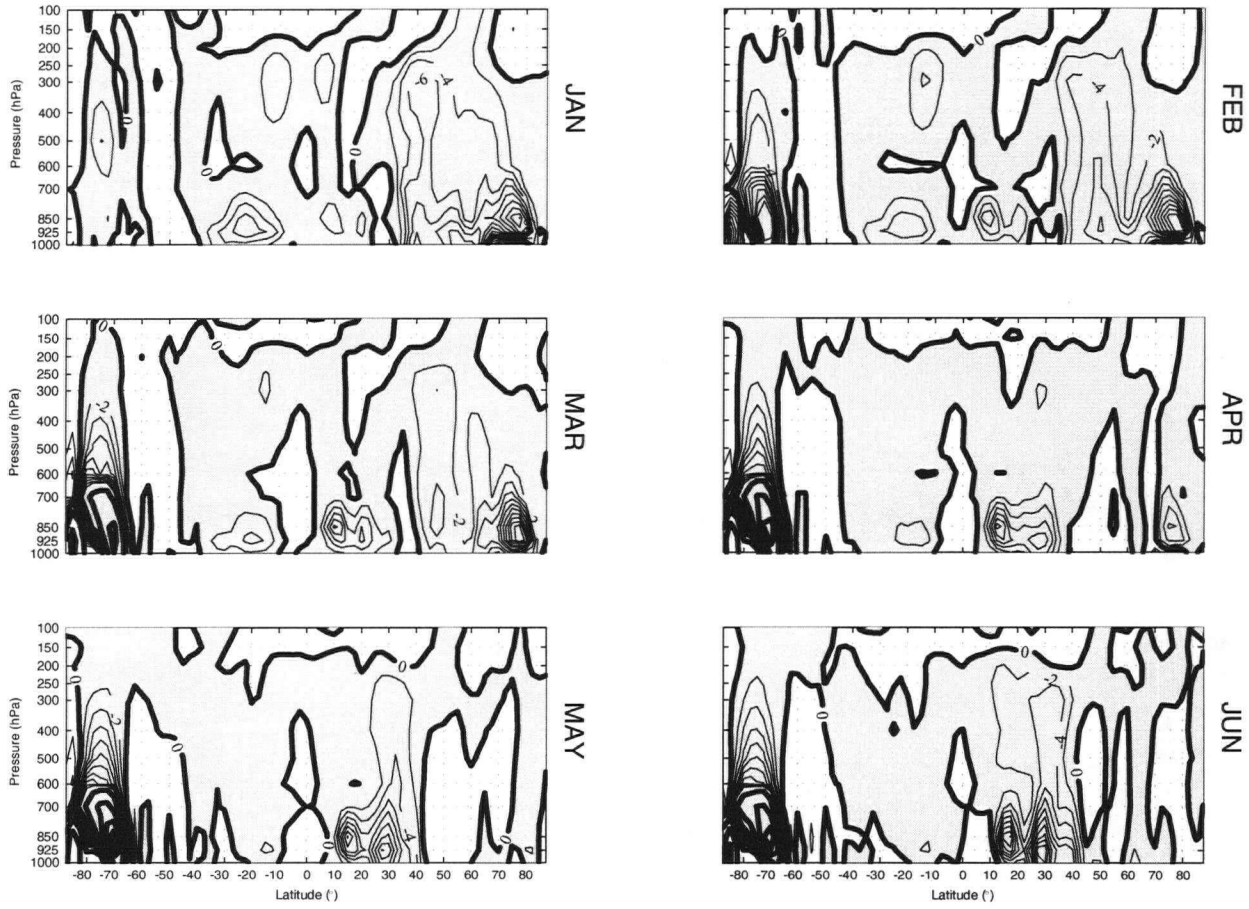

Figure D.21: January-June distributions of $[\omega^*\theta^*]$ for transient, zonally-symmetric eddies. Units are $10^{-2}\ Pa\ K\ s^{-1}$ and the contour intervals are $1 \times 10^{-2}\ Pa\ K\ s^{-1}$ (light contours) and $10 \times 10^{-2}\ Pa\ K\ s^{-1}$ (dark contours).

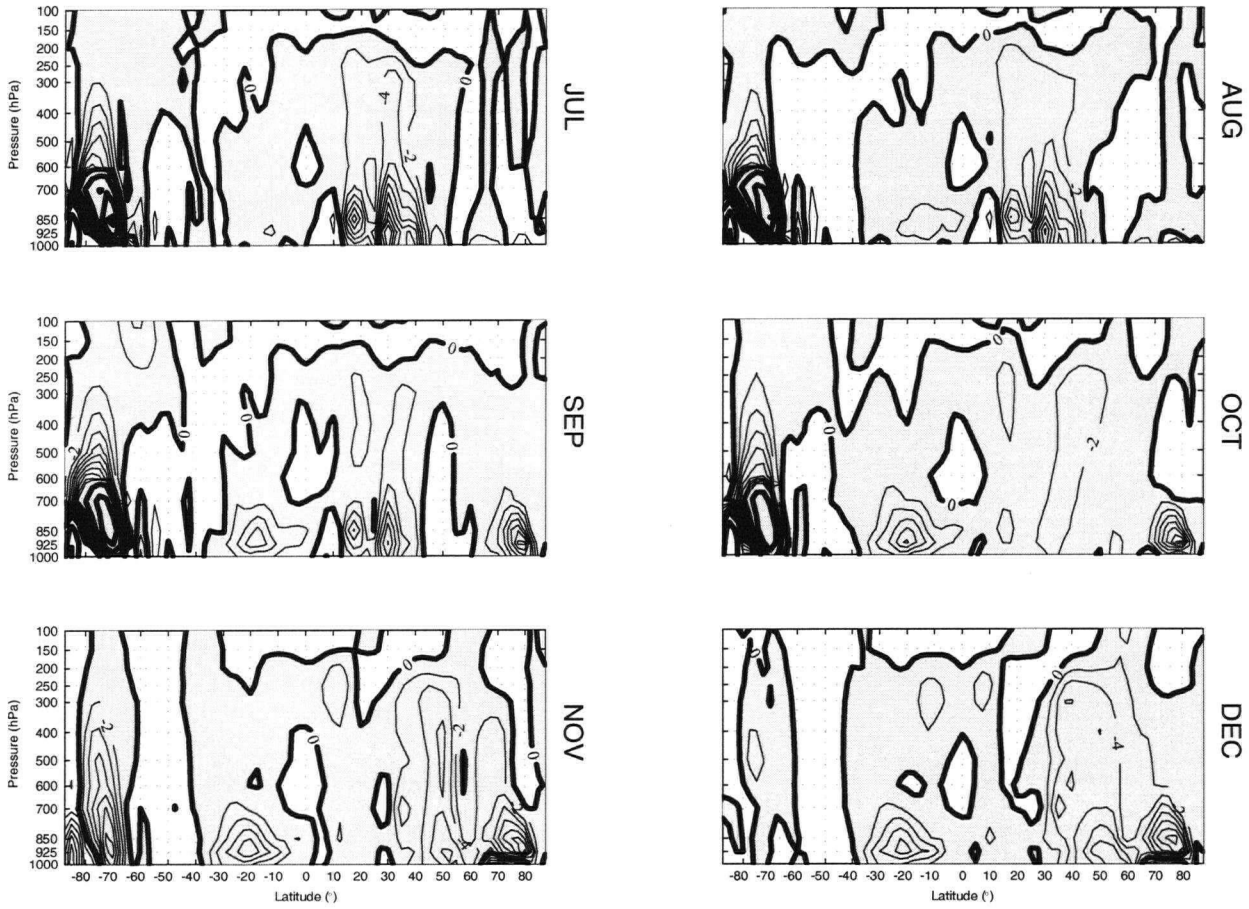

Figure D.22: July-December distributions of $[\omega^*\theta^*]$ for transient, zonally-symmetric eddies. Units are 10^{-2} Pa K s^{-1} and the contour intervals are 1×10^{-2} Pa K s^{-1} (light contours) and 10×10^{-2} Pa K s^{-1} (dark contours).

D.2.3. Transient, zonally-asymmetric eddies

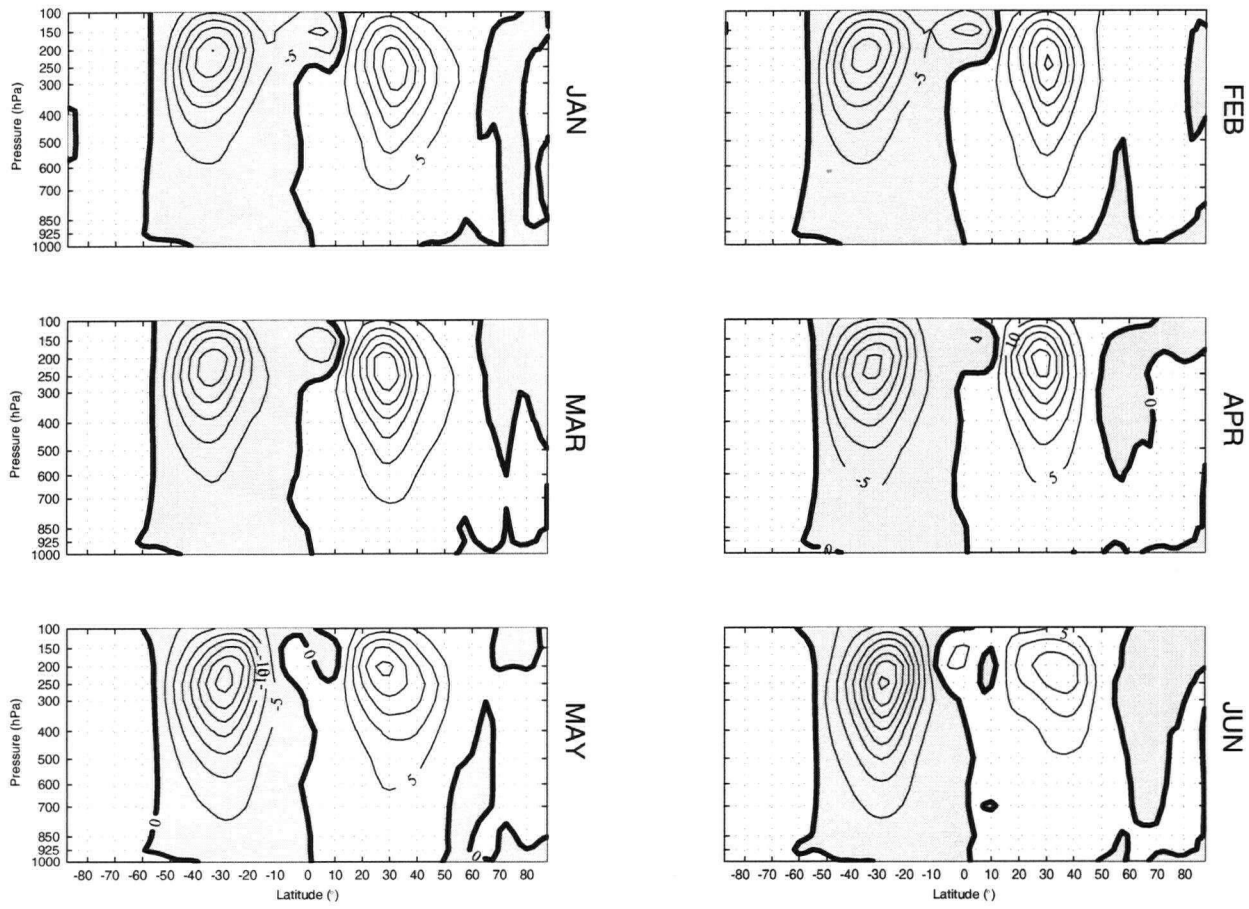

Figure D.23: January-June distributions of $[u^*v^*]\ \cos^2\phi$ for transient, zonally-asymmetric eddies. Units are $m^2\ s^{-2}$ and the contour interval is 5 $m^2\ s^{-2}$.

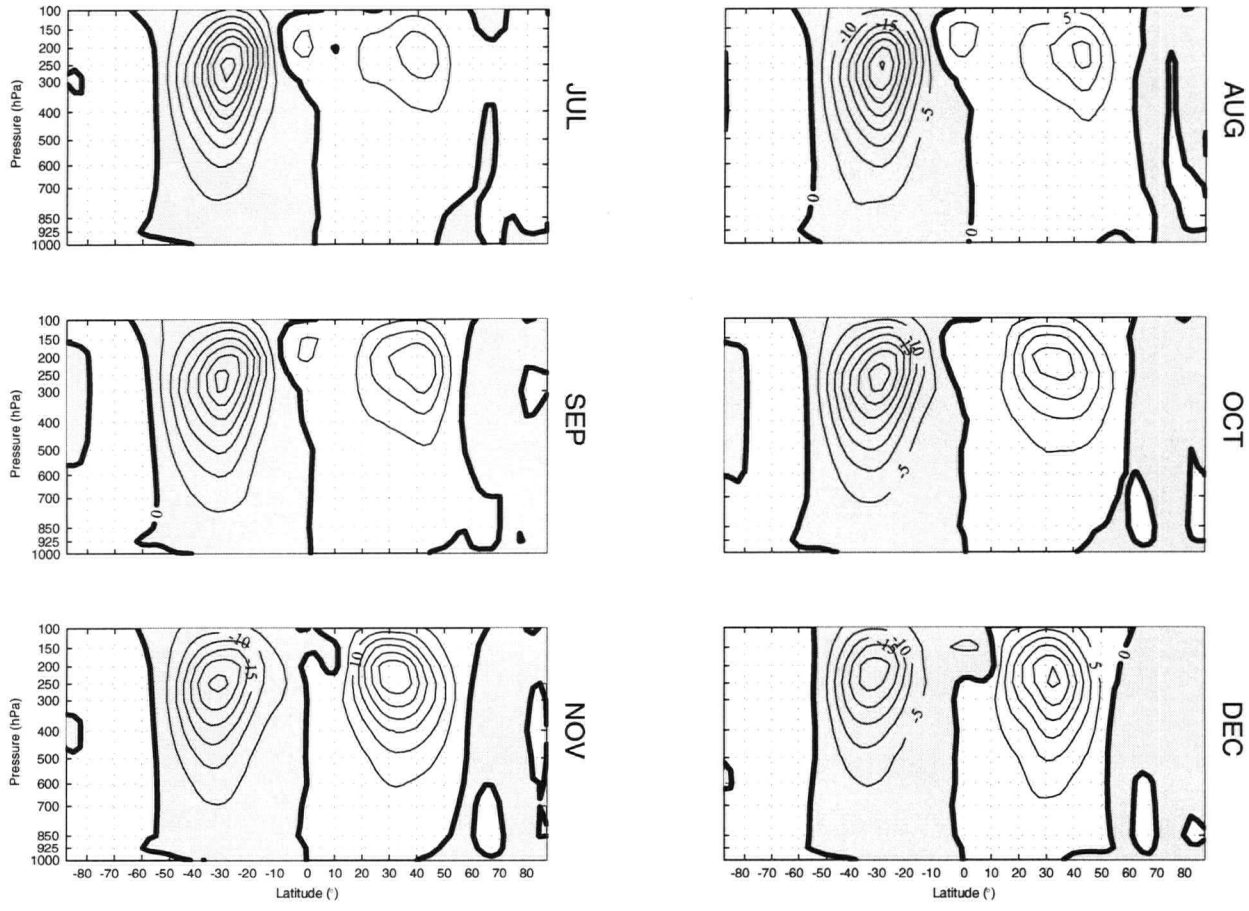

Figure D.24: July-December distributions of $[u^*v^*]\ \cos^2\phi$ for transient, zonally-asymmetric eddies. Units are $m^2\ s^{-2}$ and the contour interval is 5 $m^2\ s^{-2}$.

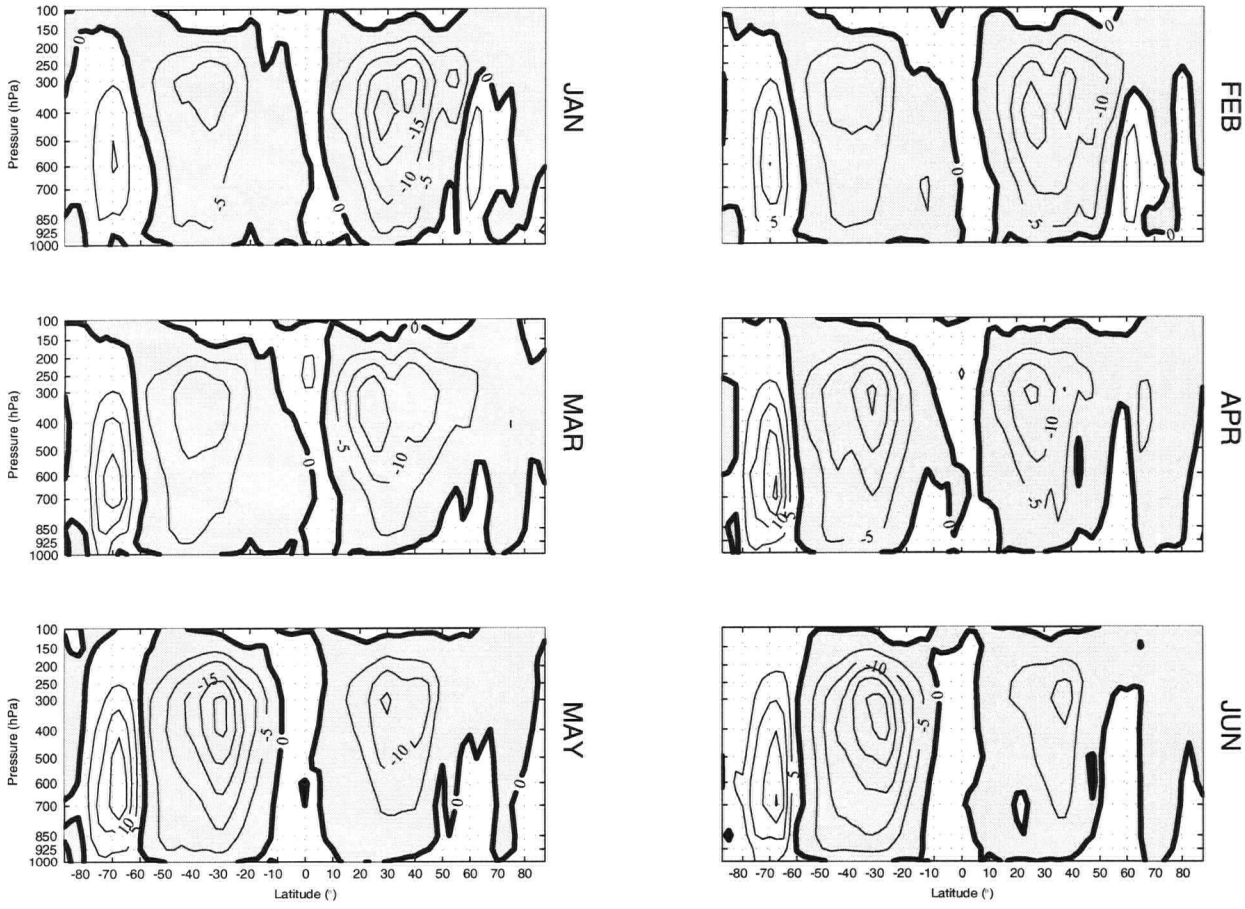

Figure D.25: January-June distributions of $[u^*\omega^*]$ for transient, zonally-asymmetric eddies. Units are $10^{-2}\ m\ Pa\ s^{-2}$ and the contour intervals are $5 \times 10^{-2}\ m\ Pa\ s^{-2}$.

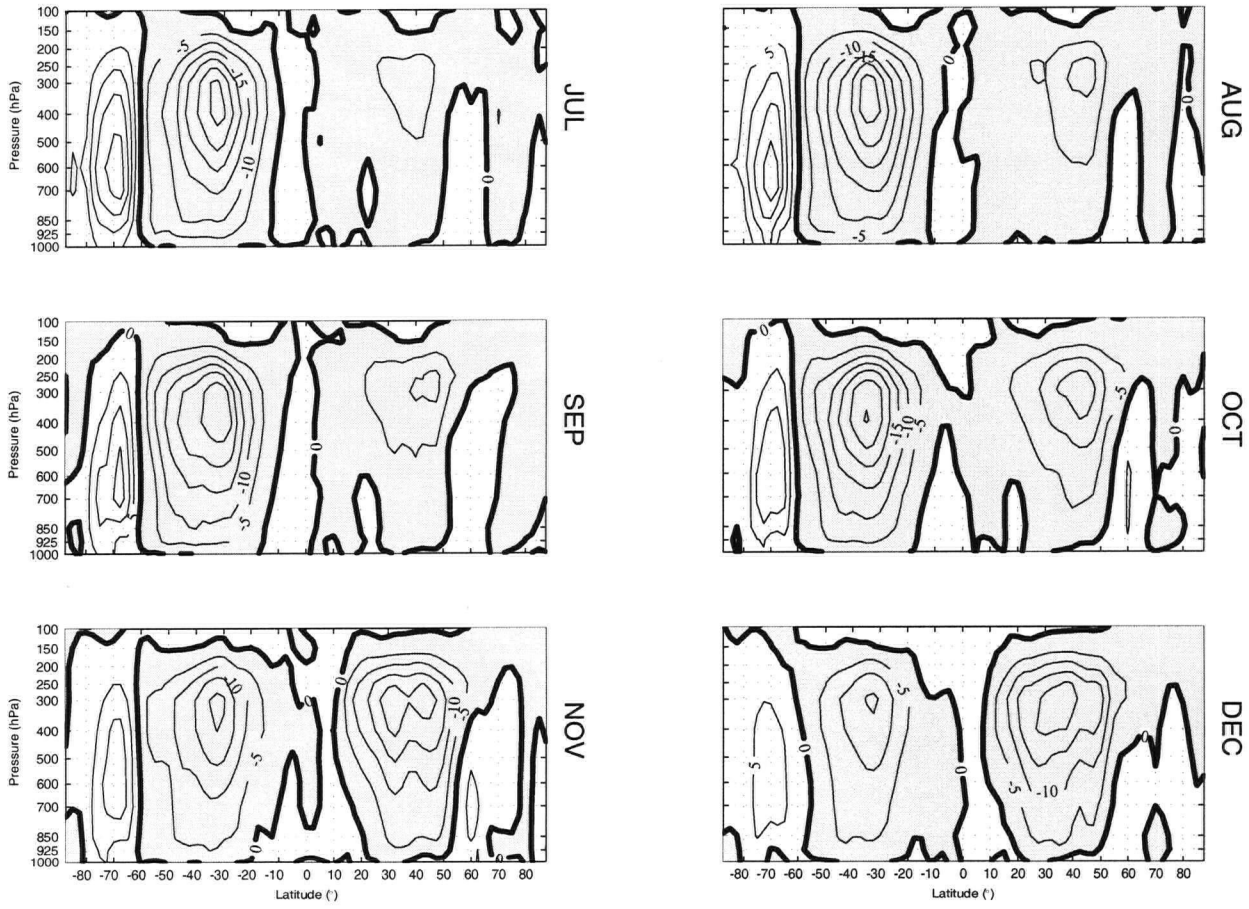

Figure D.26: July-December distributions of $[u^*\omega^*]$ for transient, zonally-asymmetric eddies. Units are $10^{-2}\ m\ Pa\ s^{-2}$ and the contour intervals are $5 \times 10^{-2}\ m\ Pa\ s^{-2}$.

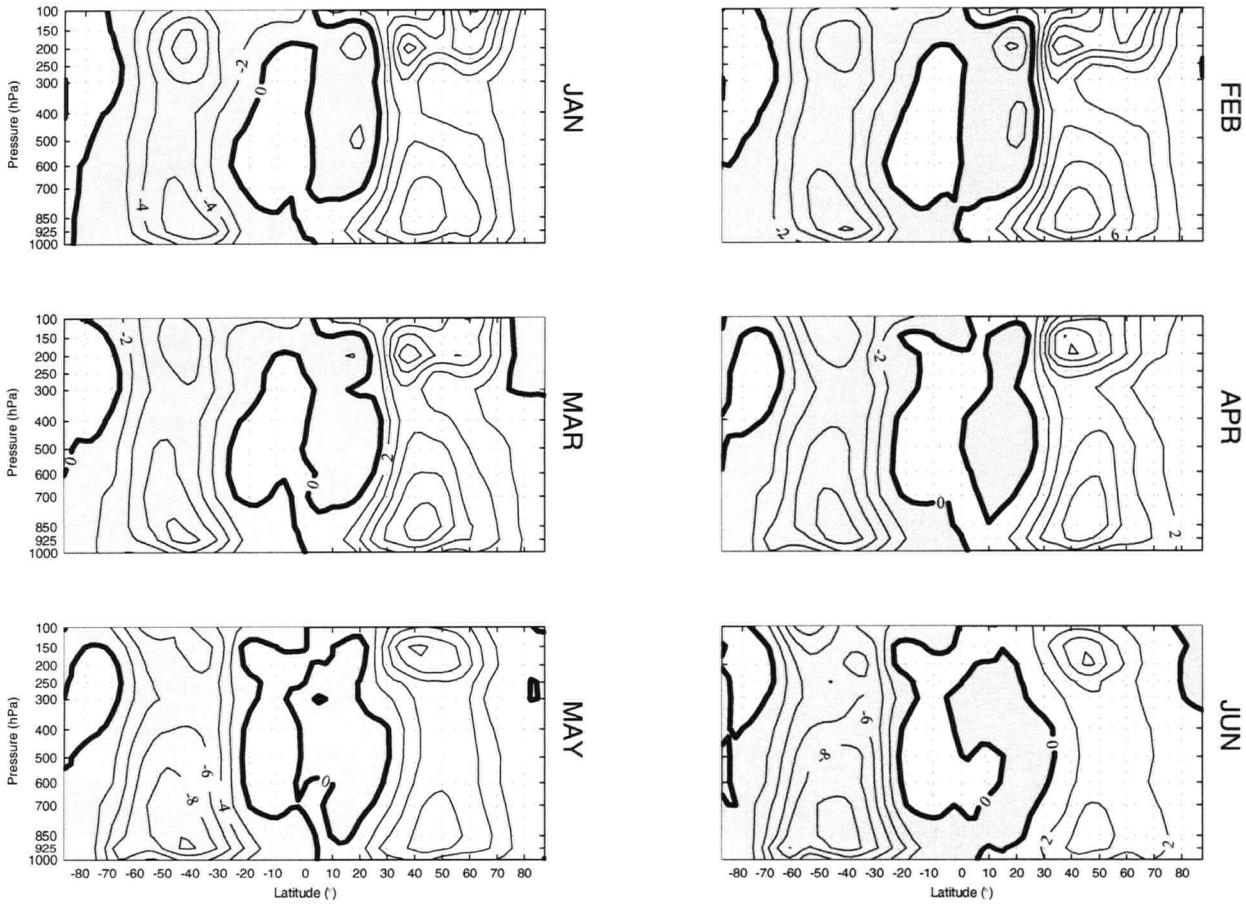

Figure D.27: January-June distributions of $[v^*\theta^*]\cos\phi$ for transient, zonally-asymmetric eddies. Units are $K\ s^{-1}$ and the contour interval is $2\ K\ s^{-1}$.

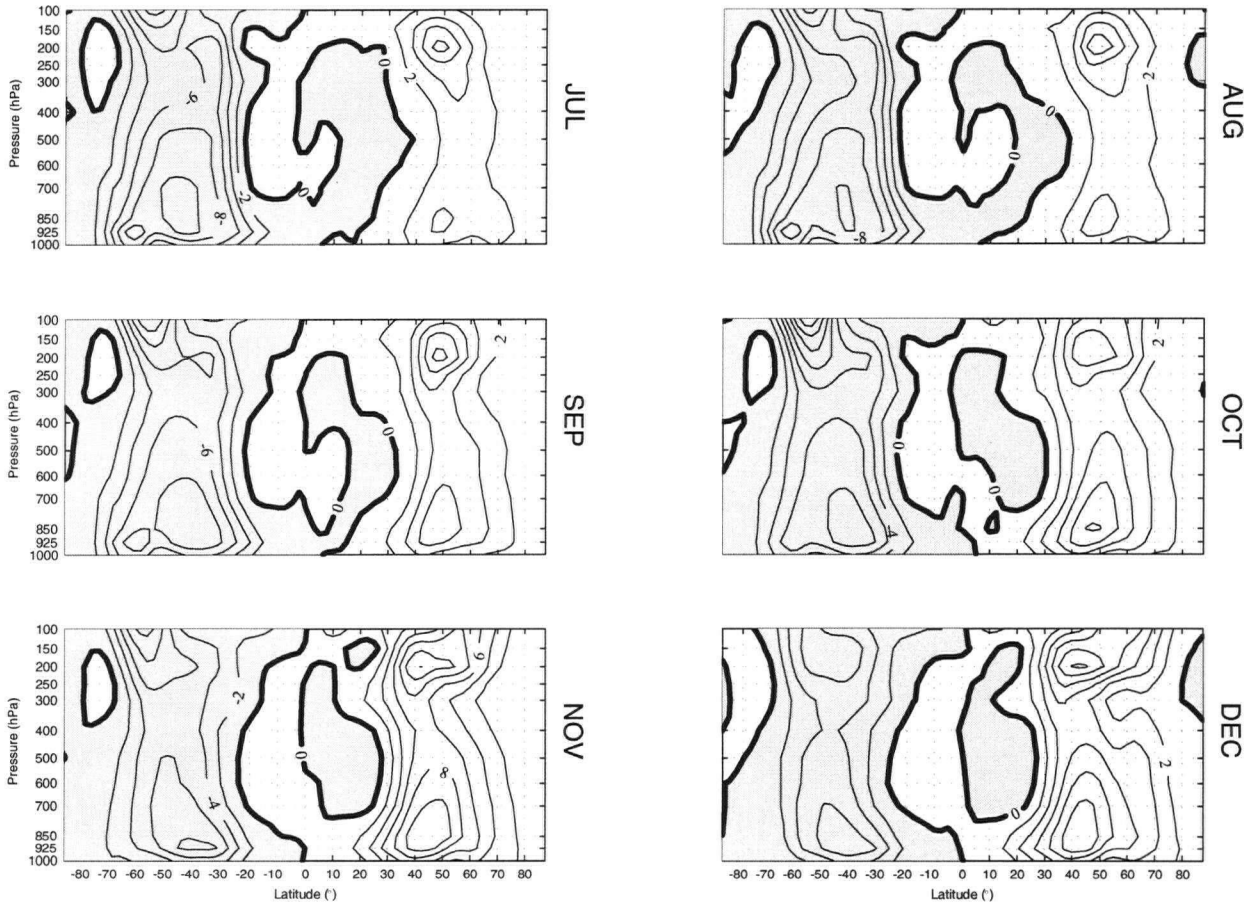

Figure D.28: July-December distributions of $[v^*\theta^*]\cos\phi$ for transient, zonally-asymmetric eddies. Units are $K\ s^{-1}$ and the contour interval is $2\ K\ s^{-1}$.

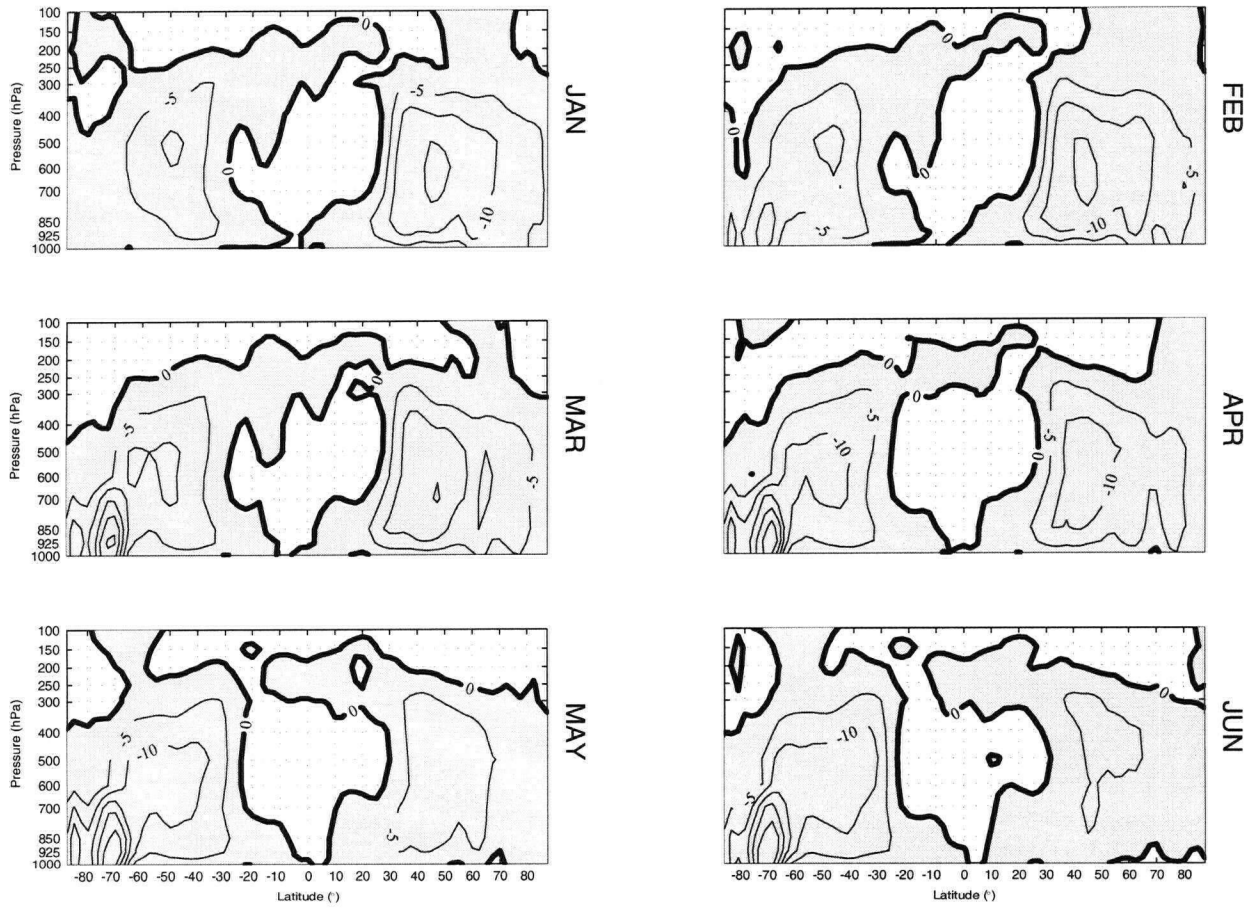

Figure D.29: January-June distributions of $[\omega^*\theta^*]$ for transient, zonally-asymmetric eddies. Units are $10^{-2}\ Pa\ K\ s^{-1}$ and the contour intervals are $5 \times 10^{-2}\ Pa\ K\ s^{-1}$.

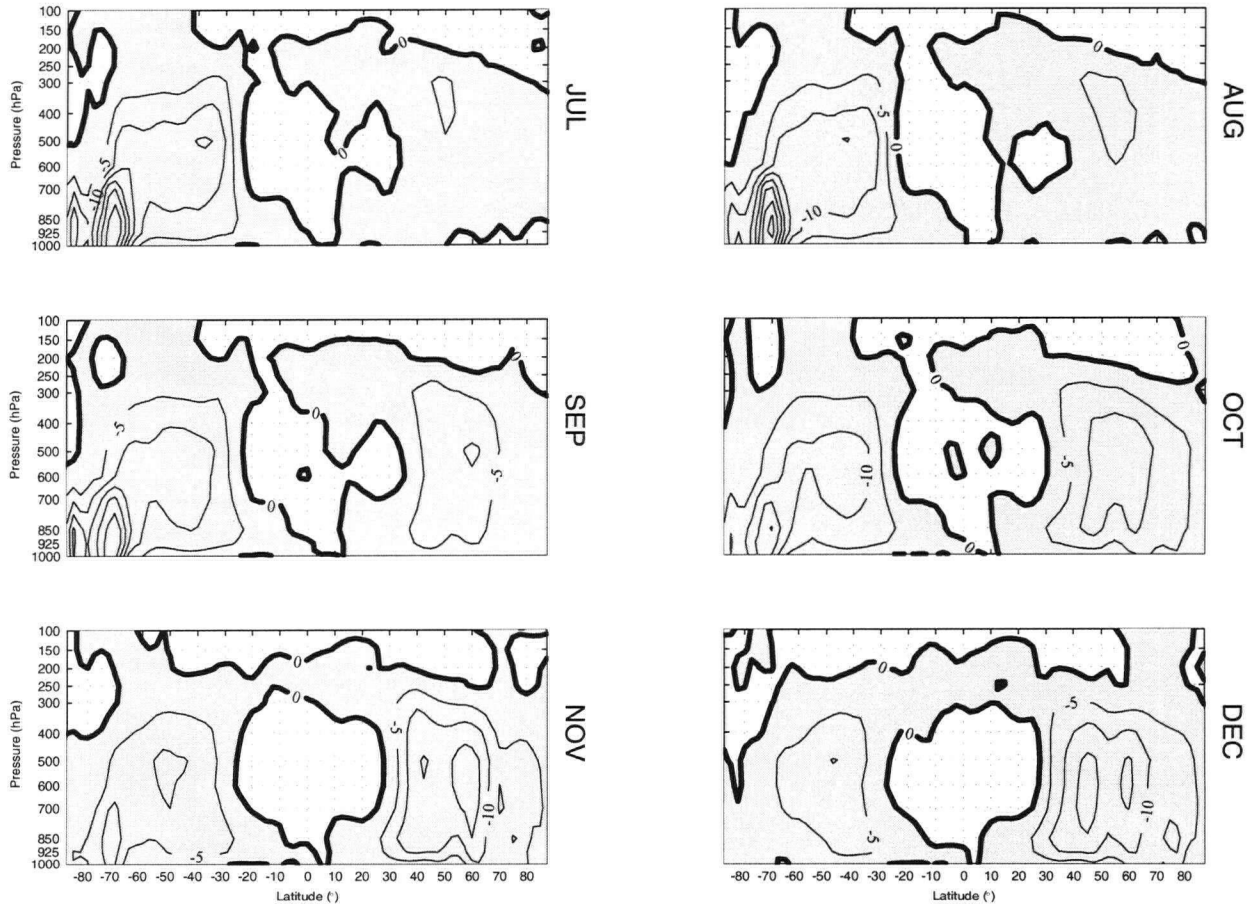

Figure D.30: July-December distributions of $[\omega^*\theta^*]$ for transient, zonally-asymmetric eddies. Units are $10^{-2}\ Pa\ K\ s^{-1}$ and the contour intervals are $5 \times 10^{-2}\ Pa\ K\ s^{-1}$.

D.3. Eddy momentum and heat fluxes

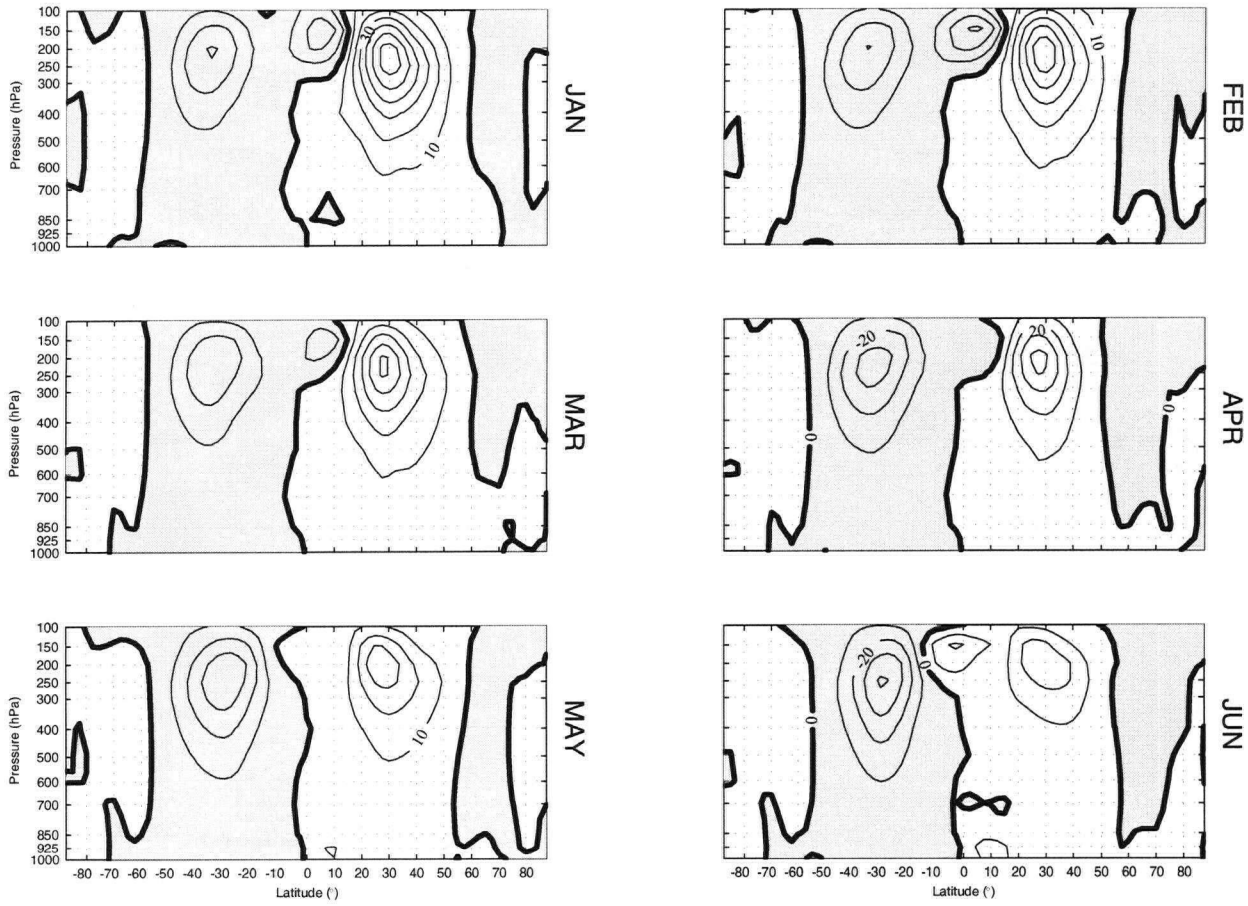

Figure D.31: January-June distributions of northward momentum flux. Units are $m^2\ s^{-2}$ and the contour interval is $10\ m^2\ s^{-2}$.

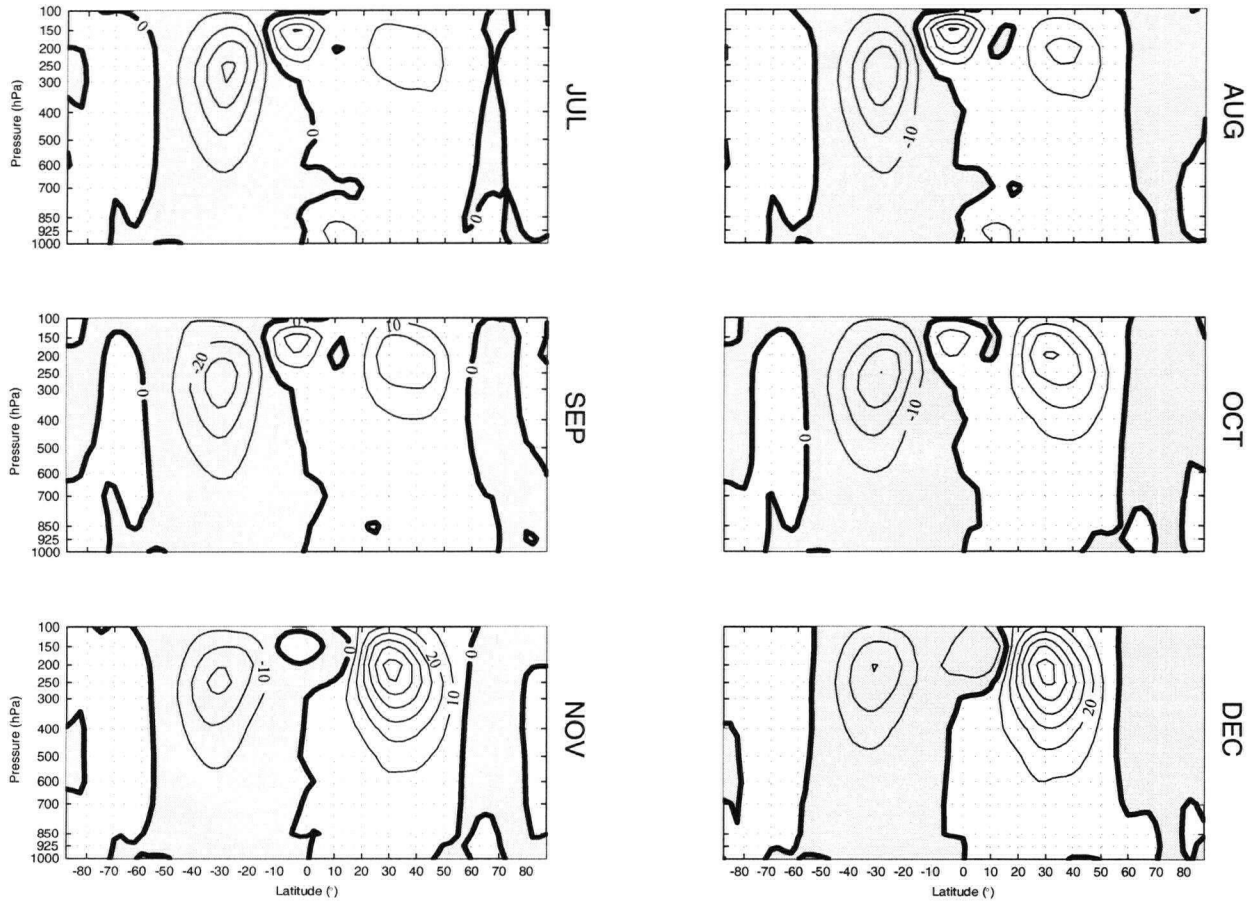

Figure D.32: July-December distributions of northward momentum flux. Units are $m^2\ s^{-2}$ and the contour interval is $10\ m^2\ s^{-2}$.

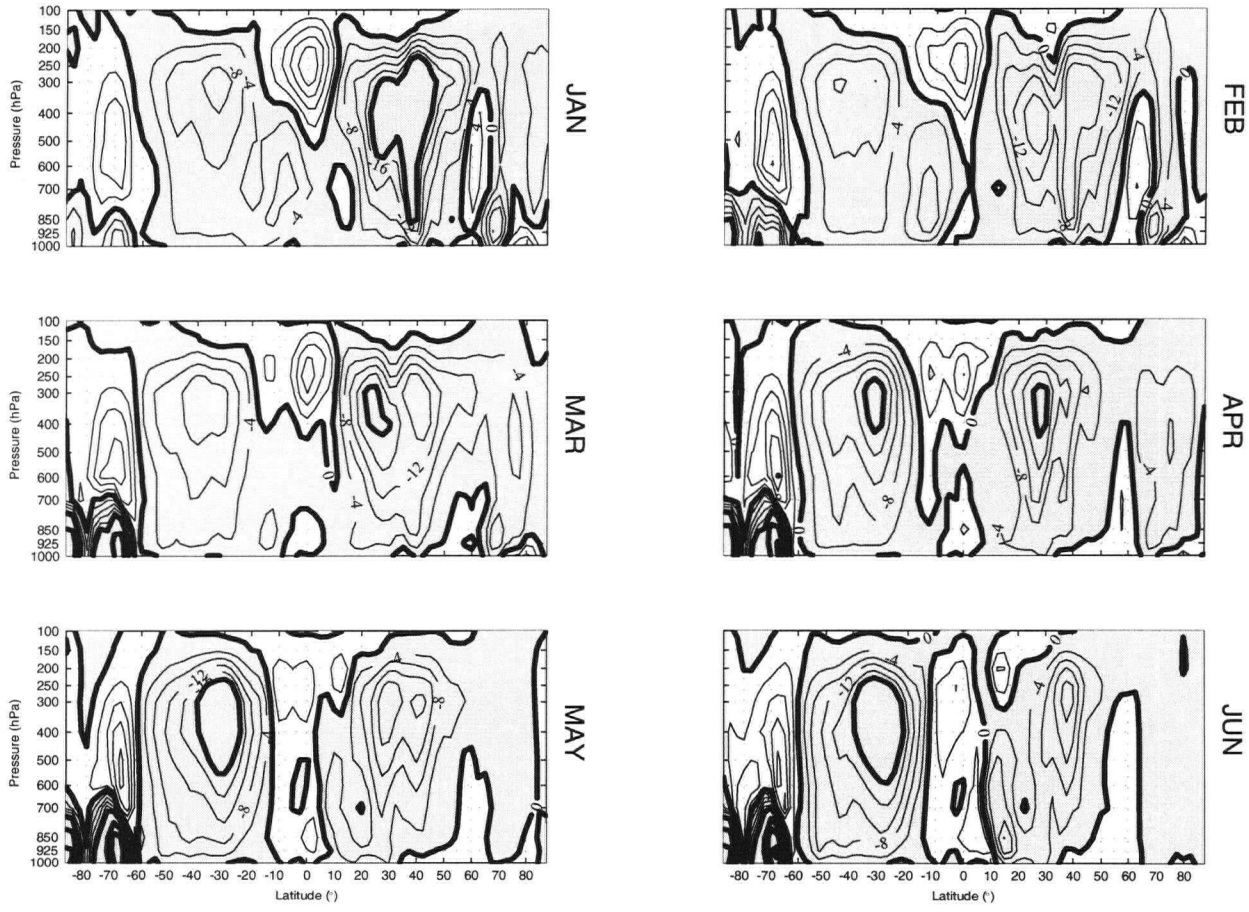

Figure D.33: January-June distributions of upward momentum flux. Units are $10^{-2}\, m\ Pa\ s^{-2}$ and the contour intervals are $4 \times 10^{-2}\, m\ Pa\ s^{-2}$ (light contours) and $20 \times 10^{-2}\, m\ Pa\ s^{-2}$ (dark contours).

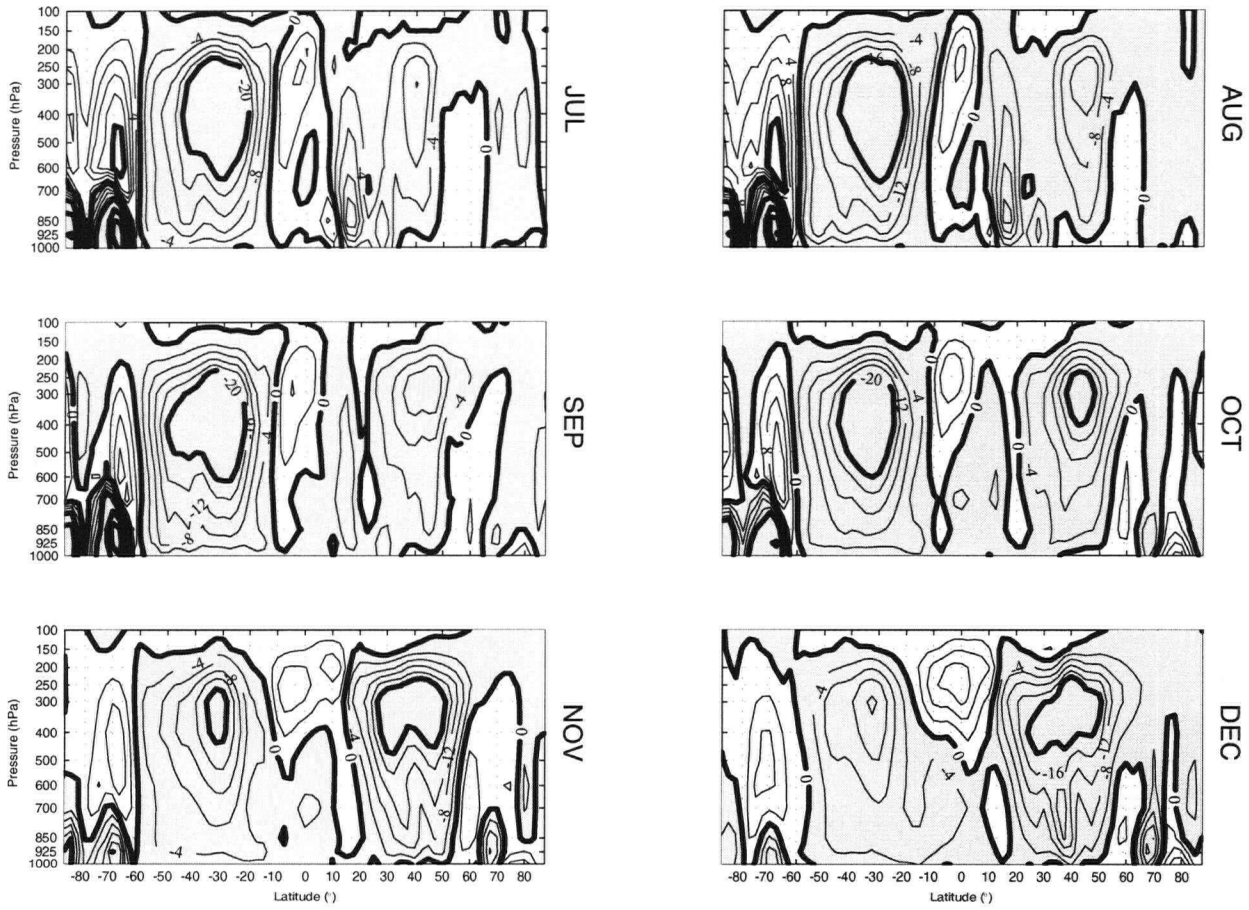

Figure D.34: July-December distributions of upward momentum flux. Units are $10^{-2}\, m\ Pa\ s^{-2}$ and the contour intervals are $4 \times 10^{-2}\, m\ Pa\ s^{-2}$ (light contours) and $20 \times 10^{-2}\, m\ Pa\ s^{-2}$ (dark contours).

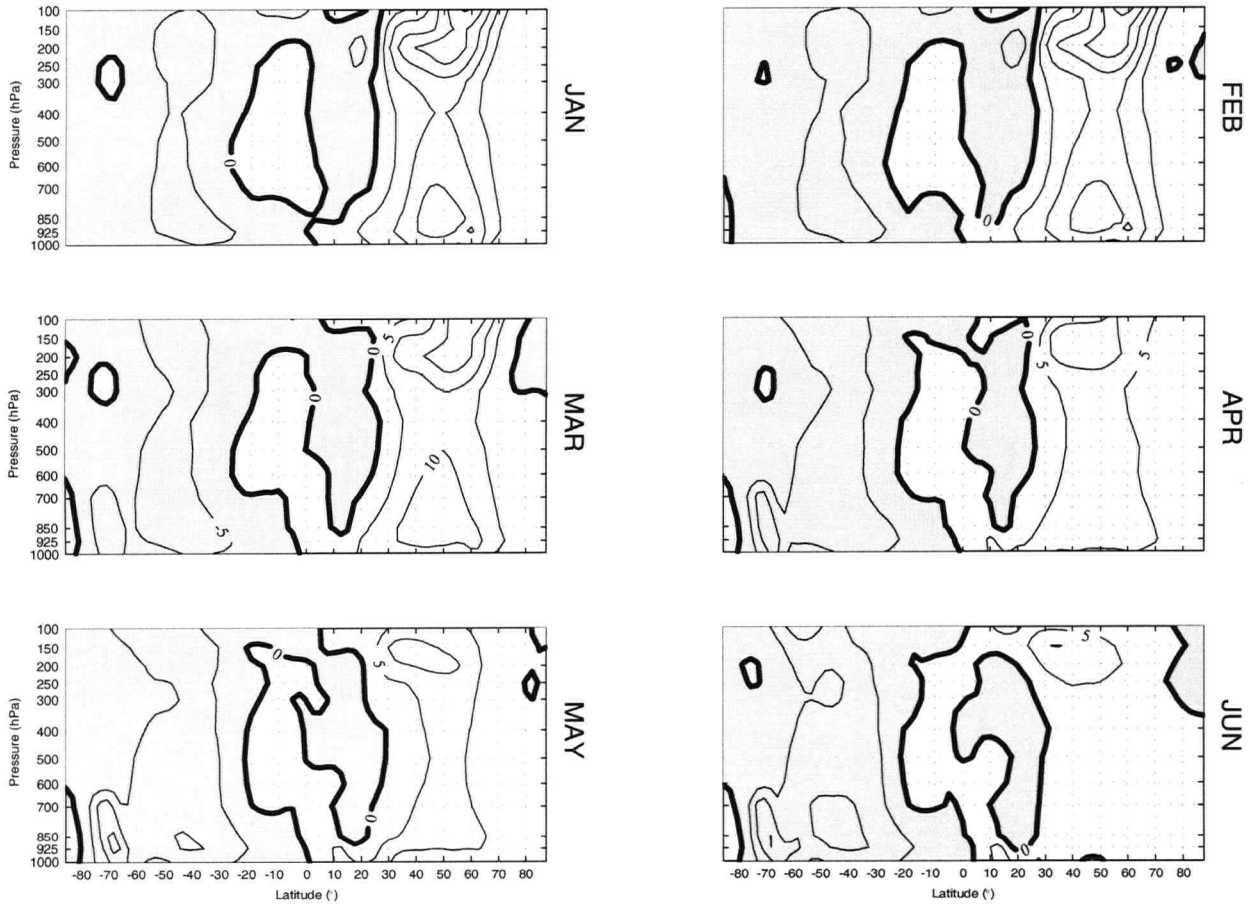

Figure D.35: January-June distributions of northward heat flux. Units are $K\ s^{-1}$ and the contour interval is $5\ K\ s^{-1}$.

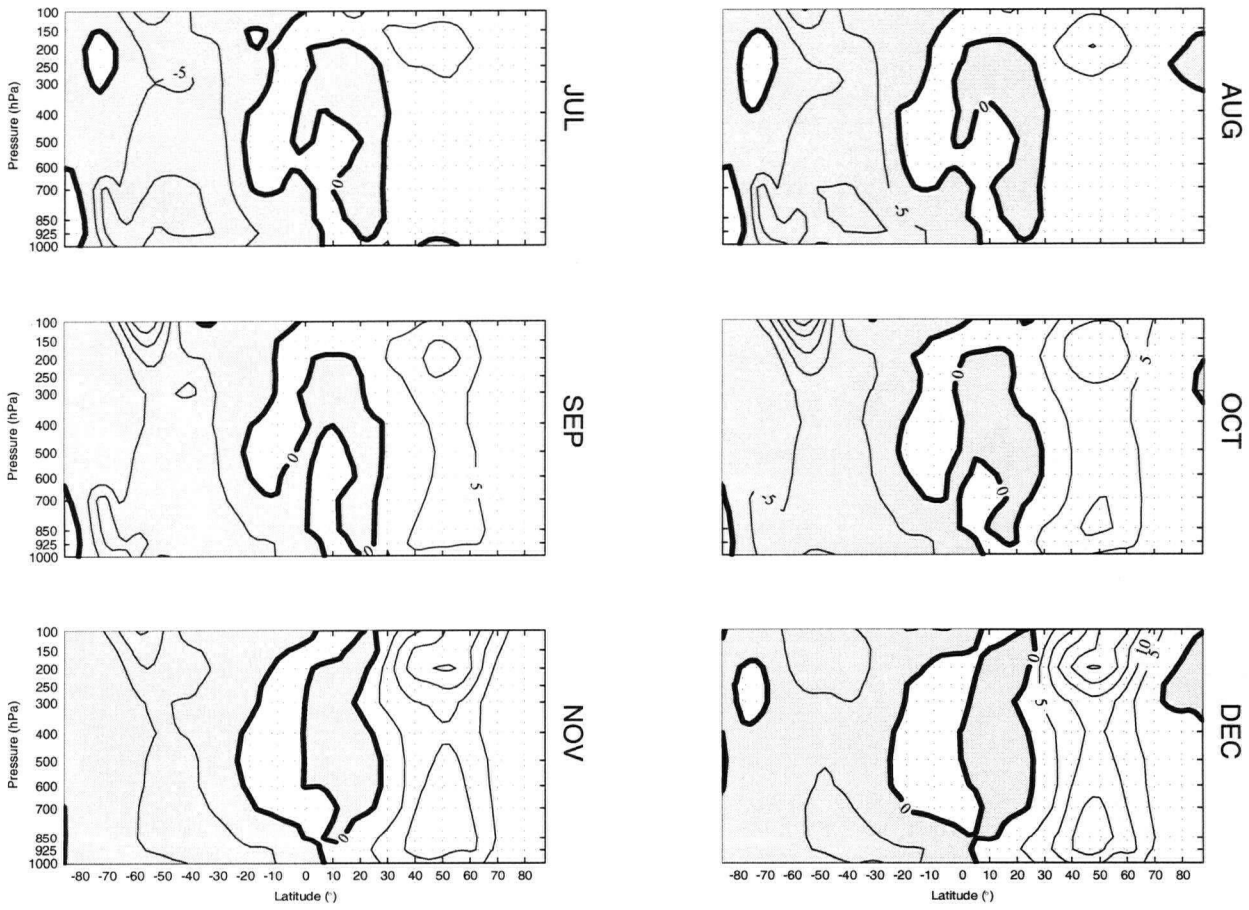

Figure D.36: July-December distributions of northward heat flux. Units are $K\ s^{-1}$ and the contour interval is $5\ K\ s^{-1}$.

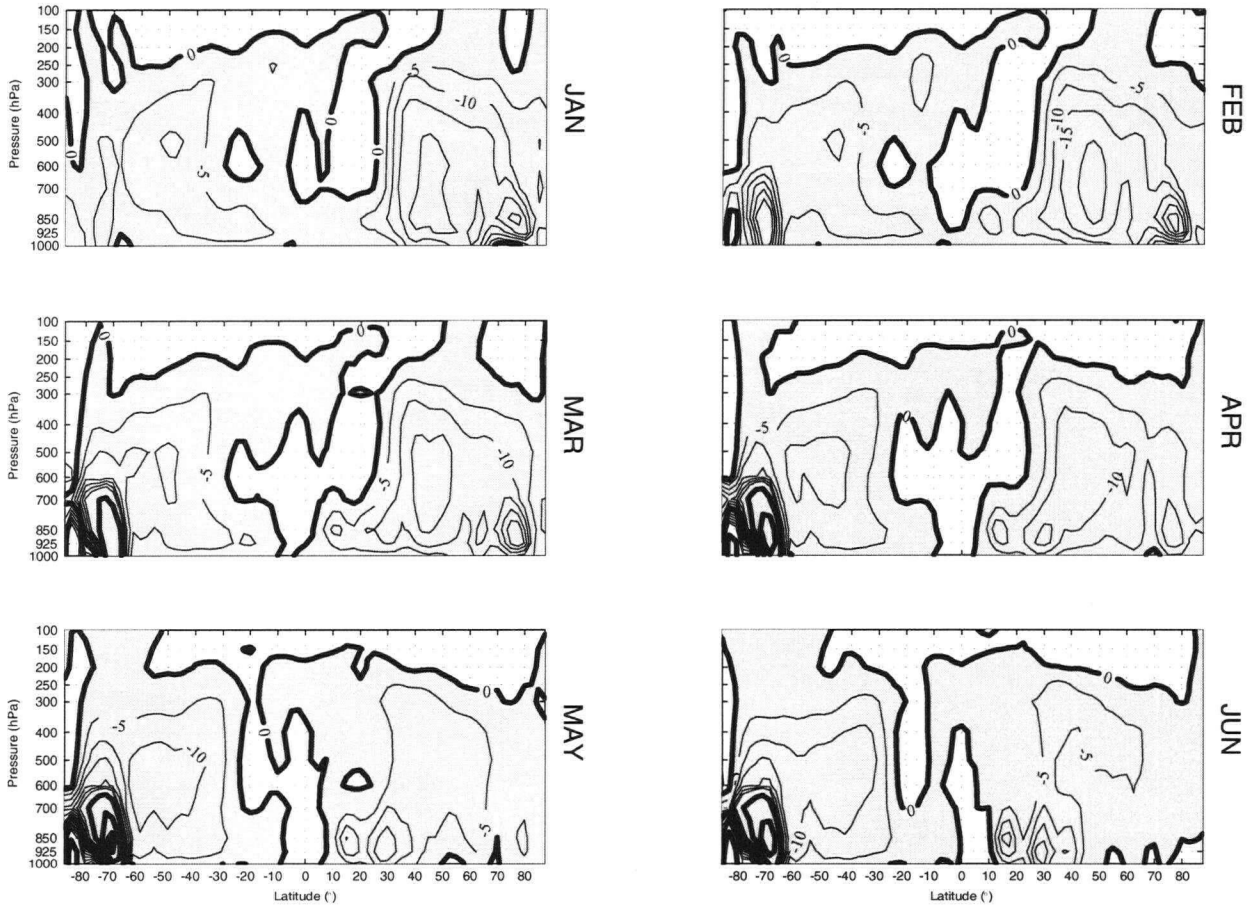

Figure D.37: January-June distributions of upward heat flux. Units are $10^{-2}\ Pa\ K\ s^{-1}$ and the contour intervals are $5 \times 10^{-2}\ Pa\ K\ s^{-1}$ (light contours) and $50 \times 10^{-2}\ Pa\ K\ s^{-1}$ (dark contours).

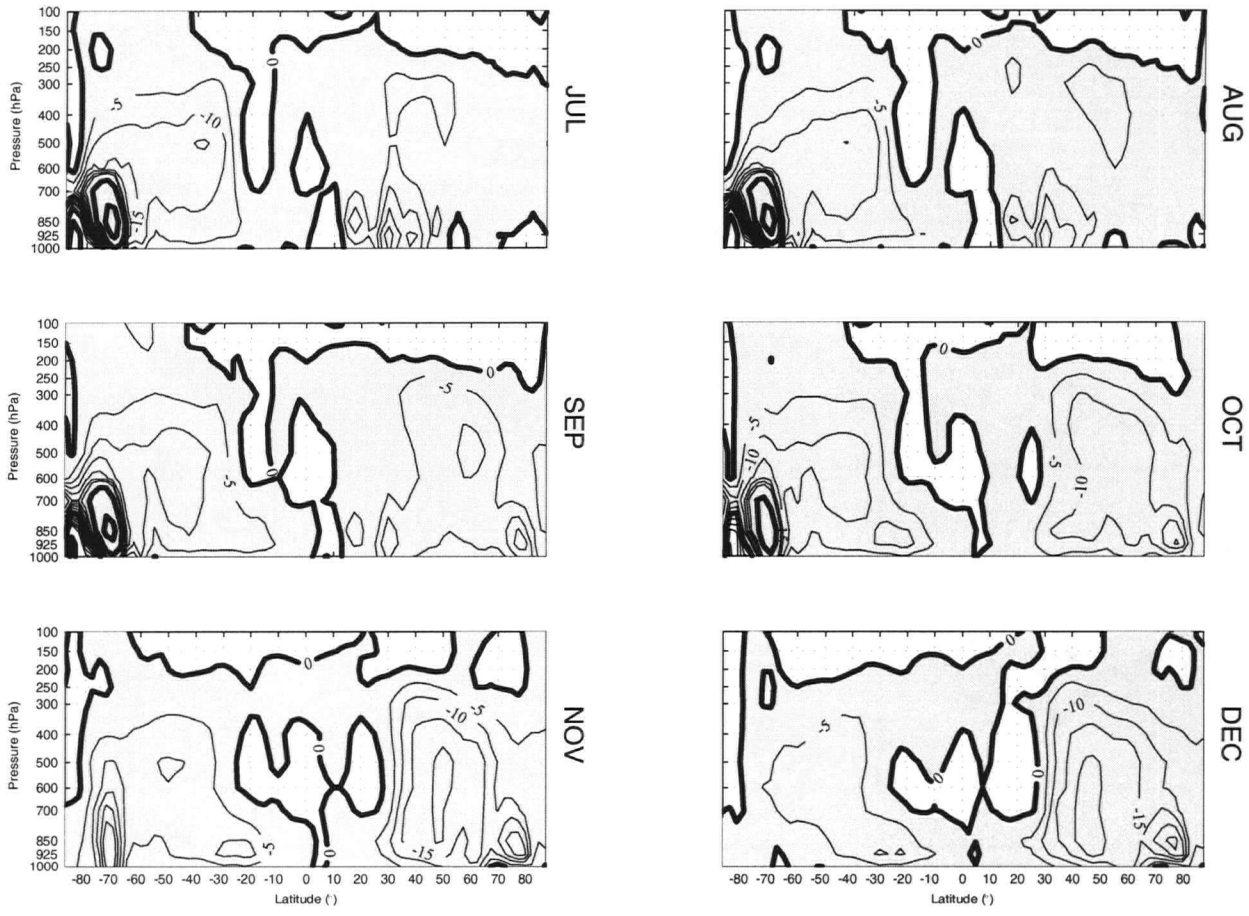

Figure D.38: July-December distributions of upward heat flux. Units are $10^{-2}\ Pa\ K\ s^{-1}$ and the contour intervals are $5 \times 10^{-2}\ Pa\ K\ s^{-1}$ (light contours) and $50 \times 10^{-2}\ Pa\ K\ s^{-1}$ (dark contours).

D.4. Streamfunction ψ

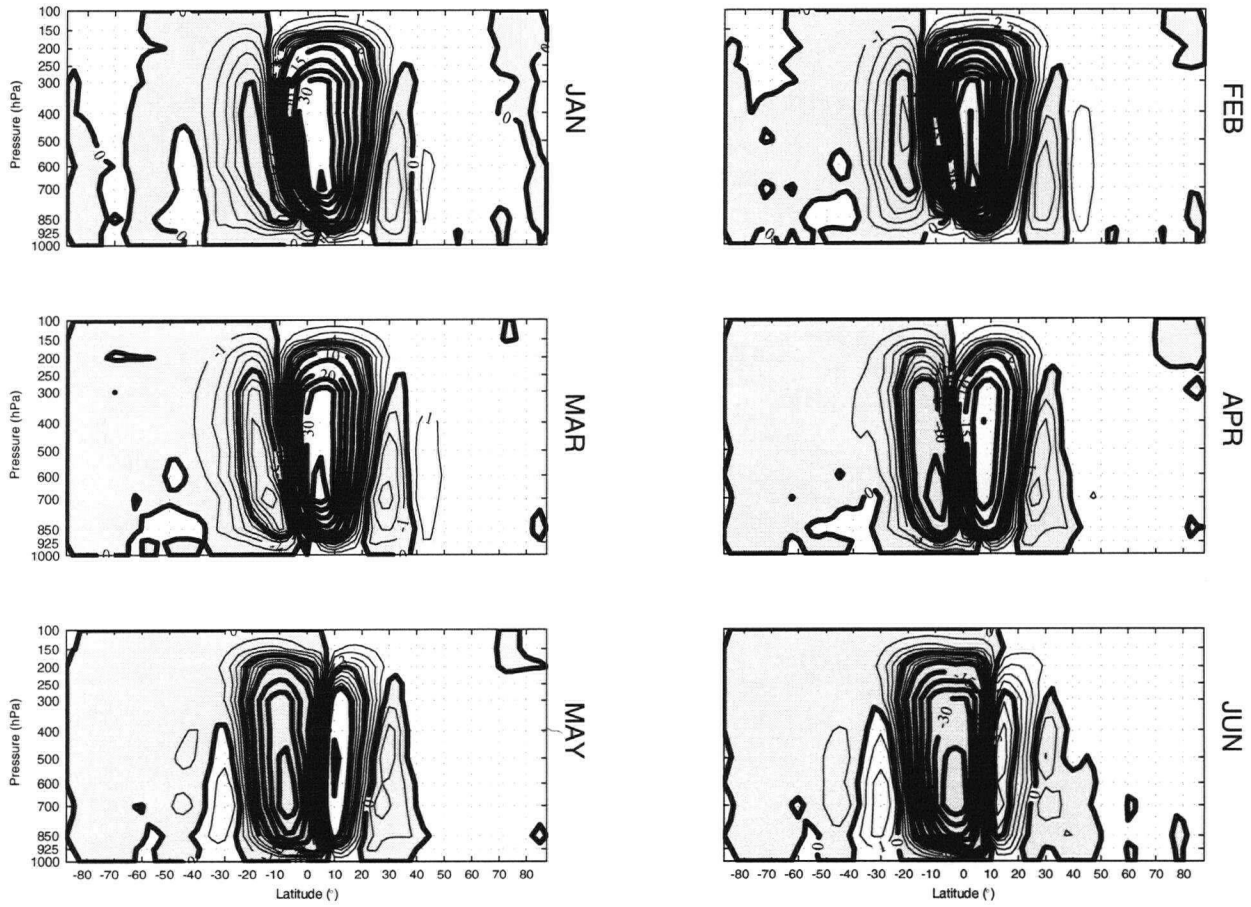

Figure D.39: January-June distributions of ψ due to diabatic heating (Hadley circulation). Units are $10^3\ m\ Pa\ s^{-1}$ and the contour intervals are $1 \times 10^3\ m\ Pa\ s^{-1}$ (light contours) and $5 \times 10^3\ m\ Pa\ s^{-1}$ (dark contours).

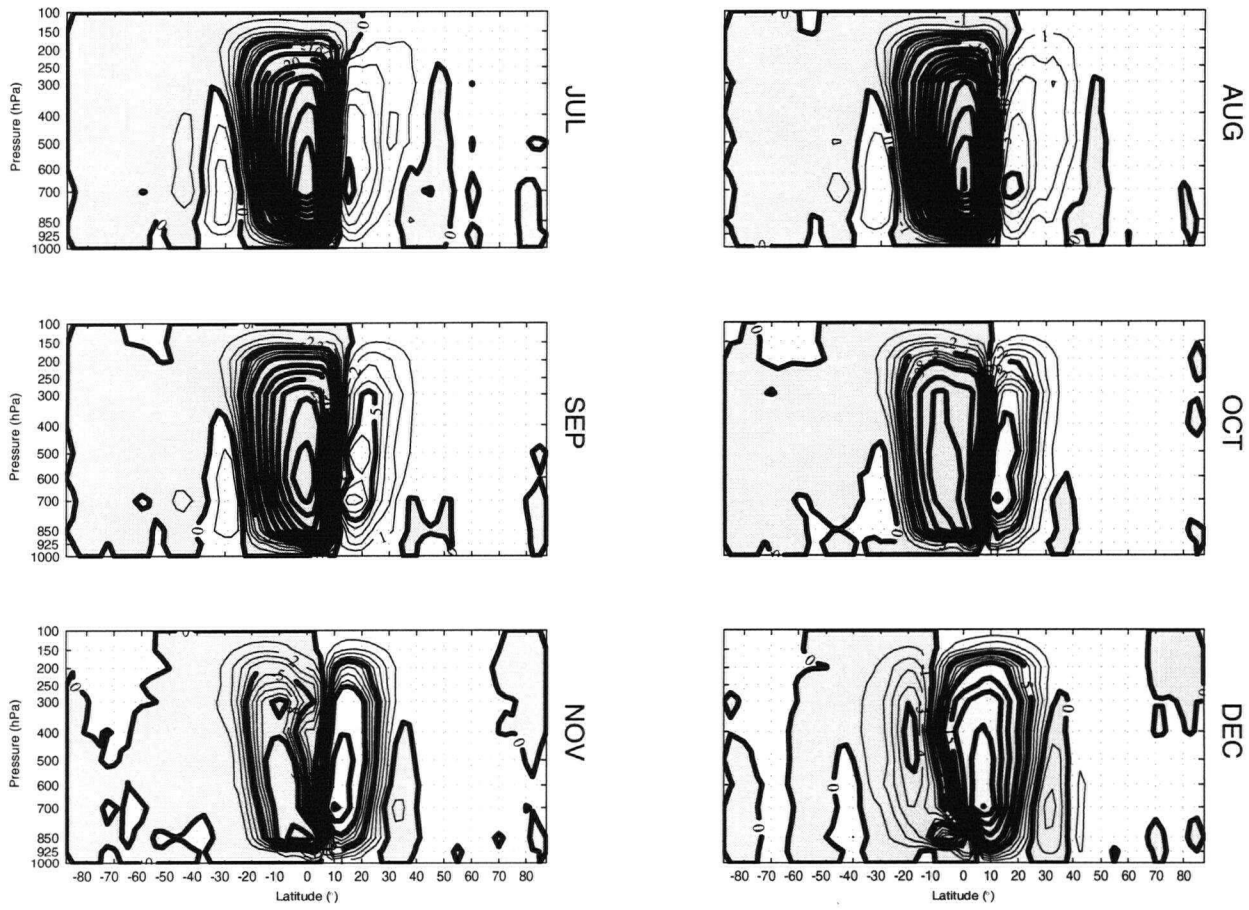

Figure D.40: July-December distributions of ψ due to diabatic heating (Hadley circulation). Units are 10^3 m Pa s^{-1} and the contour intervals are 1×10^3 m Pa s^{-1} (light contours) and 5×10^3 m Pa s^{-1} (dark contours).

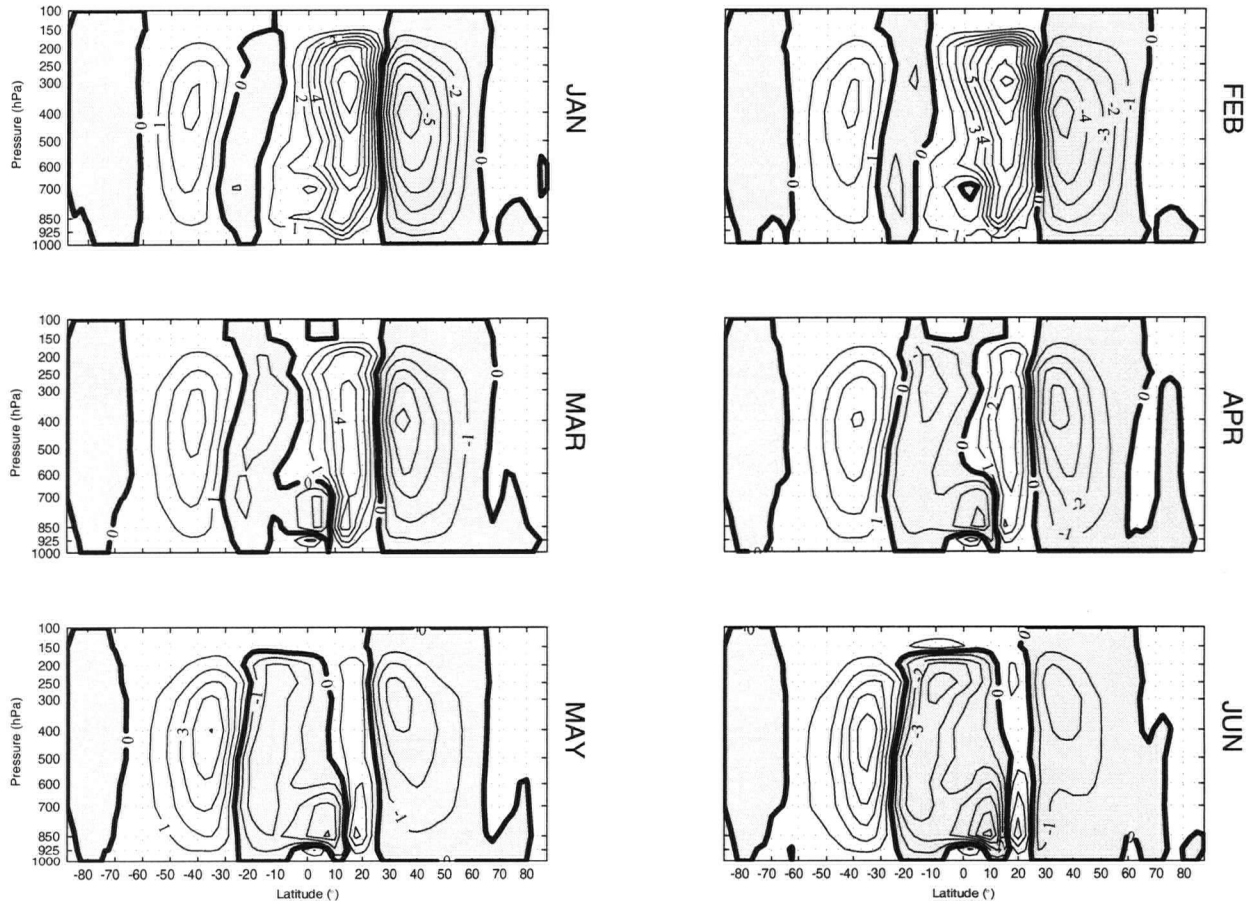

Figure D.41: January-June distributions of the eddy-induced component of ψ (Ferrel circulation). Units are $10^3\ m\ Pa\ s^{-1}$ and the contour interval is $1 \times 10^3\ m\ Pa\ s^{-1}$.

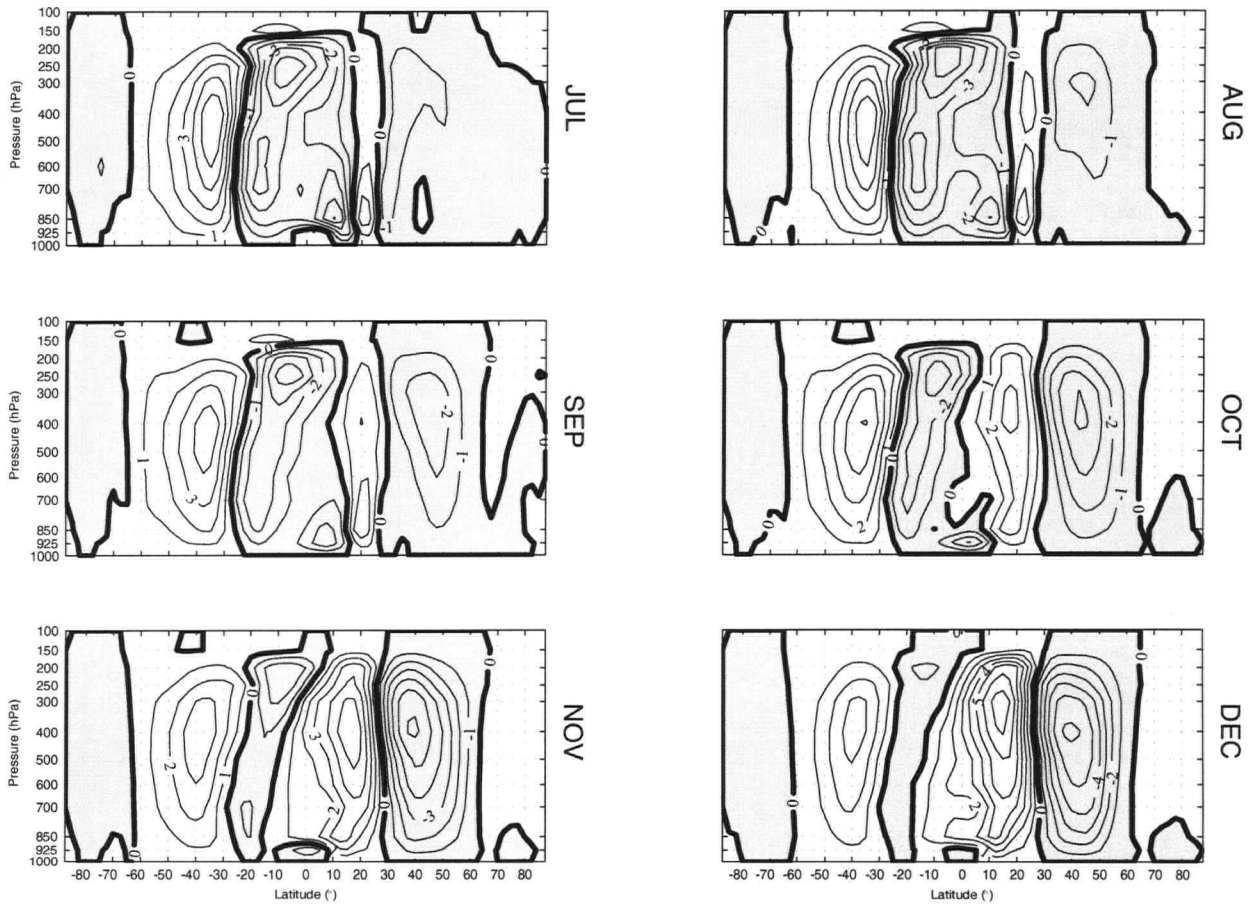

Figure D.42: July-December distributions of the eddy-induced component of ψ (Ferrel circulation). Units are $10^3\ m\ Pa\ s^{-1}$ and the contour interval is $1 \times 10^3\ m\ Pa\ s^{-1}$.

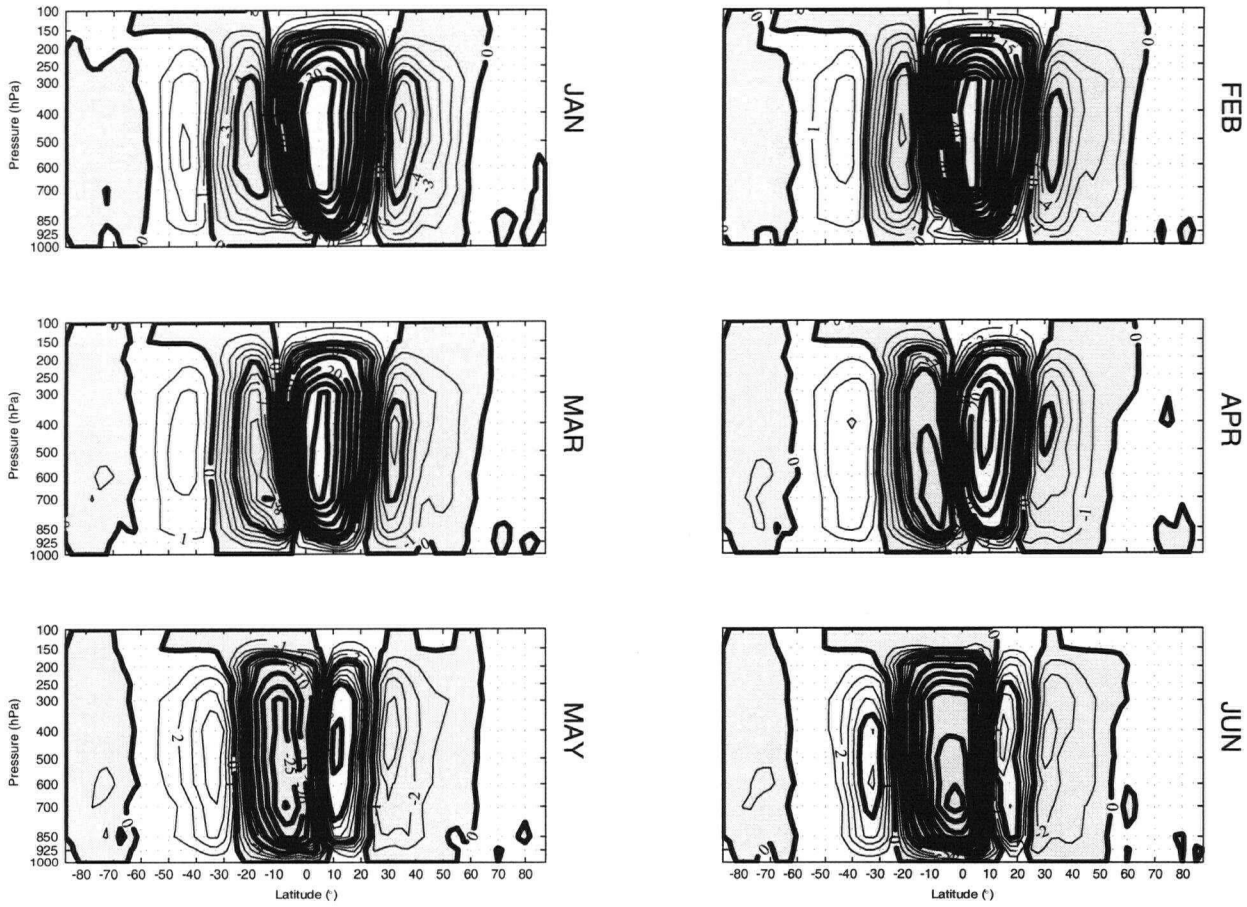

Figure D.43: January-June distributions of ψ. Units are $10^3\ m\ Pa\ s^{-1}$ and the contour intervals are $1 \times 10^3\ m\ Pa\ s^{-1}$ (light contours) and $5 \times 10^3\ m\ Pa\ s^{-1}$ (dark contours).

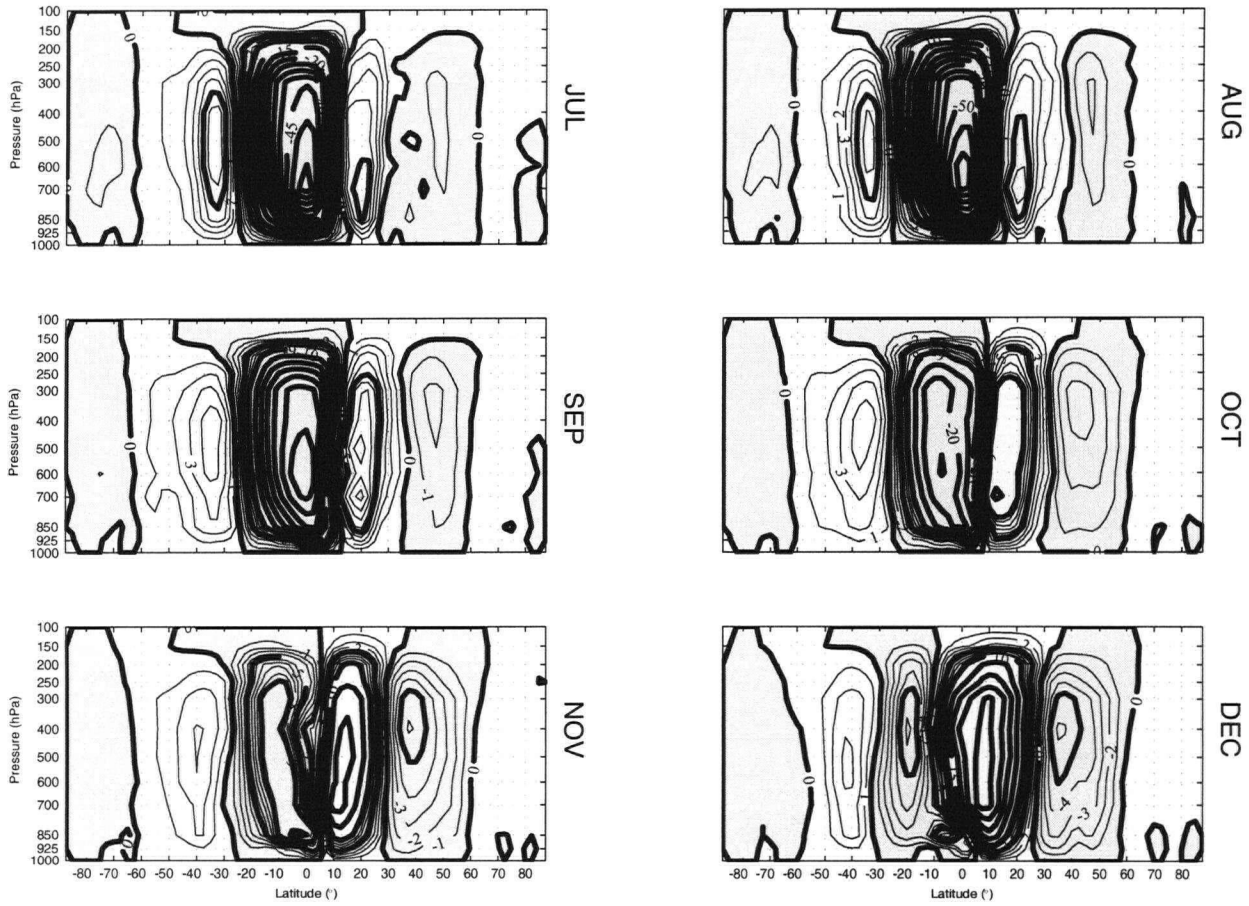

Figure D.44: July-December distributions of ψ. Units are $10^3\ m\ Pa\ s^{-1}$ and the contour intervals are $1 \times 10^3\ m\ Pa\ s^{-1}$ (light contours) and $5 \times 10^3\ m\ Pa\ s^{-1}$ (dark contours).

D.5. Zonal Kinetic Energy Production

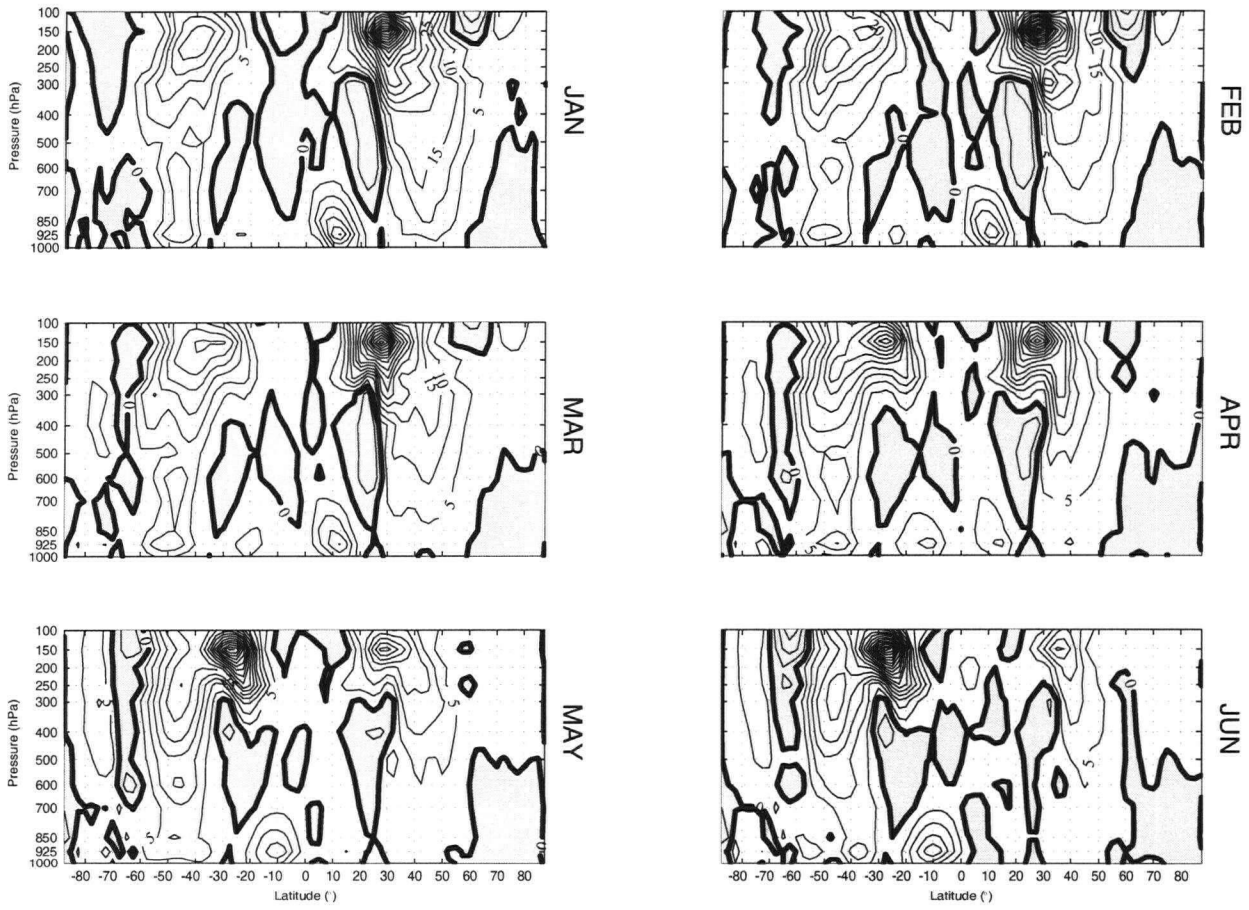

Figure D.45: January-June zonal kinetic energy production due to eddy-flux forcing. The units are $10^{-5}\ m^2\ s^{-3}$ and the contour interval is $5 \times 10^{-5}\ m^2\ s^{-3}$.

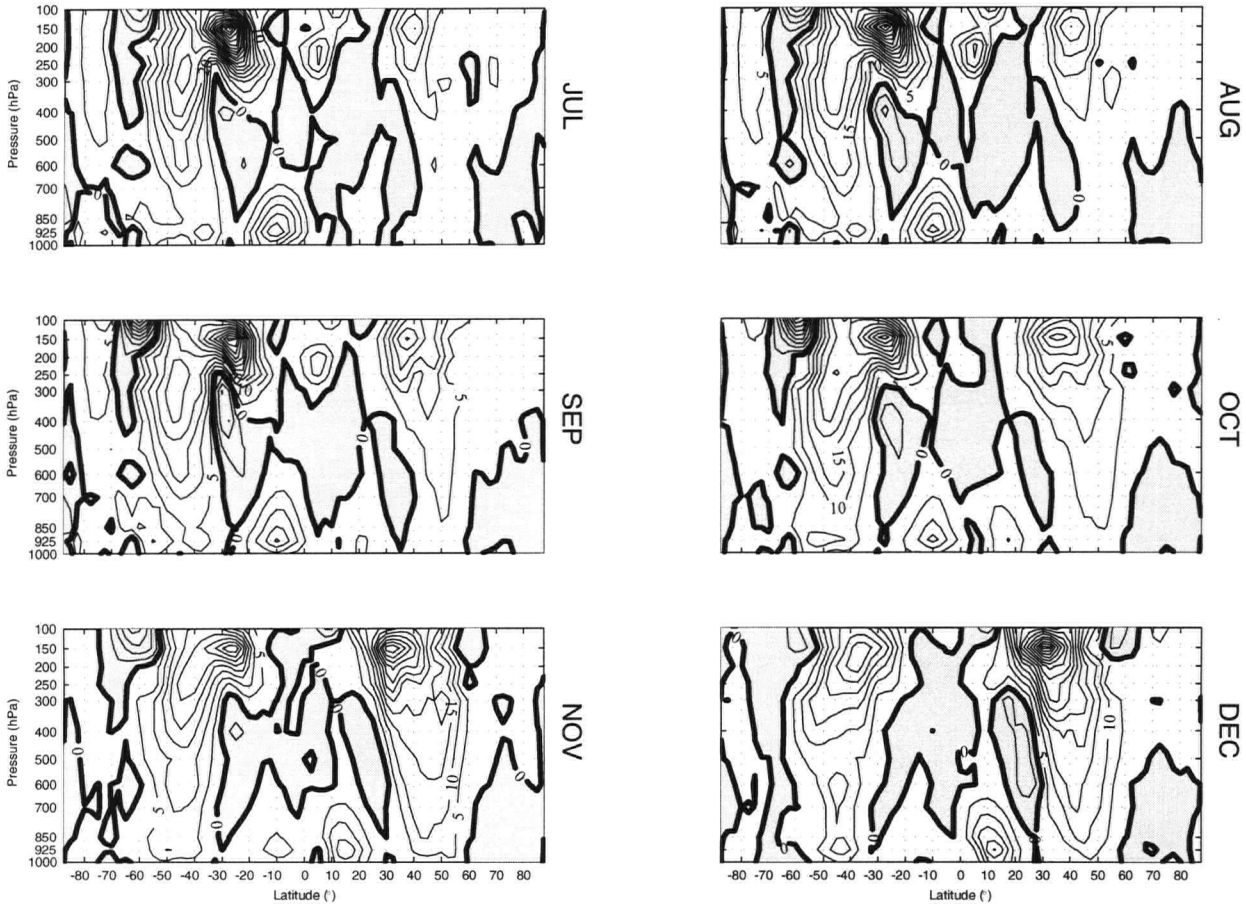

Figure D.46: July-December zonal kinetic energy production due to eddy-flux forcing. The units are $10^{-5}\ m^2\ s^{-3}$ and the contour interval is $5 \times 10^{-5}\ m^2\ s^{-3}$.